Mathematical and computational modeling of flexoelectricity at fixed and moving interfaces, fracture surfaces and contact.

Jordi Barceló Mercader

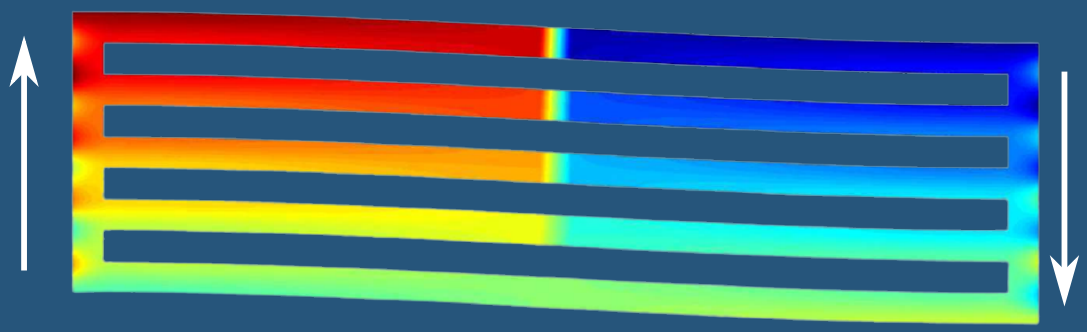

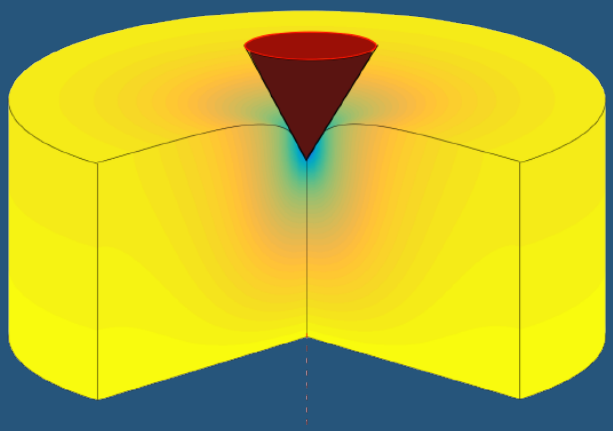

Doctoral Thesis
Barcelona, January 2023

Mathematical and computational modeling of flexoelectricity at fixed and moving interfaces, fracture surfaces and contact.

Jordi Barceló Mercader

Doctoral Thesis
Advisor: Irene Arias Vicente
Barcelo, January 2023

School of Mathematics and Statistics
Doctoral Degree in Applied Mathematics
Universitat Politècnica de Catalunya

UNIVERSITAT POLITÈCNICA DE CATALUNYA
BARCELONATECH
Facultat de Matemàtiques i Estadística

Doctoral Degree in Applied Mathematics
School of Mathematics and Statistics
Universitat Politècnica de Catalunya

Mathematical and computational modeling of flexoelectricity at fixed and moving interfaces, fracture surfaces and contact.

by

Jordi Barceló Mercader

LaCàN: Laboratory of Mathematical and Computational Modeling

Advisor: Irene Arias
Barcelona, June 27, 2023

“Pretend it’s a seed.”
–Flik. A bug’s life

Abstract

Mathematical and computational modeling of flexoelectricity at fixed and moving interfaces, fracture surfaces and contact.

Jordi Barceló Mercader

Flexoelectricity is a two-way coupling between strain gradient and polarisation or strain and polarization-gradient. Harnessing flexoelectricity as a functional property requires gradient engineering. This is a major step from the uniform-field configurations of piezoelectric devices, since piezoelectricity couples strains and polarisation. Gradients can be generated by non-uniform deformation, such as bending and torsion, or through non-uniform material distributions, electrode configurations and complex geometries. Gradient engineering thus requires accurate quantitative modelling tools capable of efficiently dealing with all these elements with high-physical fidelity in order to build engineering tools for the design of flexoelectric devices.

From a mathematical point of view, flexoelectricity is modelled as a system of coupled high-order PDEs. This poses important challenges to computationally solving boundary value problems in general multi-material samples with complex geometries and electrode configurations.

In this thesis, a theoretical and computational model for flexoelectricity in the presence of interfaces has been developed and implemented in the context of the hierarchical B-spline immersed boundary approach. This framework has been used to study physical material interfaces, as well as fictitious interfaces such as generalized periodicity unit cell boundaries. The former has been used in multimaterial symmetry-breaking arrangements up-scaling flexoelectricity in electromechanical devices. For the latter case, an elegant and efficient implementation making use of the periodicity of the B-spline bases functions has been derived and used for the design and analysis of flexoelectric architected periodic lattice metamaterials. Moving interfaces such as cracks and ferroelectric domain boundaries have also been studied by coupling phase-field models for fracture and ferroelectric microstructure accounting for flexoelectricity. Finally, flexoelectricity has been shown as a plausible cause for the asymmetric tribology observed in ferroelectrics in tight collaboration with experimentalists.

Keywords: Flexoelectricity, Continuum mechanics, Interfaces, Periodicity, Ferroelectrics, Fracture.

Acknowledgments

Me gustaría empezar dando las gracias a la persona que empezó todo el proceso y sin la cual, esta tesis no se hubiera llevado a cabo, la profesora Irene Arias.

Seguidamente, me gustaría agradecer a todas las personas que han participado dentro del proyecto de FLEXOCOMP, en especial a Onofre Marco, David Codony, Alice Mocci, Hossein Mohammadi, Prakhar Gupta, Monica Dingle, Juan Carlos Tarín y Francesco Greco. También, a parte del equipo de HiPerLife, entre ellos Guillermo Vilanova que siempre me ha ayudado cuando lo he necesitado, y a los professores Seungbum Hong y Patrycja Paruch junto con el estudiante de doctorado Seongwoo Cho con quien hemos colaborado.

Un sincero agradecimiento a la profesora Sonia Fernández-Méndez quien en muchos momentos ha sido un rayo de luz en un caos de mis pensamientos. A continuación, me gustaría dar las gracias a mi familia, sustento de mi alma, que me ha levantando en los momentos que más lo necesitaba y en quienes siempre podré confiar.

Finalmente, doy las gracias a los fondos que han financiado esta tesis doctoral, que son, European Research Council (Starting Grant 679451 to Prof. Irene Arias) y la Generalitat de Catalunya (FI AGAUR).

Contents

List of Figures

List of Tables

Chapter 1

Introduction

1.1 Motivation

When observing our surroundings, we notice that many essential tools in our daily life need a power supply to work. Human-made machines need energy to perform task that very often rely on mechanics. Energy is massively transported in form of electricity, which is supplied to the machines and needs to be transformed into mechanical action. This process is called electromechanical transduction and strongly relies on electroactive materials. Electroactive devices that convert an electric input into a mechanical output are called actuators in contrast to sensors that convert mechanical output into an electric signal. Another group of electroactive devices is the energy harvester that collects energy from an ambient mechanical source and converts it to electric energy to power autonomous electronic devices or circuits. .

Sensors are commonly used in electronic devices that, nowadays, are used all around the world, for example, the contact sensor in mobile phones or the pressure sensor in modern keyboards, among others. Still, they can be used in biomedical devices, such as blood pressure measurement devices (Terry *et al.*, 1990) or fetal ultrasounds (Karlsson *et al.*, 1996). Actuators can yield well-controlled mechanical forces with application to robotics, motors or medical devices (Ciofani and Menciassi, 2012). The last group is formed by energy harvesters; this group includes devices to harvest and store energy from the heart's motion (Dagdeviren *et al.*, 2014), muscle-driven nanogenerators (Li *et al.*, 2010) or even textile nanogenerators (Wu *et al.*, 2012), among others. We refer the reader to Dagdeviren *et al.* (2016) to see a wide range of applications illustrated in Fig. 1.1.

Most of the currently used electroactive devices rely on piezoelectric ceramics (Gautschi, 2006, Safaei *et al.*, 2019, Sinha *et al.*, 2009). Piezoelectricity is the ability to generate an electric response to a mechanical stimulus. Mathematically, it can be written as a coupling between polarisation $\boldsymbol{P}$ and stress $\boldsymbol{\sigma}$, governed by a third rank tensor of piezoelectric coefficients $\boldsymbol{d}$, as

$$P_l = d_{lij}\sigma_{ij}. \tag{1.1}$$

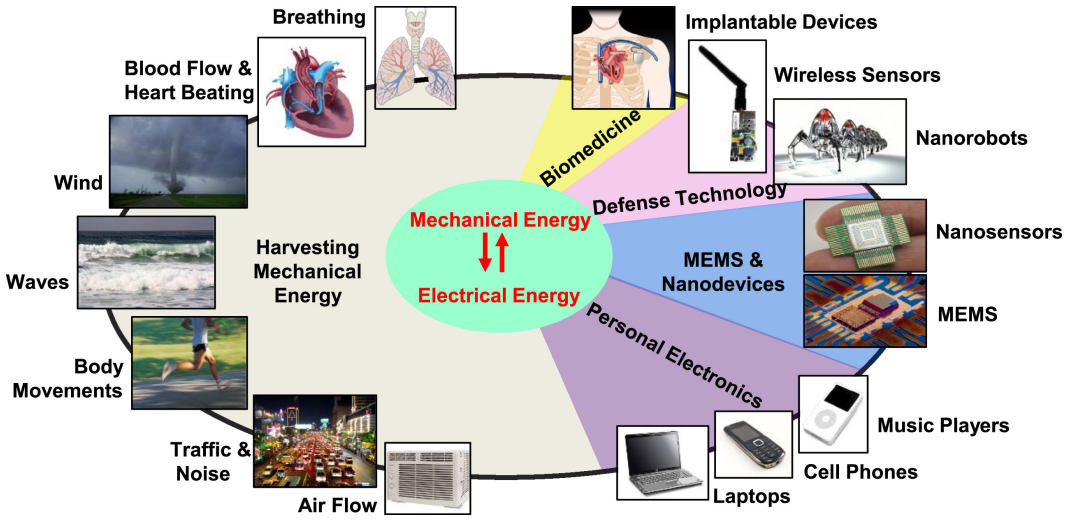

Figure 1.1: Application for electroactive materials. Some of these applications could be energy harvesters from the heart's motion, wind waves or even body movements. They can also widely be used in electronic devices as personal electronics or defence technology, among others. The image is taken from Dagdeviren *et al.* (2016).

Conversely, piezoelectrics also deform $\boldsymbol{\varepsilon}$ under an electric bias $\boldsymbol{E}$,

$$\varepsilon_{ij} = d_{lij} E_{ij}. \tag{1.2}$$

Piezoelectric materials can be either crystalline, ceramic or polymeric. In each case, piezoelectricity is the result of a different mechanism, but in all cases, it emerges from the existence of an internal electric dipole, which can be ionic or polymeric. Mechanical deformation induces changes in these dipoles, resulting in an electrical signal. Conversely, the interaction of the internal dipoles with external electric fields produces a mechanical deformation of the material. This mechanism is schematically illustrated on a cartoon of an ionic crystalline piezoelectric in Fig. 1.2. Piezoelectricity has two significant characteristics that we want to highlight. The first is reversibility, an opposite input yields an opposite output, and the second is its scale invariance.

The presence of an internal dipole in the material is thus key to piezoelectricity. For this, a non centro-symmetric arrangement of ions or molecules is mandatory. In the case of ionic crystals, of the thirty-two point groups, just twenty are non-centrosymmetric. Another limitation, the best piezoelectric materials are brittle ferroelectric ceramics, exhibiting fracture toughnesses in the order of that of glass. The most widely used piezoelectric material is PZT, with a 60% content of toxic lead. The crystalline structure of the grains depends on temperature, and the material looses its piezoelectric properties above a certain transition temperature, the Curie temperature. Common piezoelectrics have quite low Curie temperatures, precluding

their use in extreme conditions. For instance, commercial PZT compositions have a Curie temperature around 350°C, which limits the operating temperature range to 150 – 250°C. Although the world, especially Occident, is trying to replace lead-based ceramics, it is still far from achieving it (Cross, 2004, Hong *et al.*, 2016, Saito *et al.*, 2004, Wu, 2020).

Piezoelectricity has been widely investigated since its demonstration by Pierre Curie in 1880. Its coupling with other physics, like pyroelectricity (temperature) or ferroelectricity, has also been studied. Besides piezoelectricity, other electromechanical couplings are also possible. All of them have been considered and explored to potentially overcome some of the limitations of piezoelectrics in specific situations.

On one hand, soft dielectrics such as dielectric elastomers exhibit electrostriction, the elongation of the material resulting from the movement of cations in the direction of an external electric field and anions in the opposite direction. This displacement accumulates throughout the bulk material and results in an overall elongation in the direction of the field. Similarly, the Maxwell stress effect is generated by electrostatic forces between positive and negative charges on the interfaces of electrodes and dielectric elastomer films. Both effects depend quadratically on the polarisation, and thus a reversal of the applied electric field does not reverse the sign of the induced strain. Furthermore, only actuation is achieved, and sensing is not possible, i.e. these mechanisms do not induce an electric signal upon deformation.

Another electromechanical coupling mechanism is provided by flexoelectricity. Although negligible at the macroscale, it is a universal effect present in all dielectrics which is significant at submicron scales. Flexoelectricity is the two-way coupling between strain gradients and electric field or polarisation (direct effect), and a coupling between strain and electric field gradient or polarisation gradient (converse effect). The direct effect is thus the generation of polarisation or electric field due to an inhomogeneous deformation such as bending or twisting. It has been observed in Cross (2006), Hana (2007), and it is expressed mathematically as a linear property by

$$P_l = \mu_{lijk} \frac{\partial \varepsilon_{ij}}{\partial x_k}, \tag{1.3}$$

where μ is a fourth-rank tensor called the flexoelectric tensor. The inverse effect is also true, i.e. an electric field generates a strain gradient in the material (Bursian and Zaikovskii, 1968, Zubko *et al.*, 2013).

The converse effect refers to the generation of mechanical strain or stress under inhomogeneous electric or polarisation fields. It has been observed in Abdollahi *et al.* (2019), Fu *et al.* (2006), Hana *et al.* (2006). Mathematically, it is written as

$$\sigma_{ij} = f_{lijk} \frac{E_l}{\partial x_k}. \tag{1.4}$$

Like piezoelectricity, flexoelectricity is a two-way coupling. However, unlike piezoelectricity, which is restricted by symmetry, flexoelectricity is present in all dielectrics thus a universal

property in dielectrics, regardless of material symmetry, see Fig. 1.2. Another difference is that being a property involving gradients, the flexoelectric effect depends inversely on size. Because of that, flexoelectricity was not investigated until recently, when nanotechnology was sufficiently advanced, as shown in Fig. 1.3. Interestingly, advances in nanotechnologies have triggered an increasing interest in flexoelectricity.

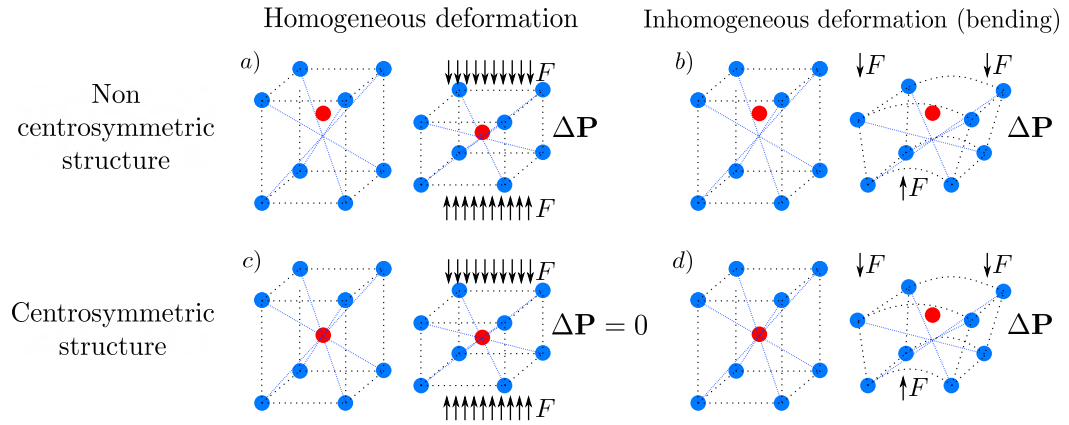

Figure 1.2: Illustration of direct piezoelectricity and flexoelectricity through homogeneous and inhomogeneous deformation in centrosymmetric and non-centrosymmetric structures. a) Applying a homogeneous force in a non-centrosymmetric structure results in a change in the net polarisation (piezoelectric effect). b) Applying an inhomogeneous deformation in a non-centrosymmetric structure also results in a change in the net polarisation (direct flexoelectric effect). c) Applying a homogeneous deformation in a centrosymmetric structure produces no electric response. d) Applying an inhomogeneous deformation in a centrosymmetric structure induces a non-zero net polarisation (direct flexoelectric effect).

1.2 Evidence of flexoelectricity

Flexoelectricity was theoretically discovered by Mashkevich and Tolpygo (1957) and mathematically formulated by Kogan (1964), but it was first observed in 1968 by Bursian and Zaikovskii (1968). The authors observed bending of a thin cantilever film in the presence of an electric field, which cannot be explained by piezoelectricity and was thus attributed to flexoelectricity. Bending was always in the direction of the positive electrode, meaning that the direction of bending could be reversed upon electric field reversal. They also observed charges on the film's surfaces when bent without any external electric field. That was the first demonstration of the two-way coupling of flexoelectricity. They needed a thin film of the order of micrometres to observe the effect. Such small sizes were out of the reach of fabrication technologies at that time, which explains why researchers lost interest in flexoelectricity until the developments of nanotechnology allowed us to fabricate and manipulate devices

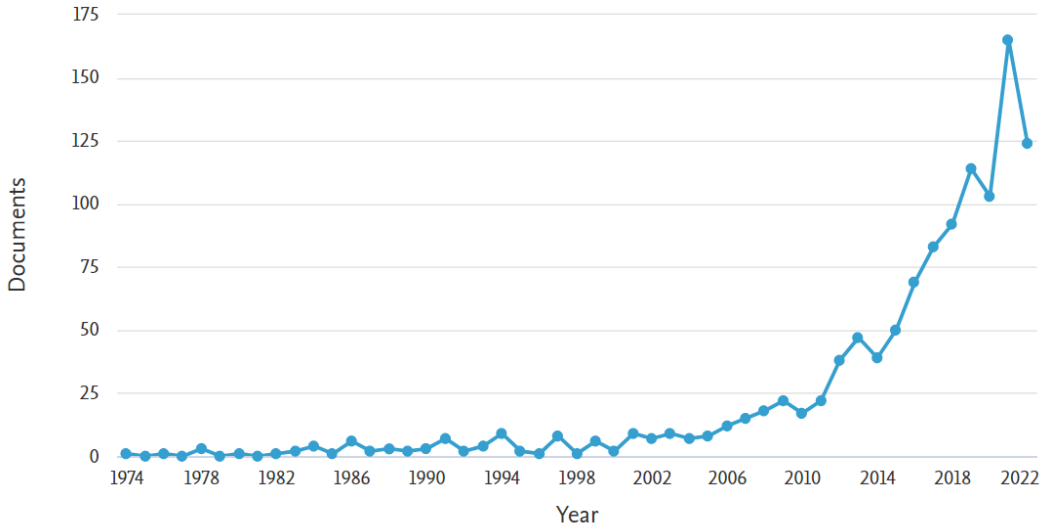

Figure 1.3: Number of publications on flexoelectricity per year. The image has been taken from Scopus, searching the word "flexoelectricity" and sorted by year.

at flexoelectrically relevant scales. Flexoelectricity is universal in dielectrics and has been observed in multiple materials. We report next the most relevant ones.

1.2.1 Flexoelectricity in liquid crystals

While investigating the piezoelectric effect in liquid crystals, Meyer (1969) found another mechanism coupled with strain gradient, which he termed flexoelectricity. Two types of molecules can be found in a crystal: a pear molecule and a banana molecule. Under a free tension configuration, both of them exhibit zero overall net polarisation, as seen in Fig. 1.4a-b. However, under the effect of an inhomogeneous deformation such as bending, they redirect themselves to minimise the total energy of the configuration giving rise to a net polarisation, as shown in Fig. 1.4c-d.

1.2.2 Flexoelectricity in biological systems

Flexoelectricity has been observed in cellular membranes (Ahmadpoor *et al.*, 2013, Ahmadpoor and Sharma, 2015, Duerloo and Reed, 2013, Petrov, 2002, Todorov *et al.*, 1991). Duerloo and Reed (2013) found that lipid bilayers can exhibit a strong coupling between curvature and electric fields. Furthermore, Duerloo and Reed showed that the bilayer had a displacement of approximately 1000 times larger than a single layer (see Fig. 1.5a). Ahmadpoor *et al.* (2013) also found that lipid molecules have some electric dipoles in the membranes, which explains their curvature (see Fig. 1.5b).

Flexoelectricity has also been found to play a role in the mammalian hearing mechanism

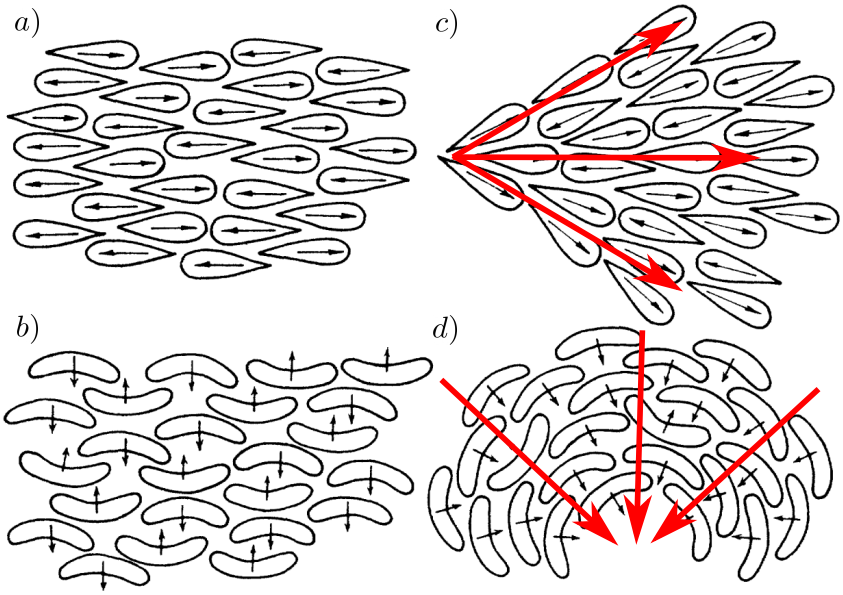

Figure 1.4: Flexoelectric effect in liquid crystal. a-b) Pear and banana molecules under free tension configuration. Both of them exhibit zero net overall polarisation. c-d) Pear and banana molecules under inhomogeneous deformation. Both of them exhibit a non-zero overall polarisation. Image extracted from Meyer (1969).

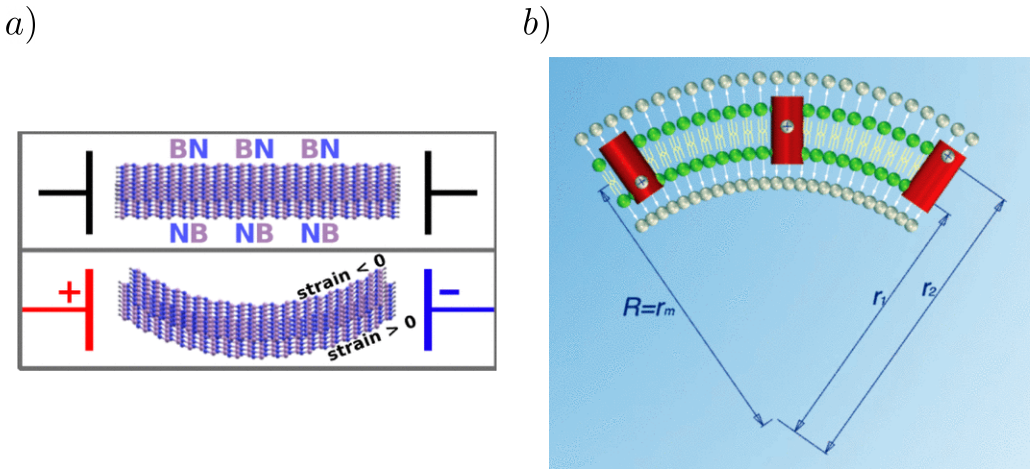

Figure 1.5: a) The lipid bilayer exhibits a strong coupling between curvature and electric fields thanks to flexoelectricity. Image adapted from Duerloo and Reed (2013). b) Lipid bilayer with some electric dipoles inside. Those dipoles create an electric field that bends the bilayer, thanks to inverse flexoelectricity. Image adapted from Ahmadpoor *et al.* (2013).

(see Fig. 1.6). Stereocilia in hair cells are biological flexoelectric sensors for sound. The hair cell membranes convert the acoustic vibration into amplified electrical signals (Ahmadpoor and Sharma, 2015, Krichen and Sharma, 2016, Oghalai *et al.*, 2000, Peng *et al.*, 2011).

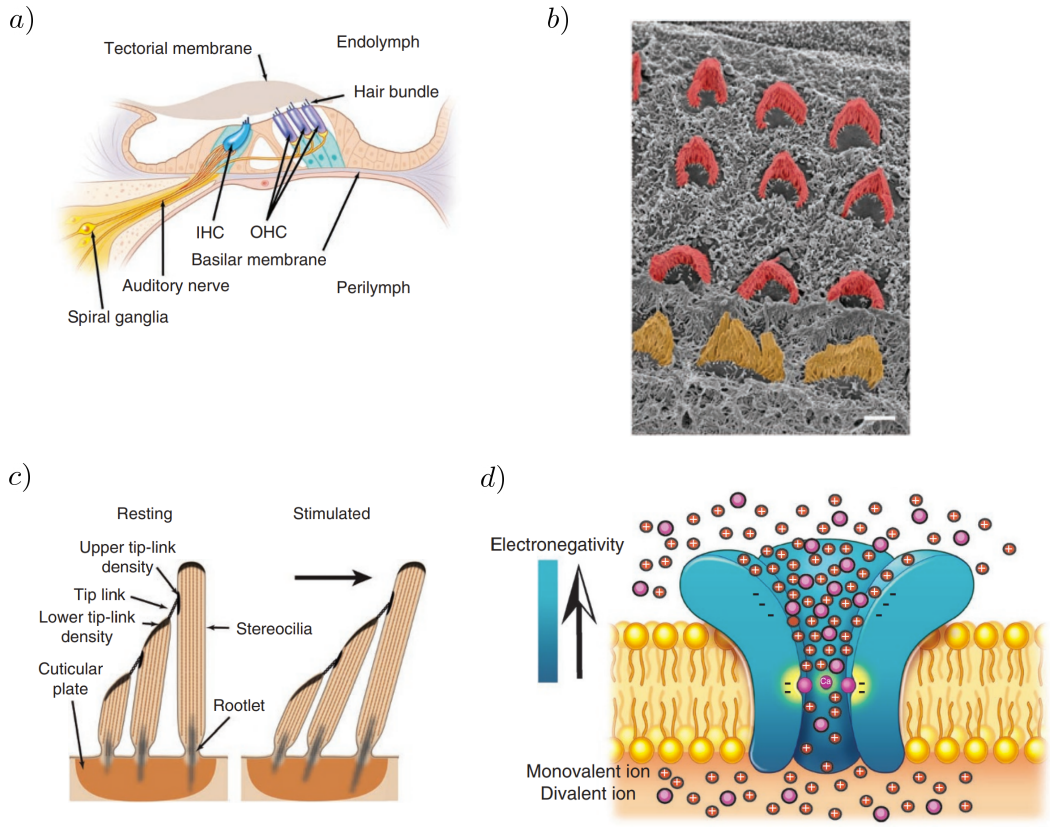

Figure 1.6: a) Cross-section of the organ of Corti pointing out the salient features relevant to hearing transduction. b) Scanning electron microscopy image looking at the apical surface of hair cells. c) Enlargement of a schematic of the hair bundle and hair cell apical surface. d) Cross-sectional view of the MET channel illustrating putative binding sites (Peng *et al.*, 2011)

It is well known that human bones are piezoelectric, due to the highly oriented and patterned structure of collagen. It has been recently claimed that flexoelectricity plays a key role in triggering the self-reparing mechanism in bones (Vasquez-Sancho *et al.*, 2018). Micro-cracks in the bones generate a very large strain gradient in the vicinity of the crack tips that induces an electric field. This effect was first attributed to piezoelectricity, but nowadays, it is known that the principal constituent of bones has a centrosymmetric structure and thus, cannot exhibit piezoelectricity. This electric field generates a stimulus able to initiate the healing process (see Fig. 1.7) (Vasquez-Sancho *et al.*, 2018). Finally, flexoelectricity plays a crucial role in enhanced toughness of the stomatopod dactyl club. It is known that the stomatopod dactyl club is one of the most damage-tolerant materials in the world. It can break materials

such as shells and is used to defend or attack prey. The claws undergo repeated high-velocity and high-force impacts. The graded structure of the club, leads to a grading in mechanical material properties. This property gradient induces a mechanical gradient that can trigger the flexoelectric effect, generating a flexoelectrically induced electric field that enhances toughness (see Fig. 1.8) (Abdollahi *et al.*, 2015a, Vásquez Sancho, 2018, Weaver *et al.*, 2012).

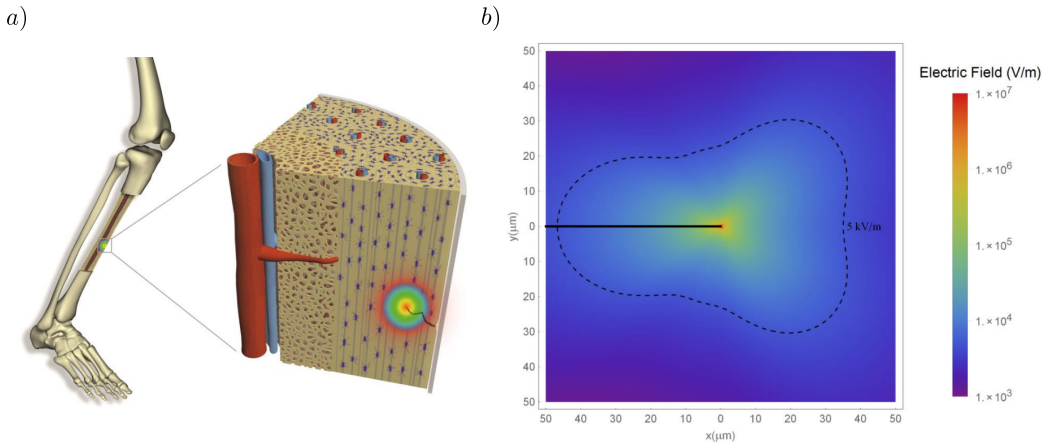

Figure 1.7: a) Recreation of a bone micro-crack b) Electric field distribution close to crack. Image adapted from Vasquez-Sancho *et al.* (2018)

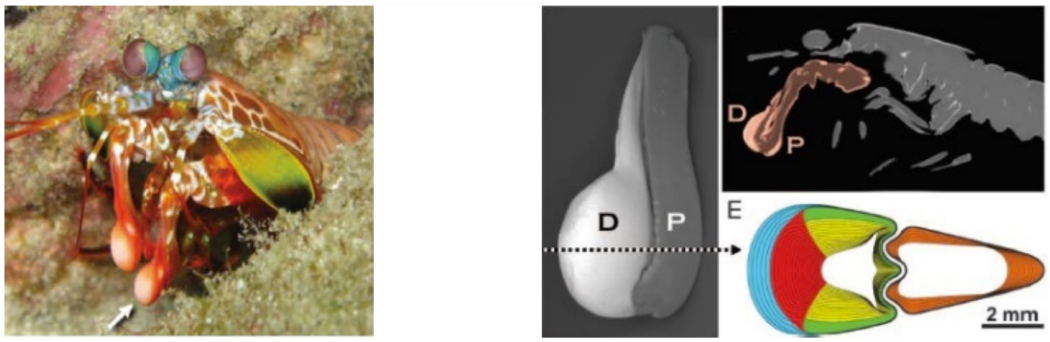

Figure 1.8: Image of a Stomatopod, the white arrow indicates the dactyl club and division of the two main segments of the club: Dactyl and propodus. Image adapted from Vásquez Sancho (2018)

1.2.3 Flexoelectricity in ionic crystals and hard ceramics

Flexoelectricity is also observed in ionic crystals and hard ceramics. Strain gradients are created upon bending on a two-dimensional plate and a difference of tension between the stretched upper and the compressed bottom part is created (see Fig. 1.2). Because of flexoelectricity, a

polarisation in the same direction of the strain gradient is generated, as seen in Cross (2006), Ma and Cross (2002, 2001a). The relationship between elastic strain gradient and electric polarisation was investigated in the relaxor ferroelectric lead magnesium niobate ceramic. Experimental studies done by Ma and Cross (2001b) indicated that flexoelectric polarisation is linearly proportional to the applied strain gradient as shown in Fig. 1.9

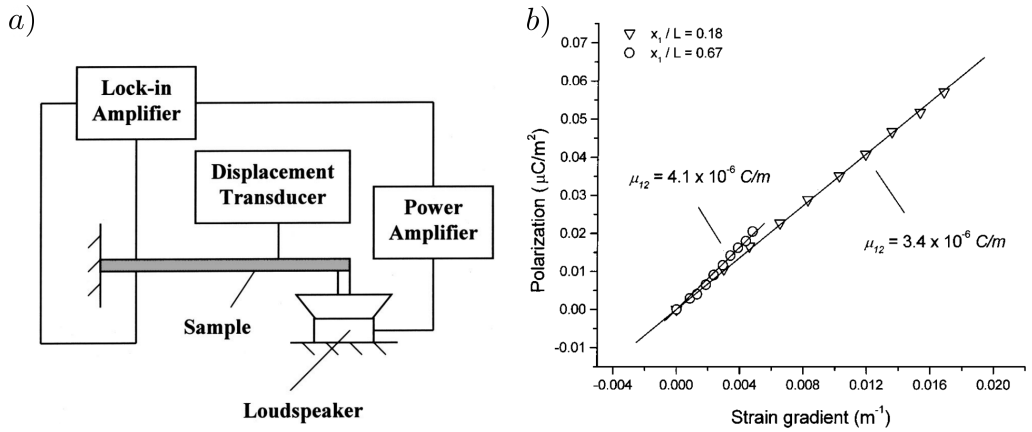

Figure 1.9: Flexoelectricity in ionic crystals and ferroelectric ceramics. a) Experimental setup for the measurement of the flexoelectric effect. The loudspeaker produces the bending of the sample and the displacement transducer measures the displacement at several positions along the sample bar. A very thin layer of sputtered gold is used as electrode at the bottom of the sample. b) The relationship between flexoelectric polarisation and strain gradient in the ceramics. Image extracted from Ma and Cross (2001b)

Domain walls in ferroelectric ceramics, which constitute an interface of strain and polarisation gradients, can trigger the flexoelectric effect as seen in Wang *et al.* (2020). Wang *et al.* (2020) showed that some typical domain wall distributions are only possible due to flexoelectricity.

1.2.4 Flexoelectricity in polymers

Most experiments in the literature report a low effect of flexoelectricity in polymers, except in some special cases. The origin of flexoelectricity in elastomers has been adressed in Grasinger *et al.* (2021). Grasinger *et al.* (2021) shows that combining stretching and bending is a mechanism for obtaining giant flexoelectricity.

Although the flexoelectric coefficients are typically smaller than those in inorganic materials, polymers have some advantages, for example, easy processing, low processing cost and desirable for practical application (Baskaran *et al.*, 2011a, 2012, 2011b, Breger *et al.*, 1976, Marvan and Havránek, 1998). Under a similar stress, polymers exhibit a stronger deformation than those created in hard ceramics, thus, a useful electromechanical response is created (Chu and Salem, 2012, Zhou *et al.*, 2017).

1.3 Characterisation of flexoelectricity

According to Eqs. (1.3-1.4), the flexoelectric tensor has rank 4, and thus, with no additional assumption, it has 54 independent parameters (Le Quang and He, 2011, Shu *et al.*, 2011). Under the premise of cubic symmetry, which is a reasonable assumption for a wide variety of materials, we reduce that number to three independent coefficients. They are the so-called longitudinal, transversal and shear coefficients, and the mathematical description of the cubic flexoelectric tensor is

$$\begin{aligned} \mu^{<\boldsymbol{x}>}{}_{iiii} &= \mu_L, & & i = 1,2,3; \\ \mu^{<\boldsymbol{x}>}{}_{ijji} &= \mu_T, & & i,j = 1,2,3 \ : \ i \neq j; \\ \mu^{<\boldsymbol{x}>}{}_{iijj} = \mu^{<\boldsymbol{x}>}{}_{ijij} &= \mu_S, & & i,j = 1,2,3 \ : \ i \neq j, \end{aligned} \tag{1.5}$$

oriented so that the vertical axis is $\boldsymbol{x}$. Even in the case of cubic flexoelectrics, flexoelectricity is difficult to measure experimentally for two reasons: the need to have a high-resolution technology and the difficulty of isolating the effect of each independent coefficient. Another simplification that could be used is isotropy and it is fulfilled if (Le Quang and He, 2011)

$$\mu_L - \mu_T - 2\mu_S = 0. \tag{1.6}$$

Flexoelectricity can be characterised either in experiments or through first-principle calculations. Next, we give a brief overview of both.

1.3.1 Experimental characterization

The longitudinal coefficient can be measured in the direct effect using the truncated pyramid setup as done in Cross (2006), Hana (2007), Marvan and Havránek (1998). In this method, a matrix of truncated pyramids is used; the difference in area between the bottom face and the top face creates a strain gradient in the vertical direction, resulting in a vertical electric field (see Fig. 1.10). Another way of determining this coefficient is creating a graded electric field and computing the vertical strain as done in Hana (2007). Most of the experiments use ionic crystals or ferroelectric ceramics because the flexoelectric coefficients are known to be proportional to the dielectricity constant, which is larger in these materials (Zubko *et al.*, 2013). There are some discrepancies between the theoretical values and the experimental values of the flexoelectric coefficients. Some reasons are the interplay between electrostriction and flexoelectricity as reported in Zubko *et al.* (2013) or the simplified analytical estimations of strain gradients in compressed pyramids that significantly overestimate flexoelectric coefficients (Abdollahi *et al.*, 2015b). For this reason, the experimental values greatly exceed the expected ones, as seen in $BaTiO_3$-based ceramics where the experimental value exceeds by 5 – 10V the theoretical one. For PMN-PT, the measured coefficients vary by orders of magnitude depending on the measurement method used (Hana, 2007, Hana *et al.*, 2006).

The transversal coefficient is the easiest one because it can be mobilised upon beam bending, which creates a transversal electric field. Two different setups can be found in the literature: cantilever beam bending (see Fig. 1.10) (Huang *et al.*, 2017, 2011, Kwon *et al.*, 2014, Li *et al.*, 2014, 2013, Shu *et al.*, 2017, 2016, 2013) and four-point bending (see Fig. 1.10) (Ma and Cross, 2003, Narvaez and Catalan, 2014, Narvaez *et al.*, 2015, Zubko *et al.*, 2007).

The quantification of shear stress is not trivial and there has yet to be a well-established method. A natural choice is torsion of flexoelectric bars. Nevertheless, torsion-induced strain gradients result in vanishing flexoelectric response in cubic systems, regardless of the shape of the bar's cross-section (Mocci, 2021, Mocci *et al.*, 2023). A significant response can be obtained by considering a varying cross-section, although the response, in this case, involves all three flexoelectric modes, and a carefully derived correction is needed, as seen in Mocci *et al.* (2023). In her thesis, Mocci proposed using a half-truncated cone under torsion to quantify the shear coefficient in cubic flexoelectrics (see Fig. 1.10).

1.3.2 First principles calculations

The first theoretical model was proposed by Kogan (1964). He stated that the flexoelectric coefficient could be approximated as

$$f \approx \frac{1}{4\pi\epsilon_0}\frac{q}{d} \tag{1.7}$$

where d is the interatomic distance, ϵ_0 is the vacuum permittivity, and q is the electronic charge. Nowadays, there are two models to quantify flexoelectric coefficients theoretically. The first relies on atomistic computation, where the flexoelectric coefficient is computed through the polarisation induced by bending using atomistic computations, such as density functional theory (DFT) (Codony *et al.*, 2021c, Dumitrică *et al.*, 2002, Kalinin and Meunier, 2008, Kumar *et al.*, 2021, Shi *et al.*, 2018), and the second relies on the first-principle theory of flexoelectricity based on density functional perturbation theory (DFPT) (Codony *et al.*, 2021b, Dreyer *et al.*, 2018, Hong and Vanderbilt, 2013, Resta, 2010, Stengel, 2013, 2014).

1.4 Flexoelectricity in technology

As electromechanical components in electronic devices are shrinking, the role of flexoelectricity is becoming increasingly significant. Understanding flexoelectricity is important, not only to harness it as a functional property, but also to understand its interaction with piezoelectricity in current electromechanical devices.

Some sensors are based on flexoelectricity, such as a microcurvature flexoelectric sensor (Yan and Jiang, 2013) or a sensor that converts the curvature of the beam into an electric signal (Huang *et al.*, 2012, Merupo *et al.*, 2017).

As commented before, common piezoelectric materials have some disadvantages that we

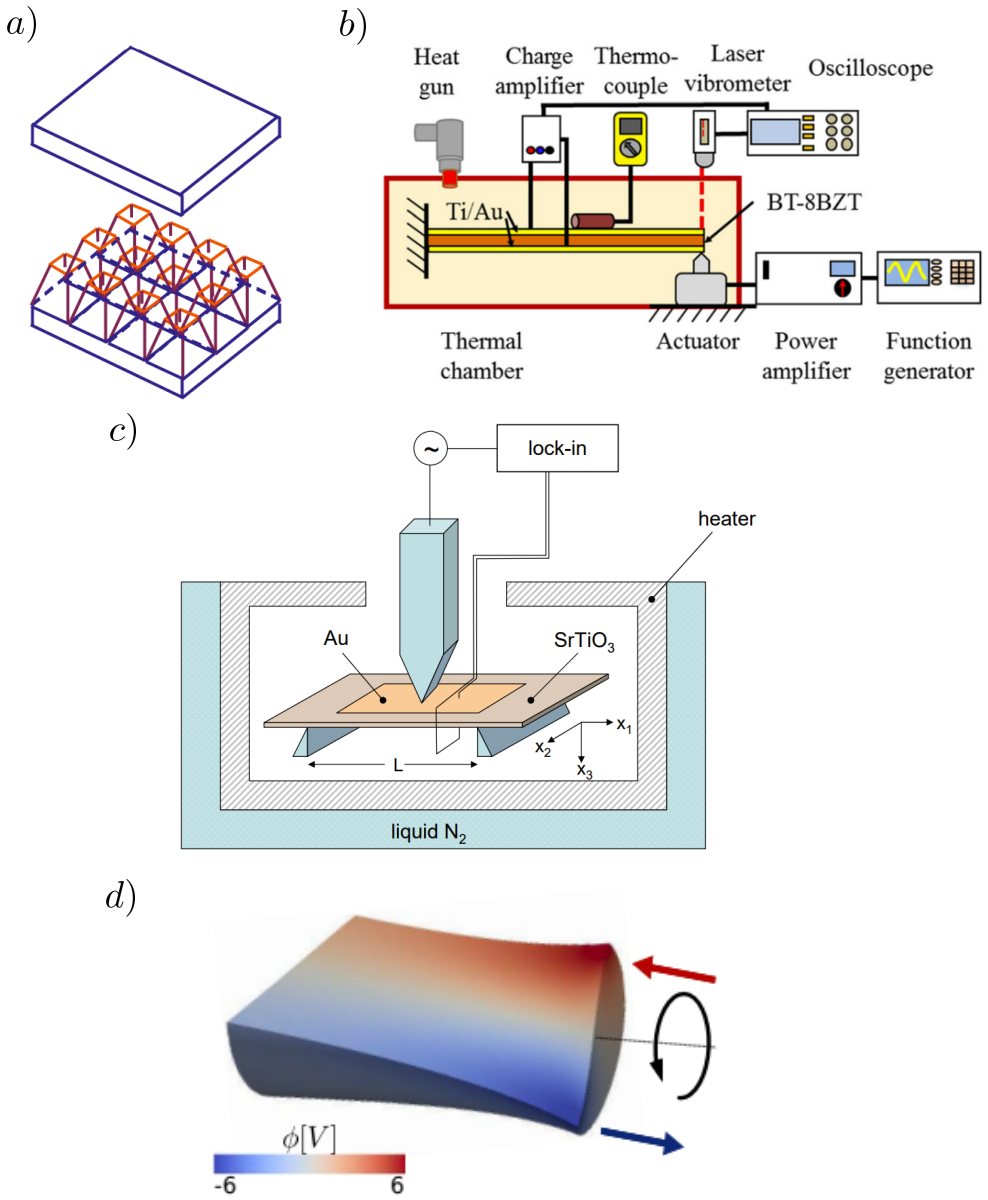

Figure 1.10: Setups for flexoelectric coefficient quantification. a) Arrangement of the truncated pyramid under vertical compression, the longitudinal coefficient can be measured. b-c)The transversal coefficient can be measured in the cantilever beam bending setup and three-point bending. d) Half truncated cone under torsion, the shear coefficient can be measured. Panel constructed using images from Hana (2007), Huang *et al.* (2017), Mocci (2021), Zubko *et al.* (2007)

should keep in mind: brittleness, toxicity resulting from high lead content and limited range of operating temperature being the main ones. For that reason, replacing materials with

flexoelectric ones is of interest. Some studies try to mimic the piezoelectric response using an architected non-piezoelectric material. This response is usually called apparent piezoelectricity. The idea is to break the symmetry of the non-piezoelectric material by the design of a fancy architected structure, such that after applying a homogeneous deformation, we obtain a net polarisation. This architecture can be done in different ways, as multi-material stacks (see Fig. 1.11a) (Liu *et al.*, 2016a), flexural thin films (see Fig. 1.11b) (Chu *et al.*, 2009), geometrically polarised cavities in the material (see Fig. 1.11c) (Deng *et al.*, 2014a, Sharma *et al.*, 2007), or juxtaposition on a plane of polar elements such as micro-pyramids (see Fig. 1.11d) (Cross, 2006, Fousek *et al.*, 1999, Fu *et al.*, 2007, Zhu *et al.*, 2006).

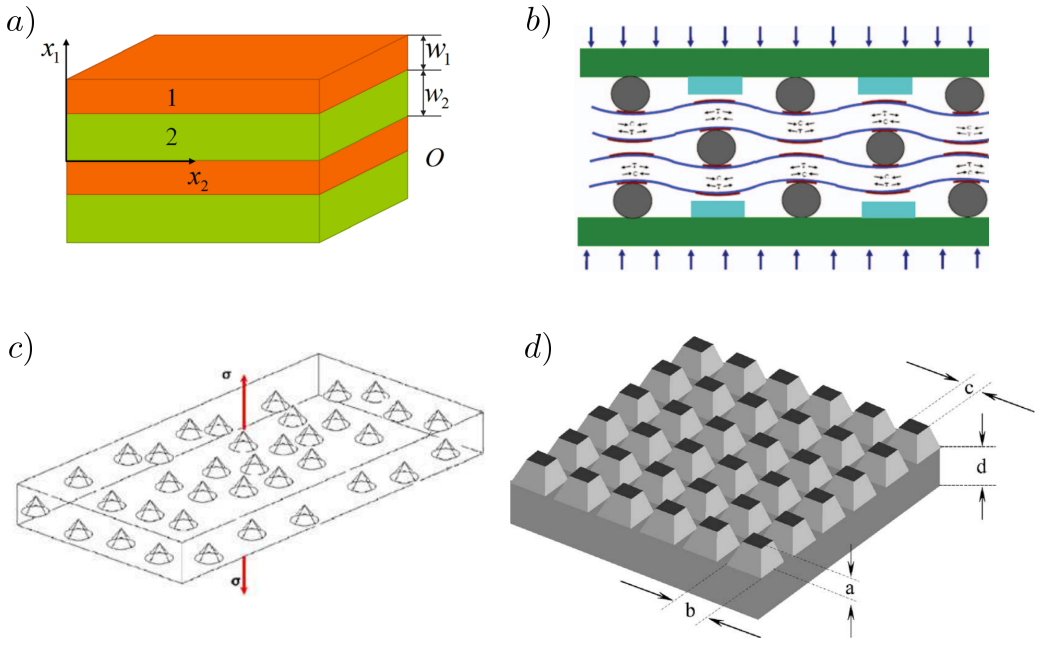

Figure 1.11: Architected structures triggering flexoelectric effect. a) Multimaterial stack from Liu *et al.* (2016a) b) Structure made by flexural thin film from Chu *et al.* (2009). c) Nanocomposite with conical inclusions from Sharma *et al.* (2007). d) Flexoelectric composite made by the arrangement of truncated pyramids from Fu *et al.* (2007).

Some studies and experiments rely on the interplay between piezoelectricity and flexoelectricity in wrinkling or buckling deformation modes (see Fig. 1.12) (Chen *et al.*, 2010, Dong *et al.*, 2020, Feng *et al.*, 2011, Han *et al.*, 2016, Park *et al.*, 2010, Su *et al.*, 2018). Indeed, flexoelectricity can either enhance or destroy piezoelectricity depending on design, as shown by Abdollahi and Arias (2015a). They studied the interplay in a bimorph, where two piezoelectric layers with opposite piezoelectric principal directions were attached, as seen in Fig. 1.13a. They observed

that at intermediate sizes where the piezoelectric and flexoelectric effects are comparable, the interplay between them could be constructive or destructive, leading to a dramatic degradation of the performance of piezoelectric devices depending for some designs, see Fig. 1.13b-c. These experiments highlight the need for flexoelectricity-aware designs at the microscale.

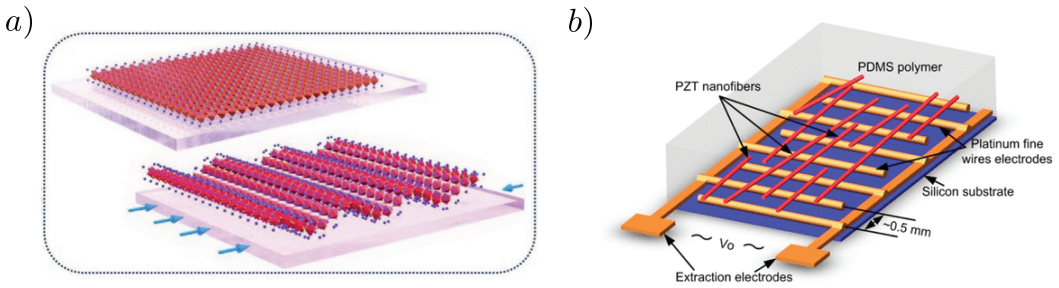

Figure 1.12: Flexoelectric devices using wrinkling or buckling deformation modes. a) Prestretch BTO membrane. The image is taken from Dong *et al.* (2020). b) Nanogenerator for mechanical energy harvesting using PZT nanofibers. The image is taken from Chen *et al.* (2010).

Last but not least, I want to comment on flexoelectricity in ferroelectrics. As will be discussed in detail in Chapter 5, one characteristic of ferroelectrics is that they exhibit spontaneous polarisation. This spontaneous polarisation is closely related to a spontaneous elongation of the ionic crystal unit cell with respect to the cubic non-polar reference configuration. In a vertically polarised thin film, polarisation can be switched 180 degrees with a vertical electric bias. Mechanical pressure can switch polarisation 90 degrees inducing a phase transformation from a vertically elongated tetragonal unit cell to a horizontally elongated tetragonal unit cell. However, uniform mechanical pressure cannot induce 180-degree switching, see Fig. 1.14. It has been shown though, that the generation of strain-gradients and the resulting flexoelectric electric fields can switch polarisation vertically upon localised pressure under an AFM tip (Catalan *et al.*, 2011, Lu *et al.*, 2012, Park *et al.*, 2018), as shown in Fig. 1.15

1.5 Objectives of the thesis

Flexoelectricity is a gradient effect and thus harnessing flexoelectricity as a functional property requires gradient engineering. This is a major step from the uniform-field configurations of piezoelectric devices, as becomes clear in the previous sections. Gradients can be generated by non-uniform deformation, such as bending and torsion, or through non-uniform material distributions, electrode configurations and complex geometries. Gradient engineering thus requires accurate quantitative modelling tools capable of efficiently dealing with all these elements with high-physical fidelity in order to construct engineering tools for the design of flexoelectric devices.

From a mathematical point of view, as hinted by Eqs. (1.3) and 1.4 and later explained in detail in chapter 2, flexoelectricity is modeled as a system of coupled high-order PDEs. This

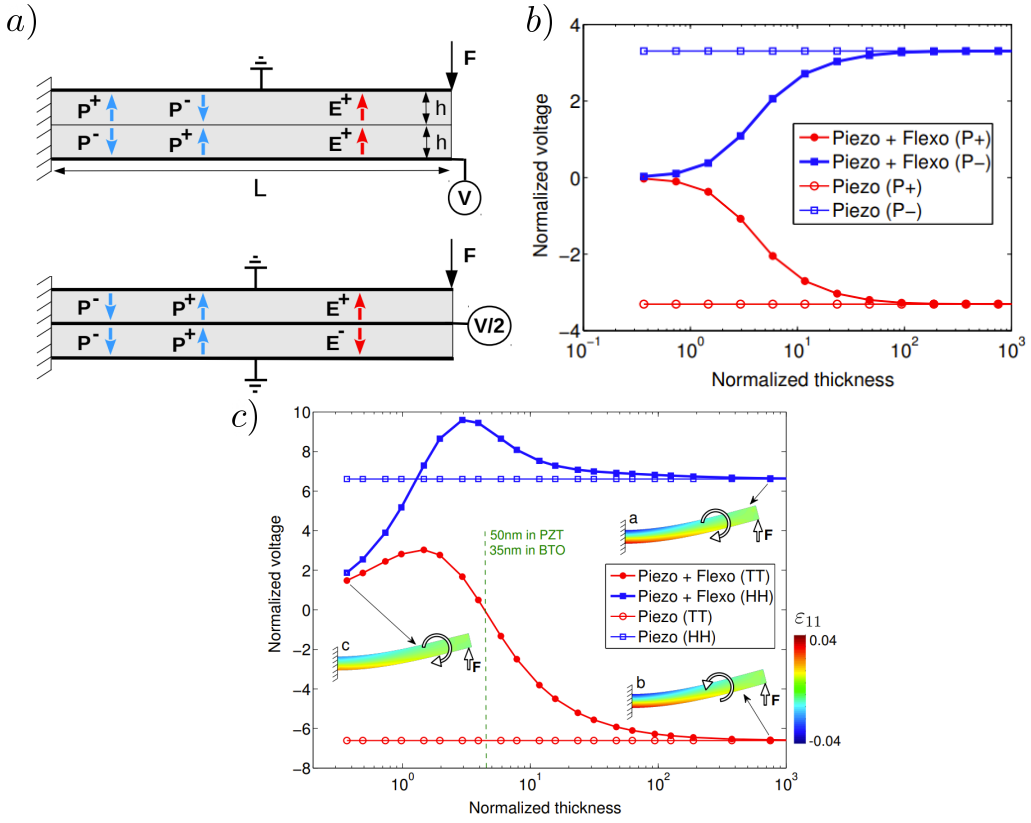

Figure 1.13: Piezoelectricity vs flexoelectricity in a bimorph. a) Setup of the experiment: a bilayer with series (top) or parallel (bottom) arrangement, clamped on the left side, fixed to the ground at the top side, and a force is applied in the top right corner. b) Normalised voltage as a function of the normalised beam thickness for the parallel bimorph arrangements. c) Normalised voltage as a function of the normalised beam thickness for the series bimorph arrangements. Image adapted from Abdollahi and Arias (2015a)

poses important challenges to computationally solving boundary value problems in general multimaterial samples with complex geometries and electrode configurations.

In this thesis we focus on the modelling of material interfaces, fictitious interfaces such as periodic boundaries of RVEs in heterogeneous media and moving phase boundaries such as ferroelectric domain walls, in the context of high-order problems.

The thesis' main goal is to formulate and implement a theoretical and computational framework and platform to solve general electromechanical boundary value problems in flexoelectric solids with interfaces. We consider both actual material interfaces in multi-material configurations, and fictitious periodicity boundaries. We use this framework to analyse flexoelectric metamaterials and devices, and explore and understand flexoelectric manifestations at moving interfaces, such as ferroelectric domain walls, cracks, and in friction.

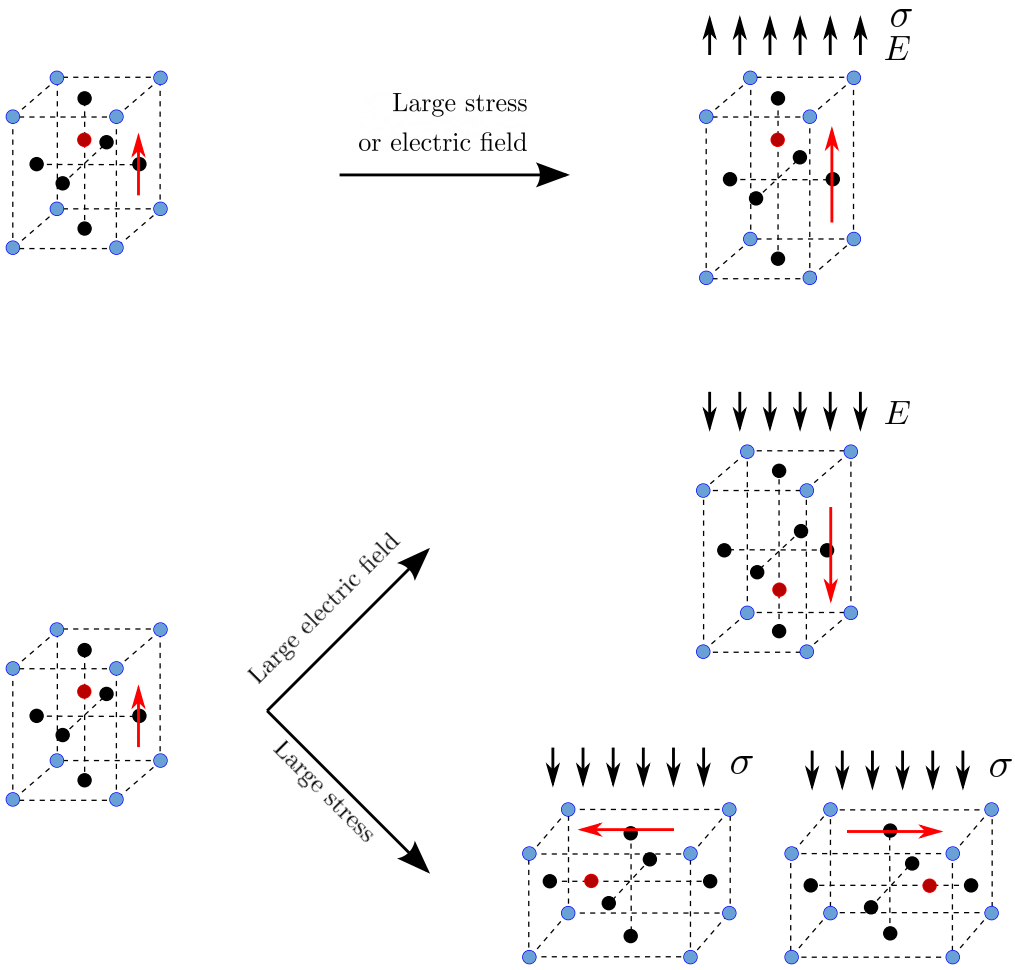

Figure 1.14: Schematic of the ferroelectric unit cell under large electric field or stress. At the top, the direction of the stress or the electric field is parallel to the electric dipole, producing a stretching of the unit cell. At the bottom, the direction of the stress or electric field is anti-parallel, producing a 180° switching in the case of the electric field and 90° in the case of the stress.

We also present a study of flexoelectricity in graded materials. This thesis is challenging since it covers theoretical and computational aspects as well as the physical understanding of flexoelectricity in complex systems.

The specific objectives of this thesis are

- Study the continuum model associated with flexoelectricity in dielectrics at infinitesimal deformations and the different variants of flexoelectricity: direct formulation and Lifshitz-invariant formulation.

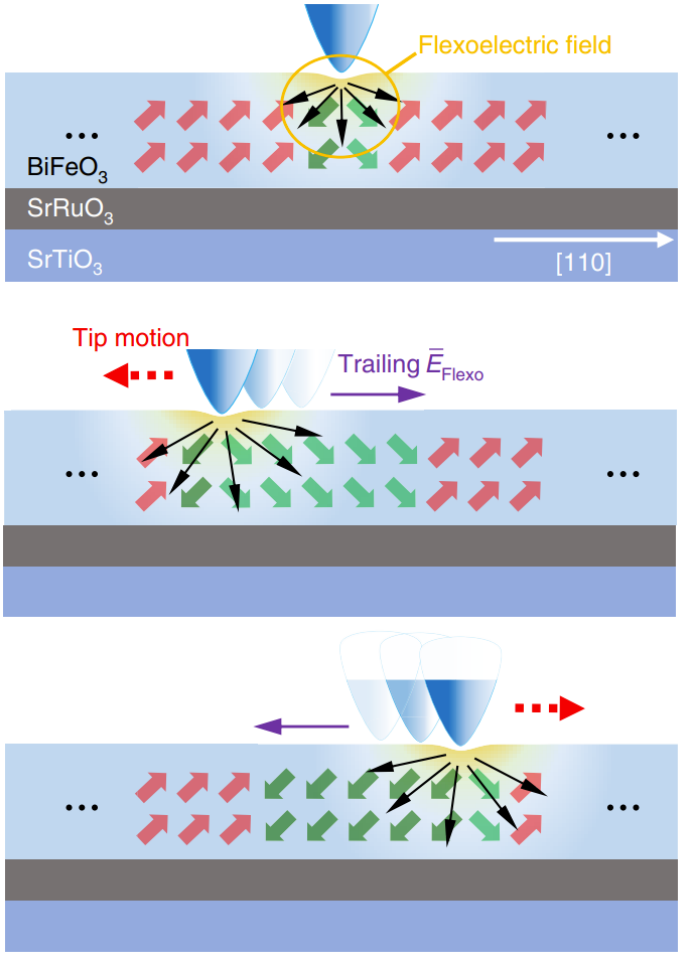

Figure 1.15: Selective control of multiple ferroelectric switching pathways using a trailing flexoelectric field. The image is taken from Park *et al.* (2018).

- Explore different numerical methods that can solve fourth-order PDE, such as the isogeometric approach with b-splines and immersed approach with b-splines.
- Extend the continuum framework for material interfaces from low-order to high-order problems. It is necessary for solving fourth-order PDE problems such as flexoelectricity.
- Formulate and implement generalised periodicity conditions for high-order electromechanical problems, and use them to simulate RVE in periodic flexoelectric metamaterials.
- Extend the formulation to non-homogeneous materials and study flexoelectricity in graded materials.

- Collaborate with experimentalists in the study of the flexoelectric effect in friction and wear under AFM scanning. Study different contact models and extend the formulation considering axisymmetric conditions. Perfom simulations of contact of AFM tip on flexoelectric thin films.
- Formulate and implement a phase field model for fracture and microstructure evolution in ferroelectric crystals accounting for flexoelectricity, strain gradient elasticity and strain gradient dielectricity in a high-performance computing platform. Study the effect of flexoelectricity at domain walls in in ferroelectrics and their interaction with fracture. Understanding phase-field modelling of polarisation and fracture and studying the characteristics of the method, including the quasi-static performance.

1.6 Outline

The manuscript is divided as follows. Chapter 2 presents in detail the continuum model for flexoelectricity. The first half of the chapter describes the direct flexoelectricity model with high-order interface conditions. Those interface conditions are extended to model also generalised periodicity conditions and are implemented using a novel Nitsche's formula. Strong generalised periodicity conditions are considered along with the macroscopic kinematics of the model, for the Lifshitz-invariant flexoelectric model which explicitly accounts for direct and converse flexoelectricity. Chapter 3 is devoted to the numerical approaches used in the thesis. On one hand, we have the isogeometric approach using the b-spline method, and on the other hand, we have the immersed approach using b-splines again. Chapter 4 shows the performance of the numerical model with several applications, including interfaces, generalised periodicity and graded structure applications. Chapter 5 particularises the model presented in Chapter 2 for axisymmetric conditions. This model is used to simulate the flexoelectric response of a dielectric sample upon indentation. Chapter 6 extends a phase-field model for microstructure and fracture evolution if ferroelectric single crystals (Abdollahi and Arias, 2011a, 2012) to account for lifshitz-invariant flexoelectricity augmented with strain gradient elasticity and gradient dielectricity. This model couples two phase-field models, one for the polarisation field and one for fracture. Chapter 7 summarises the work and presents the main conclusions.

1.7 List of publications

1.7.1 Publications in scientific journals

- **J. Barceló-Mercader** D. Codony, S. Fernández-Méndez, and I. Arias. Weak enforcement of interface continuity and generalized periodicity in high-order electromechanical problems. *International Journal for Numerical Methods in Engineering* **123**(4), 901–923 (2022).

This work presents a formulation for the weak enforcement of continuity conditions at material interfaces in high-order problems, particularised to flexoelectricity. It uses Nitsche's method, which is particularly suited for unfitted discretisations. This formulation is extended to impose generalised periodicity conditions at the unit cell boundaries of periodic structures. Optimal high-order convergence rates are obtained with an unfitted B-spline approximation, confirming the method's reliability. The numerical simulations illustrate the usefulness of the proposed approach towards the design of functional electromechanical multi-material devices and metamaterials harnessing the flexoelectric effect.

- D. Codony, A. Mocci, **J. Barceló-Mercader**, and I. Arias. Mathematical and computational modeling of flexoelectricity. *Journal of Applied Physics* **130**(23), 231102 (2021).

  This paper revisits the mathematical modelling of the flexoelectric effect in the context of continuum mechanics at infinitesimal deformations. It establishes and clarifies the relation between the different formulations, points out theoretical and numerical issues related to the resulting boundary value problems, and presents the natural extension to finite deformations. It also offers a B-spline-based computational technique to numerically solve the associated boundary value problems. It can be extended to handle unfitted meshes, allowing for arbitrarily-shaped geometries.

- **J. Barceló-Mercader**, A. Mocci D. Codony, and I. Arias. High-order generalized periodicity conditions for architected materials with application to flexoelectricity. *Submitted*

  This work presents a formulation for high-order generalised periodicity conditions particularised for flexoelectricity employing a generalised periodic space of approximation to computationally model Representative Volume Element (RVE) of periodic structures. The high-order generalised periodicity conditions are needed to solve the fourth-order flexoelectric PDE because C^1 continuity is mandatory between RVE and elements. The complex RVE is solved efficiently in an immersed boundary approach. Also, the response of architectural material against different loading angles is studied.

- A. Mocci, **J. Barceló-Mercader**, D. Codony, and I. Arias. Geometrically polarized architected dielectrics with apparent piezoelectricity. *Journal of the Mechanics and Physics of Solids* **157**, 104643 (2021).

  This paper proposes a class of low area-fraction, bending-dominated metamaterials that exhibit apparent piezoelectricity, even though the base material is not piezoelectric, thanks to flexoelectricity. It quantifies the apparent piezoresponse thanks to accurate simulations of continuum flexoelectricity. It characterises how apparent piezoelectricity depends on lattice geometry, orientation, feature size and area fraction. The paper generally provides the rules to endow any dielectric metamaterial with apparent piezoelectricity, enabling non-toxic, environmentally friendly and biocompatible artificial materials for electromechanical transduction.

- S. Cho, I. Gaponenko, K. Cordero-Edwards, **J. Barceló-Mercader**, I. Arias, C. Lichtensteiger, J. Yeom, L. Musy, H. Kim, and G. Catalan. Switchable tribology of ferroelectrics. *arXiv* 2208.11373 (2022). Under review in Nature Communications

  Artificially induced asymmetric tribological properties of ferroelectrics offer an alternative route to visualise and control ferroelectric domains. In this paper, we observe the switchable friction and wear behaviour of ferroelectrics using a nanoscale scanning probe. Down domains having lower friction coefficient than up domains can be used as smart masks as they show a slower wear rate. This asymmetry is enabled by flexoelectrically coupled polarisation in the up and down domains under a sufficiently high contact force. Moreover, we show that this polarisation-sensitive tribological asymmetry is universal across ferroelectrics with different chemical compositions and crystalline symmetry. These findings establish that ferroelectrics are electrically tunable tribological materials at the nanoscale for versatile applications.

- **J. Barceló-Mercader**, and I. Arias. Flexoelectric effect in fracture of ferroelectrics. *In preparation*

  This work presents a double phase-field model, where polarisation and damage field are described by means of two phase-field variables, along with Lifshitz-invariant formulation for flexoelectricity. It studies the evolution of the damage field in the presence of different static polarisation fields and domain walls and how flexoelectricity affects the behaviour of the cracks. Finally, it studies the evolution of crack whens the polarisation field is no longer static and has a quasi-static behaviour.

- **J. Barceló-Mercader**, S. Serrahima i Serra, and I. Arias. Flexoelectric effect in graded structures. *In preparation*

  This work explores the flexoelectric effect in graded structures. The formulation for flexoelectricity is modified to consider an anisotropic material tensor. The examples explore the possibilities of creating graded structures as sensors and actuators that exhibit apparent piezoelectricity using only flexoelectric materials.

Chapter 2

Continuum model of linear flexoelectricity with material interfaces or fictitious boundaries.

In this chapter, we present the mathematical framework for flexoelectricity in the presence of material interfaces and fictitious boundaries. The latter is common in the solution of boundary value problems in periodic structures and heterogeneous materials through the analysis of RVE. First, we review the existing continuum models for flexoelectricity focusing on enthalpy formulations, with displacement $\boldsymbol{u}$ and electric potential ϕ as primal state variables. Among those, two models are presented, that accounting in the enthalpy only for direct flexoelectricity explicitly, and that accounting explicitly for both direct and converse flexoelectricity. It is important to note that both formulations model the same physics and lead to the same governing equations. Nevertheless, as pointed out in Codony *et al.* (2021a), the models differ in the constitutive equations and the boundary conditions, and they have to be interpreted carefully when solving specific boundary value problems (Codony *et al.*, 2021a, 2019).

Mathematically, the governing equations are a system of coupled fourth-order PDEs. There are several approaches to deal with the high-order nature of the equations. An attractive choice is the use of an immersed boundary hierarchical B-spline method (Codony *et al.*, 2019), where the smooth B-spline basis functions provide the required continuity while the immersed boundary approach allows to account for general sample geometries. In this context, essential conditions on surfaces and interfaces cannot be imposed strongly since the basis functions are not interpolant at the immersed boundary (Codony *et al.*, 2019). A common approach for the weak imposition of these conditions is the use of Nitsche's method, a consistent penalty method (Fernández-Méndez and Huerta, 2004, Nitsche, 1970). Nitsche's method preserves the variational structure of the problem, since it boils down to adding new terms to the energy functional.

We first derive the equilibrium and continuity equations for material interfaces, which

are termed high-order interface conditions. We then present the corresponding variational formulation for a multimaterial flexoelectric using Nitsche's method to impose high-order interface conditions weekly.

We then particularise this formulation to fictitious boundaries with high-order generalised periodic conditions. We state these conditions for the case of horizontal and vertical periodicity, and derive the corresponding variational formulation, as a particular case of the previous one.

Finally, we generalise the formulation to account for high-order generalised periodicity in arbitrary directions. The conditions are stated and related to a macroscopic enthalpy functional. Later, the boundary value problem for flexoelectric RVE is described. Finally, ongoing work is shown where high-order interface conditions for Lifshitz-invariant flexoelectricity are stated along with Nitsche's method variational formulation.

2.1 Variational formulation of state-of-the-art flexoelectric models

The first theoretical studies of flexoelectricity were done by Mashkevich and Tolpygo (1957) and Tolpygo (1963), the first model for flexoelectricity in crystalline dielectrics was proposed by Kogan (1964), but the first work clearly distinguishing piezoelectricity and flexoelectricity was introduced by Tagantsev (1986, 1991). The complete framework considering strain gradient elasticity, flexoelectric coupling and polarisation effect was proposed by Sahin and Dost (1988). After that, a simple framework for isotropic dielectric was proposed by Maranganti *et al.* (2006a). Recently, different continuum models for flexoelectricity exist, including new physics, such as flexoelectricity in ferroelectric (Catalan *et al.*, 2004, Eliseev *et al.*, 2009a), surface effects (Shen and Hu, 2010) or even including the photovoltaic effect (Shu *et al.*, 2020, Yang *et al.*, 2018). Comprehensive reviews for flexoelectricity in solids can be seen in Krichen and Sharma (2016), Nguyen *et al.* (2013), Wang *et al.* (2019), Yudin and Tagantsev (2013), Zubko *et al.* (2013).

Different models for flexoelectricity in dielectrics are formulated depending on the choice of state variable. The most natural choice from a physical perspective is considering the displacement $\boldsymbol{u}$ and electric polarisation $\boldsymbol{P}$ as the primal unknowns. It yields a global minimisation problem of the physical free energy. This free energy functional is expressed as (Liu, 2014, Maranganti *et al.*, 2006a)

$$\Pi[\boldsymbol{u}, \boldsymbol{P}] = \int_\Omega \left(\psi^{\text{Int}}(\boldsymbol{u}, \boldsymbol{P}) + \frac{1}{2}\epsilon_0 ||\boldsymbol{E}||^2 \right) \mathrm{d}\Omega - W^{\text{Ext}}, \tag{2.1}$$

where Ω is the domain occupied by the flexoelectric material, ψ^{Int} is the internal energy density, $\frac{1}{2}\epsilon_0 ||\boldsymbol{E}||^2$ is the electrostatic energy density, with ϵ_0 the vacuum permittivity, $\boldsymbol{E}$ the electric field, and W^{Ext} is the external work. The internal energy density can be written in several different ways, e.g., considering only direct flexoelectricity explicitly, or considering both direct and

converse flexoelectricity explicitly, among others (Codony *et al.*, 2021a)

The variational principle associated with the energy functional in Eq. (2.1) is the constrained minimisation problem

$$(\boldsymbol{u}^*, \boldsymbol{P}^*) = \arg\min_{\boldsymbol{u}} \min_{\boldsymbol{P}} \Pi[\boldsymbol{u}, \boldsymbol{P}], \tag{2.2}$$

such that stationary Maxwell's equations hold:

$$\nabla \times \boldsymbol{E} = 0, \tag{2.3a}$$

$$\nabla \cdot \boldsymbol{D} = 0. \tag{2.3b}$$

An alternative model, which avoids having a constrained minimisation problem, consists of considering displacement $\boldsymbol{u}$ and electric potential ϕ as primal unknowns. The electric potential ϕ is defined such that it satisfies

$$\boldsymbol{E} = -\nabla\phi; \tag{2.4}$$

thus, Faraday's law in Eq. (2.3a) is automatically fulfilled. We define the free enthalpy as done in Abdollahi *et al.* (2014), Deng *et al.* (2014b), Zhuang *et al.* (2020) as

$$\Pi[\boldsymbol{u}, \phi] = \int_\Omega \psi_\phi(\boldsymbol{u}, \phi)\, \mathrm{d}\Omega - W^{\mathrm{Ext}}, \tag{2.5}$$

where ψ_ϕ is the free enthalpy density. The variational problem is now an unconstrained min-max problem:

$$(\boldsymbol{u}^*, \phi^*) = \arg\min_{\boldsymbol{u}} \max_{\phi} \Pi[\boldsymbol{u}, \phi]. \tag{2.6}$$

As derived in detail in Codony (2021), both formulations are related by a partial Legendre transform, and are thus equivalent. In this thesis, we consider displacement and electric potential as primal unknowns since avoiding the constraint resulting from Maxwell-Faraday's law and thus solving the unconstrained minimisation problem has some numerical advantages.

2.1.1 Direct flexoelectricity model

We follow here the notation by Codony *et al.* (2019) and Barceló-Mercader *et al.* (2022). Let Ω be a physical domain in $\mathbb{R}^2$ or $\mathbb{R}^3$. Considering just the direct form of flexoelectricity, the bulk enthalpy density in a flexoelectric material is

$$\mathcal{H}^\Omega[\boldsymbol{u}, \phi] = \frac{1}{2}\varepsilon_{ij}\mathbb{C}_{ijkl}\varepsilon_{kl} + \frac{1}{2}\varepsilon_{ij,k}h_{ijklmn}\varepsilon_{lm,n} - \frac{1}{2}E_l\epsilon_{lm}E_m - E_l e_{lij}\varepsilon_{ij} - E_l\mu_{lijk}\varepsilon_{ij,k}, \tag{2.7}$$

where

$$[\boldsymbol{\varepsilon}(\boldsymbol{u})]_{ij} = [\boldsymbol{\varepsilon}(\boldsymbol{u})]_{ji} = [\nabla^s(\boldsymbol{u})]_{ij} = \frac{1}{2}(u_{i,j} + u_{j,i}), \tag{2.8a}$$

$$[\boldsymbol{E}(\phi)]_l = -[\nabla\phi]_l = -\phi_{,l}. \tag{2.8b}$$

The first term on Eq. (2.7) corresponds to the elasticity enthalpy density with the fourth-order elasticity tensor $\mathbb{C}_{ijkl}$. The second term corresponds to the strain gradient elasticity enthalpy density with the sixth-order strain gradient elasticity tensor h_{ijklmn}. These two terms form the enthalpy density of a strain gradient elastic material form described in Mindlin (1964). The third term is the electrostatic enthalpy density with the second-order dielectricity tensor ϵ_{lm}. The fourth term corresponds to the piezoelectric enthalpy density governed by the third-order tensor of piezoelectric constants e_{lij}, and the last term is the flexoelectric enthalpy density governed by a fourth-order tensor μ_{lijk}. Piezoelectricity and flexoelectricity couple the electric field with the strain and their derivatives. Here, we are considering the direct effect of flexoelectricity explicitly, i.e. the two-way coupling between electric field and strain gradient. Note that the strain-gradient term represents the non-local elastic effect and regularises the flexoelectric effect.

Apart from the internal enthalpy, we consider the work of external loads as

$$\mathcal{W}^{\Omega}[\boldsymbol{u}, \phi] = -b_i u_i + q\phi, \tag{2.9}$$

where $\boldsymbol{b}$ is the sum of body forces applied to the body Ω per unit volume and q are the free electric charges per unit volume. The total bulk enthalpy of a flexoelectric material is then

$$\Pi^{\Omega}[\boldsymbol{u}, \phi] = \int_{\Omega} \left(\mathcal{H}^{\Omega}[\boldsymbol{u}, \phi] + \mathcal{W}^{\Omega}[\boldsymbol{u}, \phi] \right) \mathrm{d}\Omega. \tag{2.10}$$

The enthalpy associated with enthalpy contribution from imposed displacements and applied tractions, and imposed electric potential and applied surface charges on the sample boundaries must also be taken into account. Considering the standard approach where the Dirichlet boundary conditions, i.e. imposed displacements and electric potential, are strongly enforced, i.e. the functional space of the state variables is restricted to admissible states fulfilling Dirichlet boundary conditions, there is no enthalpy associated with those contributions. However, applied tractions and surface charges on the sample boundary (Neumann type boundary conditions) do contribute to the total enthalpy of the material. In order to define correctly the terms associated with boundary conditions, the boundary $\partial\Omega$ is split into several disjoint sets, as seen in Fig. 2.1, as

$$\partial\Omega = \partial\Omega_u \cup \partial\Omega_t = \partial\Omega_v \cup \partial\Omega_r = \partial\Omega_\phi \cup \partial\Omega_w, \tag{2.11}$$

where $\partial\Omega_u$, $\partial\Omega_v$ and $\partial\Omega_\phi$ correspond to those boundaries where Dirichlet boundary conditions are enforced and $\partial\Omega_t$, $\partial\Omega_r$ and $\partial\Omega_w$ correspond to those boundaries where Neumann boundary

conditions are enforced. An example of the boundary split can be seen in Fig. 2.1.

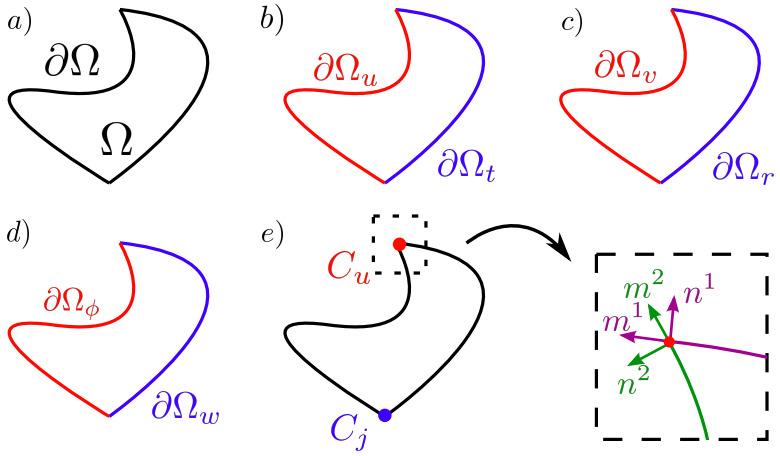

Figure 2.1: A 2D representation of the physical domain Ω and its boundary $\partial\Omega$. The boundary is split into several disjoint sets, as in Eq. (2.11) and Eq. (2.12). a) Domain and domain boundary. b) Domain boundary split based on mechanical low-order Dirichlet and Neumann mechanical boundary conditions. c) Domain boundary split based on high-order Dirichlet and Neumann mechanical boundary conditions. d) Domain boundary split based on Dirichlet and Neumann electric boundary conditions. e) Domain boundary boundary $\partial\partial\Omega$ split in Dirichlet and Neumann mechanical edge (corner in 2D) conditions.

Flexoelectricity BVP also require boundary conditions for the curves $C = \partial\partial\Omega$ (points in 2D). Consequently, the curves are split into two disjoint sets as

$$\partial\partial\Omega = C_u \cup C_j, \tag{2.12}$$

where C_u and C_j are the curves (points in 2D) where Dirichlet boundary conditions and Neumann boundary conditions are applied, respectively. This can also be seen in Fig. 2.1. The corresponding Dirichlet and Neumann boundary conditions applied are

$$\boldsymbol{u} = \boldsymbol{u}^{\mathrm{D}} \quad \text{on } \partial\Omega_u, \qquad \boldsymbol{t} = \boldsymbol{t}^{\mathrm{N}} \quad \text{on } \partial\Omega_t, \tag{2.13a}$$

$$\partial^n(\boldsymbol{u}) = \boldsymbol{v}^{\mathrm{D}} \quad \text{on } \partial\Omega_v, \qquad \boldsymbol{r} = \boldsymbol{r}^{\mathrm{N}} \quad \text{on } \partial\Omega_r, \tag{2.13b}$$

$$\phi = \phi^{\mathrm{D}} \quad \text{on } \partial\Omega_\phi, \qquad w = w^{\mathrm{N}} \quad \text{on } \partial\Omega_w, \tag{2.13c}$$

$$\boldsymbol{u} = \boldsymbol{u}^{\mathrm{D}} \quad \text{on } \partial C_u, \qquad \boldsymbol{j} = \boldsymbol{j}^{\mathrm{N}} \quad \text{on } \partial C_j, \tag{2.13d}$$

where $\boldsymbol{u}^{\mathrm{D}}$, $\boldsymbol{v}^{\mathrm{D}}$ and ϕ^{D} are the prescribed value of displacement, normal derivative of the displacement and electric potential, respectively, and $\boldsymbol{t}^{\mathrm{N}}$, $\boldsymbol{r}^{\mathrm{N}}$, w^{N} and $\boldsymbol{j}^{\mathrm{N}}$ are the prescribed value of the traction, double traction, surface charge and line force, respectively.

The total enthalpy of the system for a flexoelectric material considering direct flexoelec-

tricity $\Pi^{\mathrm{Dir}}[\boldsymbol{u}, \phi]$ is then

$$\Pi^{\mathrm{Dir}}[\boldsymbol{u}, \phi] = \Pi^{\Omega}[\boldsymbol{u}, \phi] + \Pi^{\mathrm{N}}[\boldsymbol{u}, \phi], \tag{2.14}$$

with

$$\Pi^{\mathrm{N}}[\boldsymbol{u}, \phi] = \int_{\partial\Omega_t} -u_i t_i^{\mathrm{N}} \,\mathrm{d}\Gamma + \int_{\partial\Omega_r} -\partial^n u_i r_i^{\mathrm{N}} \,\mathrm{d}\Gamma + \int_{\partial\Omega_w} \phi w^{\mathrm{N}} \,\mathrm{d}\Gamma + \int_{C_j} -u_i j_i^{\mathrm{N}} \,\mathrm{ds}, \tag{2.15}$$

As mentioned before, the total enthalpy has no contribution from Dirichlet boundary conditions in the standard approach, i.e. when Dirichlet boundary conditions are imposed strongly. We recall the variational principle stated in Eq. (2.6), which particularises in the present case to

$$(\boldsymbol{u}^*, \phi^*) = \arg \min_{\boldsymbol{u}\in\mathcal{U}_{\mathrm{D}}} \max_{\phi\in\mathcal{P}_{\mathrm{D}}} \Pi^{\mathrm{Dir}}[\boldsymbol{u}, \phi] \tag{2.16}$$

where the functional spaces $\mathcal{U}_{\mathrm{D}}$ and $\mathcal{P}_{\mathrm{D}}$ of admissible states are defined as

$$\mathcal{U}_{\mathrm{D}} = \left\{ \boldsymbol{u} \in [H^2(\Omega)]^3 | \boldsymbol{u} = \boldsymbol{u}^{\mathrm{D}} \text{ on } \partial\Omega_u \text{ and } C_u \text{ and } \partial^n(\boldsymbol{u}) = \boldsymbol{v}^{\mathrm{D}} \text{ on } \partial\Omega_v \right\}, \tag{2.17a}$$

$$\mathcal{P}_{\mathrm{D}} = \left\{ \phi \in H^1(\Omega) | \phi = \phi^{\mathrm{D}} \text{ on } \partial\Omega_\phi \right\}. \tag{2.17b}$$

A necessary condition for equilibrium is the vanishing of the first variation of the enthalpy functional $\Pi^{\mathrm{Dir}}[\mathbf{u}, \phi]$ for all admissible variations $\delta\mathbf{u}$ and $\delta\phi$, which corresponds to the weak form of the problem:

$$\text{Find } (\boldsymbol{u}, \phi) \in \mathcal{U}_{\mathrm{D}} \otimes \mathcal{P}_{\mathrm{D}} \text{ such that } \delta\Pi^{\mathrm{Dir}} = 0 \;\forall (\delta\boldsymbol{u}, \delta\phi) \in \mathcal{U}_0 \otimes \mathcal{P}_0, \tag{2.18}$$

with

$$\mathcal{U}_0 = \left\{ \boldsymbol{u} \in [H^2(\Omega)]^3 | \boldsymbol{u} = 0 \text{ on } \partial\Omega_u \text{ and } C_u \text{ and } \partial^n(\boldsymbol{u}) = 0 \text{ on } \partial\Omega_v \right\}, \tag{2.19a}$$

$$\mathcal{P}_0 = \left\{ \phi \in H^1(\Omega) | \phi = 0 \text{ on } \partial\Omega_\phi \right\}, \tag{2.19b}$$

and

$$\delta\Pi^{\mathrm{Dir}}[\boldsymbol{u}, \phi, \delta\boldsymbol{u}, \delta\phi] = \delta\Pi^{\Omega}[\boldsymbol{u}, \phi, \delta\boldsymbol{u}, \delta\phi] + \delta\Pi^{\mathrm{N}}[\boldsymbol{u}, \phi, \delta\boldsymbol{u}, \delta\phi], \tag{2.20a}$$

$$\delta\Pi^{\Omega}[\boldsymbol{u}, \phi, \delta\boldsymbol{u}, \delta\phi] = \int_{\Omega} \widehat{\sigma}_{ij}\delta\varepsilon_{ij} + \widetilde{\sigma}_{ijk}\delta\varepsilon_{ij,k} - \widehat{D}_l\delta E_l - b_i\delta u_i + q\delta\phi \,\mathrm{d}\Omega, \tag{2.20b}$$

$$\delta\Pi^{\mathrm{N}}[\boldsymbol{u}, \phi, \delta\boldsymbol{u}, \delta\phi] = \int_{\partial\Omega_t} -\delta u_i t_i^{\mathrm{N}} \,\mathrm{d}\Gamma + \int_{\partial\Omega_r} -\partial^n(\delta u_i) r_i^{\mathrm{N}} \,\mathrm{d}\Gamma + \int_{\partial\Omega_w} \delta\phi w^{\mathrm{N}} \,\mathrm{d}\Gamma + \int_{C_j} -\delta u_i j_i^{\mathrm{N}} \,\mathrm{ds}, \tag{2.20c}$$

where the Cauchy stress $\hat{\boldsymbol{\sigma}}$, the high-order stress $\tilde{\boldsymbol{\sigma}}$ and the Electric displacement $\hat{\mathbf{D}}$ are defined

as

$$\hat{\sigma}_{ij}(\boldsymbol{u},\phi) = \hat{\sigma}_{ji}(\boldsymbol{u},\phi) = \left.\frac{\partial \mathcal{H}^{\Omega}[\boldsymbol{u},\phi]}{\partial \varepsilon_{ij}}\right|_{\substack{\nabla\boldsymbol{\varepsilon} \\ \boldsymbol{E}}} = \mathbb{C}_{ijkl}\varepsilon_{kl} - e_{lij}E_l, \tag{2.21a}$$

$$\tilde{\sigma}_{ijk}(\boldsymbol{u},\phi) = \tilde{\sigma}_{jik}(\boldsymbol{u},\phi) = \left.\frac{\partial \mathcal{H}^{\Omega}[\boldsymbol{u},\phi]}{\partial \varepsilon_{ij,k}}\right|_{\substack{\boldsymbol{\varepsilon} \\ \boldsymbol{E}}} = h_{ijklmn}\varepsilon_{lm,n} - \mu_{lijk}E_l, \tag{2.21b}$$

$$\hat{D}_l(\boldsymbol{u},\phi) = -\left.\frac{\partial \mathcal{H}^{\Omega}[\boldsymbol{u},\phi]}{\partial E_l}\right|_{\substack{\boldsymbol{\varepsilon} \\ \nabla\boldsymbol{\varepsilon}}} = \epsilon_{lm}E_m + e_{lij}\varepsilon_{ij} + \mu_{lijk}\varepsilon_{ij,k}. \tag{2.21c}$$

Eq. (2.18) can be integrated by parts and, by invoking the divergence and surface divergence theorems, the Euler-Lagrange equations are derived as

$$\left(\hat{\sigma}_{ij}(\boldsymbol{u},\phi) - \tilde{\sigma}_{ijk,k}(\boldsymbol{u},\phi)\right)_{,j} + b_i = 0 \qquad \text{in } \Omega, \tag{2.22a}$$

$$\hat{D}_{l,l}(\boldsymbol{u},\phi) - q = 0 \qquad \text{in } \Omega, \tag{2.22b}$$

along with the expressions for the traction, double traction, surface charge and line force

$$t_i = \left(\hat{\sigma}_{ij} - \tilde{\sigma}_{ijk,k} + \nabla^S_l\left(n_l\right)\tilde{\sigma}_{ijk}n_k\right)n_j - \nabla^S_j\left(\tilde{\sigma}_{ijk}n_k\right) \qquad \text{on } \partial\Omega, \tag{2.23a}$$

$$r_i = \tilde{\sigma}_{ijk}n_jn_k \qquad \text{on } \partial\Omega, \tag{2.23b}$$

$$w = -\widehat{D}_l n_l \qquad \text{on } \partial\Omega, \tag{2.23c}$$

$$j_i = [\![\tilde{\sigma}_{ijk}m_jn_K]\!] \qquad \text{on } C, \tag{2.23d}$$

where $[\![\ ]\!]$ is the jump operator defined as $[\![A]\!] = A^1 + A^2$, $\nabla^S_j(\,) = \nabla_k(\,)\left(\delta_{kj} - n_kn_j\right)$ is the surface divergence operator, $\boldsymbol{n}$ is the normal vector, $\boldsymbol{m}$ is the conormal vector which is a vector tangent to the boundary and pointing outwards as in Fig. 2.1.

2.1.2 Lifshitz-invariant flexoelectricity model

This Section is presented in the same way as Section 2.1.1. The bulk internal enthalpy density of a flexoelectric material in the regime of infinitesimal deformations is expressed in terms of the displacement $\boldsymbol{u}$ and the electric potential ϕ as in Codony *et al.* (2021a)

$$\begin{aligned}\mathcal{H}^{\Omega}[\boldsymbol{u},\phi] =& \frac{1}{2}\varepsilon_{ij}\mathbb{C}_{ijkl}\varepsilon_{kl} + \frac{1}{2}\varepsilon_{ij,k}h_{ijklmn}\varepsilon_{lm,n} - \frac{1}{2}E_l\epsilon_{lm}E_m - \frac{1}{2}E_{m,n}M_{mnlk}E_{l,k} \\ & - E_le_{lij}\varepsilon_{ij} - \frac{1}{2}E_l\mu_{lijk}\varepsilon_{ij,k} + \frac{1}{2}E_{l,k}\mu_{lijk}\varepsilon_{ij},\end{aligned} \tag{2.24}$$

with the strain ε_{ij} and the electric field E_l defined in Eqs. (2.8a) and (2.8b), respectively. In contrast with Eq. (2.7), the bulk enthalpy density has a new term corresponding to the high-order electrostatics ruled by a fourth-order tensor M_{mnlk} called gradient dielectricity tensor.

The term accounting for flexoelectricity has been split into two terms, as done in Codony *et al.* (2021a): the direct flexoelectric effect coupling strain gradient with electric field and the converse flexoelectric effect coupling strain with the electric field gradient. The characterisation of the material tensor can be found in Appendix A.2.

The total bulk enthalpy of a flexoelectric material is

$$\Pi^{\Omega}[\boldsymbol{u},\phi] = \int_{\Omega} \left(\mathcal{H}^{\Omega}[\boldsymbol{u},\phi] + \mathcal{W}^{\Omega}[\boldsymbol{u},\phi] \right) \mathrm{d}\Omega. \tag{2.25}$$

where $\mathcal{W}^{\Omega}[\boldsymbol{u},\phi]$ is defined in Eq. (2.9).

The boundary $\partial\Omega$ is split again into several disjoint sets as

$$\partial\Omega = \partial\Omega_u \cup \partial\Omega_t = \partial\Omega_v \cup \partial\Omega_r = \partial\Omega_\phi \cup \partial\Omega_w = \partial\Omega_\varphi \cup \Omega_{\mathfrak{r}}, \tag{2.26}$$

where $\partial\Omega_u$, $\partial\Omega_v$, $\partial\Omega_\phi$ and $\partial\Omega_\varphi$ correspond to Dirichlet boundary conditions and $\partial\Omega_t$, $\partial\Omega_r$, $\partial\Omega_w$ and $\partial\Omega_{\mathfrak{r}}$ correspond to Neumann boundary conditions. This splitting can be seen in Fig. 2.2 similar to what we have done in Section 2.1.1.

Apart from the boundary conditions on the faces, some boundary conditions arise from the curves $C = \partial\partial\Omega$. Using the same notation as before, the curves are split into two disjoint sets as

$$\partial\partial\Omega = C_u \cup C_j = C_\phi \cup C_{\wp}, \tag{2.27}$$

where C_u, C_ϕ and C_j, $C_{\wp}$ are the curves where Dirichlet boundary conditions and Neumann boundary conditions are applied, respectively. It can be seen again in Fig. 2.2.

The corresponding boundary conditions applied are

$$\begin{aligned}
\boldsymbol{u} &= \boldsymbol{u}^{\mathrm{D}} \quad \text{on } \partial\Omega_u, & \boldsymbol{t} &= \boldsymbol{t}^{\mathrm{N}} \quad \text{on } \partial\Omega_t, && \text{(2.28a)}\\
\partial^n(\boldsymbol{u}) &= \boldsymbol{v}^{\mathrm{D}} \quad \text{on } \partial\Omega_v, & \boldsymbol{r} &= \boldsymbol{r}^{\mathrm{N}} \quad \text{on } \partial\Omega_r, && \text{(2.28b)}\\
\phi &= \phi^{\mathrm{D}} \quad \text{on } \partial\Omega_\phi, & w &= w^{\mathrm{N}} \quad \text{on } \partial\Omega_w, && \text{(2.28c)}\\
\partial^n(\phi) &= \varphi^{\mathrm{D}} \quad \text{on } \partial\Omega_\varphi, & \mathfrak{r} &= \mathfrak{r}^{\mathrm{N}} \quad \text{on } \partial\Omega_{\mathfrak{r}}, && \text{(2.28d)}\\
\boldsymbol{u} &= \boldsymbol{u}^{\mathrm{D}} \quad \text{on } C_u, & \boldsymbol{j} &= \boldsymbol{j}^{\mathrm{N}} \quad \text{on } C_j, && \text{(2.28e)}\\
\phi &= \phi^{\mathrm{D}} \quad \text{on } C_\phi & \wp &= \wp^{\mathrm{N}} \quad \text{on } C_{\wp}, && \text{(2.28f)}
\end{aligned}$$

where $\boldsymbol{u}^{\mathrm{D}}$, $\boldsymbol{v}^{\mathrm{D}}$, ϕ^{D} and φ^{D} are the prescribed value of displacement, normal derivative of the displacement, electric potential and normal derivative of the electric potential, respectively, and $\boldsymbol{t}^{\mathrm{N}}$, $\boldsymbol{r}^{\mathrm{N}}$, w^{N}, $\mathfrak{r}^{\mathrm{N}}$, $\boldsymbol{j}^{\mathrm{N}}$ and $\wp^{\mathrm{N}}$ are the prescribed value of the traction, double traction, surface charge double charge density, line force and electric charge density respectively.

The total enthalpy of the system for a flexoelectric material considering Lifshitz-invariant

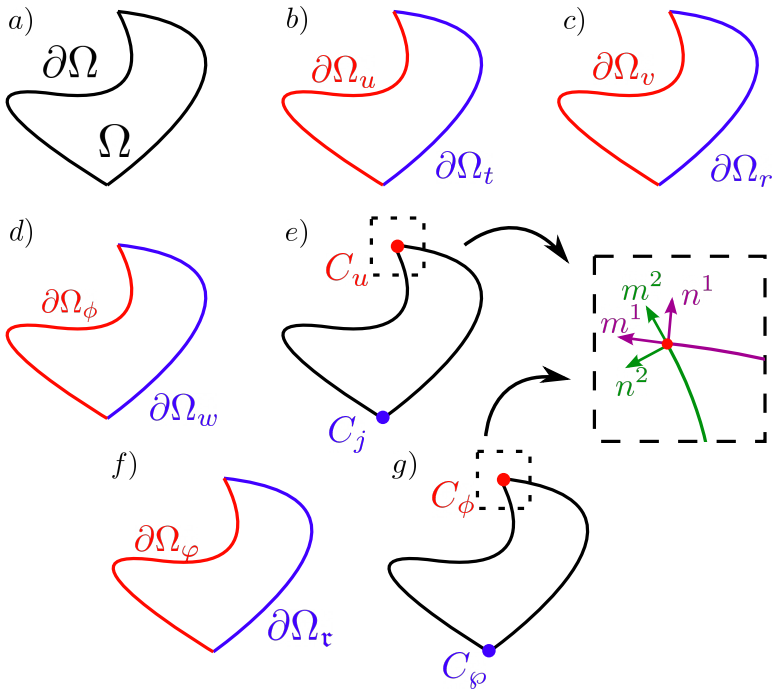

Figure 2.2: A 2D representation of the physical domain Ω and its boundary $\partial\Omega$. The boundary is split into several disjoint sets, as in Eq. (2.26) and Eq. (2.27). a) Domain and domain boundary. b) Domain boundary split based on mechanical low-order Dirichlet and Neumann mechanical boundary conditions. c) Domain boundary split based on high-order Dirichlet and Neumann mechanical boundary conditions. d) Domain boundary split based on low-order Dirichlet and Neumann electric boundary conditions. e) Domain boundary boundary $\partial\partial\Omega$ split in Dirichlet and Neumann mechanical edge (corner in 2D) conditions. f) Domain boundary split based on high-order Dirichlet and Neumann electric boundary conditions. g) Domain boundary boundary $\partial\partial\Omega$ split in Dirichlet and Neumann eletrical edge (corner in 2D) conditions.

flexoelectricity $\Pi^{\text{Lif}}[\boldsymbol{u}, \phi]$ is then

$$\Pi^{\text{Lif}}[\boldsymbol{u}, \phi] = \Pi^{\Omega}[\boldsymbol{u}, \phi] + \Pi^{\text{N}}[\boldsymbol{u}, \phi], \tag{2.29}$$

with

$$\Pi^{\text{N}}[\boldsymbol{u}, \phi] = \int_{\partial\Omega_t} -u_i t_i^{\text{N}} \,\mathrm{d}\Gamma + \int_{\partial\Omega_r} -\partial^n u_i r_i^{\text{N}} \,\mathrm{d}\Gamma + \int_{C_j} -u_i j_i^{\text{N}} \,\mathrm{d}s \tag{2.30}$$

$$+ \int_{\partial\Omega_w} \phi w^{\text{N}} \,\mathrm{d}\Gamma + \int_{\partial\Omega_\mathfrak{r}} \partial^n \phi \mathfrak{r}^{\text{N}} \,\mathrm{d}\gamma + \int_{C_\wp} \phi \wp^{\text{N}} \,\mathrm{d}s, \tag{2.31}$$

As mentioned before, the total enthalpy has no contribution from Dirichlet boundary conditions

in the standard approach. We recall the variational principle that must be fulfilled, that is

$$(\boldsymbol{u}^*, \phi^*) = \arg \min_{\boldsymbol{u} \in \mathcal{U}_{\mathrm{L}}} \max_{\phi \in \mathcal{P}_{\mathrm{L}}} \Pi^{\mathrm{Lif}}[\boldsymbol{u}, \phi] \tag{2.32}$$

where the functional spaces $\mathcal{U}_{\mathrm{L}}$ and $\mathcal{P}_{\mathrm{L}}$ are defined as

$$\mathcal{U}_{\mathrm{L}} = \left\{ \boldsymbol{u} \in [H^2(\Omega)]^3 | \boldsymbol{u} = \boldsymbol{u}^{\mathrm{D}} \text{ on } \partial\Omega_u \text{ and } C_u \text{ and } \partial^n(\boldsymbol{u}) = \boldsymbol{v}^{\mathrm{D}} \text{ on } \partial\Omega_v \right\}, \tag{2.33a}$$

$$\mathcal{P}_{\mathrm{L}} = \left\{ \phi \in H^2(\Omega) | \phi = \phi^{\mathrm{D}} \text{ on } \partial\Omega_\phi \text{ and } C_\phi \text{ and } \partial^n(\phi) = \varphi^{\mathrm{D}} \text{ on } \partial\Omega_\varphi \right\}, \tag{2.33b}$$

The weak form of the problem is deduced from the variational principle in Eq. (2.32) by enforcing $\delta\Pi^{\mathrm{Lif}} = 0$ for all admissible variations:

$$\text{Find } (\boldsymbol{u}, \phi) \in \mathcal{U}_{\mathrm{L}} \otimes \mathcal{P}_{\mathrm{L}} \text{ such that } \delta\Pi^{\mathrm{Lif}} = 0 \; \forall (\delta\boldsymbol{u}, \delta\phi) \in \mathcal{U}_0 \otimes \mathcal{P}_0, \tag{2.34}$$

with

$$\mathcal{U}_0 = \left\{ \delta\boldsymbol{u} \in [H^2(\Omega)]^3 | \delta\boldsymbol{u} = 0 \text{ on } \partial\Omega_u \text{ and } C_u \text{ and } \partial^n(\delta\boldsymbol{u}) = 0 \text{ on } \partial\Omega_v \right\}, \tag{2.35a}$$

$$\mathcal{P}_0 = \left\{ \delta\phi \in H^2(\Omega) | \delta\phi = 0 \text{ on } \partial\Omega_\phi \text{ and } C_\phi \text{ and } \partial^n(\delta\phi) = 0 \text{ on } \partial\Omega_\varphi \right\}, \tag{2.35b}$$

and

$$\delta\Pi^{\mathrm{Lif}}[\boldsymbol{u}, \phi, \delta\boldsymbol{u}, \delta\phi] = \delta\Pi^{\Omega}[\boldsymbol{u}, \phi, \delta\boldsymbol{u}, \delta\phi] + \delta\Pi^{\mathrm{N}}[\boldsymbol{u}, \phi, \delta\boldsymbol{u}, \delta\phi], \tag{2.36a}$$

$$\delta\Pi^{\Omega}[\boldsymbol{u}, \phi, \delta\boldsymbol{u}, \delta\phi] = \int_\Omega \widehat{\sigma}_{ij}\delta\varepsilon_{ij} + \tilde{\sigma}_{ijk}\delta\varepsilon_{ij,k} - \widehat{D}_l\delta E_l - b_i\delta u_i + q\delta\phi \, \mathrm{d}\Omega, \tag{2.36b}$$

$$\delta\Pi^{\mathrm{N}}[\boldsymbol{u}, \phi, \delta\boldsymbol{u}, \delta\phi] = \int_{\partial\Omega_t} -\delta u_i t_i^{\mathrm{N}} \, \mathrm{d}\Gamma + \int_{\partial\Omega_r} -\partial^n(\delta u_i) r_i^{\mathrm{N}} \, \mathrm{d}\Gamma + \int_{C_j} -\delta u_i j_i^{\mathrm{N}} \, \mathrm{d}s \tag{2.36c}$$

$$+ \int_{\partial\Omega_w} \delta\phi w^{\mathrm{N}} \, \mathrm{d}\Gamma + \int_{\partial\Omega_{\mathfrak{r}}} \partial^n(\delta\phi)\mathfrak{r}^{\mathrm{N}} \, \mathrm{d}\gamma + \int_{C_{\wp}} \delta\phi \wp^{\mathrm{N}} \, \mathrm{d}s, \tag{2.36d}$$

where the Cauchy stress $\hat{\boldsymbol{\sigma}}(\boldsymbol{u}, \phi)$, the double stress $\tilde{\boldsymbol{\sigma}}(\boldsymbol{u}, \phi)$, the local electric displacement $\hat{\boldsymbol{D}}(\boldsymbol{u}, \phi)$ and the double electric displacement $\widetilde{\boldsymbol{D}}(\boldsymbol{u}, \phi)$ are defined as

$$\hat{\sigma}_{ij}(\boldsymbol{u}, \phi) = \hat{\sigma}_{ji}(\boldsymbol{u}, \phi) = \frac{\partial\mathcal{H}^{\Omega}[\boldsymbol{u}, \phi]}{\partial\varepsilon_{ij}} = \mathbb{C}_{ijkl}\varepsilon_{kl}(\boldsymbol{u}) - e_{lij}E_l(\phi) + \frac{1}{2}\mu_{lijk}E_{l,k}(\phi), \tag{2.37a}$$

$$\tilde{\sigma}_{ijk}(\boldsymbol{u}, \phi) = \tilde{\sigma}_{jik}(\boldsymbol{u}, \phi) = \frac{\partial\mathcal{H}^{\Omega}[\boldsymbol{u}, \phi]}{\partial\varepsilon_{ij,k}} = h_{ijklmn}\varepsilon_{lm,n}(\boldsymbol{u}) - \frac{1}{2}\mu_{lijk}E_l(\phi), \tag{2.37b}$$

$$\hat{D}_l(\boldsymbol{u}, \phi) = -\frac{\partial\mathcal{H}^{\Omega}[\boldsymbol{u}, \phi]}{\partial E_l} = \epsilon_{lm}E_m(\phi) + e_{lij}\varepsilon_{ij}(\boldsymbol{u}) + \frac{1}{2}\mu_{lijk}\varepsilon_{ij,k}(\boldsymbol{u}), \tag{2.37c}$$

$$\widetilde{D}_{kl}(\boldsymbol{u}, \phi) = \widetilde{D}_{lk}(\boldsymbol{u}, \phi) = -\frac{\partial\mathcal{H}^{\Omega}[\boldsymbol{u}, \phi]}{\partial E_{l,k}} = M_{mnlk}E_{m,n}(\phi) - \frac{1}{2}\mu_{lijk}\varepsilon_{ij}(\boldsymbol{u}). \tag{2.37d}$$

The Euler-Lagrange equations are

$$\left(\hat{\sigma}_{ij}(\boldsymbol{u},\phi) - \tilde{\sigma}_{ijk,k}(\boldsymbol{u},\phi)\right)_{,j} + b_i = 0 \qquad \text{in } \Omega, \tag{2.38a}$$

$$\left(\hat{D}_l(\boldsymbol{u},\phi) - \widetilde{D}_{lk,k}(\boldsymbol{u},\phi)\right)_{,l} - q = 0 \qquad \text{in } \Omega. \tag{2.38b}$$

and

$$t_i(\boldsymbol{u},\phi) = \left(\hat{\sigma}_{ij} - \tilde{\sigma}_{ijk,k} + \nabla_l^S(n_l)\,\tilde{\sigma}_{ijk}n_k\right)n_j - \nabla_j^S\left(\tilde{\sigma}_{ijk}n_k\right) \qquad \text{on } \partial\Omega, \tag{2.39a}$$

$$r_i(\boldsymbol{u},\phi) = \tilde{\sigma}_{ijk}n_jn_k \qquad \text{on } \partial\Omega, \tag{2.39b}$$

$$w(\boldsymbol{u},\phi) = -\left(\hat{D}_l - \widetilde{D}_{lk,k} + \nabla_i^S(n_i)\widetilde{D}_{lk}n_k\right)n_l + \nabla_l^S\left(\widetilde{D}_{lk}n_k\right) \qquad \text{on } \partial\Omega, \tag{2.39c}$$

$$\mathfrak{r}(\boldsymbol{u},\phi) = -\widetilde{D}_{jk}n_jn_k \qquad \text{on } \partial\Omega, \tag{2.39d}$$

$$j_i(\boldsymbol{u},\phi) = \left[\!\left[\tilde{\sigma}_{ijk}(\boldsymbol{u},\phi)m_jn_k\right]\!\right] \qquad \text{on } C, \tag{2.39e}$$

$$\wp(\boldsymbol{u},\phi) = -\left[\!\left[\widetilde{D}_{jk}(\boldsymbol{u},\phi)m_jn_k\right]\!\right] \qquad \text{on } C, \tag{2.39f}$$

The physical stress $\boldsymbol{\sigma}$ and the physical electric displacement $\boldsymbol{D}$ are deduced from Eq. (2.38) as

$$\begin{aligned}\sigma_{ij} &= \hat{\sigma}_{ij} - \tilde{\sigma}_{ijk,k} = \mathbb{C}_{ijkl}\varepsilon_{kl}(\boldsymbol{u}) - e_{lij}E_l(\phi) - h_{ijklmn}\varepsilon_{lm,nk}(\boldsymbol{u}) + \mu_{lijk}E_{l,k}(\phi),\\ D_l &= \hat{D}_l - \widetilde{D}_{lk,k} = \kappa_{lm}E_m(\phi) + e_{lij}\varepsilon_{ij}(\boldsymbol{u}) - M_{ijlk}E_{i,jk}(\phi) + \mu_{lijk}\varepsilon_{ij,k}(\boldsymbol{u}).\end{aligned} \tag{2.40}$$

2.2 High-order interface conditions applied to direct flexoelectricity.

In order to enhance the flexoelectric effect, an arbitrary arrangement of materials with different materials properties can be beneficial. To properly define flexoelectric boundary value problems in heterogeneous materials, continuity and equilibrium conditions have to be prescribed on material interfaces. These set of conditions are termed interface conditions. Although continuity conditions for classic elasticity at material interfaces with Isogeometric analysis (IGA) have been developed (Dolbow and Harari, 2009, Jiang *et al.*, 2015), high-order interfaces in unfitted discretisations had not been addressed in the literature to the best of our knowledge, until we did in Barceló-Mercader *et al.* (2022). In this section, we present this contribution, published in Barceló-Mercader *et al.* (2022). In the context of immersed approaches, these conditions need to be imposed weakly. We derive Nitsche's method for this purpose, which is a consistent penalty method which preserves the variational structure. As a preliminary, we briefly review the Nitsche's method for the weak imposition of Dirichlet boundary conditions in the direct flexoelectricity framework (Codony *et al.*, 2019). Next, we present a rigorous and justified statement of the high-order interface conditions along arbitrary material interfaces in the context of direct flexoelectricity, accounting for strain-gradient elasticity. Finally, we

present the variational formulation for the weak imposition of these conditions through Nitsche's method. Analogously, the modified variational problem is derived by adding a new term in the total enthalpy of the system corresponding with the enthalpy associated with the interface conditions. The weak form is obtained from the variational principle.

2.2.1 Nitsche's method for direct flexoelectricity

The previous method explained in Section 2.1.1 constrains the functional space of the solution in order to enforce Dirichlet boundary conditions, and thus these conditions are strongly satisfied. Other methods enforce them in a weak sense as Lagrange multiplier (Belytschko *et al.*, 1994), penalty method (Zhu and Atluri, 1998) or the one used here, Nitsche's methods (Babuška *et al.*, 2003, Fernández-Méndez and Huerta, 2004, Griebel and Schweitzer, 2003). Nitsche's method presents not only interesting numerical advantages, such as preserving symmetry, the number of degrees of freedom and optimal convergence rates, but also theoretical advantages, such as self-consistency.

To enforce Dirichlet boundary conditions using Nitsche's method, we modify the enthalpy functional in Eq. (2.14) in such a way that the equilibrium states satisfying the variational principle necessarily satisfy the essential boundary conditions in a weak sense. This implies adding, for each variable, two types of contributions acting on the Dirichlet boundaries which penalise deviations from the corresponding essential conditions. The first type of contribution ensures coercivity of the resulting variational problem. The second is added to preserve symmetry and self-consistency. In the case of direct flexoelectricity, Nitsche's enthalpy functional is

$$\begin{aligned}\Pi^{\mathrm{D}}[\boldsymbol{u},\phi] = &\int_{\partial\Omega_u}\left(\frac{1}{2}\beta_u\left(u_i-u_i^{\mathrm{D}}\right)^2-\left(u_i-u_i^{\mathrm{D}}\right)t_i\right)\,\mathrm{d}\Gamma\\ &+\int_{\partial\Omega_v}\left(\frac{1}{2}\beta_v\left(\partial^n(u_i)-v_i^{\mathrm{D}}\right)^2-\left(\partial^n(u_i)-v_i^{\mathrm{D}}\right)r_i\right)\,\mathrm{d}\Gamma\\ &+\int_{\partial\Omega_\phi}-\left(\frac{1}{2}\beta_\phi\left(\phi-\phi^{\mathrm{D}}\right)^2+\left(\phi-\phi^{\mathrm{D}}\right)w\right)\,\mathrm{d}\Gamma\\ &+\int_{\partial C_u}\left(\frac{1}{2}\beta_{C_u}\left(u_i-u_i^{\mathrm{D}}\right)^2-\left(u_i-u_i^{\mathrm{D}}\right)t_i\right)\,\mathrm{d}s\end{aligned}\tag{2.41}$$

with positive Nitsche's parameters β_u, β_v, β_ϕ and β_{C_u}. The selection of these penalty parameters is done in section 3.3.

The modified total enthalpy of the system Π^{Dir^*} then becomes

$$\Pi^{\mathrm{Dir}}_{\mathrm{Nit}}[\boldsymbol{u},\phi] = \Pi^{\Omega}[\boldsymbol{u},\phi]+\Pi^{\mathrm{D}}[\boldsymbol{u},\phi]+\Pi^{\mathrm{N}}[\boldsymbol{u},\phi],\tag{2.42}$$

with $\Pi^{\Omega}[\boldsymbol{u},\phi]$, $\Pi^{\mathrm{D}}[\boldsymbol{u},\phi]$ and $\Pi^{\mathrm{N}}[\boldsymbol{u},\phi]$ defined in Eqs. (2.10), (2.15) and (2.41), respectively.

The variational principle associated with the enthalpy functional in Eq. (2.42) is

$$(\boldsymbol{u}^*, \phi^*) = \arg \min_{\boldsymbol{u} \in \mathcal{U}} \max_{\phi \in \mathcal{P}} \Pi^{\text{Dir}}_{\text{Nit}}[\boldsymbol{u}, \phi] \tag{2.43}$$

where $\mathcal{U}$ is the space of functions belonging to $[\mathcal{H}^2(\Omega)]^3$ with $\mathcal{L}^2$-integrable third derivative on the Dirichlet boundary $\partial\Omega_u$ and $\mathcal{P} = H^1(\Omega)$. The need for integrable third derivatives of the displacements follows from the expression of the tractions, see last term in Eq. (2.23a), now appearing in the second term of the integral on $\partial\Omega_u$. As previously done in Eq. (2.18), the weak form associated with the variational principle in Eq. (2.43) is deduced by enforcing $\delta\Pi^{\text{Dir}^*} = 0$ for all admissible variation:

$$\text{Find } (\boldsymbol{u}, \phi) \in \mathcal{U} \otimes \mathcal{P}, \text{ such that } \delta\Pi^{\text{Dir}} = 0 \; \forall (\delta\boldsymbol{u}, \delta\phi) \in \mathcal{U} \otimes \mathcal{P}, \tag{2.44}$$

with

$$\delta\Pi^{\text{Dir}}_{\text{Nit}}[\boldsymbol{u}, \phi, \delta\boldsymbol{u}, \delta\phi] = \delta\Pi^{\Omega}[\boldsymbol{u}, \phi, \delta\boldsymbol{u}, \delta\phi] + \delta\Pi^{\text{D}}[\boldsymbol{u}, \phi, \delta\boldsymbol{u}, \delta\phi] + \delta\Pi^{\text{N}}[\boldsymbol{u}, \phi, \delta\boldsymbol{u}, \delta\phi], \tag{2.45}$$

where $\delta\Pi^{\Omega}$ and $\delta\Pi^{\text{N}}$ are defined in Eqs. (2.20b) and (2.20c) respectively, and

$$\begin{aligned}
\delta\Pi^{\text{D}}[\boldsymbol{u}, \phi, \delta\boldsymbol{u}, \delta\phi] = &\int_{\partial\Omega_u} \left(\beta_u \left(u_i - u_i^{\text{D}}\right)\delta u_i - \left(u_i - u_i^{\text{D}}\right)\delta t_i - \delta u_i t_i\right) \, \text{d}\Gamma \\
&+ \int_{\partial\Omega_v} \left(\beta_v \left(\partial^n(u_i) - v_i^{\text{D}}\right)\partial^n(\delta u_i) - \left(\partial^n(u_i) - v_i^{\text{D}}\right)\delta r_i - \partial^n(\delta u_i) r_i\right) \, \text{d}\Gamma \\
&+ \int_{\partial\Omega_\phi} -\left(\beta_\phi \left(\phi - \phi^{\text{D}}\right)\delta\phi + \left(\phi - \phi^{\text{D}}\right)\delta w + \delta\phi w\right) \, \text{d}\Gamma \\
&+ \int_{\partial C_u} \left(\beta_{C_u} \left(u_i - u_i^{\text{D}}\right)\delta u_i - \left(u_i - u_i^{\text{D}}\right)\delta t_i - \delta u_i t_i\right) \, \text{ds}
\end{aligned} \tag{2.46}$$

Remark 2.1. Thanks to Nistche's method, the functional spaces of the solution and the admissible variation required by the weak form in Eq. (2.44) are the same and are unconstrained.

2.2.2 High-order electromechanical interface conditions

Let Ω be our physical domain which is conformed by several non-overlapping subdomains as $\Omega = \bigcup_{i=1}^{N} \Omega^i$. The boundary of Ω is composed of the exterior boundary, $\partial\overline{\Omega}$, and the interior boundary or interface, $\mathcal{I} = [\bigcup_{i=1}^{N} \partial\Omega^i] \backslash \partial\overline{\Omega}$. The exterior boundary and interface are illustrated in Fig. 2.3. The interface is split into multiple parts $\mathcal{I}^k$, each one corresponding to the interface shared by two subdomains, i.e. $\mathcal{I} = \bigcup_{k=1}^{n_f} \mathcal{I}^k$, with $\mathcal{I}^k = \partial\Omega^{L(k)} \cap \partial\Omega^{R(k)}$, being $\Omega^{L(k)}$ and $\Omega^{R(k)}$ the adjacent subdomains. $L(k)$ and $R(k)$ are understood as the left and right subdomains.

To define the interface conditions, we define the weighted mean and jump operators for a

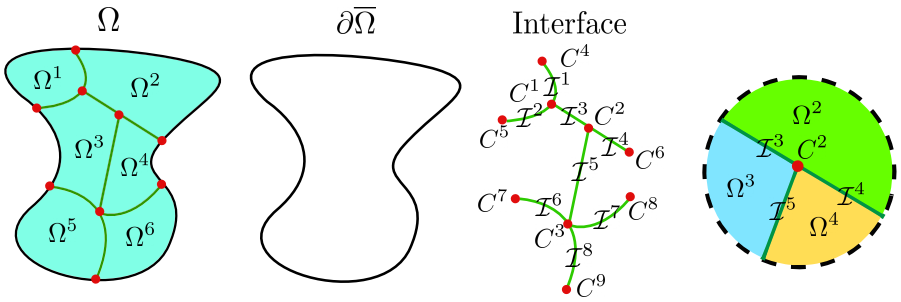

Figure 2.3: Physical domain Ω composed of six subdomains with external boundary $\partial\overline{\Omega}$ (in black) and interface $\mathcal{I}$ (in green). An example of the relative notation around one side and corner is depicted on the right. The interface $\mathcal{I}^5$ is shared by the subdomains $\Omega^{R(5)}$ and $\Omega^{L(5)}$ with $R(5) = 4$ and $L(5) = 3$. The corner C^2 is shared by 3 subdomains $\{\Omega^{P(2,k)}\}_{k=1}^{m(3)}$ with $m(3) = 3$, $P(2,1) = 2$, $P(2,2) = 3$ and $P(2,3) = 4$. Image adapted from Barceló-Mercader *et al.* (2022)

generic function A that may be discontinuous across $\mathcal{I}$, and they are expressed as

$$\{A\}_\gamma = \gamma^{L(k)} A^{L(k)} + \gamma^{R(k)} A^{R(k)} \quad \text{on} \quad \mathcal{I}^k, \tag{2.47a}$$

$$[\![A]\!] = A^{L(k)} + A^{R(k)} \quad \text{on} \quad \mathcal{I}^k, \tag{2.47b}$$

with scalar values $\gamma^{L(k)}, \gamma^{R(k)} \in (0,1)$ such that $\gamma^{L(k)} + \gamma^{R(k)} = 1$, and denoting as A^i the value of A in subdomain Ω^i. The jump operator defined in Eq. 2.23 and the one defined here in Eq. 2.47 are mostly the same, and we use the same symbol. In most cases, the arithmetic mean is usually enough ($\gamma^{L(k)} = \gamma^{R(k)} = 0.5$).

As done before in Section 2.1.1, we define the edges (corners in 2D) of the interface $\mathcal{I}$, which are the boundary of the interfaces except for the edges on the Dirichlet boundary, that is $C_\mathcal{I} = \{C^k\}_{k=1}^{n_C} = \bigcup_{f=1}^{n_f} \partial\mathcal{I}^f \backslash C_u$. For each edge C^k, there are $m(k)$ subdomains $\{\Omega^{P(k,1)}, ..., \Omega^{P(k,m(k))}\}$ adjacent to it, see Fig. 2.3. In Fig. 2.3, the corner C^2 is shared by three subdomains: Ω^2, Ω^3 and Ω^4. The weighted mean operator, which is a generalisation of the one presented in Eq. (2.47a), is also defined on C^k as

$$\langle A \rangle_{\hat{\gamma}} = \sum_{i=1}^{m(k)} \hat{\gamma}^{P(k,i)} A^{P(k,i)} \quad \text{on } C^k \subset C_\mathcal{I}, \tag{2.48}$$

with $\hat{\gamma}^{P(k,i)} \in (0,1)$ such that $\sum_{i=1}^{m(k)} \hat{\gamma}^{P(k,i)} = 1$. It represents a weighted average of the value of A in all subdomains sharing the edge.

Now, we can define interface conditions using the weighted mean and jump operator. The interface conditions that must be fulfilled at the interface and edges (corners in 2D) enforce

the continuity of the solution and equilibrium. That is,

$$\left[\!\left[\boldsymbol{u} \otimes \mathbf{n} \right]\!\right] = \mathbf{0}, \qquad \left[\!\left[\partial^n \boldsymbol{u} \right]\!\right] = \mathbf{0}, \qquad \left[\!\left[\phi \mathbf{n} \right]\!\right] = \mathbf{0}, \qquad \text{on } \mathcal{I}, \tag{2.49a}$$

$$\left[\!\left[\boldsymbol{t}(\boldsymbol{u},\phi) \right]\!\right] = \hat{\boldsymbol{t}}, \qquad \left[\!\left[\boldsymbol{r}(\boldsymbol{u},\phi) \otimes \mathbf{n} \right]\!\right] = \hat{\boldsymbol{r}} \otimes \mathbf{n}^L, \qquad \left[\!\left[w(\boldsymbol{u},\phi) \right]\!\right] = \hat{w}, \qquad \text{on } \mathcal{I}, \tag{2.49b}$$

and

$$\boldsymbol{u}^{P(k,i)} - \langle \boldsymbol{u} \rangle_{\hat{\gamma}} = \mathbf{0} \quad i = 1 \dots m(k) \qquad \text{on } C^k \subset C_{\mathcal{I}}, \tag{2.50a}$$

$$\sum_{i=1}^{m(k)} \boldsymbol{j}^{P(k,i)}(\boldsymbol{u},\phi) = \hat{\boldsymbol{j}} \qquad \text{on } C^k \subset C_{\mathcal{I}} \tag{2.50b}$$

where $\boldsymbol{u}^\alpha$ and $\boldsymbol{j}^\alpha(\boldsymbol{u},\phi)$ denote the displacement and the line force on the edge coming from the subdomain Ω^α sharing the edge. The data is $\hat{\boldsymbol{j}} = \bar{\boldsymbol{j}}$ on edges on the boundary and $\hat{\boldsymbol{j}} = \mathbf{0}$ on edges in the interior of the domain. Low-order interface conditions in Eq. (2.49a) are imposed strongly and low-order interface conditions in Eq. (2.49b) are automatically fulfilled by using the body-fitted method as standard finite element method or isogeometric analysis.

Then, Eq. (2.50) enforces that the sum of the forces from each subdomain sharing an edge C^k is in internal equilibrium or equilibrium with external boundary forces. The values of $\hat{\boldsymbol{t}}$, $\hat{\boldsymbol{r}}$ and $\hat{w}$ in Eq. (2.49) are also zero for physical problems and conveniently set for synthetic solutions.

2.2.3 Nitsche's method for high-order electromechanical interface conditions

The enthalpy associated with Eq. (2.49) and Eq. (2.50) is analogous to that of Dirichlet boundary conditions using Nitsche's method in Eq. (2.41), and Neumann boundary conditions in Eq. (2.15). Thus, the total enthalpy associated with interfaces is

$$\begin{aligned}
\Pi^{\mathrm{I}}[\boldsymbol{u},\phi] = &\int_{\mathcal{I}} \left[\frac{1}{2}\beta^{u\mathcal{I}} \left[\!\left[u_i n_j \right]\!\right]^2 - \left[\!\left[u_i n_j \right]\!\right] \left\{ t_i(\boldsymbol{u},\phi) n_j \right\}_\gamma - \hat{t}_i \left\{ u_i \right\}_{1-\gamma} \right] \mathrm{d}\Gamma + \\
&+ \int_{\mathcal{I}} \left[\frac{1}{2}\beta^{v\mathcal{I}} \left[\!\left[\partial^n u_i \right]\!\right]^2 - \left[\!\left[\partial^n u_i \right]\!\right] \left\{ r_i(\boldsymbol{u},\phi) \right\}_\gamma - \hat{r}_i n_j^L \left\{ u_{i,j} \right\}_{1-\gamma} \right] \mathrm{d}\Gamma + \\
&+ \int_{\mathcal{I}} \left[-\frac{1}{2}\beta^{\phi\mathcal{I}} \left[\!\left[\phi n_i \right]\!\right]^2 + \left[\!\left[\phi n_i \right]\!\right] \left\{ w(\boldsymbol{u},\phi) n_i \right\}_\gamma + \hat{w} \left\{ \phi \right\}_{1-\gamma} \right] \mathrm{d}\Gamma + \\
&+ \sum_{k=1}^{n_C} \int_{C^k} \left[\sum_{\alpha \in P(k,:)} \left(\frac{1}{2}\beta^{C_u \mathcal{I}} (u_i^\alpha - \langle u_i \rangle_{\hat{\gamma}})^2 - (u_i^\alpha - \langle u_i \rangle_{\hat{\gamma}}) j_i^\alpha(\boldsymbol{u},\phi) \right) - \langle u_i \rangle_{\hat{\gamma}} \hat{j}_i \right] \mathrm{ds}.
\end{aligned} \tag{2.51}$$

where $P(k,:) = \{P(k,1), ..., P(k,m(k))\}$.

As before, the penalty parameters $\beta^{u\mathcal{I}}$, $\beta^{v\mathcal{I}}$, $\beta^{\phi\mathcal{I}}$ and $\beta^{C_u\mathcal{I}}$ seen in Eq. (2.51) must be large

enough to ensure concave-up enthalpy concerning the displacement $\boldsymbol{u}$, and concave-down enthalpy for the electric potential ϕ. The selection of the penalty parameters is done in section 3.3

The total enthalpy of the domain Ω with material interfaces is then

$$\Pi[\boldsymbol{u}, \phi] = \Pi^{\Omega}[\boldsymbol{u}, \phi] + \Pi^{\mathrm{D}}[\boldsymbol{u}, \phi] + \Pi^{\mathrm{N}}[\boldsymbol{u}, \phi] + \Pi^{\mathrm{I}}[\boldsymbol{u}, \phi]. \tag{2.52}$$

The variational principle is similar to the one defined in Eq. (2.43), and it is

$$(\boldsymbol{u}^{*}, \phi^{*}) = \arg \min_{\boldsymbol{u} \in \mathcal{U}^{*}} \max_{\phi \in \mathcal{H}^{1}(\Omega)} \Pi[\boldsymbol{u}, \phi], \tag{2.53}$$

where $\mathcal{U}^{*}$ is the space of functions belonging to $[\mathcal{H}^{2}(\Omega)]^{d}$ with $\mathcal{L}^{2}$-integrable third derivative on the Dirichlet boundary $\partial\Omega_{u}$ and interface $\mathcal{I}$.

2.2.4 Variational formulation for flexoelectricity with material interfaces using Nitsche's method

The weak form of the problem is derived from the first-order stationarity condition

$$\delta\Pi[\boldsymbol{u}, \phi; \delta\boldsymbol{u}, \delta\phi] = 0, \quad \forall \delta\boldsymbol{u} \in \mathcal{U}^{*}, \ \delta\phi \in \mathcal{H}^{1}(\Omega), \tag{2.54}$$

where

$$\begin{aligned} \delta\Pi[\boldsymbol{u}, \phi; \delta\boldsymbol{u}, \delta\phi] =& \delta\Pi^{\Omega}[\boldsymbol{u}, \phi; \delta\boldsymbol{u}, \delta\phi] + \delta\Pi^{\mathrm{D}}[\boldsymbol{u}, \phi; \delta\boldsymbol{u}, \delta\phi] + \delta\Pi^{\mathrm{N}}[\delta\boldsymbol{u}, \delta\phi] \\ &+ \delta\Pi^{\mathrm{I}}[\boldsymbol{u}, \phi; \delta\boldsymbol{u}, \delta\phi], \end{aligned} \tag{2.55}$$

with $\delta\Pi^{\Omega}$, $\delta\Pi^{\mathrm{D}}$, $\delta\Pi^{\mathrm{N}}$ defined in Eqs. (2.20b), (2.20c), (2.46) and

$$\begin{aligned}
\delta\Pi^{\mathrm{I}}[\boldsymbol{u},\phi,\delta\boldsymbol{u},\delta\phi] = &\int_{\mathcal{I}}\Big[\beta^{u\mathcal{I}}\,[\![\delta u_i n_j]\!]\,[\![u_i n_j]\!] - [\![\delta u_i n_j]\!]\left\{t_i(\boldsymbol{u},\phi)n_j\right\}_{\gamma}\\
&- [\![u_i n_j]\!]\left\{t_i(\delta\boldsymbol{u},\delta\phi)n_j\right\}_{\gamma} - \hat{t}_i\left\{\delta u_i\right\}_{1-\gamma}\Big]\,\mathrm{d}\Gamma +\\
&+\int_{\mathcal{I}}\Big[\beta^{v\mathcal{I}}\left[\!\left[\partial^n\delta u_i\right]\!\right]\left[\!\left[\partial^n u_i\right]\!\right] - \left[\!\left[\partial^n\delta u_i\right]\!\right]\left\{r_i(\boldsymbol{u},\phi)\right\}_{\gamma}\\
&- \left[\!\left[\partial^n u_i\right]\!\right]\left\{r_i(\delta\boldsymbol{u},\delta\phi)\right\}_{\gamma} - \hat{r}_i n_j^L\left\{\delta u_{i,j}\right\}_{1-\gamma}\Big]\,\mathrm{d}\Gamma +\\
&+\int_{\mathcal{I}}\Big[-\beta^{\phi\mathcal{I}}\left[\!\left[\delta\phi n_i\right]\!\right]\left[\!\left[\phi n_i\right]\!\right] + \left[\!\left[\delta\phi n_i\right]\!\right]\left\{w(\boldsymbol{u},\phi)n_i\right\}_{\gamma}\\
&+ \left[\!\left[\phi n_i\right]\!\right]\left\{w(\delta\boldsymbol{u},\delta\phi)n_j\right\}_{\gamma} + \hat{w}\left\{\delta\phi\right\}_{1-\gamma}\Big]\,\mathrm{d}\Gamma +\\
+\sum_{k=1}^{n_C}\int_{C^k}\Big[&\sum_{\alpha\in P(k,:)}\Big(\beta^{C_u\mathcal{I}}\Big(u_i^{\alpha}-\langle u_i\rangle_{\hat{\gamma}}\Big)\Big(\delta u_i^{\alpha}-\langle\delta u_i\rangle_{\hat{\gamma}}\Big)\\
&-\Big(u_i^{\alpha}-\langle u_i\rangle_{\hat{\gamma}}\Big)j_i^{\alpha}(\delta\boldsymbol{u},\delta\phi) - j_i^{\alpha}(\boldsymbol{u},\phi)\delta u_i^{\alpha}\,\mathrm{d}\Gamma\\
&-\hat{\gamma}^{\alpha}\Big(\hat{j}_i - \sum_{\tau\in P(k;:)} j_i^{\tau}(\boldsymbol{u},\phi)\Big)\delta u_i^{\alpha}\Big)\Big]\,\mathrm{ds}.
\end{aligned}\tag{2.56}$$

In addition, the following conditions ensure a well-posed saddle point problem:

$$\delta_u^2\Pi[\boldsymbol{u},\phi;\delta\boldsymbol{u}] > 0, \quad \delta_\phi^2\Pi[\boldsymbol{u},\phi;\delta\phi] < 0, \quad \forall\delta\boldsymbol{u},\delta\phi. \tag{2.57}$$

Finally, the weak form of the problem is

$$\text{Find } (\boldsymbol{u},\phi)\in\mathcal{U}\otimes\mathcal{H}^1(\Omega) \text{ such that } \delta\Pi[\boldsymbol{u},\phi;\delta\boldsymbol{u},\delta\phi]=0, \forall(\delta\boldsymbol{u},\delta\phi)\in\mathcal{U}\otimes\mathcal{H}^1(\Omega). \tag{2.58}$$

2.3 Generalisation to high-order fictitious generalized-periodic horizontal and vertical boundaries

Periodic structures are obtained by periodically replicating a structural unit cell in one, two or three spatial dimensions. Boundary value problems on periodic structures can be efficiently solved by reducing them to the unit cell or RVE with so-called generalised periodic conditions in the direction of periodicity (Hassani and Hinton, 1998, Kolpakov, 1991). These conditions want to replicate the macroscopic loading conditions of a unit cell in an infinitely periodic structure and are thus devoid of sample's finite-size effects. In our case, these macroscopic loading conditions can be mapped to jumps of the primary variables, displacement $\boldsymbol{u}$ and electric potential ϕ, between the unit cell fictitious periodic boundaries. Since flexoelectricity

governing equations are a system of fourth-order PDEs, generalised periodicity needs to be complemented with appropriate periodicity conditions for the high-order fields, enforcing C^1 continuity of the primary fields $\boldsymbol{u}$ and ϕ. In unfitted discretisations, high-order generalised periodicity conditions can be enforced weakly using the formalism for physical interfaces presented in Section 2.2, as described next. For the sake of simplicity, we consider in this section high-order generalised periodicity along the horizontal and vertical directions.

2.3.1 High-order Generalised periodicity conditions along the horizontal and vertical directions

For the sake of simplicity, let us restrict ourselves to a 2D lattice that is periodically replicated along $x-$ and $y-$ spatial directions. The generalisation of the 3D case is straightforward. The unit cell Ω is embedded in a rectangle $R = [0, L_x] \times [0, L_y]$, as shown in the example in Fig. 2.4. The boundary of the domain Ω is composed of generalised periodic boundaries, $\mathcal{I}^y = \{(x, 0) \in \partial\Omega\} \equiv \{(x, L_y) \in \partial\Omega\}$ and $\mathcal{I}^x = \{(0, y) \in \partial\Omega\} \equiv \{(L_x, y) \in \partial\Omega\}$, and physical boundaries in the interior of the rectangle, $\partial\Omega\backslash[\mathcal{I}^x \cup \mathcal{I}^y]$.

We define C^x as the set of values of the y-component of the corners in $\mathcal{I}^x$ and C^y as the set of values of the x-component of the corners in $\mathcal{I}^y$, see Fig. 2.4. In the example in Fig. 2.4 we can set a unit cell from a solid structure with circular voids. The boundary of each void is considered the physical boundary and the other ones are considered the generalised periodic boundaries.

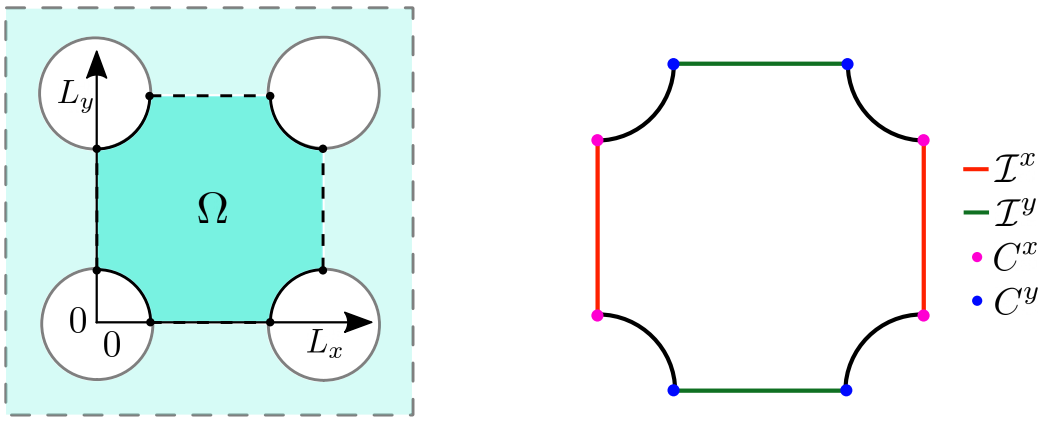

Figure 2.4: Example of one unit cell of a periodic structure, $C^x = \{L_y/4, 3L_y/4\}$ and $C^y = \{L_x/4, 3L_x/4\}$. This image represents the unit cell of a solid structure with a circular void. Image adapted from Barceló-Mercader *et al.* (2022)

The generalised periodicity conditions of the unit cell are then

$$
\begin{aligned}
&[\![\boldsymbol{u}]\!]^y = \check{\boldsymbol{u}}^y, && \boldsymbol{t}(\boldsymbol{u},\phi)|_{y=L_y} + \boldsymbol{t}(\boldsymbol{u},\phi)|_{y=0} = \boldsymbol{0}, && \text{on } \mathcal{I}^y\\
&\left[\!\!\left[\frac{\partial \boldsymbol{u}}{\partial y}\right]\!\!\right]^y = \boldsymbol{0}, && [\![\boldsymbol{r}(\boldsymbol{u},\phi)]\!]^y = \boldsymbol{0}, && \text{on } \mathcal{I}^y\\
&[\![\phi]\!]^y = \check{\phi}^y, && w(\boldsymbol{u},\phi)|_{y=L_y} + w(\boldsymbol{u},\phi)|_{y=0} = \boldsymbol{0} && \text{on } \mathcal{I}^y,\\
&[\![\boldsymbol{u}]\!]^y = \check{\boldsymbol{u}}^y, && \boldsymbol{j}(\boldsymbol{u},\phi)|_{y=L_y} + \boldsymbol{j}(\boldsymbol{u},\phi)|_{y=0} = \boldsymbol{0} && \text{for } x \in \mathcal{C}^y,\\
&[\![\boldsymbol{u}]\!]^x = \check{\boldsymbol{u}}^x, && \boldsymbol{t}(\boldsymbol{u},\phi)|_{x=L_x} + \boldsymbol{t}(\boldsymbol{u},\phi)|_{x=0} = \boldsymbol{0}, && \text{on } \mathcal{I}^x\\
&\left[\!\!\left[\frac{\partial \boldsymbol{u}}{\partial x}\right]\!\!\right]^x = \boldsymbol{0}, && [\![\boldsymbol{r}(\boldsymbol{u},\phi)]\!]^x = \boldsymbol{0}, && \text{on } \mathcal{I}^x\\
&[\![\phi]\!]^x = \check{\phi}^x, && w(\boldsymbol{u},\phi)|_{x=L_x} + w(\boldsymbol{u},\phi)|_{x=0} = \boldsymbol{0} && \text{on } \mathcal{I}^x,\\
&[\![\boldsymbol{u}]\!]^x = \check{\boldsymbol{u}}^x, && \boldsymbol{j}(\boldsymbol{u},\phi)|_{x=L_x} + \boldsymbol{j}(\boldsymbol{u},\phi)|_{x=0} = \boldsymbol{0} && \text{for } y \in \mathcal{C}^x,
\end{aligned}
\tag{2.59}
$$

where the jump on the periodic boundaries is defined as

$$
[\![A]\!]^y = A(x, L_y) - A(x, 0), \quad [\![A]\!]^x = A(L_x, y) - A(0, y), \tag{2.60}
$$

for convenience. The jumps $\check{\boldsymbol{u}}^y$, $\check{\boldsymbol{u}}^x$, $\check{\phi}^y$ and $\check{\phi}^x$ can be either given constants (mapped from the applied load at the macroscopic level) or unknown constants that have to be determined assuming a prescribed value of their macroscopic work-conjugate (generally, but not necessarily, null). We are interested in four different cases:

- Unconfined vertical displacement sensor: a vertical macroscopic strain is applied, $\check{\boldsymbol{u}}^y = (0, \check{u}^y)$, with $\check{u}^y$ a known constant, and the displacement jump $\check{\boldsymbol{u}}^x$, and electric potential jumps, $\check{\phi}^y$ and $\check{\phi}^x$, are unknown to be computed assuming vanishing macroscopic tractions on the vertical unit cell boundaries and that no surface charges accumulate on unit cell boundaries, i.e. $\boldsymbol{D} \cdot \mathbf{n} = 0$ on $\mathcal{I}^x$ and $\mathcal{I}^y$, $\boldsymbol{D}$ being the macroscopic physical electric displacement.

- Confined vertical displacement sensor: a vertical macroscopic strain is applied, $\check{\boldsymbol{u}}^y = (0, \check{u}^y)$, with $\check{u}^y$ a known constant, the displacement jump $\check{\boldsymbol{u}}^x$ is constrained $\check{\boldsymbol{u}}^x = (0, 0)$, and electric potential jumps, $\check{\phi}^y$ and $\check{\phi}^x$, are unknowns to be computed assuming vanishing macroscopic tractions on all unit cell boundaries and that no surface charges accumulate on unit cell boundaries, i.e. $\boldsymbol{D} \cdot \mathbf{n} = 0$ on $\mathcal{I}^x$ and $\mathcal{I}^y$.

- Unconfined vertical displacement actuator: an electric potential difference is applied macroscopically, which can be mapped to known electric potential jumps in the unit cell, $\check{\phi}^y$ and $\check{\phi}^x$, and the unknown displacement jumps $\check{\boldsymbol{u}}^y$ and $\check{\boldsymbol{u}}^x$.

- Confined vertical displacement actuator: an electric potential difference is applied macroscopically, which can be mapped to known electric potential jumps in the unit cell, $\check{\phi}^y$ and $\check{\phi}^x$, and the unknown displacement jump $\check{\boldsymbol{u}}^y$ and $\check{\boldsymbol{u}}^x = (0, 0)$.

If the corners of the rectangle lie inside the material domain, then generalised periodicity conditions for both $\mathcal{I}_x$ and $\mathcal{I}_y$ must be enforced simultaneously. For instance, the definition in Eq. (2.60) becomes

$$[\![A]\!]^y = A(L_x, L_y) - A(L_x, 0) + A(0, L_y) - A(0, 0), \quad [\![A]\!]^x = A(L_x, L_y) - A(0, L_y) + A(L_x, 0) - A(0, 0), \tag{2.61}$$

at the vertex. This situation can be avoided in general by a suitable choice of the unit cell. In the next section, the generalised periodicity condition will be applied in a differently, where this remark is no longer necessary.

The total enthalpy of the system is

$$\Pi[\boldsymbol{u}, \phi, \check{\boldsymbol{u}}, \check{\phi}] = \Pi^{\Omega}[\boldsymbol{u}, \phi] + \Pi^{\mathrm{D}}[\boldsymbol{u}, \phi] + \Pi^{\mathrm{N}}[\boldsymbol{u}, \phi] + \Pi^{\mathrm{P,y}}[\boldsymbol{u}, \phi, \check{\boldsymbol{u}}, \check{\phi}] + \Pi^{\mathrm{P,x}}[\boldsymbol{u}, \phi, \check{\boldsymbol{u}}, \check{\phi}], \tag{2.62}$$

with $\Pi^{\Omega}[\boldsymbol{u}, \phi]$, $\Pi^{\mathrm{D}}[\boldsymbol{u}, \phi]$ and $\Pi^{\mathrm{N}}[\boldsymbol{u}, \phi]$ defined in Eqs. (2.14), (2.41) and (2.15). The enthalpy associated with periodic boundaries is (Barceló-Mercader *et al.*, 2022)

$$\begin{aligned}
\Pi^{\mathrm{P,y}}[\boldsymbol{u}, \phi, \check{\boldsymbol{u}}, \check{\phi}] = &\int_{\mathcal{I}^y} \left[\frac{1}{2}\beta^{uy} \left([\![u_i]\!]^y - \check{u}_i^y \right)^2 - \left([\![u_i]\!]^y - \check{u}_i^y \right) [\![t_i(\boldsymbol{u}, \phi)]\!]_\gamma^y \right] \mathrm{d}\Gamma \\
&+ \int_{\mathcal{I}^y} \left[\frac{1}{2}\beta^{vy} \left(\left[\!\left[\frac{\partial u_i}{\partial y} \right]\!\right]^y \right)^2 - \left[\!\left[\frac{\partial u_i}{\partial y} \right]\!\right]^y \left\{ r_i(\boldsymbol{u}, \phi) \right\}_\gamma^y \right] \mathrm{d}\Gamma + \\
&+ \int_{\mathcal{I}^y} \left[-\frac{1}{2}\beta^{\phi y} \left([\![\phi]\!]^y - \check{\phi}^y \right)^2 + \left([\![\phi]\!]^y - \check{\phi}^y \right) [\![w(\boldsymbol{u}, \phi)]\!]_\gamma^y \right] \mathrm{d}\Gamma + \\
&+ \sum_{x \in C^y} \left[\frac{1}{2}\beta^{C_u y} \left([\![u_i]\!]^y - \check{u}_i^y \right)^2 - \left([\![u_i]\!]^y - \check{u}_i^y \right) [\![j_i(\boldsymbol{u}, \phi)]\!]_\gamma^y \right],
\end{aligned} \tag{2.63}$$

$$\begin{aligned}
\Pi^{\mathrm{P,x}}[\boldsymbol{u}, \phi, \check{\boldsymbol{u}}, \check{\phi}] = &\int_{\mathcal{I}^x} \left[\frac{1}{2}\beta^{ux} \left([\![u_i]\!]^x - \check{u}_i^x \right)^2 - \left([\![u_i]\!]^x - \check{u}_i^x \right) [\![t_i(\boldsymbol{u}, \phi)]\!]_\gamma^x \right] \mathrm{d}\Gamma \\
&+ \int_{\mathcal{I}^x} \left[\frac{1}{2}\beta^{vx} \left(\left[\!\left[\frac{\partial u_i}{\partial x} \right]\!\right]^x \right)^2 - \left[\!\left[\frac{\partial u_i}{\partial x} \right]\!\right]^x \left\{ r_i(\boldsymbol{u}, \phi) \right\}_\gamma^x \right] \mathrm{d}\Gamma + \\
&+ \int_{\mathcal{I}^x} \left[-\frac{1}{2}\beta^{\phi x} \left([\![\phi]\!]^x - \check{\phi}^x \right)^2 + \left([\![\phi]\!]^x - \check{\phi}^x \right) [\![w(\boldsymbol{u}, \phi)]\!]_\gamma^x \right] \mathrm{d}\Gamma + \\
&+ \sum_{y \in C^x} \left[\frac{1}{2}\beta^{C_u x} \left([\![u_i]\!]^x - \check{u}_i^x \right)^2 - \left([\![u_i]\!]^x - \check{u}_i^x \right) [\![j_i(\boldsymbol{u}, \phi)]\!]_\gamma^x \right],
\end{aligned} \tag{2.64}$$

where $\check{\boldsymbol{u}} = \{\check{\boldsymbol{u}}^x, \check{\boldsymbol{u}}^y\}$, $\check{\phi} = \{\check{\phi}^x, \check{\phi}^y\}$ and the weighted means and jumps on the periodic bound-

aries are defined as

$$\{A\}_\gamma^y = \gamma A(x, L_y) + (1-\gamma)A(x, 0) \qquad \{A\}_\gamma^x = \gamma A(L_x, y) + (1-\gamma)A(0, y) \tag{2.65a}$$

$$[\![A]\!]_\gamma^y = \gamma A(x, L_y) - (1-\gamma)A(x, 0) \qquad [\![A]\!]_\gamma^x = \gamma A(L_x, y) - (1-\gamma)A(0, y) \tag{2.65b}$$

with $\gamma \in (0, 1)$. The definition of the weighted mean is analogous to the one in Eq. (2.47a).

In Eqs. (2.63) and (2.64), it is important to distinguish the cases where the jumps $\check{\boldsymbol{u}}^{(\cdot)}$ or $\check{\phi}^{(\cdot)}$ are prescribed or unknown. For prescribed values of $\check{\boldsymbol{u}}^{(\cdot)}$ or $\check{\phi}^{(\cdot)}$, we directly substitute $\check{\boldsymbol{u}}^{(\cdot)}$ or $\check{\phi}^{(\cdot)}$ by its prescribed value $\hat{\boldsymbol{u}}^{(\cdot)}$ or $\hat{\phi}^{(\cdot)}$ so that Eqs. (2.63) and (2.64) are analogous to Eq. (2.56). For unknown values of $\check{\boldsymbol{u}}^{(\cdot)}$ or $\check{\phi}^{(\cdot)}$, Eqs. (2.63) and (2.64) weakly enforce a constraint between state variables and therefore do not admit penalty terms. For example, the corresponding $\beta^{(\cdot)}$ must be set to zero. The four situations described before would mean:

- Unconfined vertical displacement sensor: $\check{\boldsymbol{u}}^y$ is the only known constant, $\check{\boldsymbol{u}}^x$, $\check{\phi}^y$ and $\check{\phi}^x$ are unknown values and thus $\beta^{\phi y} = \beta^{ux} = \beta^{\phi x} = \beta^{C_u x} = 0$.
- Confined vertical displacement sensor: $\check{\boldsymbol{u}}^y$ and $\check{\boldsymbol{u}}^x$ are the known constants, $\check{\phi}^y$ and $\check{\phi}^x$ are unknown values and thus $\beta^{\phi y} = \beta^{\phi x} = 0$.
- Unconfined vertical displacement actuator: $\check{\phi}^y$ and $\check{\phi}^x$ are the known constants, $\check{\boldsymbol{u}}^y$ and $\check{\boldsymbol{u}}^x$ are unknown values and thus $\beta^{uy} = \beta^{C_u y} = \beta^{ux} = \beta^{C_u x} = 0$.
- Confined vertical displacement actuator: $\check{\phi}^y$, $\check{\phi}^x$ and $\check{\boldsymbol{u}}^x$ are the known constants, $\check{\boldsymbol{u}}^y$ is the only unknown values and thus $\beta^{uy} = \beta^{C_u y} = 0$.

For the sake of simplicity, we now restrict to the case of a vertical displacement sensor, where a constant vertical strain is applied at the macroscopic level, allowing free macroscopic transversal deformation of the material and assuming that no surface charges accumulate macroscopically. Any other generalised periodic boundary value problems are straightforward.

2.3.2 Variational formulation and weak form

We are in the first situation of the four ones described before. The condition to be imposed weakly is $\check{\boldsymbol{u}}^y = \hat{\boldsymbol{u}}^y$, with a prescribed vertical displacement jump $\hat{\boldsymbol{u}}^y$ mapped from the applied vertical macroscopic strain. The horizontal jump of the displacement $\check{\boldsymbol{u}}^x$ and the electric potential jump $\check{\phi}$ are unknown constants values. Hence, in Eqs. (2.63) and (2.64), the penalty parameters β^{ux}, $\beta^{C_u x}$, $\beta^{\phi x}$ and $\beta^{\phi y}$ must be set to 0, and $\check{\boldsymbol{u}}^y = \hat{\boldsymbol{u}}^y$, as explained before. The solution of the associated boundary value problem then follows from the variational principle

$$(\boldsymbol{u}^*, \phi^*, \check{\boldsymbol{u}}^{x^*}, \check{\phi}^*) = \arg \min_{\boldsymbol{u} \in \mathcal{U}} \max_{\phi \in \mathcal{H}^1(\Omega)} \max_{\check{\boldsymbol{u}}^x \in \mathbb{R}^2} \min_{\check{\phi} \in \mathbb{R}^2} \Pi[\boldsymbol{u}, \phi, \check{\boldsymbol{u}}^x, \check{\phi}]. \tag{2.66}$$

The weak form of the problem follows from the stationarity of the enthalpy functional in Eq. (2.62)

$$\delta\Pi[\boldsymbol{u},\phi,\check{\boldsymbol{u}}^x,\check{\phi};\delta\boldsymbol{u},\delta\phi,\delta\check{\boldsymbol{u}}^x,\delta\check{\phi}] = 0; \quad \forall\delta\boldsymbol{u},\delta\phi,\delta\check{\boldsymbol{u}}^x,\delta\check{\phi}, \tag{2.67}$$

where

$$\begin{aligned}\delta\Pi[\boldsymbol{u},\phi,\check{\boldsymbol{u}}^x,\check{\phi};\delta\boldsymbol{u},\delta\phi,\delta\check{\boldsymbol{u}}^x,\delta\check{\phi}] &= \delta\Pi^{\Omega}[\boldsymbol{u},\phi;\delta\boldsymbol{u},\delta\phi] + \delta\Pi^{\mathrm{D}}[\boldsymbol{u},\phi;\delta\boldsymbol{u},\delta\phi]\\ &+ \delta\Pi^{\mathrm{N}}[\delta\boldsymbol{u},\delta\phi] + \delta\Pi^{\mathrm{P,y}}[\boldsymbol{u},\phi,\check{\boldsymbol{u}}^x,\check{\phi};\delta\boldsymbol{u},\delta\phi,\delta\check{\boldsymbol{u}}^x,\delta\check{\phi}]\\ &+ \delta\Pi^{\mathrm{P,x}}[\boldsymbol{u},\phi,\check{\boldsymbol{u}}^x,\check{\phi};\delta\boldsymbol{u},\delta\phi,\delta\check{\boldsymbol{u}}^x,\delta\check{\phi}],\end{aligned} \tag{2.68}$$

$\delta\Pi^{\Omega}$, $\delta\Pi^{\mathrm{D}}$ and $\delta\Pi^{\mathrm{N}}$ are defined in Eqs. (2.20b), (2.46) and (2.20c) and

$$\begin{aligned}&\delta\Pi^{\mathrm{P,y}}[\boldsymbol{u},\phi,\check{\boldsymbol{u}}^x,\check{\phi};\delta\boldsymbol{u},\delta\phi,\delta\check{\boldsymbol{u}}^x,\delta\check{\phi}] =\\ &\int_{\mathcal{I}^y}\left[\beta^{uy}\,[\![\delta u_i]\!]^y\left([\![u_i]\!]^y-\hat{u}_i^y\right)-[\![\delta u_i]\!]^y\,[\![t_i(\boldsymbol{u},\phi)]\!]^y_\gamma-\left([\![u_i]\!]^y-\hat{u}_i^y\right)[\![t_i(\delta\boldsymbol{u},\delta\phi)]\!]^y_\gamma\right]\mathrm{d}\Gamma\\ &+\int_{\mathcal{I}^y}\left[\beta^{vy}\left[\!\left[\frac{\partial u_i}{\partial y}\right]\!\right]^y\left[\!\left[\frac{\partial\delta u_i}{\partial y}\right]\!\right]^y-\left[\!\left[\frac{\partial\delta u_i}{\partial y}\right]\!\right]^y\left\{r_i(\boldsymbol{u},\phi)\right\}^y_\gamma-\left[\!\left[\frac{\partial u_i}{\partial y}\right]\!\right]^y\left\{r_i(\delta\boldsymbol{u},\delta\phi)\right\}^y_\gamma\right]\mathrm{d}\Gamma+\\ &+\int_{\mathcal{I}^y}\left[\left([\![\delta\phi]\!]^y-\delta\check{\phi}^y\right)[\![w(\boldsymbol{u},\phi)]\!]^y_\gamma+\left([\![\phi]\!]^y-\check{\phi}^y\right)[\![w(\delta\boldsymbol{u},\delta\phi)]\!]^y_\gamma\right]\mathrm{d}\Gamma\\ &+\sum_{x\in C^y}\left[\beta^{C_uy}\,[\![\delta u_i]\!]^y\left([\![u_i]\!]^y-\hat{u}_i^y\right)-[\![\delta u_i]\!]^y\,[\![j_i(\boldsymbol{u},\phi)]\!]^y_\gamma-\left([\![u_i]\!]^y-\hat{u}_i^y\right)[\![j_i(\delta\boldsymbol{u},\delta\phi)]\!]^y_\gamma\right],\end{aligned} \tag{2.69}$$

$$\begin{aligned}&\delta\Pi^{\mathrm{P,x}}[\boldsymbol{u},\phi,\check{\boldsymbol{u}}^x,\check{\phi};\delta\boldsymbol{u},\delta\phi,\delta\check{\boldsymbol{u}}^x,\delta\check{\phi}] =\\ &\int_{\mathcal{I}^x}\left[-\left([\![\delta u_i]\!]^x-\delta\check{u}_i^x\right)[\![t_i(\boldsymbol{u},\phi)]\!]^x_\gamma-\left([\![u_i]\!]^x-\check{u}_i^x\right)[\![t_i(\delta\boldsymbol{u},\delta\phi)]\!]^x_\gamma\right]\mathrm{d}\Gamma\\ &+\int_{\mathcal{I}^x}\left[\beta^{vx}\left[\!\left[\frac{\partial u_i}{\partial x}\right]\!\right]^x\left[\!\left[\frac{\partial\delta u_i}{\partial x}\right]\!\right]^x-\left[\!\left[\frac{\partial\delta u_i}{\partial x}\right]\!\right]^x\left\{r_i(\boldsymbol{u},\phi)\right\}^x_\gamma-\left[\!\left[\frac{\partial u_i}{\partial x}\right]\!\right]^x\left\{r_i(\delta\boldsymbol{u},\delta\phi)\right\}^x_\gamma\right]\mathrm{d}\Gamma+\\ &+\int_{\mathcal{I}^x}\left[\left([\![\delta\phi]\!]^x-\delta\check{\phi}^x\right)[\![w(\boldsymbol{u},\phi)]\!]^x_\gamma+\left([\![\phi]\!]^x-\check{\phi}^x\right)[\![w(\delta\boldsymbol{u},\delta\phi)]\!]^x_\gamma\right]\mathrm{d}\Gamma\\ &+\sum_{y\in C^x}\left[-\left([\![\delta u_i]\!]^x-\delta\check{u}_i^x\right)[\![j_i(\boldsymbol{u},\phi)]\!]^x_\gamma-\left([\![u_i]\!]^x-\check{u}_i^x\right)[\![j_i(\delta\boldsymbol{u},\delta\phi)]\!]^x_\gamma\right],\end{aligned} \tag{2.70}$$

being $\delta\check{\boldsymbol{u}}$ and $\delta\check{\phi}$ admissible variations of $\check{\boldsymbol{u}}$ and $\check{\phi}$, respectively. Finally, the weak form associated with the boundary value problem reads

$$\text{Find } (\boldsymbol{u}, \phi, \check{\boldsymbol{u}}^x, \check{\phi}) \in \mathcal{U} \otimes \mathcal{H}^1(\Omega) \otimes \mathbb{R}^2 \otimes \mathbb{R}^2 \text{such that } \delta\Pi[\boldsymbol{u}, \phi, \check{\boldsymbol{u}}^x, \check{\phi}; \delta\boldsymbol{u}, \delta\phi, \delta\check{\boldsymbol{u}}^x, \delta\check{\phi}] = 0,$$
$$\forall (\delta\boldsymbol{u}, \delta\phi, \delta\check{\boldsymbol{u}}^x, \delta\check{\phi}) \in \mathcal{U} \otimes \mathcal{H}^1(\Omega) \otimes \mathbb{R}^2 \otimes \mathbb{R}^2. \tag{2.71}$$

where $\mathcal{U}$ is the space of functions belonging to $[\mathcal{H}^2(\Omega)]^2$ with $\mathcal{L}^2$-integrable third derivative on the Dirichlet boundary $\partial\Omega_u$.

2.4 High-order generalised periodicity in arbitrary directions

As seen in Section 2.3, we are interested in simulating a single unit cell under generalised periodic conditions, which directly provides the bulk response of a unit cell on a periodic structure. Those generalised periodicity eliminates the presence of external boundaries and, therefore, the finite-size effects related to them. In a finite element (or max-ent meshless) context, enforcing 0-th order periodicity conditions is relatively easy by the intrinsic Kronecker delta property of the basis function on the boundary. It boils down to constructing a mesh with matching nodes (or max-ent particles) at $x = 0$ and $x = L_x$ and assigning the same degrees of freedom at the matching nodes particles on each side (Barceló-Mercader, 2018). However, as seen in Section 2.3.1, higher-order conditions are not so trivially enforced since they would have to be explicitly introduced as external constraints yielding different equations and degrees of freedom in the case of Lagrange multipliers or additional terms in the current equations with numerical penalty parameters in the case of penalty or Nitsche methods (Barceló-Mercader *et al.*, 2022).

An alternative procedure to automatically fulfil high-order periodicity conditions consists of constructing a high-order periodic approximation space for f, considering high-order periodic basis functions. This approach, if possible, is the most convenient one since it yields an unconstrained boundary value problem, avoiding the issues above from explicitly including additional constraints. The immersed boundary B-spline framework is particularly well-suited to the simulation of periodic domains since the construction of a high-order-periodic B-spline basis is trivial, and the cuboidal shape of the fictitious domain can be immediately identified with the unit cell of the architected material.

The section is organised as follows. Macroscopic conditions for flexoelectric RVE via high-order generalised periodicity are shown, along with high-order generalised periodicity conditions. The last part is similar to the one in Section 2.3.1, but now all terms are described more precisely. Thanks to that, macroscopic kinematics and how these kinematics are encoded through a macroscopic enthalpy functional with conjugate variables can be deduced. Finally, the boundary value problem for flexoelectric RVE is presented.

2.4.1 Macroscopic conditions for flexoelectric RVE via high-order generalised periodicity

In this section, we introduce high-order generalised periodicity conditions, and we state the conditions on the state variables of an RVE that must hold to reproduce the bulk response of an infinitely sizeable periodic structure Ω_∞. The resulting macroscopic state variables and their corresponding macroscopic enthalpy functional are also analysed.

The periodic structure Ω_∞ is formed by concatenating a unit cell Ω^{RVE} in each dimension indefinitely. Our domain Ω is the intersection between the periodic structure and the unit cell $\Omega = \Omega_\infty \cap \Omega^{\mathrm{RVE}}$. The boundary of the domain $\partial\Omega$ is split in two parts, $\partial\Omega = \Gamma^{\mathrm{fict}} \cup \Gamma^{\mathrm{actual}}$ with $\Gamma^{\mathrm{fict}} = \partial\Omega^{\mathrm{RVE}} \cap \Omega_\infty$ and $\Gamma^{\mathrm{actual}} = \partial\Omega_\infty \cap \Omega^{\mathrm{RVE}}$ (see Fig. 2.6).

For the sake of simplicity, and as is common in periodically arranged architected structures, we consider homogeneous Neumann conditions at every physical boundary of the RVE, and disregard external volumetric loads, that is,

$$\partial\Omega_u = \partial\Omega_v = \partial\Omega_\phi = \partial\Omega_\varphi = \emptyset, \tag{2.72a}$$

$$\boldsymbol{t}^{\mathrm{N}} = \boldsymbol{r}^{\mathrm{N}} = \boldsymbol{j}^{\mathrm{N}} = \boldsymbol{b} = 0, \tag{2.72b}$$

$$w^{\mathrm{N}} = \mathfrak{r}^{\mathrm{N}} = \wp^{\mathrm{N}} = q = 0. \tag{2.72c}$$

2.4.1.1 High-order generalised periodicity conditions in arbitrary direction

The generalised periodicity conditions for a generic 1D field $f(x) \in \mathbb{R}, x \in \Omega^{\mathrm{RVE}} = [0, L_x] \subset \mathbb{R}$ are usually stated as

$$f(L_x) - f(0) = \langle\!\langle f \rangle\!\rangle_x \,, \tag{2.73}$$

with $\langle\!\langle f \rangle\!\rangle_x \in \mathbb{R}$. Standard periodicity conditions are obtained for $\langle\!\langle f \rangle\!\rangle_x = 0$, and *generalised* periodicity conditions otherwise. In a fourth-order PDE context, this condition is required but insufficient since the extension of f over $\mathbb{R}$ is required to belong to $H^2(\mathbb{R})$ (i.e. it must be at least C^1-continuous), which is not necessarily true at $x = m_x L_x$, $m_x \in \mathbb{Z}$. An extra necessary condition is then

$$\frac{\partial f(L_x)}{\partial x} - \frac{\partial f(0)}{\partial x} = 0. \tag{2.74}$$

The difference between low-order and high-order periodicity conditions is shown in Fig. 2.5. The extension of high-order generalised periodicity conditions to higher dimensions is trivial. Let us consider a cuboidal unit cell $\Omega^{\mathrm{RVE}} = [0, L_x] \times [0, L_y] \times [0, L_z] \in \mathbb{R}^3$ as depicted in Fig. 2.6 for the 2D case.

The high-order generalised periodicity conditions of the mechanical and electrical fields

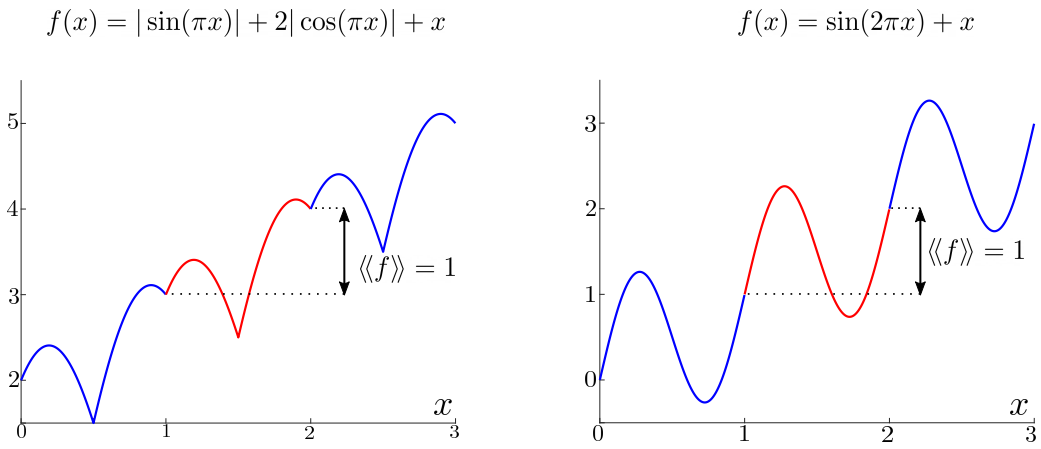

Figure 2.5: Example of low-order a periodic function, $f(x) = |\sin(\pi x)| + 2|\cos(\pi x)| + x$, on the left and example of high-order periodic function $f(x) = \sin(2\pi x) + x$ on the right.

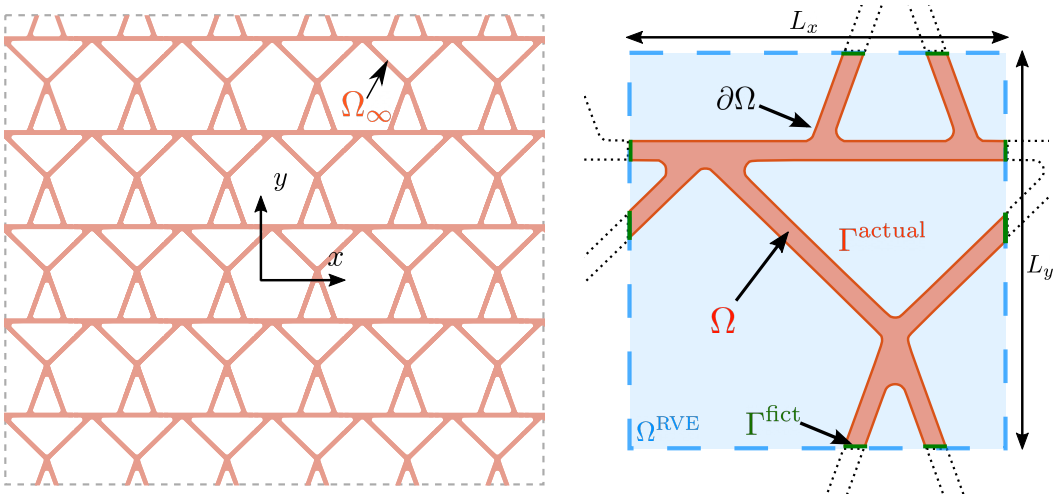

Figure 2.6: Architected structure Ω^∞ on the left and unit cell Ω^{RVE} on the right. The fictitious boundary is $\Gamma^{\text{fict}} = \partial\Omega \cup \Omega^{\text{RVE}}$, the actual boundary is $\Gamma^{\text{actual}} = \partial\Omega \cup \partial\Omega_\infty$, and their boundaries are $C^{\text{fict}} = \partial\Gamma^{\text{fict}}$ and $C^{\text{actual}} = \partial\Gamma^{\text{actual}}$.

are:

$$\boldsymbol{u}(\zeta = L_\zeta) - \boldsymbol{u}(\zeta = 0) = \langle\langle \boldsymbol{u} \rangle\rangle_\zeta\,, \qquad \phi(\zeta = L_\zeta) - \phi(\zeta = 0) = \langle\langle \phi \rangle\rangle_\zeta\,, \tag{2.75a}$$

$$\frac{\partial \boldsymbol{u}(\zeta = L_\zeta)}{\partial \zeta} - \frac{\partial \boldsymbol{u}(\zeta = 0)}{\partial \zeta} = 0, \qquad \frac{\partial \phi(\zeta = L_\zeta)}{\partial \zeta} - \frac{\partial \phi(\zeta = 0)}{\partial \zeta} = 0, \tag{2.75b}$$

for $\zeta = \{x, y, z\}$.

2.4.1.2 High-order equilibrium conditions

On top of the continuity conditions stated above, we need to impose high-order equilibrium of the solution fields across the RVE boundaries that is (Barceló-Mercader *et al.*, 2022)

$$\begin{aligned} \boldsymbol{t}(\zeta = L_\zeta) + \boldsymbol{t}(\zeta = 0) = 0, \qquad & w(\zeta = L_\zeta) + w(\zeta = 0) = 0, \\ \boldsymbol{r}(\zeta = L_\zeta) - \boldsymbol{r}(\zeta = 0) = 0, \qquad & \mathfrak{r}(\zeta = L_\zeta) - \mathfrak{r}(\zeta = 0) = 0, \\ \boldsymbol{j}(\zeta = L_\zeta) + \boldsymbol{j}(\zeta = 0) = 0, \qquad & \wp(\zeta = L_\zeta) + \wp(\zeta = 0) = 0. \end{aligned} \tag{2.76}$$

Eq. (2.76) is required even if Eqs. (2.75b) hold since the Neumann quantities $(\boldsymbol{t}, \boldsymbol{r}, \boldsymbol{j}, w, \mathfrak{r}, \wp)$ also depend on second and third-order derivatives of the state variables $(\boldsymbol{u}, \phi)$ that are not periodic in general.

2.4.2 Macroscopic kinematics

The additional unknowns $\langle\!\langle f \rangle\!\rangle_\zeta$ arising from the generalised periodicity conditions represent the jump (or difference between boundaries) on Ω^{RVE} of the field $f(\boldsymbol{x})$ with $\boldsymbol{x} \in \Omega$ along the Cartesian direction ζ. From a macroscopic point of view, they are regarded as the state variables that characterise the macroscopic behaviour of a homogenised field on Ω^{RVE}, regardless of the evolution of $f(\boldsymbol{x})$ within Ω or even the shape of Ω. See Fig. 2.7.

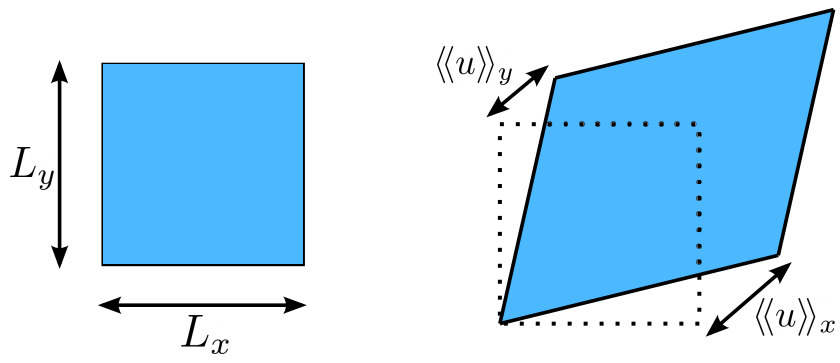

Figure 2.7: An initial unit cell or RVE Ω^{RVE} is represented on the left and the final configuration on the right. The jumps on the displacement can be seen.

We are interested in capturing the macroscopic behaviour of the state variables: displacement $\boldsymbol{u}(\boldsymbol{x})$ through the macroscopic displacement gradient $\overline{\nabla \boldsymbol{u}}$ with nine unknowns in $\mathbb{R}^3$ and electric potential $\phi(\boldsymbol{x})$ through the macroscopic electric field $\overline{\nabla \boldsymbol{E}}$ with three unknowns. In 2D $\overline{\nabla \boldsymbol{u}}$ and $\overline{\nabla \boldsymbol{E}}$ would have four and two unknowns, respectively. Considering these macroscopic entities and the dimensions of Ω^{RVE}, the displacement $\boldsymbol{u}$ and electric potential ϕ are split into a microscopic part and a macroscopic one. The microscopic part captures the unit cell's internal

behaviour, and the macroscopic part can be seen externally. The split is done as

$$\boldsymbol{u}(\boldsymbol{x}) = \boldsymbol{u}^{\mathrm{P}}(\boldsymbol{x}) + \overline{\nabla \boldsymbol{u}} \cdot \boldsymbol{x}, \tag{2.77a}$$

$$\phi(\boldsymbol{x}) = \phi^{\mathrm{P}}(\boldsymbol{x}) - \overline{\nabla \boldsymbol{E}} \cdot \boldsymbol{x}, \tag{2.77b}$$

where $\boldsymbol{u}^{\mathrm{P}}(\boldsymbol{x})$ and $\phi^{\mathrm{P}}(\boldsymbol{x})$ are periodic functions that fulfil

$$\boldsymbol{u}^{\mathrm{P}}(\zeta = L_\zeta) - \boldsymbol{u}^{\mathrm{P}}(\zeta = 0) = 0, \qquad \frac{\partial \boldsymbol{u}^{\mathrm{P}}(\zeta = L_\zeta)}{\partial \zeta} - \frac{\partial \boldsymbol{u}^{\mathrm{P}}(\zeta = 0)}{\partial \zeta} = 0, \tag{2.78a}$$

$$\phi^{\mathrm{P}}(\zeta = L_\zeta) - \phi^{\mathrm{P}}(\zeta = 0) = 0, \qquad \frac{\partial \phi^{\mathrm{P}}(\zeta = L_\zeta)}{\partial \zeta} - \frac{\partial \phi^{\mathrm{P}}(\zeta = 0)}{\partial \zeta} = 0, \tag{2.78b}$$

and the macroscopic displacement gradient and electric field are

$$\overline{\nabla \boldsymbol{u}} = \begin{bmatrix} \langle\!\langle u_x \rangle\!\rangle_x / L_x & \langle\!\langle u_y \rangle\!\rangle_x / L_x & \langle\!\langle u_z \rangle\!\rangle_x / L_x \\ \langle\!\langle u_x \rangle\!\rangle_y / L_y & \langle\!\langle u_y \rangle\!\rangle_y / L_y & \langle\!\langle u_z \rangle\!\rangle_y / L_y \\ \langle\!\langle u_x \rangle\!\rangle_z / L_z & \langle\!\langle u_y \rangle\!\rangle_z / L_z & \langle\!\langle u_z \rangle\!\rangle_z / L_z \end{bmatrix}, \tag{2.79}$$

$$\overline{\boldsymbol{E}} = -\overline{\nabla \phi} = \begin{bmatrix} -\langle\!\langle \phi \rangle\!\rangle_x / L_x \\ -\langle\!\langle \phi \rangle\!\rangle_y / L_y \\ -\langle\!\langle \phi \rangle\!\rangle_z / L_z \end{bmatrix}. \tag{2.80}$$

The microscopic behaviour is governed by the terms $\boldsymbol{u}^{\mathrm{P}}(x)$ and $\phi^{\mathrm{P}}(x)$ in Eq. (2.77), and the macroscopic behaviour is governed by the terms $\overline{\nabla \boldsymbol{u}} \cdot \boldsymbol{x}$ and $\overline{\nabla \boldsymbol{E}} \cdot \boldsymbol{x}$ in Eq. (2.77).

In turn, the macroscopic displacement gradient can be uniquely decomposed into its symmetric and antisymmetric parts as

$$\overline{\nabla \boldsymbol{u}} = \overline{\boldsymbol{\varepsilon}} + \overline{\mathbf{R}}, \tag{2.81a}$$

$$\overline{\boldsymbol{\varepsilon}} = \frac{1}{2}\left(\overline{\nabla \boldsymbol{u}} + \overline{\nabla \boldsymbol{u}}^T\right), \tag{2.81b}$$

$$\overline{\mathbf{R}} = \frac{1}{2}\left(\overline{\nabla \boldsymbol{u}} - \overline{\nabla \boldsymbol{u}}^T\right). \tag{2.81c}$$

The macroscopic strain $\overline{\boldsymbol{\varepsilon}}$ and the macroscopic rotation $\overline{\mathbf{R}}$ are constant tensors that characterise the macroscopic (homogenised) mechanical behaviour of Ω^{RVE} under a generalised periodic displacement field $\boldsymbol{u}(\boldsymbol{x})$ defined on Ω. They are invariants concerning the RVE size and relative position within a given periodically-arranged architected material. Note that the components in $\overline{\mathbf{R}}$ do not correspond to any deformation measure but to uniform rigid body rotations instead. That is, the energy functional of the system is invariant with respect to $\overline{\mathbf{R}}$. In order to prevent infinite solutions differing in rigid body rotations only, $\overline{\mathbf{R}}$ must be *a priori* enforced (i.e. three degrees of freedom in $\mathbb{R}^3$ and one in $\mathbb{R}^2$). In the remainder of the thesis, and without loss of

generality, we consider $\overline{\mathbf{R}} = \mathbf{0}$. We assume symmetric macroscopic displacement gradients ($\overline{\nabla \boldsymbol{u}} = \overline{\boldsymbol{\varepsilon}}$).

Remark 2.2. Note that assuming $\boldsymbol{u}, \phi$ generalised-periodic implies that the macroscopic state variables $\overline{\boldsymbol{\varepsilon}}, \overline{\boldsymbol{E}}$ are constant tensors. Therefore, the macroscopic strain gradient and electric field gradient vanish. Loading cases on a periodically-arranged architected material yielding non-vanishing macroscopic strain gradient and electric field gradients are out of the scope of this thesis.

Remark 2.3. Eq. (2.77) implies that the strain field and electric field are decomposed as

$$\boldsymbol{\varepsilon} = \boldsymbol{\varepsilon}\left(\boldsymbol{u}^{\mathrm{P}}\right) + \overline{\boldsymbol{\varepsilon}} \tag{2.82a}$$

$$\boldsymbol{E} = \boldsymbol{E}\left(\phi^{\mathrm{P}}\right) + \overline{\boldsymbol{E}}. \tag{2.82b}$$

2.4.3 Macroscopic enthalpy functional and conjugate variables

Since the macroscopic response of the architected structure is uniquely characterised by the macroscopic state variables, our goal is to rationalise the existence of a macroscopic enthalpy functional depending on macroscopic state variables only. Such functional should fulfil the condition that the variation of the actual bulk enthalpy of the system or microscopic bulk enthalpy Π^{b} in one unit cell is equivalent to the variation of the enthalpy of a homogeneous media of size L_x, L_y and L_z or macroscopic enthalpy $\overline{\Pi}$:

$$\delta\Pi^{\mathrm{b}}[\boldsymbol{\varepsilon}, \nabla\boldsymbol{\varepsilon}, \boldsymbol{E}, \nabla\boldsymbol{E}] = \delta\overline{\Pi}\left[\overline{\boldsymbol{\varepsilon}}, \overline{\boldsymbol{E}}\right]. \tag{2.83}$$

In order to find the functional described in Eq. (2.83) we consider the high-order equilibrium conditions from Eq. (2.76) in a weak way as

$$0 = \int_{\Gamma_{\mathrm{fict}}} \left(-t_i \delta u_i^{\mathrm{P}} - r_i \partial^n \delta u_i^{\mathrm{P}} + w\delta\phi^{\mathrm{P}} + \mathfrak{r}\partial^n\delta\phi^{\mathrm{P}}\right) \mathrm{d}\Gamma + \int_{C_{\mathrm{fict}}} \left(-j_i\delta u_i^{\mathrm{P}} + \wp\delta\phi^{\mathrm{P}}\right) \mathrm{d}l. \tag{2.84}$$

By taking into account homogeneous microscopic Neumann conditions in Eq. (2.72), Eq. (2.84) is extended to $\Gamma^{\mathrm{fict}} \cup \Gamma^{\mathrm{actual}} = \partial\Omega$, $C^{\mathrm{fict}} \cup C^{\mathrm{actual}} = C$ (see Fig. 2.6 to view the difference between $\Gamma^{\mathrm{fict}}, \Gamma^{\mathrm{actual}}$, C^{fict} and C^{actual}), so

$$0 = \int_{\partial\Omega} \left(-t_i \delta u_i^{\mathrm{P}} - r_i \partial^n \delta u_i^{\mathrm{P}} + w\delta\phi^{\mathrm{P}} + \mathfrak{r}\partial^n\delta\phi^{\mathrm{P}}\right) \mathrm{d}\Gamma + \int_{C} \left(-j_i\delta u_i^{\mathrm{P}} + \wp\delta\phi^{\mathrm{P}}\right) \mathrm{d}l. \tag{2.85}$$

Upon application of integration by parts, the divergence theorem and the surface divergence theorem, as done in Codony *et al.* (2021a) and considering the strong form of the problem in Eq. (2.38) with zero source terms Eq. (2.72) leads to

$$0 = \int_{\Omega} \left(\hat{\sigma}_{ij}\delta\varepsilon_{ij}\left(\boldsymbol{u}^{\mathrm{P}}\right) + \tilde{\sigma}_{ijk}\delta\varepsilon_{ij,k}\left(\boldsymbol{u}^{\mathrm{P}}\right) - \widehat{D}_l\delta E_l\left(\phi^{\mathrm{P}}\right) - \widetilde{D}_{lk}\delta E_{k,l}\left(\phi^{\mathrm{P}}\right)\right) \mathrm{d}\Omega. \tag{2.86}$$

By using the decomposition of the strain and electric field in Eq. (2.82), we have

$$\int_\Omega \left(\hat{\sigma}_{ij}\delta\varepsilon_{ij} + \tilde{\sigma}_{ijk}\delta\varepsilon - \widehat{D}_l\delta E_l - \widetilde{D}_{lk}\delta E_{kl} \right) \mathrm{d}\Omega = \int_\Omega \hat{\sigma}_{ij}\delta\overline{\varepsilon}_{ij}\,\mathrm{d}\Omega - \int_\Omega \hat{D}_l\delta\overline{E}_l\,\mathrm{d}\Omega$$
$$= |\Omega^{\mathrm{RVE}}| \left(\overline{\sigma}_{ij}\delta\overline{\varepsilon}_{ij} - \overline{D}_l\delta\overline{E}_l \right). \tag{2.87}$$

where the term $\overline{\boldsymbol{\sigma}}$ in Eq. (2.87) corresponds to the macroscopic stress and $\overline{\boldsymbol{D}}$ is the macroscopic electric displacement. Comparing Eq. (2.83) with Eq. (2.87), the variation of microscopic bulk enthalpy corresponds to the integral over Ω of the bulk internal enthalpy density variation in Eq. (2.83) as

$$\delta\Pi^{\mathrm{b}}[\boldsymbol{\varepsilon}, \nabla\boldsymbol{\varepsilon}, \boldsymbol{E}, \nabla\boldsymbol{E}] = \int_\Omega \left(\delta\mathcal{H}^{\Omega}[\boldsymbol{u}, \phi] \right) \mathrm{d}\Omega = \int_\Omega \left(\hat{\sigma}_{ij}\delta\varepsilon_{ij} - \hat{D}_i\delta E_i + \tilde{\sigma}_{ijk}\delta\varepsilon_{ij,k} - \widetilde{D}_{ij}\delta E_{i,j} \right) \mathrm{d}\Omega, \tag{2.88}$$

and the variation of the macroscopic enthalpy is

$$\delta\overline{\Pi}[\overline{\boldsymbol{\varepsilon}}, \overline{\boldsymbol{E}}] = \int_{\Omega^{\mathrm{RVE}}} \left(\widehat{\sigma}_{ij}\delta\overline{\varepsilon}_{ij} - \widehat{D}_i\delta\overline{E}_i \right) \mathrm{d}\Omega = |\Omega^{\mathrm{RVE}}| \left(\overline{\sigma}_{ij}\delta\overline{\varepsilon}_{ij} - \overline{D}_i\delta\overline{E}_i \right), \tag{2.89}$$

where the second equality in Eq. (2.89) holds by considering that the macroscopic quantities do not depend on the position $\boldsymbol{x}$, and $|\Omega^{\mathrm{RVE}}| = L_x L_y L_z$ corresponds to the macroscopic volume of the RVE. The macroscopic stress and macroscopic electric displacement are conjugates of the macroscopic strain and macroscopic electric field, respectively, and they are defined as

$$\overline{\sigma}_{ij} = \frac{1}{|\Omega^{\mathrm{RVE}}|}\int_\Omega \hat{\sigma}_{ij}\,\mathrm{d}\Omega, \qquad \overline{D}_i = \frac{1}{|\Omega^{\mathrm{RVE}}|}\int_\Omega \hat{D}_i\,\mathrm{d}\Omega. \tag{2.90}$$

As a result, the macroscopic stress is nothing but the macroscopic average of the microscopic Cauchy stress over Ω, and the macroscopic electric displacement is the macroscopic average of the microscopic local electric displacement over Ω. Eqs. (2.90) can be regarded as an extension of the Hill-Mandel theorem (Hill, 1963, 1967) to high-order electromechanics.

Finally, we have proved that Eq. (2.87) is the weak equation that generalised periodic state variables $\boldsymbol{u}(\boldsymbol{x})$, $\phi(\boldsymbol{x})$ must fulfil in order to reproduce the electromechanical state of an infinitely sizeable periodic structure over Ω^∞.

2.4.4 Boundary value problem for flexoelectric RVE

In the generalised periodicity framework described in the above Sections, $\overline{\boldsymbol{\varepsilon}}$ and $\overline{\boldsymbol{E}}$ are additional state variables whose components can be specified a priori or obtained due to the boundary value problem. To this end, their components are split into two disjoint sets (as other boundary

conditions), the macroscopic Dirichlet components

$$\overline{\varepsilon}_{ij} = \overline{\varepsilon}^{\mathrm{D}}_{ij} \qquad \text{for } (i,j) \in \mathcal{T}^{\boldsymbol{\varepsilon}}, \tag{2.91a}$$

$$\overline{E}_i = \overline{E}^{\mathrm{D}}_i \qquad \text{for } i \in \mathcal{T}^{\boldsymbol{E}}, \tag{2.91b}$$

and the macroscopic Neumann components

$$\overline{\sigma}_{ij} = \overline{\sigma}^{\mathrm{N}}_{ij} \qquad \text{for } (i,j) \in \{1,2,3\} \times \{1,2,3\} \setminus \mathcal{T}^{\boldsymbol{\varepsilon}}, \tag{2.92a}$$

$$\overline{D}_i = \overline{D}^{\mathrm{N}}_i \qquad \text{for } i \in \{1,2,3\} \setminus \mathcal{T}^{\boldsymbol{E}}, \tag{2.92b}$$

where $\mathcal{T}^{\boldsymbol{\varepsilon}} \subseteq \{1,2,3\} \times \{1,2,3\}$ such that if $(i,j) \in \mathcal{T}^{\boldsymbol{\varepsilon}}$ then $(j,i) \in \mathcal{T}^{\boldsymbol{\varepsilon}}$, and $\mathcal{T}^{\boldsymbol{E}} \subseteq \{1,2,3\}$, are the subsets of components where macroscopic Dirichlet conditions are imposed. The r.h.s. of Eq. (2.87) is split into Dirichlet and Neumann components accordingly. Macroscopic Dirichlet conditions are applied strongly, projecting the solution to a functional space that satisfies macroscopic Dirichlet conditions. On the other hand, macroscopic Neumann conditions remain in weak form. The macroscopic Neumann conditions can be seen as the natural macroscopic conditions of the boundary value problem since the neglect of the macroscopic Neumann term leads to homogeneous macroscopic Neumann conditions.

The weak form of the flexoelectric generalised problem is

$$\begin{aligned}
&\text{Find } \left(\boldsymbol{u}^{\mathrm{P}}, \phi^{\mathrm{P}}, \overline{\boldsymbol{\varepsilon}}, \overline{\boldsymbol{E}}\right) \in \mathcal{U}^{\mathrm{P}} \otimes \mathcal{P}^{\mathrm{P}} \otimes \overline{\mathcal{U}}^{\mathrm{D}} \otimes \overline{\mathcal{P}}^{\mathrm{D}} \text{ such that} \\
&\int_\Omega \left(\delta\varepsilon_{ij}\widehat{\sigma}_{ij} + \delta\varepsilon_{ij,k}\widetilde{\sigma}_{ijk} - \delta E_l \widehat{D}_l - \delta E_{l,m}\widetilde{D}_{lm} \right) \mathrm{d}\Omega = |\Omega^{\mathrm{RVE}}| \overline{\sigma}^N_{ij} \delta\overline{\varepsilon}_{ij} - |\Omega^{\mathrm{RVE}}| \overline{D}^N_i \delta\overline{E}_i, \\
&\forall \left(\delta\boldsymbol{u}^{\mathrm{P}}, \delta\phi^{\mathrm{P}}, \delta\overline{\boldsymbol{\varepsilon}}, \delta\overline{\boldsymbol{E}}\right) \in \mathcal{U}^{\mathrm{P}} \otimes \mathcal{P}^{\mathrm{P}} \otimes \overline{\mathcal{U}}^{0} \otimes \overline{\mathcal{P}}^{0},
\end{aligned} \tag{2.93}$$

where

$$\mathcal{U}^{\mathrm{P}} = \left\{ \boldsymbol{u}^{\mathrm{P}} \in [\mathcal{H}^2(\Omega)]^3 \mid \text{Eq. (2.78a) holds (high-order periodicity on } \boldsymbol{u}^{\mathrm{P}}) \right\}, \tag{2.94a}$$

$$\mathcal{P}^{\mathrm{P}} = \left\{ \phi^{\mathrm{P}} \in \mathcal{H}^2(\Omega) \mid \text{Eq. (2.78b) holds (high-order periodicity on } \phi^{\mathrm{P}}) \right\}, \tag{2.94b}$$

$$\overline{\mathcal{U}}^{\mathrm{D}} = \left\{ \overline{\boldsymbol{\varepsilon}} \in \left[\mathbb{R}^3\right]^2 \mid \text{Eq. (2.91a) holds (Dirichlet conditions on } \overline{\boldsymbol{\varepsilon}}) \text{ and } \overline{\varepsilon}_{ij} = \overline{\varepsilon}_{ji} \right\}, \tag{2.94c}$$

$$\overline{\mathcal{P}}^{\mathrm{D}} = \left\{ \overline{\boldsymbol{E}} \in \mathbb{R}^3 \mid \text{Eq. (2.91b) holds (Dirichlet conditions on } \overline{\boldsymbol{E}}) \right\}, \tag{2.94d}$$

$$\overline{\mathcal{U}}^{0} = \left\{ \delta\overline{\boldsymbol{\varepsilon}} \in \left[\mathbb{R}^3\right]^2 \mid \delta\overline{\varepsilon}_{ij} = 0 \text{ for } (i,j) \in \mathcal{T}^{\boldsymbol{\varepsilon}} \right\}, \tag{2.94e}$$

$$\overline{\mathcal{P}}^{0} = \left\{ \delta\overline{\boldsymbol{E}} \in \mathbb{R}^3 \mid \delta\overline{E}_i = 0 \text{ for } i \in \mathcal{T}^{\boldsymbol{E}} \right\}. \tag{2.94f}$$

2.5 Ongoing work

In this section, the ongoing work is presented, that is, interface conditions for the lifshitz-invariant flexoelectric formulation along with the interface enthalpy associated with Nitsche's

method and the formulation for graded structure considering the standard approach.

2.5.1 High-order interface conditions for Lifshitz-invariant flexoelectricity

Interface conditions described in Section 2.2.2 are only valid for direct flexoelectricity. Interface conditions for Lifshitz-invariant flexoelectricity are slightly different and they are

$$\left[\!\left[\boldsymbol{u} \otimes \mathbf{n} \right]\!\right] = \mathbf{0}, \qquad \left[\!\left[\partial^n \boldsymbol{u} \right]\!\right] = \mathbf{0}, \qquad \text{on } \mathcal{I}, \tag{2.95a}$$

$$\left[\!\left[\phi \mathbf{n} \right]\!\right] = \mathbf{0}, \qquad \left[\!\left[\partial^{\mathrm{n}} \phi \right]\!\right] = \mathbf{0}, \qquad \text{on } \mathcal{I}, \tag{2.95b}$$

$$\left[\!\left[\boldsymbol{t}(\boldsymbol{u}, \phi) \right]\!\right] = \hat{\boldsymbol{t}}, \qquad \left[\!\left[\boldsymbol{r}(\boldsymbol{u}, \phi) \otimes \mathbf{n} \right]\!\right] = \hat{\boldsymbol{r}} \otimes \mathbf{n}^L, \qquad \text{on } \mathcal{I}, \tag{2.95c}$$

$$\left[\!\left[w(\boldsymbol{u}, \phi) \right]\!\right] = \hat{w}, \qquad \left[\!\left[\mathfrak{r}(\boldsymbol{u}, \phi) \mathbf{n} \right]\!\right] = \hat{\mathfrak{r}} \mathbf{n}^L, \qquad \text{on } \mathcal{I}, \tag{2.95d}$$

and

$$\boldsymbol{u}^{P(k,i)} - \langle \boldsymbol{u} \rangle_{\hat{\gamma}} = \mathbf{0} \quad i = 1 \dots m(k) \qquad \text{on } C^k \subset C_{\mathcal{I}}, \tag{2.96a}$$

$$\sum_{i=1}^{m(k)} \boldsymbol{j}^{P(k,i)}(\boldsymbol{u}, \phi) = \hat{\boldsymbol{j}} \qquad \text{on } C^k \subset C_{\mathcal{I}}, \tag{2.96b}$$

$$\phi^{P(k,i)} - \langle \phi \rangle_{\hat{\gamma}} = \mathbf{0} \quad i = 1 \dots m(k) \qquad \text{on } C^k \subset C_{\mathcal{I}}, \tag{2.96c}$$

$$\sum_{i=1}^{m(k)} \wp^{P(k,i)}(\boldsymbol{u}, \phi) = \hat{\wp} \qquad \text{on } C^k \subset C_{\mathcal{I}}, \tag{2.96d}$$

where $\mathcal{I}$, $C_{\mathcal{I}}$ and C^k were defined in Section 2.2.2. The main difference between these interface conditions and the ones defined in Section 2.2.2 is the high-order interface conditions for the electric potential. Now, the interface conditions for the displacement and the electric potential

are analogous. The interface enthalpy associated with $\Pi_L^{\text{Interface}}$ is now

$$\begin{aligned}
\Pi_L^{\text{Interface}}[\boldsymbol{u},\phi] = &\int_{\mathcal{I}} \left[\frac{1}{2}\beta^{u\mathcal{I}} \left[\!\left[u_i n_j \right]\!\right]^2 - \left[\!\left[u_i n_j \right]\!\right] \left\{ t_i(\boldsymbol{u},\phi) n_j \right\}_\gamma - \hat{t}_i \left\{ u_i \right\}_{1-\gamma} \right] \mathrm{d}\Gamma + \\
&+ \int_{\mathcal{I}} \left[\frac{1}{2}\beta^{v\mathcal{I}} \left[\!\left[\partial^n u_i \right]\!\right]^2 - \left[\!\left[\partial^n u_i \right]\!\right] \left\{ r_i(\boldsymbol{u},\phi) \right\}_\gamma - \hat{r}_i n_j^L \left\{ u_{i,j} \right\}_{1-\gamma} \right] \mathrm{d}\Gamma + \\
&+ \int_{\mathcal{I}} \left[-\frac{1}{2}\beta^{\phi\mathcal{I}} \left[\!\left[\phi n_i \right]\!\right]^2 + \left[\!\left[\phi n_i \right]\!\right] \left\{ w(\boldsymbol{u},\phi) n_i \right\}_\gamma + \hat{w} \left\{ \phi \right\}_{1-\gamma} \right] \mathrm{d}\Gamma + \\
&+ \int_{\mathcal{I}} \left[-\frac{1}{2}\beta^{\varphi\mathcal{I}} \left[\!\left[\partial^n \phi \right]\!\right]^2 + \left[\!\left[\partial^n \phi \right]\!\right] \left\{ \mathfrak{r}(\boldsymbol{u},\phi) \right\}_\gamma + \mathfrak{r} n_i^L \left\{ \phi_{,i} \right\}_{1-\gamma} \right] \mathrm{d}\Gamma + \\
&+ \sum_{k=1}^{n_C} \int_{C^k} \left[\sum_{\alpha \in P(k,:)} \left(\frac{1}{2}\beta^{C_u\mathcal{I}} (u_i^\alpha - \langle u_i \rangle_{\hat{\gamma}})^2 - (u_i^\alpha - \langle u_i \rangle_{\hat{\gamma}}) j_i^\alpha(\boldsymbol{u},\phi) \right) - \langle u_i \rangle_{\hat{\gamma}} \hat{j}_i \right] \mathrm{d}s + \\
&+ \sum_{k=1}^{n_C} \int_{C^k} \left[- \sum_{\alpha \in P(k,:)} \left(\frac{1}{2}\beta^{C_\phi\mathcal{I}} (\phi^\alpha - \langle \phi \rangle_{\hat{\gamma}})^2 + (\phi^\alpha - \langle \phi \rangle_{\hat{\gamma}}) \wp^\alpha(\boldsymbol{u},\phi) \right) + \langle \phi \rangle_{\hat{\gamma}} \hat{\wp} \right] \mathrm{d}s. \qquad (2.97)
\end{aligned}$$

where $P(k,:) = \{P(k,1), ..., P(k,m(k))\}$.

2.5.2 Direct flexoelectricity model for graded structure

This subsection derives the formulation for graded structure which is very similiar to the one presented in Section 2.1.1. Let Ω be a physical domain in $\mathbb{R}^2$ or $\mathbb{R}^3$. For the sake of simplicity we consider that only the elasticity tensor depends on the position $\mathbb{C}_{ijkl}(\boldsymbol{x})$. Considering just the direct form of flexoelectricity, the bulk enthalpy density in a flexoelectric material is

$$\mathcal{H}^\Omega[\boldsymbol{u},\phi] = \frac{1}{2}\varepsilon_{ij}\mathbb{C}_{ijkl}(\boldsymbol{x})\varepsilon_{kl} + \frac{1}{2}\varepsilon_{ij,k}h_{ijklmn}\varepsilon_{lm,n} - \frac{1}{2}E_l\epsilon_{lm}E_m - E_l e_{lij}\varepsilon_{ij} - E_l\mu_{lijk}\varepsilon_{ij,k}, \qquad (2.98)$$

Apart from the internal enthalpy, we consider the work of external loads as

$$\mathcal{W}^\Omega[\boldsymbol{u},\phi] = -b_i u_i + q\phi, \qquad (2.99)$$

and the total bulk enthalpy of a flexoelectric material is then

$$\Pi^\Omega[\boldsymbol{u},\phi] = \int_\Omega \Big(\mathcal{H}^\Omega[\boldsymbol{u},\phi] + \mathcal{W}^\Omega[\boldsymbol{u},\phi] \Big)\, \mathrm{d}\Omega. \qquad (2.100)$$

Considering the standard approach where the Dirichlet boundary conditions, i.e. imposed displacements and electric potential, are strongly enforced, i.e the functional space of the state variables is restricted to admissible states fulfilling Dirichlet boundary conditions, there is no enthalpy associated with those contributions. However, applied tractions and surface charges on the sample boundary (Neumann type boundary conditions) do contribute to the

total enthalpy of the material. In order to define correctly the terms associated with boundary conditions, the boundary $\partial\Omega$ is split into several disjoint sets as

$$\partial\Omega = \partial\Omega_u \cup \partial\Omega_t = \partial\Omega_v \cup \partial\Omega_r = \partial\Omega_\phi \cup \partial\Omega_w, \tag{2.101}$$

and the curves are split into two disjoint sets as

$$\partial\partial\Omega = C_u \cup C_j, \tag{2.102}$$

where C_u and C_j are the curves (points in 2D) where Dirichlet boundary conditions and Neumann boundary conditions are applied, respectively. The corresponding Dirichlet and Neumann boundary conditions applied are

$$\boldsymbol{u} = \boldsymbol{u}^{\mathrm{D}} \quad \text{on } \partial\Omega_u, \qquad \boldsymbol{t} = \boldsymbol{t}^{\mathrm{N}} \quad \text{on } \partial\Omega_t, \tag{2.103a}$$

$$\partial^n(\boldsymbol{u}) = \boldsymbol{v}^{\mathrm{D}} \quad \text{on } \partial\Omega_v, \qquad \boldsymbol{r} = \boldsymbol{r}^{\mathrm{N}} \quad \text{on } \partial\Omega_r, \tag{2.103b}$$

$$\phi = \phi^{\mathrm{D}} \quad \text{on } \partial\Omega_\phi, \qquad w = w^{\mathrm{N}} \quad \text{on } \partial\Omega_w, \tag{2.103c}$$

$$\boldsymbol{u} = \boldsymbol{u}^{\mathrm{D}} \quad \text{on } \partial C_u, \qquad \boldsymbol{j} = \boldsymbol{j}^{\mathrm{N}} \quad \text{on } \partial C_j, \tag{2.103d}$$

where $\boldsymbol{u}^{\mathrm{D}}$, $\boldsymbol{v}^{\mathrm{D}}$ and ϕ^{D} are the prescribed value of displacement, normal derivative of the displacement and electric potential, respectively, and $\boldsymbol{t}^{\mathrm{N}}$, $\boldsymbol{r}^{\mathrm{N}}$, w^{N} and $\boldsymbol{j}^{\mathrm{N}}$ are the prescribed value of the traction, double traction, surface charge and line force, respectively.

The total enthalpy of the system for a flexoelectric material considering direct flexoelectricity $\Pi^{\mathrm{Dir}}[\boldsymbol{u}, \phi]$ is then

$$\Pi^{\mathrm{Dir}}[\boldsymbol{u}, \phi] = \Pi^{\Omega}[\boldsymbol{u}, \phi] + \Pi^{\mathrm{N}}[\boldsymbol{u}, \phi], \tag{2.104}$$

with

$$\Pi^{\mathrm{N}}[\boldsymbol{u}, \phi] = \int_{\partial\Omega_t} -u_i t_i^{\mathrm{N}} \,\mathrm{d}\Gamma + \int_{\partial\Omega_r} -\partial^n u_i r_i^{\mathrm{N}} \,\mathrm{d}\Gamma + \int_{\partial\Omega_w} \phi w^{\mathrm{N}} \,\mathrm{d}\Gamma + \int_{C_j} -u_i j_i^{\mathrm{N}} \,\mathrm{d}s, \tag{2.105}$$

As mentioned before, the total enthalpy has no contribution from Dirichlet boundary conditions in the standard approach, i.e. when Dirichlet boundary conditions are imposed strongly. We recall the variational principle stated in Eq. (2.6), which particularises in the present case to

$$(\boldsymbol{u}^*, \phi^*) = \arg \min_{\boldsymbol{u} \in \mathcal{U}_{\mathrm{D}}} \max_{\phi \in \mathcal{P}_{\mathrm{D}}} \Pi^{\mathrm{Dir}}[\boldsymbol{u}, \phi] \tag{2.106}$$

where the functional spaces $\mathcal{U}_{\mathrm{D}}$ and $\mathcal{P}_{\mathrm{D}}$ of admissible states are defined as

$$\mathcal{U}_{\mathrm{D}} = \left\{ \boldsymbol{u} \in [H^2(\Omega)]^3 | \boldsymbol{u} = \boldsymbol{u}^{\mathrm{D}} \text{ on } \partial\Omega_u \text{ and } C_u \text{ and } \partial^n(\boldsymbol{u}) = \boldsymbol{v}^{\mathrm{D}} \text{ on } \partial\Omega_v \right\}, \tag{2.107a}$$

$$\mathcal{P}_{\mathrm{D}} = \left\{ \phi \in H^1(\Omega) | \phi = \phi^{\mathrm{D}} \text{ on } \partial\Omega_\phi \right\}. \tag{2.107b}$$

A necessary condition for equilibrium is the vanishing of the first variation of the enthalpy functional $\Pi^{\mathrm{Dir}}[\mathbf{u}, \phi]$ for all admissible variations $\delta\mathbf{u}$ and $\delta\phi$, which corresponds to the weak form of the problem:

$$\text{Find } (\boldsymbol{u}, \phi) \in \mathcal{U}_{\mathrm{D}} \otimes \mathcal{P}_{\mathrm{D}} \text{ such that } \delta\Pi^{\mathrm{Dir}} = 0 \; \forall (\delta\boldsymbol{u}, \delta\phi) \in \mathcal{U}_0 \otimes \mathcal{P}_0, \tag{2.108}$$

with

$$\mathcal{U}_0 = \left\{ \boldsymbol{u} \in [H^2(\Omega)]^3 | \boldsymbol{u} = 0 \text{ on } \partial\Omega_u \text{ and } C_u \text{ and } \partial^n(\boldsymbol{u}) = 0 \text{ on } \partial\Omega_v \right\}, \tag{2.109a}$$

$$\mathcal{P}_0 = \left\{ \phi \in H^1(\Omega) | \phi = 0 \text{ on } \partial\Omega_\phi \right\}, \tag{2.109b}$$

and

$$\delta\Pi^{\mathrm{Dir}}[\boldsymbol{u}, \phi, \delta\boldsymbol{u}, \delta\phi] = \delta\Pi^{\Omega}[\boldsymbol{u}, \phi, \delta\boldsymbol{u}, \delta\phi] + \delta\Pi^{\mathrm{N}}[\boldsymbol{u}, \phi, \delta\boldsymbol{u}, \delta\phi], \tag{2.110a}$$

$$\delta\Pi^{\Omega}[\boldsymbol{u}, \phi, \delta\boldsymbol{u}, \delta\phi] = \int_\Omega \widehat{\sigma}_{ij}\delta\varepsilon_{ij} + \tilde{\sigma}_{ijk}\delta\varepsilon_{ij,k} - \widehat{D}_l\delta E_l - b_i\delta u_i + q\delta\phi \, \mathrm{d}\Omega, \tag{2.110b}$$

$$\delta\Pi^{\mathrm{N}}[\boldsymbol{u}, \phi, \delta\boldsymbol{u}, \delta\phi] = \int_{\partial\Omega_t} -\delta u_i t_i^{\mathrm{N}} \, \mathrm{d}\Gamma + \int_{\partial\Omega_r} -\partial^n(\delta u_i) r_i^{\mathrm{N}} \, \mathrm{d}\Gamma + \int_{\partial\Omega_w} \delta\phi w^{\mathrm{N}} \, \mathrm{d}\Gamma + \int_{C_j} -\delta u_i j_i^{\mathrm{N}} \, \mathrm{ds}, \tag{2.110c}$$

where the Cauchy stress $\hat{\boldsymbol{\sigma}}$, the high-order stress $\tilde{\boldsymbol{\sigma}}$ and the Electric displacement $\hat{\mathbf{D}}$ are defined as

$$\hat{\sigma}_{ij}(\boldsymbol{u}, \phi) = \hat{\sigma}_{ji}(\boldsymbol{u}, \phi) = \left. \frac{\partial \mathcal{H}^{\Omega}[\boldsymbol{u}, \phi]}{\partial \varepsilon_{ij}} \right|_{\substack{\nabla\boldsymbol{\varepsilon} \\ \boldsymbol{E}}} = \mathbb{C}_{ijkl}(\boldsymbol{x})\varepsilon_{kl} - e_{lij}E_l, \tag{2.111a}$$

$$\tilde{\sigma}_{ijk}(\boldsymbol{u}, \phi) = \tilde{\sigma}_{jik}(\boldsymbol{u}, \phi) = \left. \frac{\partial \mathcal{H}^{\Omega}[\boldsymbol{u}, \phi]}{\partial \varepsilon_{ij,k}} \right|_{\substack{\boldsymbol{\varepsilon} \\ \boldsymbol{E}}} = h_{ijklmn}\varepsilon_{lm,n} - \mu_{lijk}E_l, \tag{2.111b}$$

$$\hat{D}_l(\boldsymbol{u}, \phi) = -\left. \frac{\partial \mathcal{H}^{\Omega}[\boldsymbol{u}, \phi]}{\partial E_l} \right|_{\substack{\boldsymbol{\varepsilon} \\ \nabla\boldsymbol{\varepsilon}}} = \epsilon_{lm}E_m + e_{lij}\varepsilon_{ij} + \mu_{lijk}\varepsilon_{ij,k}. \tag{2.111c}$$

Eq. (2.108) can be integrated by parts and, by invoking the divergence and surface divergence theorems, the Euler-Lagrange equations are derived as

$$\left(\hat{\sigma}_{ij}(\boldsymbol{u}, \phi) - \tilde{\sigma}_{ijk,k}(\boldsymbol{u}, \phi)\right)_{,j} + b_i = 0 \qquad \text{in } \Omega, \tag{2.112a}$$

$$\hat{D}_{l,l}(\boldsymbol{u}, \phi) - q = 0 \qquad \text{in } \Omega, \tag{2.112b}$$

along with the expressions for the traction, double traction, surface charge and line force

$$t_i = \left(\hat{\sigma}_{ij} - \tilde{\sigma}_{ijk,k} + \nabla_l^S\left(n_l\right)\tilde{\sigma}_{ijk}n_k\right)n_j - \nabla_j^S\left(\tilde{\sigma}_{ijk}n_k\right) \quad \text{on } \partial\Omega, \tag{2.113a}$$

$$r_i = \tilde{\sigma}_{ijk}n_j n_k \quad \text{on } \partial\Omega, \tag{2.113b}$$

$$w = -\widehat{D}_l n_l \quad \text{on } \partial\Omega, \tag{2.113c}$$

$$j_i = \left[\!\left[\tilde{\sigma}_{ijk}m_j n_K\right]\!\right] \quad \text{on } C, \tag{2.113d}$$

where $[\![\ ]\!]$ is the jump operator defined as $[\![A]\!] = A^1 + A^2$, $\nabla_j^S(\,) = \nabla_k(\,)\left(\delta_{kj} - n_k n_j\right)$ is the surface divergence operator, $\boldsymbol{n}$ is the normal vector, $\boldsymbol{m}$ is the conormal vector which is a vector tangent to the boundary and pointing outwards.

Note that the only difference between Section 2.1.1 and this one is the spatial dependence in the elasticity material tensor in Eq. 2.111a.

Chapter 3

Computational methods for multimaterial and generalised periodic flexoelectric BVPs

This chapter presents the numerical methods used in this thesis to solve flexoelectric boundary value problems. We focus on the computational aspects particularly arising when dealing with multimaterial samples with general geometries and electrode configurations, periodic lattice materials with general architectures, and graded materials. Firstly, we present an overview of the state of the art of computational approaches for high-order problems, and flexoelectricity in particular, pointing out their advantages and disadvantages. B-splines method is the one adopted in the whole thesis. This method is divided into three different categories. The first is the body-fitted B-spline approach, where the support of the approximation space is the same as the physical body Ω. The second is the immersed B-spline approach, where the support of the approximation space is bigger than the physical body Ω. The last is the high-order generalised periodic approximation space approach, where we modify the immersed approximation space to fulfil the generalised periodicity conditions.

The numerical approach provided here is part of an in-house computational framework called iHB-FEM (Immersed hierarchical B-spline-finite element method). Onofre Marco and David Codony initially created this framework. Then, more people participated in incorporating new functionalities, such as the extension to the body-fitted approach and periodic functional space of approximation, to which I contributed. I should mention all the people who contributed to having a powerful tool like that. They are, apart from the people I just mentioned and me, Alice Mocci, Hossein Mohammadi, Monica Dingle, Francesco Greco and Juan Carlos Tarín.

This code was initially created in MATLAB; now, part of the code has been translated to another in-house code HiPerLife. HiPerLife is a parallel C code created by the group of Prof. Marino Arroyo. All the codes developed are part of the FLEXOCOMP group led by Prof. Irene

Arias.

3.1 State of the art

The numerical solution of boundary value problems involving systems of high-order partial differential equations (PDE) requires either (1) specialised finite elements compatible with C^0 approximations, such as mixed methods (Brezzi *et al.*, 1987) and interior penalty methods (Engel *et al.*, 2002), or (2) approximations based on smooth basis functions. In mixed finite elements, the primal field variables and their derivatives are interpolated as independent variables with C^0 basis functions. Mixed finite elements have been successfully used in strain-gradient elasticity (Amanatidou and Aravas, 2002) or Cahn-Hilliard equation (Feng and Prohl, 2004). They suffer however from stability issues and from cumbersome model-dependent implementations, as well as from a higher computational cost due to the large number of additional unknowns. C^0 penalty methods also consider standard C0 finite element approximations and impose the required continuity across elements weakly (Ventura *et al.*, 2021).

The approach to high-order PDE based on smooth basis functions is much more direct and only requires the approximation of the primal fields. The drawback is that it is, in general, more difficult to define smooth approximation spaces. One option is to use meshfree methods, which easily enable local refinement (Fish and Belytschko, 2007). However, these methods are very expensive due to quadrature and to the large sparsity pattern resulting from the significant overlap of basis functions required in higher-order problems. Furthermore, the treatment of boundary conditions on curved and non-convex geometries can be cumbersome. Another option is Isogeometric analysis (IGA) based on B-splines or NURBS (Cottrell *et al.*, 2009). Isogeometric methods describe boundary geometry with high fidelity and can deal with high-order PDE, but are too rigid in the bulk, e.g. to model composites. B-spline approximations in higher dimensions are constructed from tensor products and thus rely on cartesian meshes, incompatible in principle with general boundary geometries.

This limitation can be circumvented by combining B-Splines with immersed boundary methods, which use meshes non-conforming to the boundary of the domain. This boundary is defined independently of the background mesh, and thus immersed boundary methods overcome the rigidity of tensor product B-Spline approximates (Codony *et al.*, 2019). In immersed boundary methods, essential boundary conditions cannot be enforced strongly since the basis functions are not interpolant at the boundary, and are often enforced weakly through Nitsche's method (Fernández-Méndez and Huerta, 2004, Nitsche, 1970). Similarly, continuity conditions at material interfaces or generalised periodic conditions at fictitious boundaries cannot be imposed strongly. Although continuity conditions for classic elasticity at material interfaces with Isogeometric analysis (IGA) have been developed (Dolbow and Harari, 2009, Jiang *et al.*, 2015), high-order interfaces in unfitted discretisations have not been addressed in the literature to the best of our knowledge.

3.1.1 B-spline basis functions

B-splines are curves or surfaces which are piecewise polynomials. We refer the reader to Piegl and Tiller (2012) for an extensive explanation of B-splines and NURBS. Let $\xi = \{\xi_0, \xi_1, \dots, \xi_m\}$ a non-decreasing sequence of real numbers. ξ is called the knot vector, and ξ_i are the knots. The i-th B-spline basis of degree q is defined recursively as

$$B_i^0(\xi) = \begin{cases} 1 & \xi_i \leq \xi < \xi_{i+1} \\ 0 & \text{otherwise} \end{cases}; \tag{3.1}$$

$$B_i^k(\xi) = \frac{\xi - \xi_i}{\xi_{i+k} - \xi_i} B_i^{k-1}(\xi) + \frac{\xi_{i+k+1} - \xi}{\xi_{i+k+1} - \xi_{i+1}} B_{i+1}^{k-1}(\xi); \qquad \begin{matrix} k = 1, \dots, q \\ i = 0, \dots, m + q - k - 1. \end{matrix} \tag{3.2}$$

Note that a B-spline of degree q is the linear combination of two B-splines of degree $q-1$, and the B-spline of degree 0 is just the step function. We called the multiplicity of a knot ξ_i, the number of times that this knot is repeated in the knot vector. This multiplicity reduces the continuity of the basis function at that point once for each time the knot is repeated. Without any multiplicity, the continuity of the basis function is C^{q-1}. B-splines have some properties that we need to recall:

- Local support: $B_i^k(\xi) = 0 \quad \forall \xi \notin [\xi_i, \xi_{i+q+1})$.
- For each knot span $[\xi_i, \xi_{i+1})$ there are at most $q+1$ B-splines with support inside.
- Non-negativity: $B_i^k(\xi) \geq 0 \quad \forall i, k, \xi$.

Fig. 3.1 shows two representations of the B-spline basis function. The first one of degree 1 with knot vector $\{0, 1, 2, 3, 4, 5, 6, 7\}$ and the second one of degree 2 with knot vector $\{0, 0, 0, 1, 2, 4, 4, 5, 6, 6\}$. Note that in the second example, knot 0 has multiplicity three and knots 4 and 6 have multiplicity two. As knot 4 has multiplicity 2, it implies that the basis function B_4^2 is only C^0 at that point.

B-splines are defined in a multivariate space by the tensor product of univariate ones:

$$B_{\boldsymbol{i}}^q([\xi, \eta, \tau]) = B_{i_\xi}^q(\xi) B_{i_\eta}^q(\eta) B_{i_\tau}^q(\tau). \tag{3.3}$$

Different kinds of B-spline bases are obtained depending on the choice of the knot vector. We mainly focus on two: open B-spline and uniform B-spline.

3.1.2 High-order approximation space: Body fitted B-spline approach

Imposing Dirichlet boundary conditions strongly, as done in Section 2.1.1, requires the basis function to be interpolant on the boundary. In order to get interpolant basis function we use

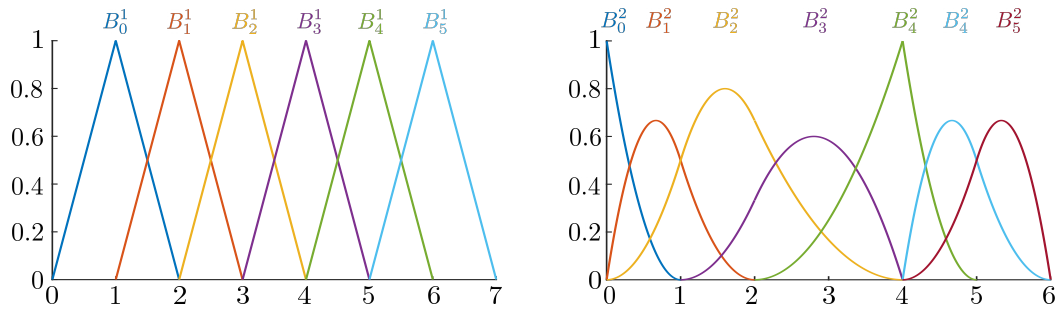

Figure 3.1: Example of B-spline basis function. (left) The knot vector used is $\{0, 1, 2, 3, 4, 5, 6, 7\}$ and the degree is 1. (right) The knot vector used is $\{0, 0, 0, 1, 2, 4, 4, 5, 6, 6\}$ and the degree is 2.

.

an open knot vector. An open knot vector is one whose first and last element of the knot vector have multiplicity $q + 1$, as seen in Fig. 3.2.

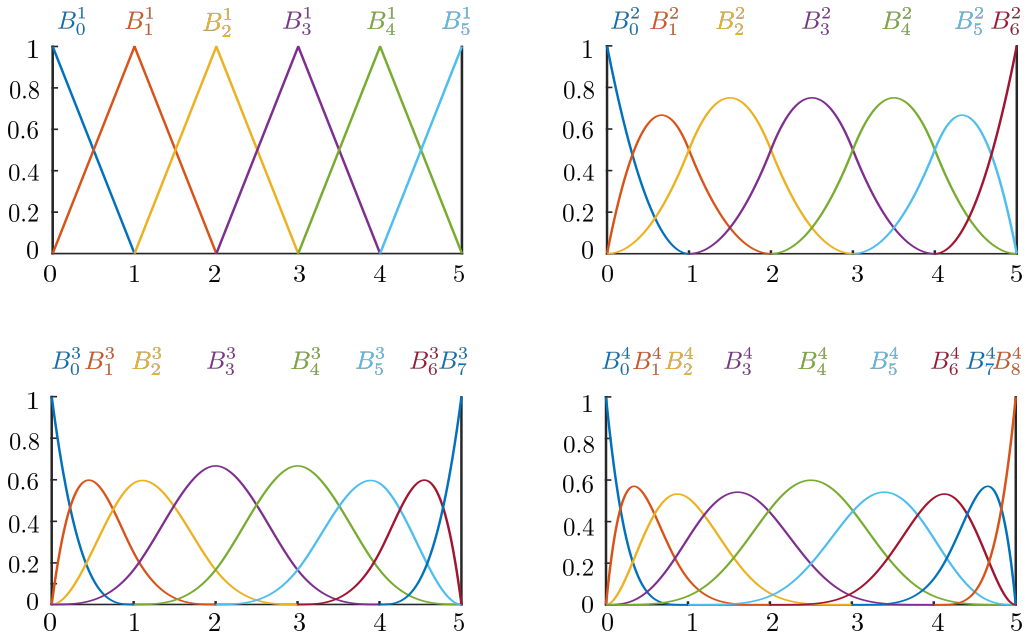

Figure 3.2: Example of open B-spline basis functions for different degrees. From left to right and top and bottom, the different degrees and knot vectors are: degree=1 and knotvector={0,0,1,2,3,4,5,5}, degree=2 and knotvector={0,0,0,1,2,3,4,5,5,5}, degree=3 and knotvector={0,0,0,0,1,2,3,4,5,5,5,5} and degree=4 and knotvector={0,0,0,0,0,1,2,3,4,5,5,5,5,5}.

Firstly, we define the geometrical maps φ which map a given point in the parametric space

$\xi \in \Xi$ to a given point in the physical space $\boldsymbol{x} \in \Omega$ as

$$\begin{aligned} \varphi &: \Xi \longrightarrow \Omega \\ \xi &\longrightarrow \varphi(\xi) = \boldsymbol{x} \end{aligned} \tag{3.4}$$

The basis functions in the physical space $N_i^q(\boldsymbol{x})$ are constructed as $N_i^q = B_i^q \circ \varphi^{-1}$ and the state variables are approximated as

$$[\boldsymbol{u}(\boldsymbol{x})]_d \approx [\boldsymbol{u}^h(\boldsymbol{x})]_d = N_i(\boldsymbol{x}) a_{id}^u = B_i(\xi, \eta, \tau) a_{id}^u, \tag{3.5a}$$

$$\phi(\boldsymbol{x}) \approx \phi^h(\boldsymbol{x}) = N_i(\boldsymbol{x}) a_i^\phi = B_i(\xi, \eta, \tau) a_i^\phi, \tag{3.5b}$$

where $\{\boldsymbol{a}^u, \boldsymbol{a}^\phi\}$ are the degrees of freedom of u^h and ϕ^h. We have omitted the superscript q for convenience. The geometrical map in Eq. (3.4) is straightforward in the context of B-spline because we restrict ourselves to rectangular meshes. Then the geometrical map is $\varphi(\xi, \eta, \tau) = [h_x \xi; h_y \eta; h_z \tau]$, where each element of the mesh has dimensions $[h_x; h_y; h_z]$.

Once the interpolant basis function is defined, we can reduce the space of approximation to impose Dirichlet conditions as done in Eq. (2.17). Low-order PDEs, as in the Laplace equation, need to impose the first and the last B-spline because these two are the only ones with a value different from 0 at the boundary. For fourth-order PDEs, as flexoelectricity, we need to impose the first two and the last two B-spline to impose the first and second-order Dirichlet conditions. In 1D, the imposition is as easy as setting the value of the B-spline equal to the boundary condition, but in 2D or 3D, we need to make a *L2* projection to impose them, as done in Barceló-Mercader (2018).

3.1.3 High-order approximation space: Immersed B-spline approach

Being Ω the physical domain, in the approach of Section 3.1.2, Ω was restricted to a rectangular shape. In order to deal with any arbitrary shape, we define an embedded domain $\Omega_\square$ such that $\Omega \in \Omega_\square$ (see Fig. 3.3). The geometrical map is now

$$\begin{aligned} \varphi &: \Xi \longrightarrow \Omega_\square \\ \xi &\longrightarrow \varphi(\xi) = \boldsymbol{x} \end{aligned} \tag{3.6}$$

Note that the geometrical map φ is independent of the physical domain. To preserve the Jacobian and the properties explained in Section 3.1.2, the embedded domain is assumed to have a rectangular shape of dimensions, for instance, in 3D (L_x, L_y, L, z), but the physical domain has no longer a rectangular shape. The B-spline basis functions used in this method could be defined using the open knot vector defined in Section 3.1.2. However, as the Dirichlet boundary condition cannot be imposed strongly because the boundary of the embedded domain may not be the same as the physical domain, we use a uniform B-spline basis function instead.

Every knot of the knot vector is now equidistant with the next and the previous one. For

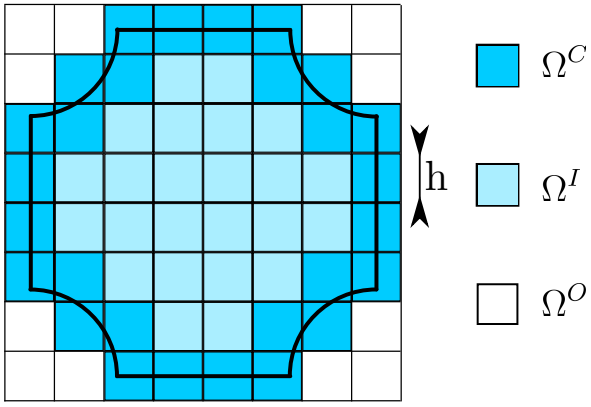

Figure 3.3: 2D Mesh for the immersed boundary approach. In dark blue, there is depicted the cut cells Ω^C; in light blue, there is depicted the inner cells Ω^I; and in white, there is depicted the outer cells Ω^O.

.

example, in Fig. 3.4, we can see some plots of the uniform B-spline basis function for degrees between one and four. The main disadvantage of using this kind of B-spline is that they are not interpolant at the boundary, meaning that the Dirichlet boundary condition cannot be applied strongly. However, our embedded domain might not share the boundary with the physical one, so it is no longer a problem.

In this approach, Dirichlet boundary conditions cannot be imposed strongly and have to be imposed weakly, as done using Nitsche's method explained in Section 2.2.1. One advantage of using uniform B-splines is that all basis functions are the same but translated in space. Therefore, their expression of them can be computed once for one spline and then translated it.

3.1.3.1 Cut-cell integration and stabilisation

Integration of the physical domain is the most challenging part of the immersed boundary method. Firstly, each element of the Cartesian mesh has to be classified into three disjoint groups (see Fig. 3.3):

- Inner cells (Ω^I): These cells are entirely inside of the physical domain ($\Omega^I \subseteq \Omega$).
- Outer cells (Ω^O): These cells are entirely outside of the physical domain ($\Omega^O \cap \Omega = \emptyset$).
- Cut cells (Ω^C): These cells have a portion inside the physical domain, and the rest lie outside it ($\Omega^C \cap \Omega \neq \emptyset$ & $\Omega^C \not\subseteq \Omega$).

Once each element has been classified, we distinguish two kinds of integration: integration of the bulk and integration of the boundary.

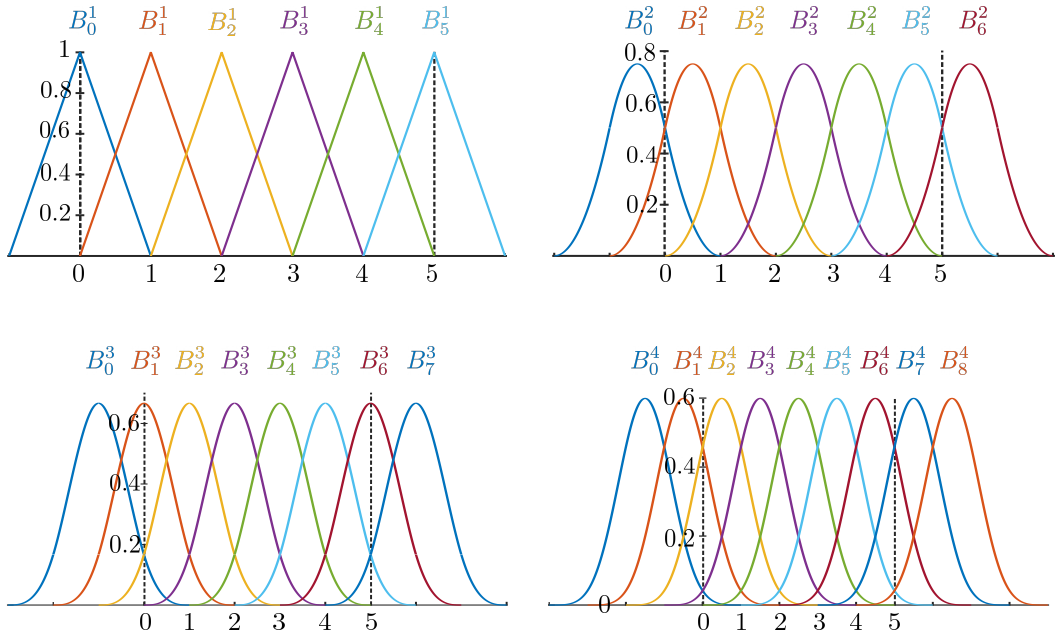

Figure 3.4: Example of uniform B-spline basis functions for different degrees. From left to right and top and bottom, the different degrees and knot vectors are: degree=1 and knotvector={-1,0,1,2,3,4,5,6}, degree=2 and knotvector={-2,-1,0,1,2,3,4,5,6,7}, degree=3 and knotvector={-3,-2,-1,0,1,2,3,4,5,6,7,8} and degree=4 and knotvector={-4,-3,-2,-1,0,1,2,3,4,5,6,7,8,9}.

Integration of the bulk of inner cells can be done with standard quadrature for polynomials (Witherden and Vincent, 2015), and no boundary integration is needed. For cut cells, an excellent representation of the boundary is needed. NEFEM approach based on the NURBS representation of the geometry is used in this thesis (Legrain, 2013, Marco *et al.*, 2015, Sevilla and Fernández-Méndez, 2011, Sevilla *et al.*, 2008, 2011a,b), because it preserves the high convergence rate of the B-spline method. Then, each cut cell is divided into several subdomains using an algorithm based on the marching cubes algorithm (Marco *et al.*, 2015).

The system of equations built with the discretisation of the weak form in Section 2.2.4 using the immersed approach can suffer from ill-conditioning (de Prenter *et al.*, 2016). This phenomenon may happen when a cut cell has a tiny portion inside the physical domain. To minimise ill-conditioning, some strategies can be used. One can be the ghost penalty method (Burman, 2010), another adding artificial stiffness (Düster *et al.*, 2008, Schillinger and Ruess, 2015), and finally, the one used in this thesis, the extended B-spline method (Höllig *et al.*, 2012, 2001, Rüberg and Cirak, 2012, Rüberg *et al.*, 2016).

Essentially, the extended B-spline method consists of reducing the space of approximation, changing the basis function with very little support with a linear combination of other basis functions that lie inside o almost inside the physical domain.

That particular method is well-suited for our approach because it can be applied using

a constraint matrix that will pre-multiply and post-multiply the matrix of the system of equations.

3.2 High-order generalised periodicity approximation space

Simulating a unit cell of an architected material is a complex problem because you need to apply high-order periodicity condition, as stated in Section 2.4.1. A way of enforcing them in a fancy way is by creating a high-order generalised periodicity approximation space. Any function approximated with high-order generalised periodicity space will fulfil the high-order generalised periodicity conditions by construction. A set of periodic basis function and a high-order generalised periodic basis function create this periodicity space.

3.2.1 Periodic basis function

Following the explanation described in Barceló-Mercader *et al.* (2023). Being $\Omega^{\text{RVE}} = [0, L_x] \otimes [0, L_y] \otimes [0, L_z] \subset \mathbb{R}^3$ the unit cell of an architected materials as seen in Fig. 3.5. The condition that must fulfil the Cartesian mesh $\Omega_\square$ is that it must have element sizes (h_x, h_y, h_z) such that $L_\zeta / h_\zeta = n_\zeta \in \mathbb{N}^+, \zeta = \{x, y, z\}$, where n_ζ is the number of cells along the ζ-th dimension.

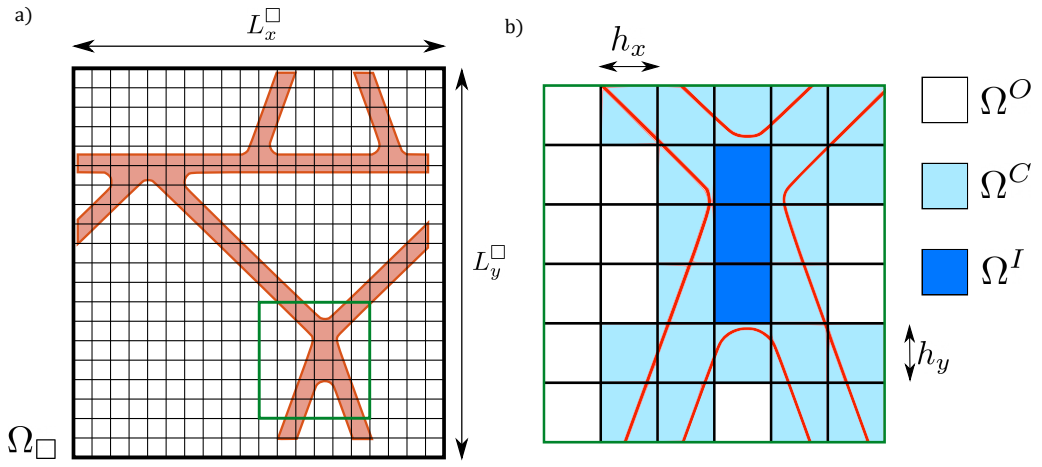

Figure 3.5: a) Embedded mesh $\Omega_\square$ of size $L_x^\square$ and $L_y^\square$. Note that $\Omega_\square \supset \Omega^{\text{RVE}}$ The number of elements per dimension is 20: $n_x = n_y = 19$, and the shift is: $s_x = 0.9$ and $s_y = 0.1$. b) Zoom in of the mesh, outer cells are depicted in white, cut cells in light red and inner cells in dark blue. Image taken from Barceló-Mercader *et al.* (2023)

The dimensions $(L_x^\square, L_y^\square, L_z^\square)$ of the computational domain $\Omega_\square$ are

$$L_\zeta^\square = \begin{cases} h_\zeta \cdot n_\zeta & \text{if } L_\zeta^\square = L_\zeta, \\ h_\zeta \cdot (n_\zeta + 1) & \text{if } L_\zeta^\square > L_\zeta. \end{cases} \tag{3.7}$$

The simplest case happens when the equality holds for every direction and then $\Omega_\square \equiv \Omega^{\text{RVE}}$. Nevertheless, we use a general case where the inequality holds for every direction, obtaining $\Omega_\square \supset \Omega^{\text{RVE}}$. Taking into account the shifting parameters $s_\zeta \in (0, 1)$, which moves the Cartesian mesh an arbitrary number (to avoid very bad cut elements), the embedding domain $\Omega_\square$ spans $[h_\zeta \cdot (s_\zeta - 1), L_\zeta + h_\zeta \cdot s_\zeta]$ in the ζ-th dimension.

To obtain the periodic B-spline basis $B_i^{\text{P}}(\xi, \eta, \tau)$, we identify the basis with its corresponding periodic images whose distance is $(m_x n_x, m_y n_y, m_z n_z)$, $m_x, m_y, m_z \in \mathbb{Z}$ creating a unique degree of freedom. It can be seen in Fig. 3.6. This strategy creates a high-order periodic basis that satisfies standard periodic conditions as stated in Section 2.4.1 . Using this strategy, the unit cell Ω^{RVE} is cut by $\partial\Omega$ but not by $\partial\Omega^{\text{RVE}}$.

3.2.2 High-order generalised periodic basis

A generalised periodicity approximation space is constructed by adding a periodic space with a functional space spanned with global basis functions $\overline{B}_\zeta(\xi, \eta, \tau)$ that fulfil

$$\overline{B}_\zeta\left(\varrho = n_\varrho\right) - \overline{B}_\zeta\left(\varrho = 0\right) = \delta_{\zeta\varrho}, \tag{3.8a}$$

$$\partial^n \overline{B}_\zeta\left(\varrho = n_\varrho\right) - \partial^n \overline{B}_\zeta\left(\varrho = 0\right) = 0, \tag{3.8b}$$

where $\zeta, \varrho \in \{\xi, \eta, \tau\}$ and $\delta_{\zeta\varrho}$ is the Kronecker delta.

The definition of the basis function $\overline{B}_\zeta(\xi, \eta, \tau)$ is not unique. The simplest approach $\overline{B}_\zeta(\xi, \eta, \tau)$ is the linear function $\overline{B}_\zeta(\xi, \eta, \tau) = \zeta / n_\zeta$. However, it spans the whole Ω^{RVE}, substantially increasing the fill-in of the resulting system matrix. An efficient alternative in the context of B-spline basis that involves minimal fill-in and straightforward implementation consists of defining $\overline{B}_\zeta(\xi, \eta, \tau)$ as the addition of all the non-vanishing original B-spline basis $B_i(\xi, \eta, \tau)$ on the cell $\Omega_\square^c$ intersected by $\partial\Omega^{\text{RVE}} = L_\zeta$, as seen in Fig. 3.7. Thanks to the partition of unity property of B-spline basis, seen in Section 3.1.1, $\overline{B}_\zeta(\xi, \eta, \tau)$ evaluates to 1 within the aforementioned cell and 0 for all derivatives. At the opposite boundary $\partial\Omega^{\text{RVE}} = 0$, $\overline{B}_\zeta(\xi, \eta, \tau)$ and its derivatives vanish, fulfiling the conditions in Eq. (3.8). The generalized-periodic functional space has C^{q-1} continuity.

An advantage of defining the periodic basis as done in Section 3.2.1 and the generalised periodic basis in this way is that they can be implemented as a linear constraint on the original approximation space during or after the assembly stage, as done in Section 3.1.3.1 with the extended B-spline method.

In conclusion, the components of $\boldsymbol{u}$ and ϕ are approximated by the high-order generalised periodicity functional spaces spanned by the basis functions $\left\{B_i^{\text{P}}(\xi, \eta, \tau); \overline{B}_\zeta(\xi, \eta, \tau)\right\}$ and

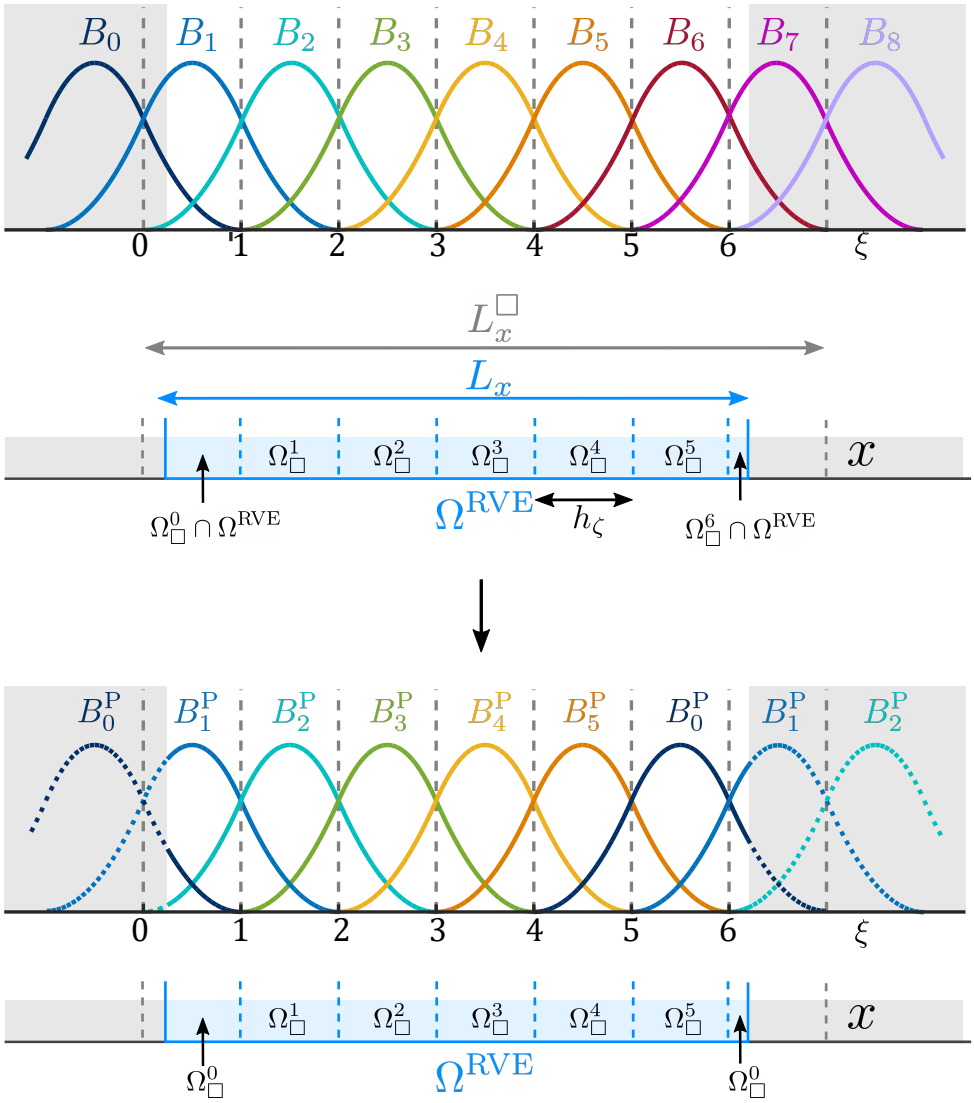

Figure 3.6: Univariate periodic basis of degree $q = 2$. Originally (top), the functional space is spanned by nine B-spline bases $B_i(\xi)$, $i = 0, \dots, 8$, defined onto a mesh of $L_x/h_x = n_x = 6$ cells. Note that Ω^{RVE} does not coincide with $\Omega_{\square}$, and therefore cut cells ($\Omega_0^{\square} \cap \Omega^{\mathrm{RVE}}$ and $\Omega_6^{\square} \cap \Omega^{\mathrm{RVE}}$) are generated. In order to create a high-order-periodic functional space (bottom), the basis functions at a distance n_x on Ω^{RVE} are identified with the same degree of freedom, yielding a functional space spanned by only six periodic B-Spline bases $B_i^{\mathrm{P}}(\xi)$, $i = 0 \dots 5$. The periodic nature of the basis implies periodicity on Ω^{RVE} too, which does not have cells cut by the periodic boundary $\partial\Omega^{\mathrm{RVE}}$ anymore. Image adapted from Barceló-Mercader *et al.* (2023)

control variables $\left\{ \boldsymbol{u}^{\mathrm{P}}, \phi^{\mathrm{P}}; \overline{\boldsymbol{\varepsilon}}, \overline{\boldsymbol{E}} \right\}$ as follows:

$$u_a(x,y,z) \approx \sum_i \left[B_i^{\mathrm{P}} \circ \varphi^{-1}(x,y,z) \right] u_a^{\mathrm{P}} + \left[\overline{B}_b \circ \varphi^{-1}(x,y,z) \right] \overline{\varepsilon}_{ab} \tag{3.9a}$$

$$\phi(x,y,z) \approx \sum_i \left[B_i^{\mathrm{P}} \circ \varphi^{-1}(x,y,z) \right] \phi^{\mathrm{P}} + \left[\overline{B}_b \circ \varphi^{-1}(x,y,z) \right] \overline{E}_b \tag{3.9b}$$

where $a, b \in \{x, y, z\}$. Note that the solution is determined up to a constant, which means that rigid body translation is not fixed. To impose it, we usually set the first basis function to zero without loss of generality.

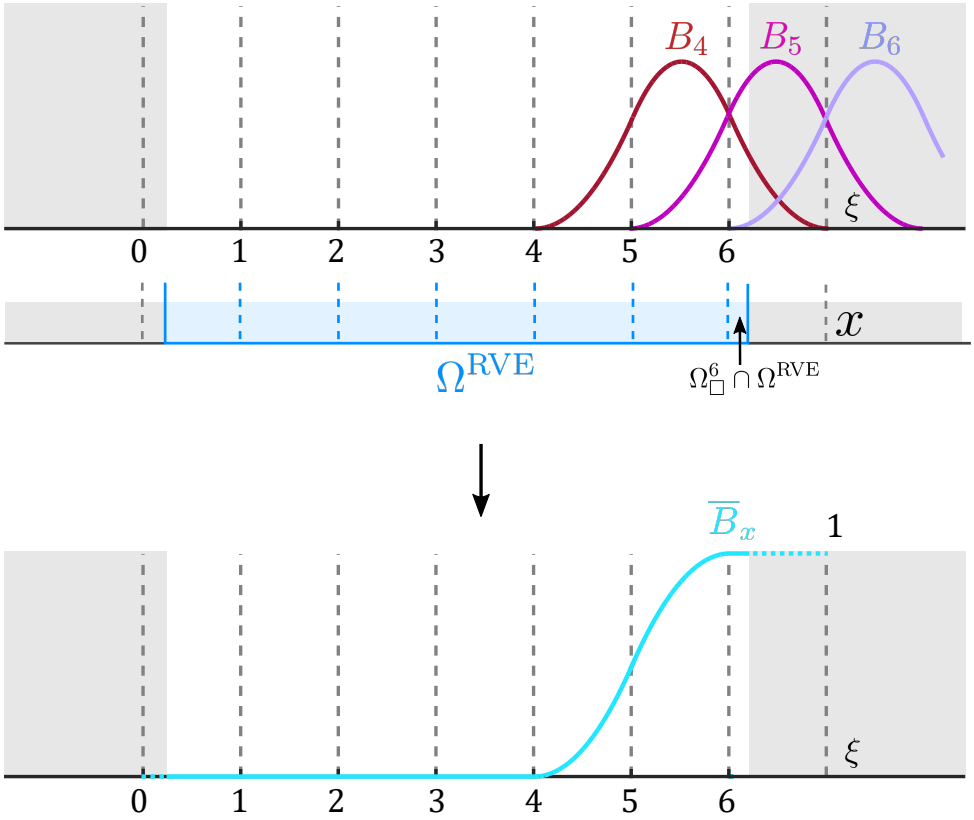

Figure 3.7: Univariate generalised periodic basis of degree $q = 2$. Originally (top), the functional space over the cut cell $\Omega^6_\square \cap \Omega^{\text{RVE}}$ is spanned by three B-spline basis functions $B_i(\xi)$, $i = \{4, 5, 6\}$. The addition of these basis functions yields the global basis function $\overline{B}_x(\xi)$, which inherits the regularity of the original B-spline basis and fulfils the admissibility condition in Eq. (3.8). The union of $\overline{B}_x$ with the periodic B-spline basis in Fig. 3.6 spans a high-order generalised periodic functional space on Ω^{RVE}. Image adapted from Barceló-Mercader *et al.* (2023)

Remark 3.1. The critical basis functions of the high-order generalised periodic functional space, that is, those whose support is intersected by $\partial\Omega$ in a tiny proportion, can be stabilised through the extended B-spline stabilisation technique as any other basis function.

3.2.3 Enforcement of macroscopic kinematics

Discretising the weak for in Eq. (2.93) on the generalised periodic space, we get the following system of equations:

$$\begin{pmatrix} \boldsymbol{K}_{PP} & \boldsymbol{K}_{PG} \\ \boldsymbol{K}_{GP} & \boldsymbol{K}_{GG} \end{pmatrix} \begin{pmatrix} \boldsymbol{X}_P \\ \boldsymbol{X}_G \end{pmatrix} = \begin{pmatrix} 0 \\ \boldsymbol{f}_G \end{pmatrix} \tag{3.10}$$

where the subscript P denotes the periodic basis functions stated in Section 3.2.1, and the subscript G denotes the global basis functions described in Section 3.2.2.

In our case, we have $\boldsymbol{X}_G = \{\overline{\boldsymbol{\varepsilon}}, \overline{\boldsymbol{E}}\}$, $\boldsymbol{X}_P = \{\boldsymbol{u}^{\mathrm{P}}, \phi^{\mathrm{P}}\}$ and $\boldsymbol{f}_G = |\Omega^{\mathrm{RVE}}|\{\overline{\boldsymbol{\sigma}}, \overline{\boldsymbol{D}}\}$. The sets $\boldsymbol{X}_G$ and $\boldsymbol{f}_G$ are split into two subsets, one corresponding to macroscopic Dirichlet conditions $\boldsymbol{X}_G^D$ and $\boldsymbol{f}_G^D$, and another one corresponding to macroscopic Neumann conditions $\boldsymbol{X}_G^N$ and $\boldsymbol{f}_G^N$. Macroscopic Dirichlet conditions in Eq. (2.91) are strongly enforced on the system of equations 3.10 by prescribing the values of $\boldsymbol{X}_G^D$, and microscopic Neumann conditions in Eq. (2.92) are enforced by prescribing the values of $\boldsymbol{f}_G^N$.

3.2.4 Macroscopic kinematics rotation

The macroscopic conditions derived previously have been applied along the directions (x, y, z) of the Cartesian frame. However, macroscopic conditions can be applied along a rotating frame by considering

$$\begin{aligned} \overline{\boldsymbol{\varepsilon}}^R &= \boldsymbol{R} \cdot \overline{\boldsymbol{\varepsilon}} \cdot \boldsymbol{R}^T, & \overline{\boldsymbol{\sigma}}^R &= \boldsymbol{R} \cdot \overline{\boldsymbol{\sigma}} \cdot \boldsymbol{R}^T, \\ \overline{\boldsymbol{E}}^R &= \boldsymbol{R} \cdot \overline{\boldsymbol{E}}, & \overline{\boldsymbol{D}}^R &= \boldsymbol{R} \cdot \overline{\boldsymbol{D}}. \end{aligned} \tag{3.11}$$

where $\boldsymbol{R}$ is a given rotation matrix from the Cartesian frame to the rotating frame:

$$\boldsymbol{R} = \begin{pmatrix} \cos\alpha & -\sin\alpha & 0 \\ \sin\alpha & \cos\alpha & 0 \\ 0 & 0 & 1 \end{pmatrix} \cdot \begin{pmatrix} \cos\beta & 0 & \sin\beta \\ 0 & 1 & 0 \\ -\sin\beta & 0 & \cos\beta \end{pmatrix} \cdot \begin{pmatrix} 1 & 0 & 0 \\ 0 & \cos\gamma & -\sin\gamma \\ 0 & \sin\gamma & \cos\gamma \end{pmatrix}, \tag{3.12}$$

being α, β, γ the angles called yaw, pitch and roll typically used in aeronautics. This approach is useful, especially in sensitivity analysis as in the loading direction example in Section 4.4, since a continuous response can be obtained by continuously increasing the rotation angle covering all the parameter space. This task can be performed very efficiently by implementing a *for* loop during or after the assembly stage, avoiding the re-computation of volume integrals in the approximation space. The new rotating system of equations is

$$\begin{pmatrix} \boldsymbol{K}_{PP} & \boldsymbol{K}_{PG}^R \\ \boldsymbol{K}_{GP}^R & \boldsymbol{K}_{GG}^R \end{pmatrix} \begin{pmatrix} \boldsymbol{X}_P \\ \boldsymbol{X}_G^R \end{pmatrix} = \begin{pmatrix} 0 \\ \boldsymbol{f}_G^R \end{pmatrix}, \tag{3.13}$$

where $\boldsymbol{K}_{PG}^R = \boldsymbol{K}_{PG} \cdot \boldsymbol{R}^T$, $\boldsymbol{K}_{GP}^R = \boldsymbol{R} \cdot \boldsymbol{K}_{GP}$, $\boldsymbol{K}_{GG}^R = \boldsymbol{R} \cdot \boldsymbol{K}_{GG} \cdot \boldsymbol{R}^T$, $\boldsymbol{X}_G^R = \{\overline{\boldsymbol{\varepsilon}}^R, \overline{\boldsymbol{E}}^R\}$ and $\boldsymbol{f}_G^R = |\Omega^{\mathrm{RVE}}|\{\overline{\boldsymbol{\sigma}}^R, \overline{\boldsymbol{D}}^R\}$. The macroscopic Dirichlet and Neumann conditions can be applied directly

to $\boldsymbol{X}_G^{\boldsymbol{R}}$ and $\boldsymbol{f}_G^{\boldsymbol{R}}$ along the directions of the rotating frame.

3.3 Selection of numerical parameters

This section reviews the selection of the penalty parameters of the Nitsche's method in Eqs. 2.41 and 2.51, and the γ-parameter of the weighted mean in Eqs. 2.47a and 2.48.

3.3.1 Penalty parameter of Nitsche's method

The penalty parameters β^u, β^v, β^{C_u} and β^ϕ in Eq. 2.41 can be computed by solving an eigenvalue problem (Griebel and Schweitzer, 2003), or they can be approximated by writing them as a function of some material parameters (Barceló-Mercader *et al.*, 2022, Codony *et al.*, 2021a, 2019) as

$$\beta^u = \frac{E}{h}\zeta, \qquad \beta^v = \frac{\ell^2 E}{h}\zeta, \qquad \beta^{C_u} = \frac{\ell^2 E}{h^2}\zeta, \qquad \beta^\phi = \frac{\epsilon}{h}\zeta. \tag{3.14}$$

As these values are valid for a wide range of ζ, we will take $\zeta = 100$, which gives accurate results for all examples in the thesis. They do not depend on the intersection of the mesh with the body thanks to the extended B-spline method, which has been presented previously in section 3.1.3.1.

The penalty parameters $\beta^{u\mathcal{I}}, \beta^{v\mathcal{I}}, \beta^{C_u\mathcal{I}}, \beta^{\phi\mathcal{I}} \in \mathbb{R}^+$ in Eq. 2.51 are defined in terms of a dimensionless parameter $\zeta \in \mathbb{R}^+$ as a generalisation of the ones seen in Eq. (3.14) as

$$\begin{aligned} \beta^{u\mathcal{I}} &= \frac{\max(E^{(1)}, E^{(2)})}{h}\zeta, & \beta^{v\mathcal{I}} &= \frac{\ell^2 \max(E^{(1)}, E^{(2)})}{h}\zeta, \\ \beta^{C_u\mathcal{I}} &= \frac{\ell^2 \max(E^{(1)}, E^{(2)}, ..., E^{(n)})}{h^2}\zeta, & \beta^{\phi\mathcal{I}} &= \frac{\max(\epsilon^{(1)}, \epsilon^{(2)})}{h}\zeta, \end{aligned} \tag{3.15a}$$

where h denotes the physical cell size of the mesh, and E, ϵ and ℓ denote Young's modulus, the dielectric permittivity and the internal length scale arising from strain gradient elasticity, see Appendix A.1.

3.3.2 Weighted mean parameter

Numerical oscillations around the interface may appear in some critical cases when one element has a much smaller portion in one domain than in the other, as previously reported in Annavarapu *et al.* (2012a,b), Dolbow and Harari (2009), Laursen *et al.* (2012). To improve the conditioning, we consider the following simplified version of γ-parameters reported in Annavarapu *et al.* (2012a,b), which yields accurate results:

$$\gamma^{L(k)} = \frac{meas(S_{\Omega(L)})}{meas(S_{\Omega(L)}) + meas(S_{\Omega(R)})}, \qquad \gamma^{R(k)} = \frac{meas(S_{\Omega(R)})}{meas(S_{\Omega(L)}) + meas(S_{\Omega(R)})}, \tag{3.16}$$

where $meas(S_{\Omega(i)})$ denotes the physical measure of the cut cell. Other expressions of these parameters include the material parameter of the physical domains as the Young modules or Poisson ratio. We refer the reader to Annavarapu *et al.* (2012a,b) to find more complex expressions and explanations.

The choice of the $\hat{\gamma}$-parameter in Eq. (2.48) in Barceló-Mercader *et al.* (2022) is also a generalisation of the γ-parameters defined in Eq. (3.16) as

$$\hat{\gamma}^{P(k,i)} = \frac{meas(S_{\Omega(i)})}{\sum_{j=1}^{m(k)} meas(S_{\Omega(j)})}. \tag{3.17}$$

3.4 Validation of numerical method

The last section of this chapter consists of two convergence tests of continuum modelling and numerical methods. One for the 2D flexoelectric model and one for the 3D flexoelectric model.

3.4.1 Convergence test for interfaces

We start with a 2D convergence test. Being the synthetic solution defined as

$$\begin{aligned} u_x(x,y) &= 4\sin(2\pi x), \\ u_y(x,y) &= 3\sin(2\pi y), \\ \phi(x,y) &= 2\sin(2\pi x) + \sin(2\pi y). \end{aligned} \tag{3.18}$$

The physical domain Ω consists of three triangles that create an equilateral triangle of size 3, as seen in Fig. 3.8. Interface and Dirichlet conditions, consistent with the synthetic solution, are the ones applied here, and they can also be seen in Fig. 3.8. The material parameters used are in Table 3.1. Note that, as this is a convergence test, the material parameters are dimensionless for convenience.

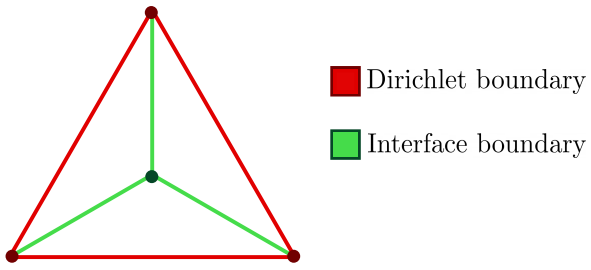

Figure 3.8: Physical domain and boundary conditions applied to the 2D convergence test. The physical domain consists of three triangles forming an equilateral triangle of size 2.

Ω	E	ν	l	ϵ	$\boldsymbol{d}$	e_L	e_T	e_S	μ_L	μ_T	μ_S
1	87	0.33	1	141	**y**	8.8	-4.4	4.4	150	110	110
2	58	0.3	1	11	**y**	3.8	-2.4	2.4	100	10	00
3	33	0.25	1	85	**y**	5.3	-3.2	2.6	10	180	180

Table 3.1: Material parameters for the three subdomains in Fig. 3.8

The convergence analysis is done by computing the $\mathcal{L}^2$, $\mathcal{H}^1$, $\mathcal{H}^2$ and $\mathcal{H}^3$ errors using two different degrees of approximation, $q = 3$ and $q = 4$. $\log_2(h_0/h)$ is the mesh refinement level, and $h_0 = 1$ is a normalisation length. The convergence analysis can be seen in Fig. 3.9, and optimal convergence is obtained.

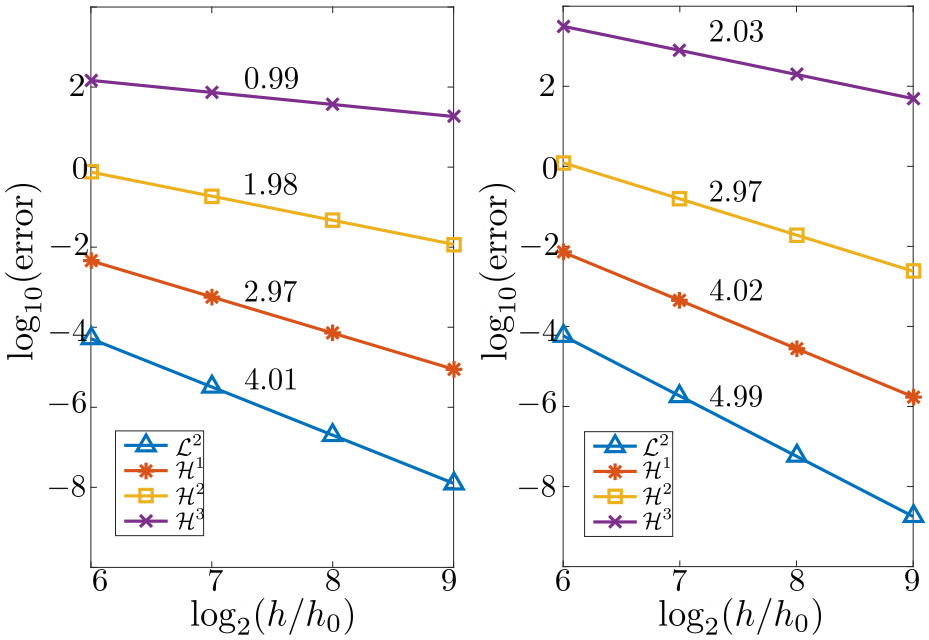

Figure 3.9: Convergence plots for $\mathcal{L}^2$, $\mathcal{H}^1$, $\mathcal{H}^2$ and $\mathcal{H}^3$ norms, with degree $q = 3$ (left) and $q = 4$ (right) for the 2D interface analysis. The number for each plot is the slope of the least square fitting.

A similar 3D convergence test is done. Let us consider an arrangement of four cubes of size 2 forming a parallelepiped. Two different materials are used, and they are in Table 3.2.

Ω	E	ν	l	ϵ	$\boldsymbol{d}$	e_L	e_T	e_S	μ_L	μ_T	μ_S
1	98	0.33	1	141	**z**	8.8	-4.4	4.4	150	110	110
2	42	0.3	1	11	**z**	3.8	-2.4	2.4	110	10	10

Table 3.2: Material parameters for the two subdomains in Fig. 3.10

Dirichlet boundary conditions are imposed on the outer boundary and interface conditions on the inner ones (see Fig. 3.10), consistent with the following synthetic solution:

$$\begin{aligned} u_x(x,y,z) &= 4\sin(0.2x), \\ u_y(x,y,z) &= 8\cos(0.2y), \\ u_z(x,y,z) &= 7\cos(0.2y) + 2\sin(0.2z), \\ \phi(x,y,z) &= 1\sin(0.2x) - 3\cos(0.2y) + 2\sin(0.2z). \end{aligned} \tag{3.19}$$

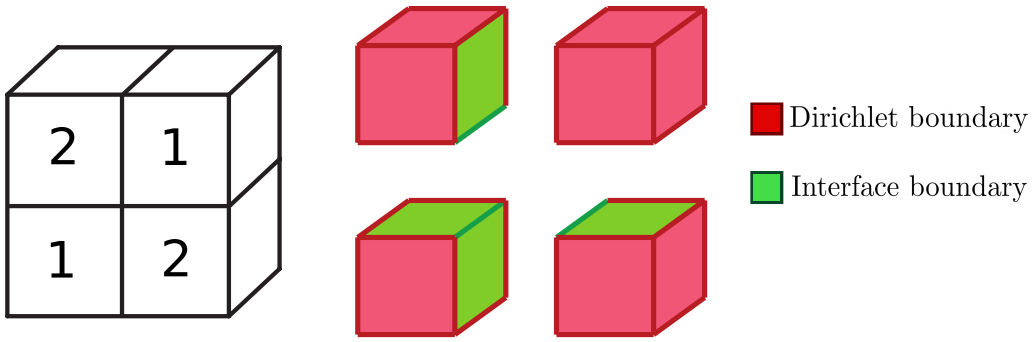

Figure 3.10: Physical domain and boundary conditions applied to the 3D convergence test. The physical domain consists of an arrangement of four cubes of size 2.

The convergence analysis is done computing the $\mathcal{L}^2$, $\mathcal{H}^1$, $\mathcal{H}^2$ and $\mathcal{H}^3$ errors using two different degrees of approximation, $q = 3$ and $q = 4$. $\log_2(h_0/h)$ is the mesh refinement level, and $h_0 = 1$ is a normalisation length. The convergence analysis can be seen in Fig. 3.11 and optimal convergence is obtained.

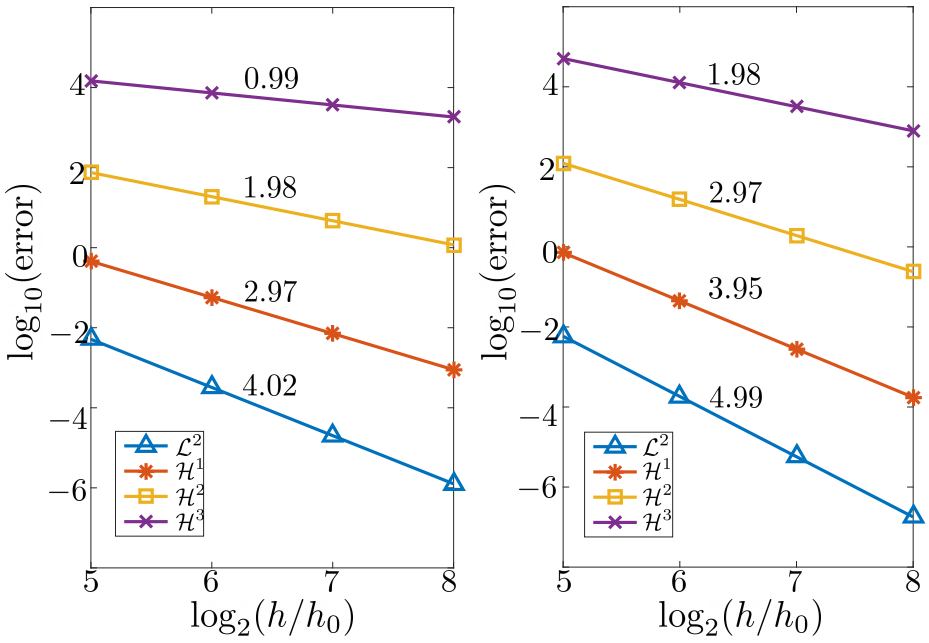

Figure 3.11: Convergence plots for $\mathcal{L}^2$, $\mathcal{H}^1$, $\mathcal{H}^2$ and $\mathcal{H}^3$ norms, with degree $q = 3$ (left) and $q = 4$ (right) for the 3D interface analysis. The number for each plot is the slope of the least square fitting.

Chapter 4

Flexoelectricity in non-homogeneous materials

This chapter presents several examples of flexoelectric BVPs in non-homogeneous materials. First, a comb-like flexoelectric device is presented. In this design, a non-centrosymmetric arrangement of material inclusions is used to accumulate and upscale the local flexoelectric response. Next, two periodic metamaterials are analysed in vertical sensor mode, i.e. a macroscopic vertical displacement is applied and the resulting macroscopic electric bias is computed. The metamaterials are analysed by considering the unit cell subject to generalised periodic conditions. The two methods derived in this thesis are considered: that based on Nitsche's method (Section 2.3) for the first example and that taking advantage of the periodicity of the B-spline basis functions (Section 3.2) for the second. Both examples validate the model of generalised periodicity comparing the response of a unit cell or RVE against that obtained for a finite structure formed by a finite but sufficiently large number of unit cells. Then, second method is used to analyse a 2D flexoelectric architected material. The apparent piezoelectric coefficients are computed for different operation modes as a function of the design orientations, showing the material anisotropy. After that, a 3D flexoelectric architected material is considered. We compare the response of the 3D architected material with a 2D unit cell with plane strain and the same shape. Finally, graded structures are studied considering a linearly varying Young modulus.

4.1 Comb-like flexoelectric harvester

We consider an electromechanical device consisting of two comb-like structures of a non-piezoelectric dielectric joint together by a very low-dielectricity material at the tip of the beams, see Fig. 4.1. The application of a shear motion at the left and right sides of the structure, induces beam bending and triggers the flexoelectric effect. This local flexoelectrically generated electric potential is accumulated through the structure, as shown in Fig. 4.1. By breaking the overall

centrosymmetry of the system (thanks to the insulator in the middle), the low-dielectricity material inclusions preclude internal cancellation of the local flexoelectrically generated electric potential, thereby endowing the device with an effective piezoelectric behaviour, even when the base material is a non-piezoelectric dielectric (Mocci *et al.*, 2021, Sharma *et al.*, 2010).

A device with ten beams is considered for illustration purposes. The beams are 100 nm long by 10 nm wide, and the insulator is a square of side 10 nm. Material properties are given in Table 4.1. Displacements, $\boldsymbol{u}_L = (0, 5)$ nm and $\boldsymbol{u}_R = (0, -5)$ nm are prescribed on the left and right sides of the structure, and the top-right half side of the structure is electrically grounded, Fig. 4.1. Natural boundary conditions are assumed otherwise. The effective piezoelectric response of the structure manifests in a net potential difference between the ground electrode and the top-left half side of the structure.

Ω	E[GPa]	ν	l[nm]	ϵ[nJ V^{-2} m^{-1}]	μ_L[μJ V^{-1} m^{-1}]	μ_T	μ_S
1	152	0.33	1	141	150	110	110
2	152	0.33	1	141×10^{-7}	0	0	0

Table 4.1: Material properties of the material tensors described in Section 4.1. The piezoelectric tensor is zero for all materials.

4.2 Sensor under vertical compression using generalised periodicity and interface conditions.

The validation of generalised periodicity conditions is done by comparing the response of a sizeable periodic arrangement of triangular voids on a dielectric matrix to that of the periodic unit cell, as seen in Fig. 4.2. Such structure has been proposed as a means to generate a local flexoelectric response in a non-piezoelectric material in such a way that a net electric potential is generated under macroscopic homogeneous deformation (Barceló-Mercader *et al.*, 2022, Mocci *et al.*, 2021, Sharma *et al.*, 2010). For a massive structure under a prescribed strain, we expect the solution in the central part of the structure to be unaffected by boundary effects and thus exhibit generalised periodicity. In Fig. 4.2, we compare the solution obtained on the generalised periodic unit cell with the central unit cell of a vertical stack of N unit cells. In the first simulation, we consider a unit cell with generalised periodic conditions in both directions. A displacement jump along the vertical direction y

$$\hat{\boldsymbol{u}}^y = (0, -0.1) \ \text{nm}. \tag{4.1}$$

is prescribed, and all other jumps in Eq. (2.59), $\check{\boldsymbol{u}}^x$, $\check{\phi}^x$ and $\check{\phi}^y$, are left free (unconfined vertical displacement sensor), see discussion under Eq. (2.60). The unit cell is a square of side 4 μm with a triangular void of $\frac{3\sqrt{3}}{2}$μm. The material properties correspond to the first material in Table 4.1.

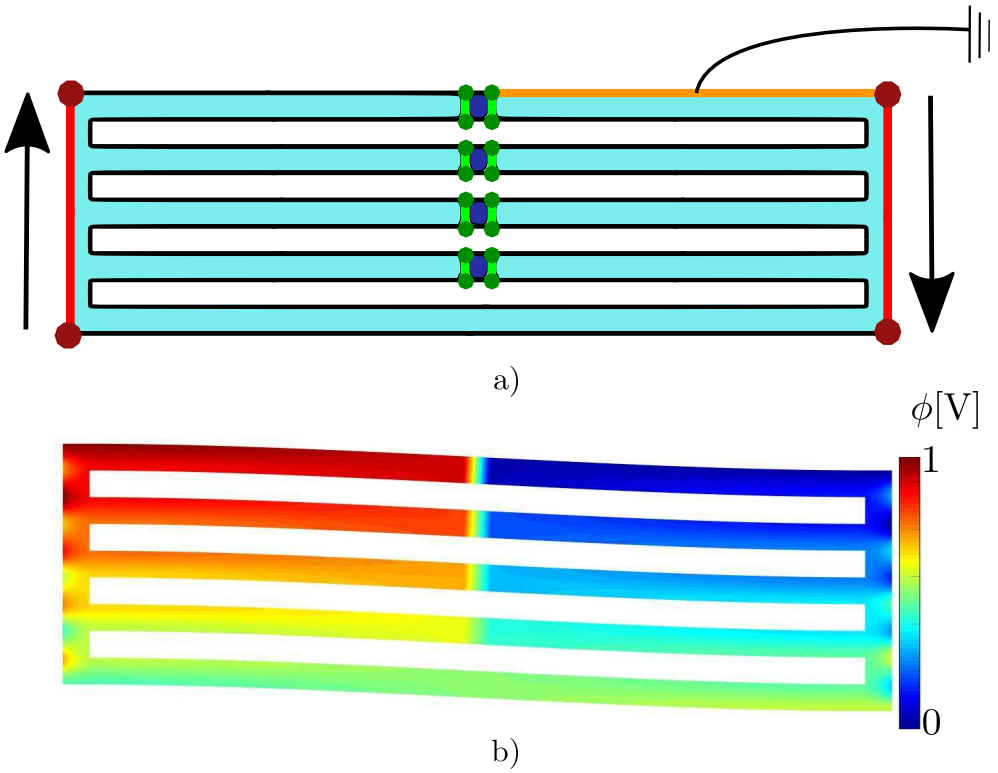

Figure 4.1: (a) Geometry of the comb with flexoelectric material in Ω_1 (in light blue) and insulator in Ω_2 (in dark blue). The interface, $\mathcal{I}$, and its corners, $\mathcal{C}$, are also shown in green. The Dirichlet boundary is depicted in red, and the electrical ground side is shown in orange. (b) Deformed shape of the material and electric potential distribution. Image adapted from Barceló-Mercader *et al.* (2022).

Figure 4.2 shows the unit cell and the resulting electric potential distribution. In the second simulation, we consider a stack of N=19 such unit cells subject to prescribed displacements on the top and bottom faces matching, in the limit, the previous generalised periodicity conditions, i.e.

$$\boldsymbol{u}|_{y=y_{max}} = N\hat{\boldsymbol{u}}^y \qquad \boldsymbol{u}|_{y=0} = \boldsymbol{0}, \tag{4.2}$$

and unconstrained generalised periodicity conditions for $\boldsymbol{u}$ and ϕ in the horizontal direction. As the electric potential is determined up to a constant, we set it to zero at the centre of the structure. Figure 4.2 shows the vertical structure and the electric potential distribution, with a zoom around the central cell. For comparison purposes, the scale of the electric potential for the second simulation is adjusted to show perfect agreement with the generalised periodic

unit cell result, Fig. 4.2. That error is smaller than 0.1% in all points inside the unit cell. For

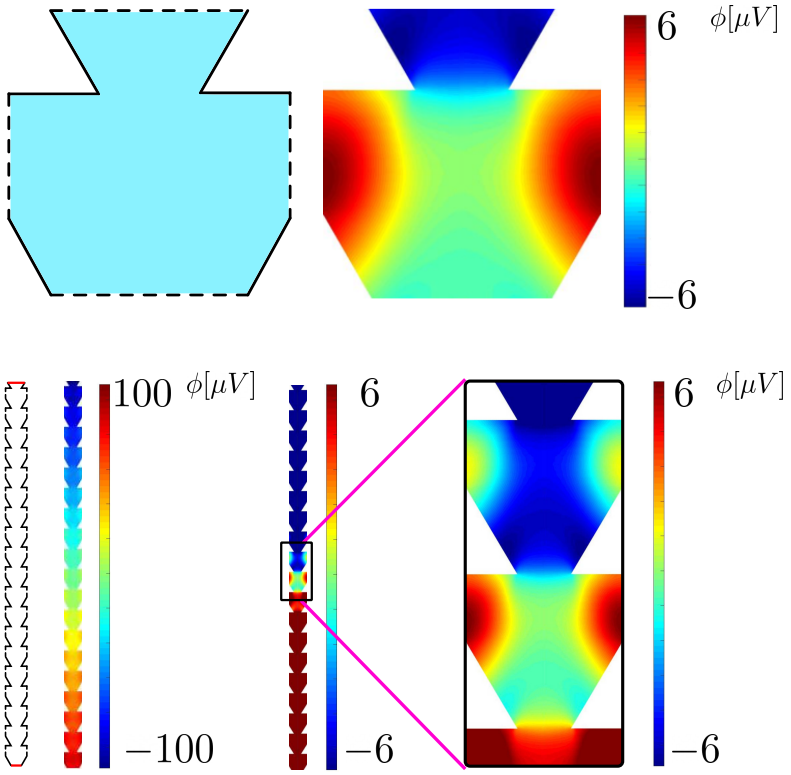

Figure 4.2: (a) Unit cell and electric potential distribution with generalised periodic conditions in both directions. (b) Distribution of the electric potential in a structure formed by 19 unit cells prescribed displacements at the top and bottom. Results on the central generalised periodic unit cell are shown with the same scale as a) for direct comparison purposes. Image extracted from Barceló-Mercader *et al.* (2022)

stacks of a large number of unit cells, we expect the average electric potential difference on a unit cell to tend to the generalised periodicity electric potential jump $\check{\phi}^y$, i.e.

$$\lim_{N\to\infty} \frac{\overline{\Delta\phi}}{N} = \check{\phi}^y, \tag{4.3}$$

where $\overline{\Delta\phi}$ is the electric potential difference between the top and bottom boundaries of the structure in Fig. 4.2. For quantitative validation purposes, we plot in Fig. 4.3 the value of $\overline{\Delta\phi}/N$ for stacks of an increasing number of unit cells from $N = 1$ to $N = 20$ and compare it against the generalised periodicity electric potential jump $\check{\phi}^y$ obtained in the generalised periodic unit cell simulation, Fig. 4.2. From this plot, the limit in Eq. (4.3) is apparent. The electromechanical response of a unit cell under generalised periodicity conditions is thus

shown to represent the bulk response of a periodic material built from that unit cell under the corresponding macroscopic conditions on its boundaries. Although we only show the validation for a sensor mode considering generalised periodicity in the y-direction, actuator mode and different generalised periodicity have been considered. All of them have the same agreement as the one presented here.

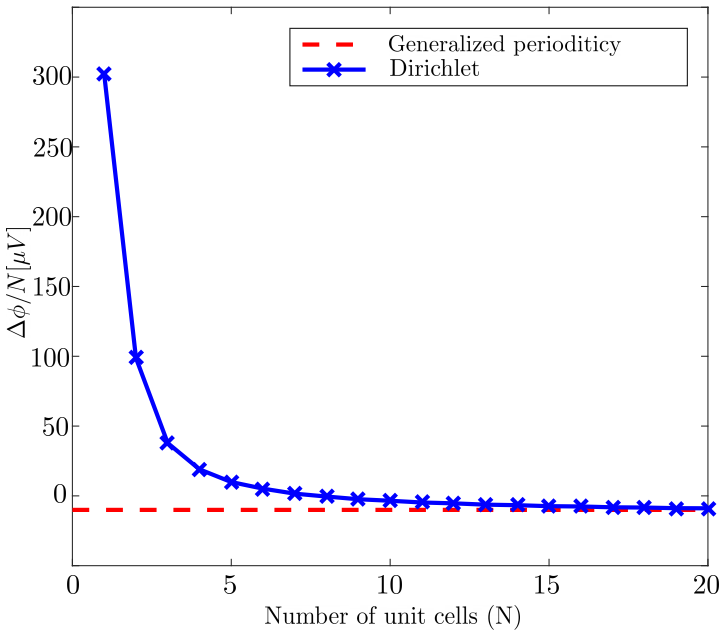

Figure 4.3: Plot of the difference of electric potential, $\Delta\phi$, per unit cell, versus the number of unit cells N (in blue) and potential difference, $\check{\phi}^y$, for one unit cell considering generalised periodicity in both directions (in red). Image extracted from Barceló-Mercader *et al.* (2022)

4.3 Sensor under vertical compression using generalised periodicity and high-order generalised periodicity space

In this section, we follow the validation test done in Section 4.2. We compare the response of a large two-dimensional structure to that of the unit cell. The structure is built using an arrangement of squares of length size 4 µm with equilateral triangular voids of length size $\frac{3\sqrt{3}}{2}$ µm as can be seen in Fig. 4.4.

First, we perform the simulation associated with the RVE (see Fig. 4.4), imposing the following generalised periodicity conditions:

$$\overline{\varepsilon}_{yy} = -0.1, \tag{4.4}$$

while other components of the macroscopic strain and the macroscopic electric field are left

free:

$$\overline{\sigma}_{xx} = \overline{\sigma}_{xy} = \overline{\sigma}_{yx} = \overline{D}_x = \overline{D}_y = 0. \tag{4.5}$$

This condition represents imposing a homogeneous unconfined compression along the y-direction like done in Mocci *et al.* (2021), Sharma *et al.* (2010). The material properties are reported in Table 4.2.

E $[GPa]$	ν -	ℓ_{mech} $[n\text{m}]$	κ $[nC/V\text{m}]$	ℓ_{elec} $[n\text{m}]$	μ_ℓ $[nC/\text{m}]$	μ_t $[nC/\text{m}]$	μ_s $[nC/\text{m}]$
152	0.33	1	45	0	40	40	0

Table 4.2: Material parameters in Section 4.3

The unit cell and the resulting electric potential distribution can be seen in Fig. 4.4. The macroscopic electric field of the unit cell is $\overline{E}_y = -1.6028 V/\text{m}$.

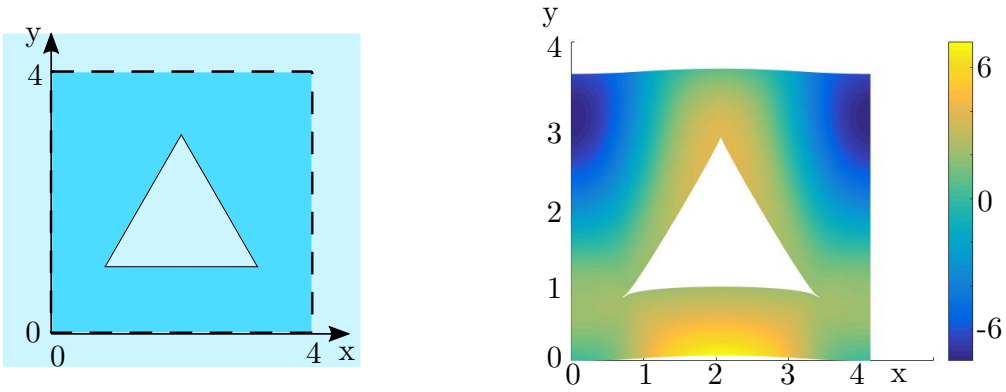

Figure 4.4: (Left) Unit cell simulated. (Right) Deformed shape and electric potential distribution inside a unit cell, considering generalised periodicity. Image taken from Barceló-Mercader *et al.* (2023).

After the simulation of the RVE, we perform the simulation of the full arrangement. Let consider an arrangement of $N \in \{1, \dots, 20\}$ concatenated unit cells under prescribed displacements on top and bottom faces matching, in the limit of $N \longrightarrow \infty$, the previous generalised periodicity conditions, that is,

$$\boldsymbol{u}|_{y=4N} = (0, -0.4N) \qquad \boldsymbol{u}|_{y=0} = 0, \tag{4.6}$$

As the bottom of the structure is grounded (see Fig. 4.5), the difference in the electric potential between top and bottom is, simply, the average of the electric potential at the top. Natural boundary conditions are considered in all other boundaries, as seen in Fig. 4.5.

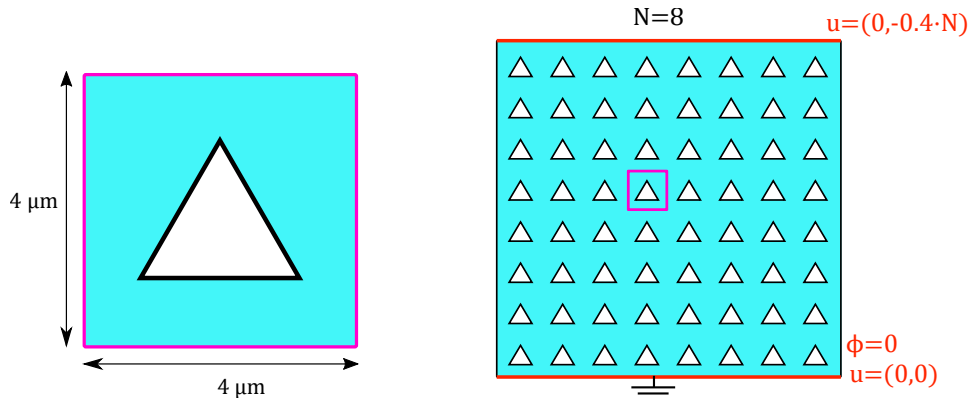

Figure 4.5: Unit cell (left) and structure formed by $N = 8$ cells per dimension (right). The Dirichlet boundary conditions are depicted in red, and natural boundary conditions are applied on all other boundaries. Image adapted from Barceló-Mercader *et al.* (2023)

In the limit of stacking unit cells, the difference of electric potential between top and bottom faces divided by the vertical length should tend to minus the macroscopic electric field $\overline{E}_y$, that is,

$$\lim_{N\to\infty} \frac{-\Delta\phi}{L_y} = \lim_{N\to\infty} E_y = \overline{E}_y. \tag{4.7}$$

The value of E_y for different numbers of unit cells can be seen in Fig. 4.6. Also, the value of the macroscopic electric field is plotted in red, showing that the limit in Eq. (4.7) is apparent. The difference between the value considering $N = 20$ cells and the one obtained using generalised periodicity is less than 0.05%. Although in this example, only one set of generalised periodicity conditions has been validated, the result using any other generalised periodicity condition is the same.

4.4 2D flexoelectric architected material

An alternative route for technologies based on electromechanical transduction could be achieved by flexoelectricity. Architected metamaterials, if well designed, can overcome any dielectric presenting apparent piezoelectricity, as seen in Mocci *et al.* (2021), Sharma *et al.* (2007). We are interested in bending-dominated lattices and low-area fractions, as shown in Mocci *et al.* (2021). Apparent piezoelectricity is exhibited by the lattice thanks to flexoelectricity and the non-centrosymmetric arrangement of the constituents. The metamaterial is created by an arrangement of periodic unit cells with a thickness of $t = 160$nm and length $\ell = 1.6$µm.

Using the generalised periodicity conditions, the metamaterial is reduced to a single unit

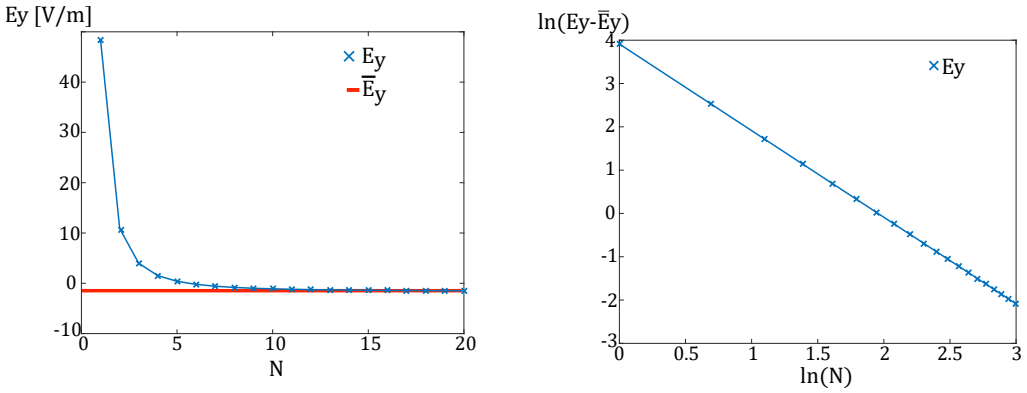

Figure 4.6: Plot of the electric field resulting from stacking N cells per dimension versus the number of cells stacked (left). The red line is the value resulting considering generalised periodicity conditions. Plot of the difference between the electric field resulting from stacking N cells per dimension and the one obtained using generalised periodicity conditions versus the number of cells stacked (right) . Image adapted from Barceló-Mercader *et al.* (2023).

cell, as seen in Fig. 4.7(a). We simulate two different setups for the actuator mode. Both have applied a macroscopic electric field in the vertical direction $\overline{E}_y$, and the mechanical response is left free in the vertical direction. In the horizontal direction, we consider two different conditions, the first one is a strain-free configuration $\overline{\varepsilon}_{xx} = \overline{\varepsilon}_{xy} = 0$, and the second one is a stress-free configuration $\overline{\sigma}_{xx} = \overline{\sigma}_{xy} = 0$. Both of them are presented in Fig. 4.7. The material parameters are chosen accordingly to Mocci *et al.* (2021) and reported in table 4.3.

Material	Y $[GPa]$	ν -	ℓ_{mech} $[nm]$	κ $[nC/V\text{m}]$	ℓ_{elec} $[nm]$	μ_ℓ $[\mu C/\text{m}]$	μ_t $[\mu C/\text{m}]$	μ_s $[\mu C/\text{m}]$
BST	152	0.33	50	8	300	1.21	1.10	0.055

Table 4.3: Material in Section 4.4

For quantitative characterisation, two different apparent coefficients $\bar{d}, \hat{d}$ are calculated, as

$$\bar{d} = \left.\frac{\partial \bar{\varepsilon}}{\partial \bar{E}}\right|_{\bar{\sigma}_{xx}=0} = 0.42\ pm/V, \quad \hat{d} = \left.\frac{\partial \bar{\varepsilon}}{\partial \bar{E}}\right|_{\bar{\varepsilon}_{xx}=0} = 0.51\ pm/V. \tag{4.8}$$

It can be seen that the rigid device shows over a 20% performance improvement concerning the soft device.

The next step is studying the anisotropic behaviour of the lattice. This step can be achieved by considering different angles of orientation of the mechanical and electrical inputs. In this case, the sensor mode and the actuator mode are studied. For the sensor mode, the apparent piezoelectric coefficient is $\bar{h}$, and for the actuator mode is $\bar{d}$. Both of them have been normalised using Young's modulus and dielectric permittivity.

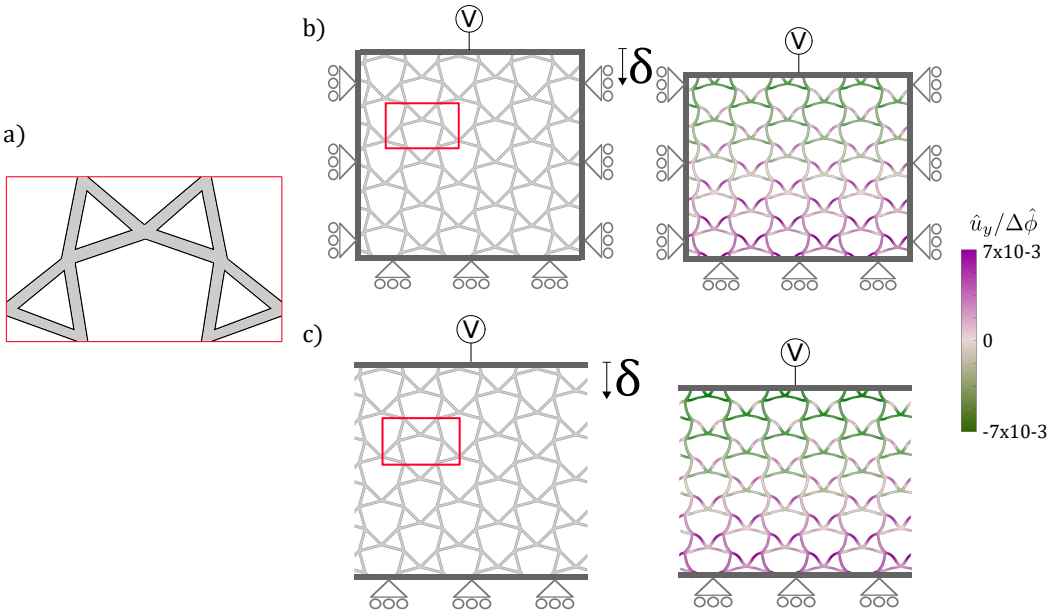

Figure 4.7: Geometrically-polarised, bending-dominated lattice in actuation mode. The RVE is represented in a). A macroscopic electric field is applied in the vertical direction. However, two different approaches are considered in the horizontal direction: strain-free configuration in b) and stress-free configuration in c). The normalised y-displacements $\hat{u}_y = u_y/\ell$ are depicted on the deformed configuration considering the normalised electric potential $\hat{\phi} = \phi\kappa/\mu$. Image taken from Barceló-Mercader *et al.* (2023)

The polar plots obtained are shown in Fig. 4.8, showing that the response of the lattice is anisotropic. Note that no polarisation is shown when the load has a horizontal direction. This fact is in agreement with having a horizontal symmetry of the lattice. Apart from the previous symmetry, a $2\pi/3$ rotation symmetry is also shown.

4.5 3D flexoelectric architected material

The structure is formed by an arrangement of unit cells in which each unit cell is a cube of size $\ell = 2\mu$m with a truncated conical void inside. The truncated cone has a radius 1µm and 0.2µm and a height 1µm. The material parameters are the same as the previous application, and it can be seen in Table 4.3. Macroscopic strain is applied in the vertical direction $\overline{\varepsilon}_{zz} = -0.1$, and standard periodicity is applied in the other directions, which means $\overline{\varepsilon}_{xx} = \overline{\varepsilon}_{yy} = \overline{\varepsilon}_{xz} = \overline{\varepsilon}_{xy} = \overline{\varepsilon}_{yz} = 0$ and $\overline{D}_x = \overline{D}_y = \overline{D}_z = 0$. Thanks to the non-centrosymmetry of the metamaterial, the lattice shows a macroscopic electric field in the vertical direction. Note that the macroscopic electric field in the other two directions is zero due to the symmetry of the structure. It can be seen in Fig. 4.9.

Finally, we compare the response of the 3D metamaterial with a 2D RVE with plane strain

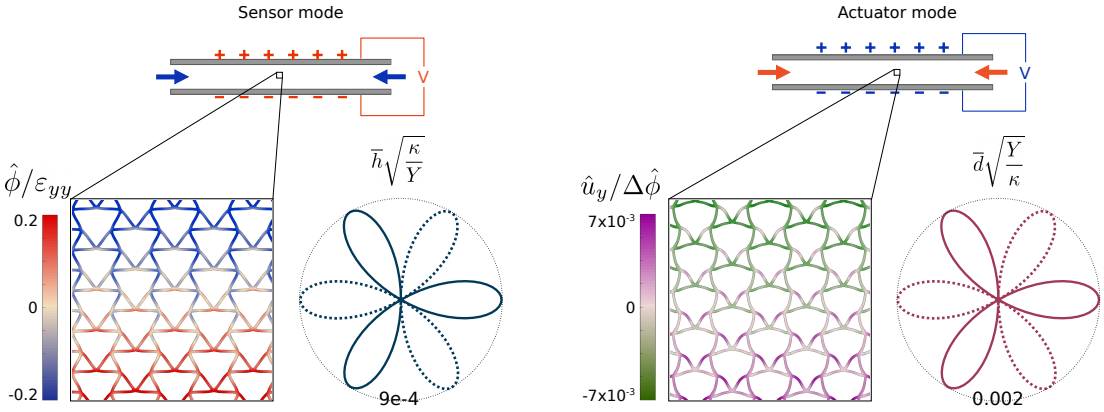

Figure 4.8: Anisotropy of the normalised apparent piezoelectric coefficients $\bar{h}\sqrt{\kappa/Y}$ and $\bar{d}\sqrt{Y/\kappa}$ for sensor and actuator modes, respectively. Solid lines mean positive values of the apparent piezoelectric coefficient, and dashed lines mean negative values. The normalised electric potential $\hat{\phi} = \phi\kappa/\mu$ and y-displacements $\hat{u}_y = u_y/l$ are plotted on the deformed configuration. Image taken from Barceló-Mercader *et al.* (2023).

approximation. To do that, we created the 2D model as the cross-section of the 3D model by the middle, as seen in Fig. 4.10. The 3D model has the generalised periodicity condition stated previously, while the generalised periodicity condition for the 2D model is $\overline{\varepsilon}_{yy} = -0.1$ with $\overline{\varepsilon}_{xy} = \overline{\varepsilon}_{xx} = 0$ and $\overline{D}_x = \overline{D}_y = 0$. The results shown in Fig. 4.10 clarify that although plane strain is a good approximation, it is not enough for accurate quantitative results.

4.6 Graded material

Avoiding centrosymmetric deformations is mandatory to trigger the flexoelectric effect. For this reason, inhomogeneous deformation as bending is commonly used. Another way of obtaining flexoelectricity with a homogeneous deformation is having a graded structure. Graded structures are ubiquitous in nature and they are helpful in making damage-tolerant structures as the ones seen in the stomatopod (Weaver *et al.*, 2012, Yaraghi *et al.*, 2016), the human teeth (Cuy *et al.*, 2002) or human bones (Wegst *et al.*, 2015).

Bones present a gradient of porosity, with the centre being hollow. The outer layers are more compact than the inner layers, as seen in Fig. 4.11. This hierarchical structure helps to stabilise cracks, increasing fracture toughness. Teeth also have a hierarchical structure with gradients of Young's modulus that prevents cracking of the brittle enamel as seen in Fig. 4.12. The last example is the stomatopod's club. The stomatopod is a crustacean with an incredibly strong club that can break the shells of its prey. The impact region of the club is responsible for absorbing most of the impact energy and presents a hierarchical structure, as seen in Fig. 4.13.

We use graded structures to create a flexoelectric sensor that works under homogeneous deformation, as shown in Fig. 4.14. We will consider a graded structure with varying Young's

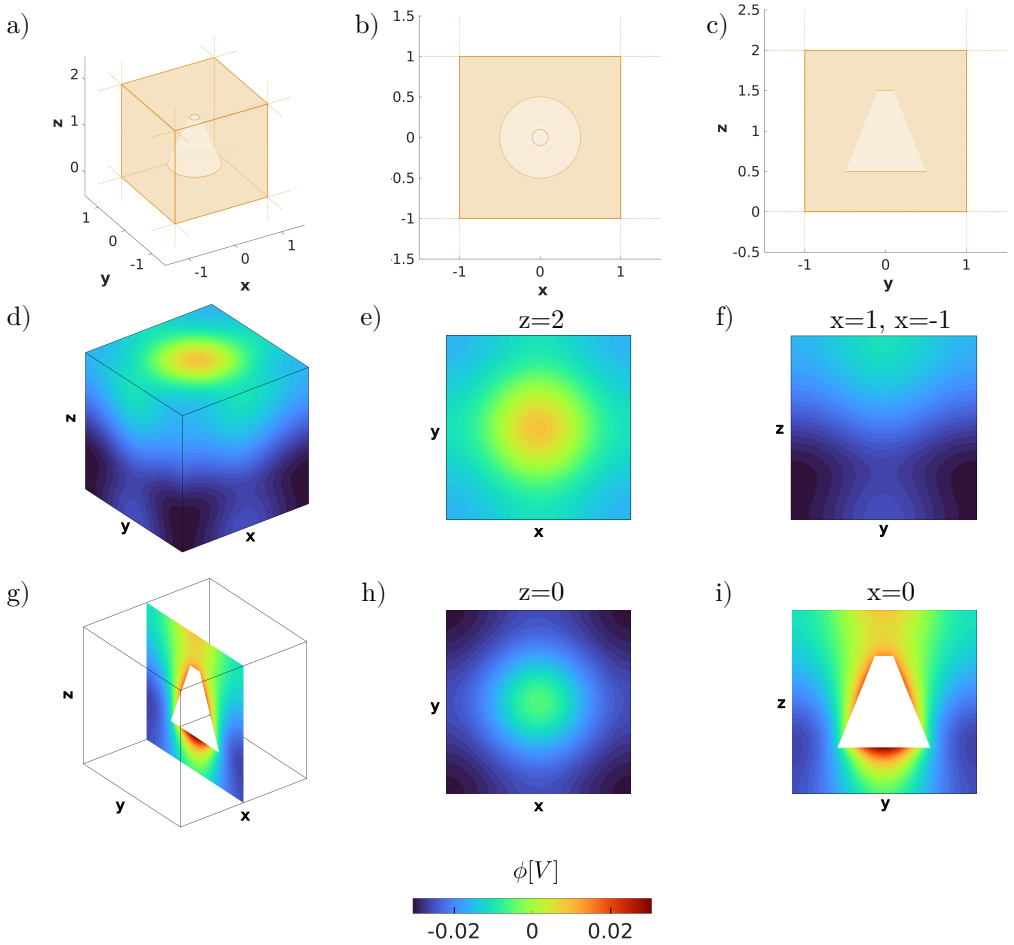

Figure 4.9: 3D flexoelectric device simulation. The geometrical model in 3D is shown in a) while some 2D cuts are shown in b-c). The electric potential distribution is seen for the 3D cube in d) and some arbitrary 2D cuts in e-i). Image taken from Barceló-Mercader *et al.* (2023).

modulus and isotropic flexoelectricity, as seen in table 4.4. We remark that the piezoelectric tensor is neglected. The young modulus varies linearly, following the law

$$E = E_0 + A_i x_i \tag{4.9}$$

with $E_0 = 200\text{GPa}$ with the centre of the rectangle at $(0, 0)$.

ν	l[nm]	ϵ[nJ V^{-2} m^{-1}]	μ_L[μJ V^{-1} m^{-1}]	μ_T [μJ V^{-1} m^{-1}]	μ_S [μJ V^{-1} m^{-1}]
0.33	1	141	15	11	2

Table 4.4: Material properties of the material tensors described in Section 4.6. The piezoelectric tensor is zero.

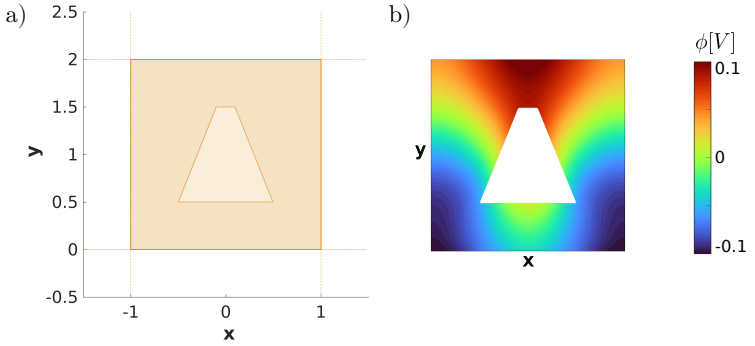

Figure 4.10: a) Geometrical model and b) electric potential distribution when macroscopic strain in the vertical direction is applied. Image adapted from Barceló-Mercader *et al.* (2023).

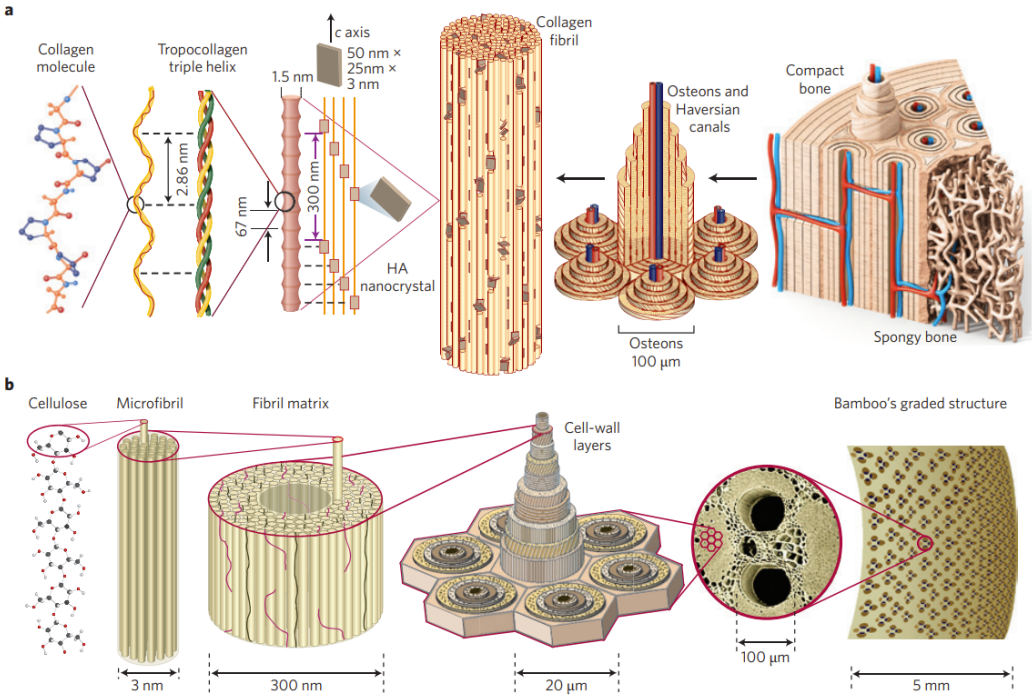

Figure 4.11: The hierarchical structure of bones (a) and bamboo (b) is shown. Both structures share the same pattern, with the outer layers being more compact and the inner layers more porous. Image taken from Wegst *et al.* (2015).

The first experiments show that, as we thought, these graded structures can mobilise a non negligible flexoelectric effect, as seen in Fig. 4.15 . The flexoelectric effect could be optimised by changing the gradient direction of the Young's modulus, as shown in the anisotropic plot in Fig. 4.15. These preliminary results create a path towards the creation of functional

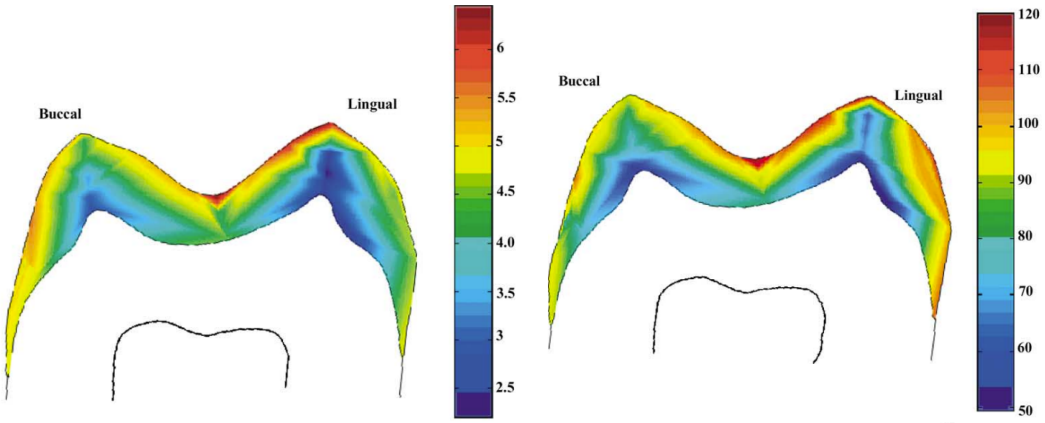

Figure 4.12: Enamel Hardness in GPa (left) and Young's modulus in GPa (right) for the mesial half of the maxillary determined by nanoindentation. Image taken from Cuy *et al.* (2002).

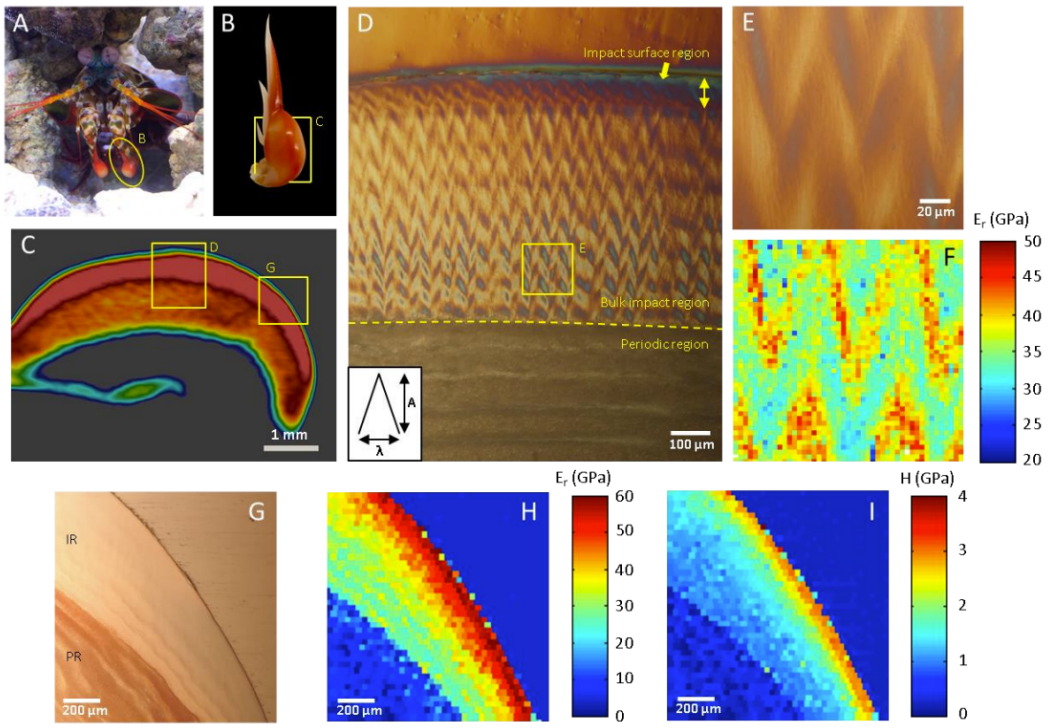

Figure 4.13: Optical microscopy and high-resolution nanoindentation of the impact region. Graded Young's modulus is seen in picture H. Image taken from Yaraghi *et al.* (2016).

flexoelectric-graded structure sensors or actuators.

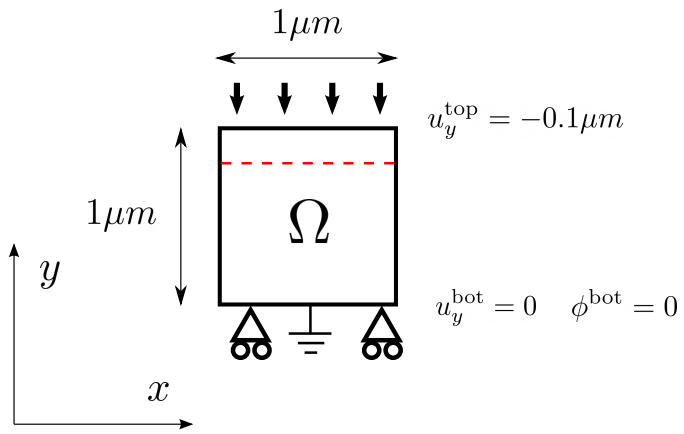

Figure 4.14: Sketch of the boundary conditions applied. Vertical displacement is fixed at the top and bottom sides; the bottom side is also grounded. The physical domain is a square of size $1\mu m$.

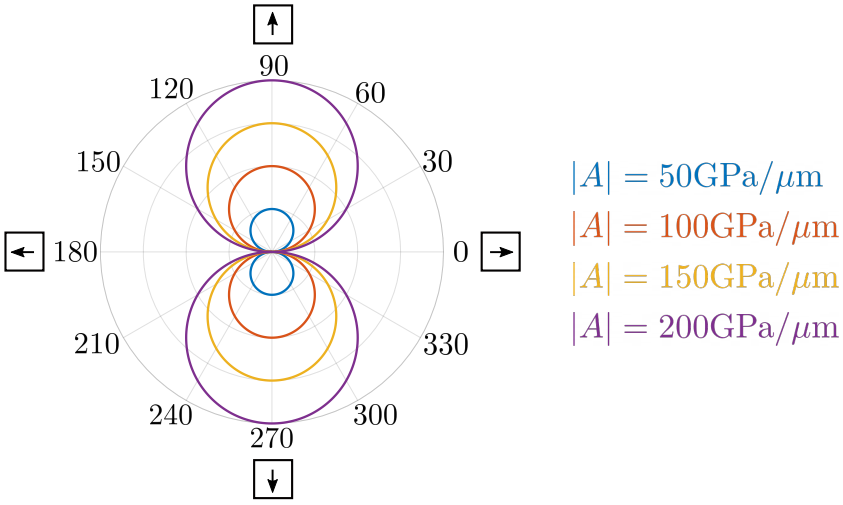

Figure 4.15: Polar plot of the electric potential at the top side considering different angles of graded young modulus. The young modulus at the centre of the structure is always constant E_0 = 200 GPa.

Chapter 5

Flexoelectric effect at domain walls and fracture in ferroelectrics

Ferroelectric materials are extensively used in a variety of sensor and actuator applications, where the coupling between mechanical and electrical fields are of primary interest. They develop microstructures with domains corresponding to different crystallographic variants. Ferroelectric domains are separated by domain walls which can be seen as topological defects in the parent crystal structure of the material. Due to the extremely small width of domain walls (nanometer scale dimensions), the change of polarisation direction (polarisation gradient) is noticeable at domain walls, highlighting them as a ground to search for field gradient effects. In particular, flexoelectricity should be significant at domain walls. Furthermore, Ferroelectric crystals are very brittle, with fracture toughness in the order of that of glass. Fracture and fatigue is the main cause of the short life of ferroelectric components. Fracture is also a source of large strain gradients, the largest that a material can sustain. The effect of flexoelectricity in fracture physics of piezoelectric materials has been studied theoretically (Abdollahi *et al.*, 2015a) and experimentally (Cordero-Edwards *et al.*, 2019), revelling interesting asymmetries as a consequence of the interplay of flexoelectricity and piezoelectricity. The interplay between ferroelectric domain microstructure evolution and fracture in ferroelectric single crystals and ceramics is very rich, and has been studied using a coupled phase-field model (Abdollahi and Arias, 2011a, 2012, Miehe *et al.*, 2010).

In this chapter, we study the manifestation of flexoelectricity in ferroelectric single crystals. Specifically, we study the role of flexoelectricity in the ferroelectric domain microstructure, and in the fracture response. The outline of the chapter is the following. We first motivate the study and introduce ferroelectric materials and describe a previously developed model for combined microstructure evolution and fracture. Using this model as a starting point, we incorporate flexoelectricity and study different relevant situations. We conclude and hint some directions of ongoing and future work.

5.1 Origin and phenomenology of ferroelectricity

Ferroelectricity is a property of certain dielectric materials exhibiting a spontaneous electric polarisation that can be reversed by the application of an external electric field, and also mechanically. The origin of ferroelectricity is tightly connected to its atomic or molecular structure. In ionic crystals, the emergence of a spontaneous dipole can be illustrated on the crystal lattice unit cell of a typical ferroelectric of the perovskite family, Barium Titanate, see Fig. 5.1.

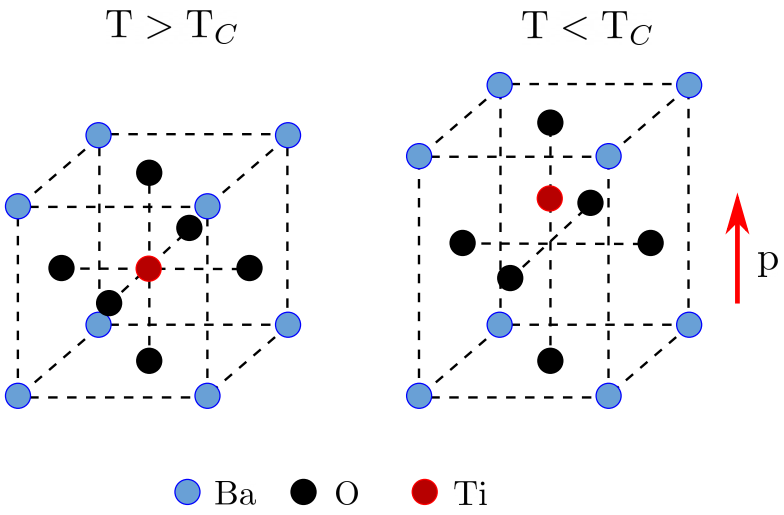

Figure 5.1: Unit cell of Barium titanate above and below the Curie Temperature.

Above the Curie temperature, a critical transition temperature, the unit cell is cubic with Barium cations located at the corners, Oxygen anions at the centre of the faces and the titanium cation at the centre of the cube. In this configuration, the unit cell is centrosymmetric and thus cannot sustain any electric dipole. This phase is termed paraelectric, and it is neither piezoelectric nor ferroelectric. Below a critical transition temperature, termed Curie temperature, the cubic crystalline structure becomes tetragonal and the Titanium cation moves with respect to the centre of the tetragon at the equilibrium state, thereby inducing a spontaneaous electric dipole. This polar tetragonal structure is piezoelectric, since small homogeneous deformations of the crystal lattice change the relative position of the ions and thus the associated dipole, and conversely an external electric field displaces cations in the direction of the electric field and anions in the opposite direction, thereby deforming the unit cell. The polar tetragonal structure can be oriented along six directions in space, giving rise to six energetically equivalent variants (see Fig. 5.2).

From a thermodynamical modelling perspective, these variants correspond to equal-energy wells in a non-convex multiple-well energetic landscape. Depending on the macroscopic mechanical and electric loads, some variants become more favourable than others, and the

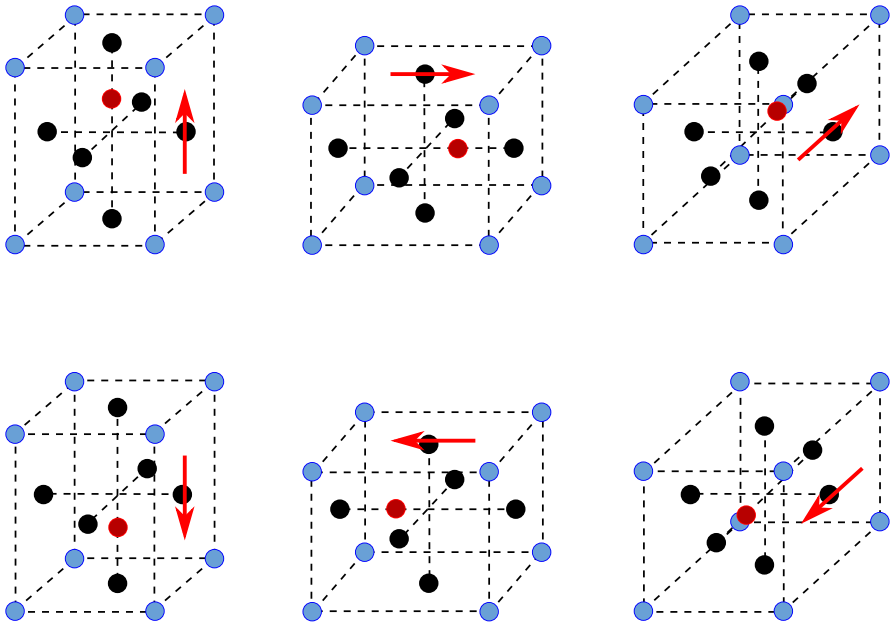

Figure 5.2: Six energetically equivalent tetragonal phases in Barium titanate.

material accommodates external loads by switching between variants. Consider a vertically polarised unit cell. When applying a small vertical stress or electric field, the potential energy tilts and the unit cell stretches or compresses but it is not enough to reverse polarisation, as illustrated in Fig. 5.3 (top). When applying a large vertical stress or electric field, the unit cell stretches. If the electric field is anti-parallel with respect to the electric dipole, the unit cell exhibits a 180° switching, as seen in Fig. 5.4 (middle). If the stress is anti-parallel with respect to the electric dipole, the unit cell exhibits a 90° switching, as seen in Fig. 5.4 (bottom). This is due to the transition from one well of the potential energy to another one that is more favourable.

This switching ability gives rise to the typical ferroelectric polarisation and butterfly loops (see Fig. 5.5) which characterise the ferroelectric phenomenology. The energetic barrier to transition between variants for the whole crystal at once is too high, and thus the material finds a lower energy path by nucleating switching at specific sites in the crystals, usually defects, and propagation the switch domain throughout the crystal. This gives rise to the typical ferroelectric microstructures with domains corresponding to different variants, see Fig. 5.6

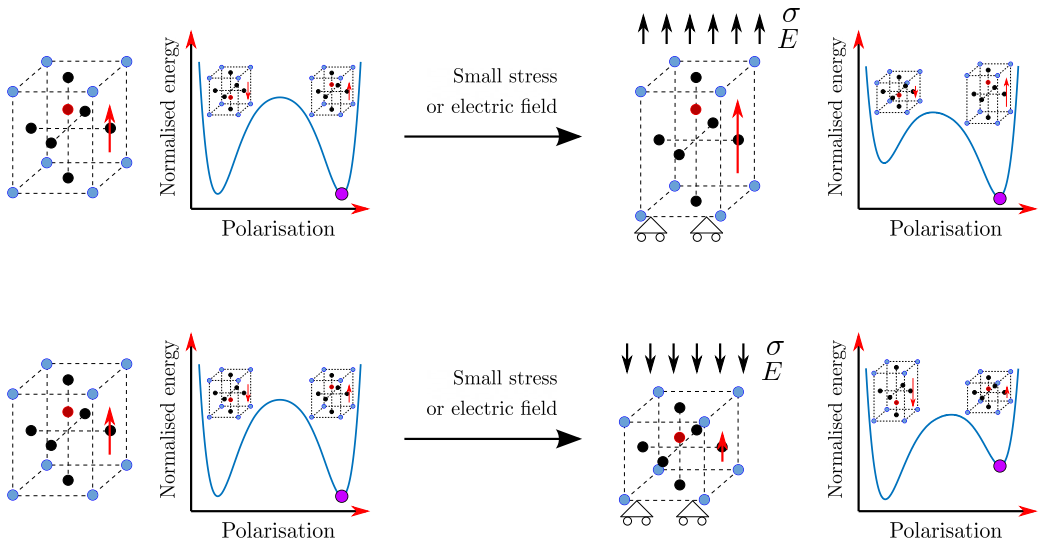

Figure 5.3: Schematic of the ferroelectric unit cell under small electric field or stress. At the top, the direction of the stress or the electric field is parallel to the electric dipole, producing a stretching of the unit cell. At the bottom, the direction of the stress or electric field is anti-parallel, producing a compression of the unit cell.

5.2 Phase-field modelling of fracture in ferroelectric materials

Phase-field models are ideally suited to deal with moving interface problems (Landau, 1937, Miehe *et al.*, 2010). Phase-field modelling has been used in a lot of applications such as fracture(Francfort and Marigo, 1998), image segmentation (Beneš *et al.*, 2004), multi-phase flows (Jacqmin, 1999), among others. In these models, the interface is assumed as a diffuse or smeared entity, as opposed to a sharp interface, and is described by a continuous phase-field variable defined over the whole domain, transitioning from a value (typically 0) at the interface to 1 everywhere else. This transition controls the "width" of the interface. The position of the interface results from an energy minimisation problem, where the energy cost of creating the interface competes with other physics of the problem. The variational structure allows us to naturally couple multiple physics, e.g. crack propagation and microstructure evolution in ferroelectrics (Abdollahi and Arias, 2011a, 2012). In quasi-static problems, the kinetics of the interface can then be modelled by a gradient flow of the electromechanical enthalpy, introducing an interface mobility parameter. In the case of fully dynamic problems, dynamic phase-field models have also been proposed in the literature (Borden *et al.*, 2012).

5.2.1 Phenomenological electromechanical enthalpy

The phenomenology of ferroelectrics as described in Section 5.1, is traditionally modelled by taking the polarisation vector as a continuous phase variable (Landau and Lifshitz, 2013). The

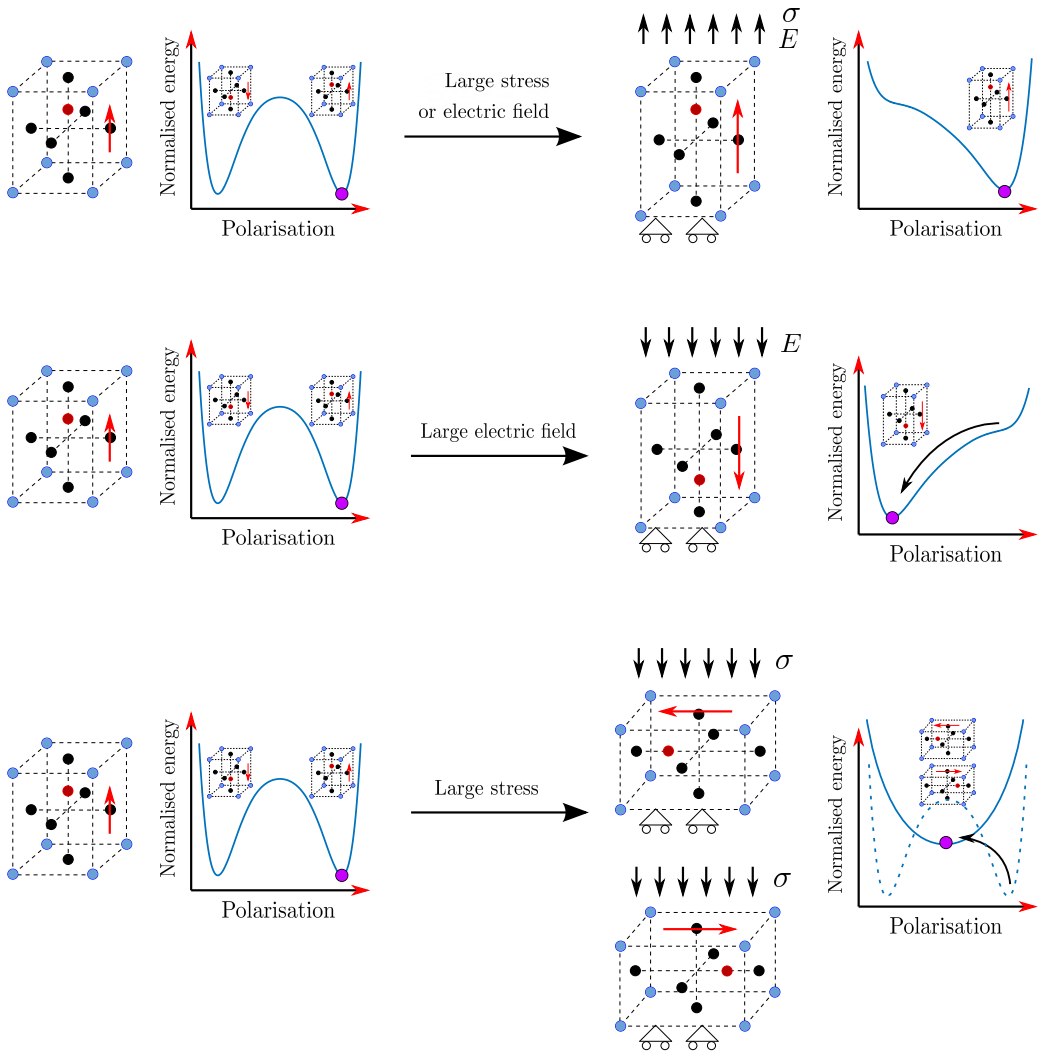

Figure 5.4: Schematic of the ferroelectric unit cell under large electric field or stress. At the top, the direction of the stress or the electric field is parallel to the electric dipole, producing a stretching of the unit cell. At the middle, the direction of the electric field is anti-parallel, producing a 180° switching. At the bottom, the direction of the stress is anti-parallel, producing a 90° switching. Note that left and right configurations are equally energetically favourable.

electromechanical enthalpy density of a ferroelectric material is (Abdollahi and Arias, 2011a, Zhang and Bhattacharya, 2005):

$$\mathcal{H}^{\text{ferro}}(\boldsymbol{u}, \boldsymbol{p}, \phi) = U(\boldsymbol{p}) + W(\boldsymbol{u}, \boldsymbol{p}) + \chi(\boldsymbol{p}) - \frac{\varepsilon_0}{2}\phi_{,i}\phi_{,i} - \phi_{,i}p_i \tag{5.1}$$

where $\boldsymbol{u}$, $\boldsymbol{p}$ and ϕ are the displacement, electric polarisation and electric potential, respectively. The functions U, W and χ are derived in Devonshire (1951, 1949) for a plane polarisation and

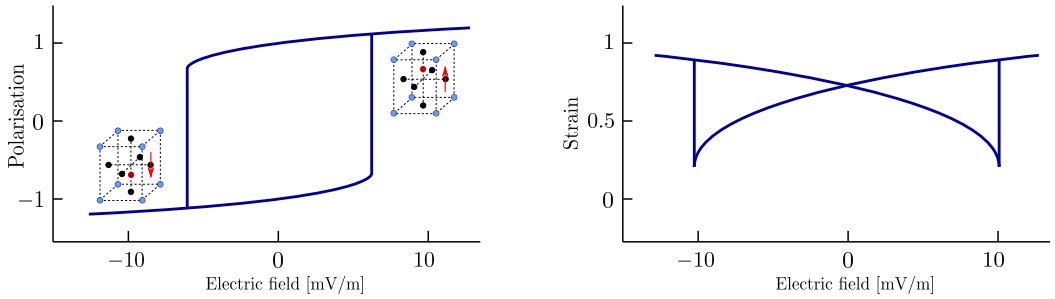

Figure 5.5: Hysteresis and butterfly loops for a ferroelectric material under an external electric field. Due to the external electric field the unit cell suffers from a 180° switching between up and down polarisation

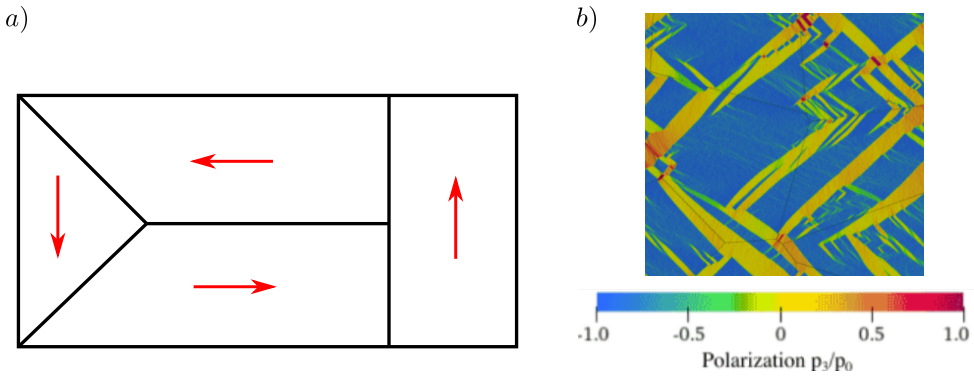

Figure 5.6: Ferroelectric microstructure. Different domains are separated by domain walls. a) Two types of domain walls can be produced inside ferroelectric materials: 90° and 180° domain walls separating orthogonal and anti-parallel phases, respectively. b) Microstucture in PZT showing 180° and 90° domain walls. Image partially extracted from (Indergand *et al.*, 2020)

plane strain state as

$$U(\boldsymbol{p}) = \frac{a_0}{2}\left(p_{1,1}^2 + p_{1,2}^2 + p_{2,1}^2 + p_{2,2}^2\right), \tag{5.2}$$

$$\begin{aligned} W(\boldsymbol{u},\boldsymbol{p}) = &-\frac{b_1}{2}\left(\varepsilon_{11}p_1^2 + \varepsilon_{22}p_2^2\right) - \frac{b_2}{2}\left(\varepsilon_{11}p_2^2 + \varepsilon_{22}p_1^2\right) - b_3\left(\varepsilon_{21} + \varepsilon_{12}\right)p_1p_2 \\ &+ \frac{c_1}{2}\left(\varepsilon_{11}^2 + \varepsilon_{22}^2\right) + c_2\varepsilon_{11}\varepsilon_{22} + \frac{c_3}{2}\left(\varepsilon_{12}^2 + \varepsilon_{21}^2\right), \end{aligned} \tag{5.3}$$

$$\chi(\boldsymbol{p}) = \frac{a_1}{2}\left(p_1^2 + p_2^2\right) + \frac{a_2}{4}\left(p_1^4 + p_2^4\right) + \frac{a_3}{2}p_1^2p_2^2 + \frac{a_4}{6}\left(p_1^6 + p_2^6\right) + \frac{a_5}{4}\left(p_1^4p_2^4\right). \tag{5.4}$$

The terms $W + \chi$ correspond to the Landau-Ginzburg energy density, while U is the domain wall energy, and depends on the scaling parameter a_0. The constants b_i are the constant of the electro-mechanical coupling, and c_i are the elastic constants. Dimensionless variables are selected as $x_i' = x_i\sqrt{c_0/a_0}/p_0$, $p_i' = p_i/p_0$, $\varepsilon_i' = \varepsilon_i c_0/p_0^2$, $\phi' = \phi/\sqrt{a_0 c_0}$, $a_1' = a_1 p_0^2/c_0$, $a_2' = a_2 p_0^4/c_0$, $a_3' = a_3 p_0^4/c_0$, $a_4' = a_4 p_0^6/c_0$, $a_5' = a_5 p_0^8/c_0$, $b_i' = b_i p_0^2/c_0$ and $c_i' = c_i/c_0$. The normalisation constants are chosen to fit the behaviour of single crystals of barium titanate ($BaTiO_3$) at room temperature, taking $c_0 = 1$ GPa, a value for the spontaneous polarisation of $p_0 = 0.26$ C/m^2, the resulting relative spontaneous strains are $\varepsilon_a = -0.44\%$ along a-axis and $\varepsilon_c = 0.65\%$ along c-axis (Wang *et al.*, 2007, Zhang and Bhattacharya, 2005). The domain wall scaling parameter is set to $a_0 = 3.710^{-9}$ Vm^3/C which gives a domain wall width of 0.5 nanometers for the normalised unit length $x' = 1$. The normalised parameter values can be seen in Table 5.1

a_0'	a_1'	a_2'	a_3'	a_4'	a_5'	b_1'	b_2'	b_3'	c_1'	c_2'	c_3'
1	−0.007	−0.009	0.018	0.0261	5	1.4282	−0.185	0.8066	185	111	74

Table 5.1: Normalised material parameters for ferroelectric phase-field

The parameters of the phenomenological model a_i, b_i, c_i are obtained from characterisation experiments (Wang *et al.*, 2007, Zhang and Bhattacharya, 2005). The stress can be computed as

$$\sigma_{11} = \frac{\partial \mathcal{H}^{\text{ferro}}}{\partial \varepsilon_{11}} = c_1\varepsilon_{11} + c_2\varepsilon_{22} - \frac{b_1}{2}p_1^2 - \frac{b_2}{2}p_2^2, \tag{5.5a}$$

$$\sigma_{22} = \frac{\partial \mathcal{H}^{\text{ferro}}}{\partial \varepsilon_{22}} = c_1\varepsilon_{22} + c_2\varepsilon_{11} - \frac{b_1}{2}p_2^2 - \frac{b_2}{2}p_1^2, \tag{5.5b}$$

$$\sigma_{12} = \frac{\partial \mathcal{H}^{\text{ferro}}}{\partial \varepsilon_{12}} = c_3\varepsilon_{12} - b_3 p_1 p_2. \tag{5.5c}$$

Taking into account a stress-free state, that means $\sigma_{11} = \sigma_{22} = \sigma_{12} = 0$, the spontaneous strain is

$$\varepsilon_{11}^0 = \frac{(c_1 b_1 - c_2 b_2)p_1^2 + (c_1 b_2 - c_2 b_1)p_2^2}{2(c_1^2 - c_2^2)}, \tag{5.6a}$$

$$\varepsilon_{22}^0 = \frac{(c_1 b_2 - c_2 b_1)p_1^2 + (c_1 b_1 - c_2 b_2)p_2^2}{2(c_1^2 - c_2^2)}, \tag{5.6b}$$

$$\varepsilon_{12}^0 = \frac{b_3 p_1 p_2}{c_3}. \tag{5.6c}$$

The normalised Landau-Devonshire energy is plotted in the Fig. 5.7 using the spontaneous strain derived in Eq. (5.6) and p_1' and p_2' as primal variables, considering a crystal axis oriented with respect to x_3. The four minima in Fig. 5.7 correspond to the four variants of the tetragonal phase in 2D with normalised polarisation.

In the absence of body loads and volume charges, the total enthalpy of the system for a

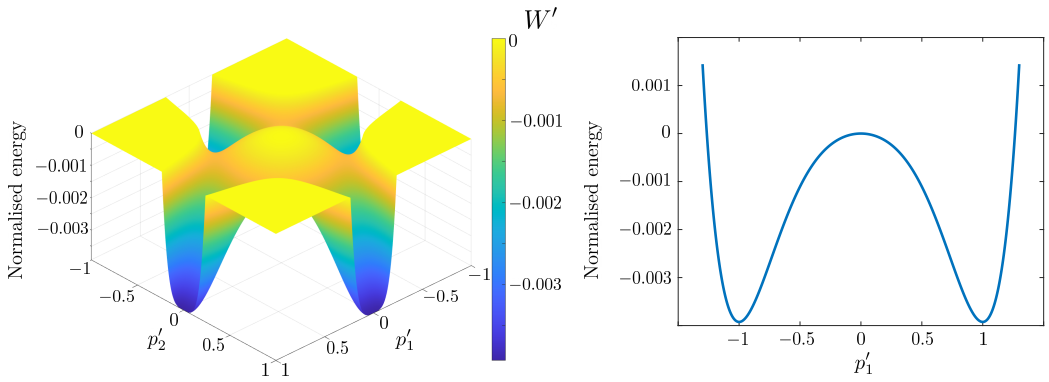

Figure 5.7: Normalised Landau-Devonshire energy for the free stress configuration. (left) 3D normalised Landau-Devonshire energy. Four minima are seen whose coordinates are: $(0, 1)$, $(0, -1)$, $(1, 0)$ and $(-1, 0)$. The plot is truncated for energy values greater than 0 for convenience. (right) 2D normalised Landay-Devonshire energy considering $p_2 = 0$. Two minima are seen whose coordinates: are $p_1 = 1$ and $p_1 = -1$.

ferroelectric body Ω is

$$E(\boldsymbol{u}, \boldsymbol{P}, \phi) = \int_{\Omega} \mathcal{H}^{\text{ferro}}(\boldsymbol{u}, \boldsymbol{P}, \phi)\, \mathrm{d}\Omega - \int_{\Gamma_t} t_i u_i \, \mathrm{d}S + \int_{\Gamma_w} w\phi \, \mathrm{d}S, \tag{5.7}$$

where t_i and w are the traction and surface charge density, respectively.

5.2.2 Regularised fracture energy

We consider the variational regularised model of Griffith's fracture (Ambrosio and Tortorelli, 1990, Bourdin *et al.*, 2000, Francfort and Marigo, 1998). This model allows naturally for crack nucleation, interaction between multiple cracks and, branching. It smears the crack in contrast with some other models like cohesive methods (Camacho and Ortiz, 1996, Xu and Needleman, 1994), sharp methods as extended finite element method (Moës *et al.*, 1999), and the strong discontinuity approach (Oliver *et al.*, 2002).

The total energy of an elastic body made of brittle material occupying a region Ω can be written in terms of the scalar field v as

$$E(\boldsymbol{u}, v) = \int_{\Omega} (v^2 + \eta) F(\boldsymbol{u})\, \mathrm{d}\Omega + G_c \int_{\Omega} \left[\frac{(1 - v)^2}{4\kappa} + \kappa v_{,i} v_{,i} \right] \mathrm{d}\Omega - \int_{\Gamma} t_i u_i \, \mathrm{d}S, \tag{5.8}$$

where F is the elastic energy, G_c is the critical energy release rate, and κ is a positive regularisation constant controlling the size of the fracture zone. The residual stiffness η avoids singularities in the resulting stiffness matrix upon discretisation corresponding to entries from elements located in the fully fractured region of the domain. It has been shown mathematically using Γ-convergence that the regularised model in Eq. (5.8) tends in the limit of $\kappa \longrightarrow 0$ to Gif-

fith's model of brittle fracture, i.e. a traction-free sharp-crack model (Ambrosio and Tortorelli, 1990, Francfort and Marigo, 1998). The traction-free crack face conditions are

$$\sigma^{+} \cdot \boldsymbol{n} = \sigma^{-} \cdot \boldsymbol{n} = 0, \tag{5.9}$$

where σ^{+} and σ^{-} mean the top and bottom stress on the sharp-crack faces. The damage field v takes value $v = 1$ for the unbroken state of the material and value $v = 0$ for the broken one.

Eq. 5.8 sets up a competition by storing energy in the bulk and using it to create new cracks, which can be seen as the bulk elastic energy stored, and the second term, which is the surface energy of the crack. When the elastic energy stored reaches a certain value determined by G_c, the crack initiates, and the energy of the bulk is transferred to the energy of crack propagation. The width of the crack is governed by the regularisation parameter κ.

Bourdin *et al.* (2008) stated that the profile of the phase-field variable v, for a given value of the regularisation parameter κ, on a line orthogonal to the crack passing through x with a distance function $d(x)$ is

$$v_\kappa(x) = \begin{cases} 0 & \text{if } d(x) \le \alpha \\ 1 - e^{(d(x)-\alpha)/2\kappa} & \text{otherwise} \end{cases} \tag{5.10}$$

where 2α indicates the fully fracture region where $v = 0$. This profile is seen in Fig. 5.8 in contrast to sharp-crack models, where the crack faces are geometrically defined in the computational model.

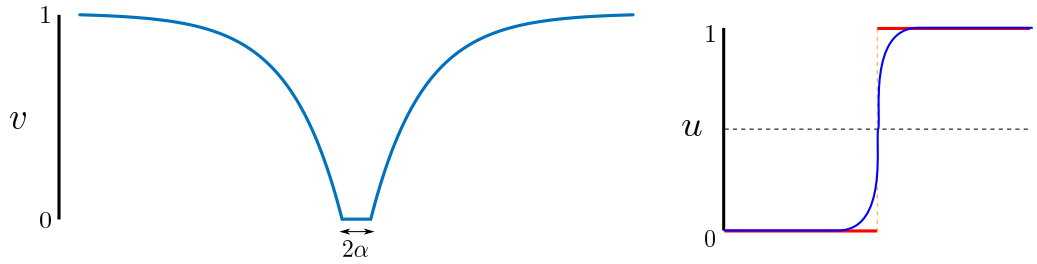

Figure 5.8: Smeared crack using the profile in Eq. (5.10) and displacement for sharp-crack models (red) and phase-field models (blue).

5.2.3 Regularised electromechanical enthalpy for a fractured ferroelectric

Following Abdollahi and Arias (2012), the electro-mechanical enthalpy for fracture in ferroelectrics is (Abdollahi and Arias, 2011a)

$$E(\boldsymbol{u},\boldsymbol{p},\phi,v) = \int_\Omega \left[(v^2+\eta)\left(U(\boldsymbol{p}) + W(\boldsymbol{u},\boldsymbol{p})\right) + \chi(\boldsymbol{p}) - \frac{\epsilon_0}{2}\phi_{,i}\phi_{,i} - \phi_{,i}p_i\right] \mathrm{d}\Omega + \tag{5.11}$$

$$G_c \int_\Omega \left[\frac{(1-v)^2}{4\kappa} + \kappa v_{,i} v_{,i}\right] \mathrm{d}\Omega - \int_{\Gamma_t} t_i u_i \,\mathrm{d}S + \int_{\Gamma_w} w\phi \,\mathrm{d}S. \tag{5.12}$$

In sharp-crack models for electromechanical materials, crack face conditions have to be defined, corresponding to different physical conditions. Traditionally, cracks are assumed to be mechanically traction-free, or cohesive. Electrically, they can be permeable, impermeable, or semi-permeable. In fact, for a well-posed problem, cracks face conditions should be energetically consistent. In phase-field models of fracture, where cracks are not boundaries of the computational domain but rather features of the solution within the domain, and hence the different sharp-crack conditions have to be modelled in the phase-field partial differential equations (Abdollahi and Arias, 2012). As shown by Abdollahi and Arias (2012), the electromechanical enthalpy in Eq. (5.11) encodes traction-free and electrically permeable crack face condition. In the limiting sharp-crack model to which this model converges, these conditions mean: the electric potential and the normal component of the electric displacement are continuous across the crack,

$$\phi^+ = \phi^- \tag{5.13a}$$

$$\boldsymbol{D}^+ \cdot \boldsymbol{n} = \boldsymbol{D}^- \cdot \boldsymbol{n}. \tag{5.13b}$$

free-polarisation along the crack which means that the polarisation is unaffected by the presence of the crack,

$$\nabla\boldsymbol{p}^+ \cdot \boldsymbol{n} = \nabla\boldsymbol{p}^- \cdot \boldsymbol{n} = 0. \tag{5.14}$$

and the traction-free,

$$\sigma^+ \cdot \boldsymbol{n} = \sigma^- \cdot \boldsymbol{n} = 0, \tag{5.15}$$

Other electro-mechanical conditions can be the electrical impermeable crack model which assumes that the crack face is treated as a charge-free surface:

$$\boldsymbol{D}^+ \cdot \boldsymbol{n} = \boldsymbol{D}^- \cdot \boldsymbol{n} = 0 \tag{5.16}$$

or the zero-polarisation which assumes that the polarisation vanishes in the crack gap and

also it is continuous at the interface:

$$\boldsymbol{p}^{+} = \boldsymbol{p}^{-} = 0. \tag{5.17}$$

It is known that the fracture behaviour strongly depends on the electromechanical crack-face conditions (Abdollahi and Arias, 2012). Here, only traction-free, permeable, and polarisation-free cracks are considered. Consideration of other crack face conditions is left for future studies.

5.2.4 Electromechanical enthalpy of a ferroelectric and flexoelectric solid

As done in previous chapters, flexoelectricity is incorporated into the model by adding the flexoelectric coupling term in the enthalpy. The lifshitz-invariant enthalpy density of flexoelectricity, similar to the one presented in Ahluwalia *et al.* (2014), is

$$\begin{aligned} f(\boldsymbol{u},\boldsymbol{p}) = &-\frac{f_L}{2}\left(p_1\varepsilon_{11,1} + p_2\varepsilon_{22,2} - \varepsilon_{11}p_{1,1} - \varepsilon_{22}p_{2,2}\right) \\ &-\frac{f_T}{2}\left(p_1\varepsilon_{22,1} + p_2\varepsilon_{11,2} - \varepsilon_{11}p_{2,2} - \varepsilon_{22}p_{1,1}\right) \\ &-\frac{f_S}{2}\left(p_1(\varepsilon_{12,2} + \varepsilon_{21,2}) + p_2(\varepsilon_{12,1} + \varepsilon_{21,1}) - (\varepsilon_{12} + \varepsilon_{21})(p_{2,1} + p_{1,2})\right) \end{aligned} \tag{5.18}$$

and the total enthalpy density of a ferroelectric taking into account flexoelectricity is

$$\mathcal{H}^{\text{ferro+flexo}}(\boldsymbol{u},\boldsymbol{p},\phi) = U(\boldsymbol{p}) + W(\boldsymbol{u},\boldsymbol{p}) + \chi(\boldsymbol{p}) + f(\boldsymbol{u},\boldsymbol{p}) - \frac{\varepsilon_0}{2}\phi_{,i}\phi_{,i} - \phi_{,i}p_i \tag{5.19}$$

In the absence of body loads and volume charges and surface contributions, the total enthalpy of the system for a ferroelectric and flexoelectric body Ω is

$$E(\boldsymbol{u},\boldsymbol{P},\phi) = \int_\Omega \mathcal{H}^{\text{ferro+flexo}}(\boldsymbol{u},\boldsymbol{P},\phi)\,\mathrm{d}\Omega - \int_{\Gamma_t} t_i u_i\,\mathrm{d}S + \int_{\Gamma_w} w\phi\,\mathrm{d}S - \int_{\Gamma_r} r_i\partial^n u_i\,\mathrm{d}S - \sum_{C_j} j_i u_i, \tag{5.20}$$

where r and j are the double traction and line force respectively. The flexoelectric coefficients are converted into dimensionless coefficients following:

$$f_L' = f_L\frac{1}{\sqrt{a_0 c_0}}, \qquad f_T' = f_T\frac{1}{\sqrt{a_0 c_0}} \qquad \text{and} \qquad f_S' = f_S\frac{1}{\sqrt{a_0 c_0}}. \tag{5.21}$$

5.2.5 Electromechanical enthalpy of a fractured ferroelectric and flexoelectric solid

In the spirit of section 5.2.3, and following Abdollahi *et al.* (2015a), the phase-field of fracture in ferroelectrics accounting for flexoelectricity is constructed by adding the flexoelectric

contribution to the enthalpy density in Eq. (5.11). In order to encode traction-free, polarisation-free and surface-charge-free sharp-crack face conditions into the phase-field framework, the flexoelectric contribution needs to be multiplied by the degradation function (Abdollahi *et al.*, 2015a). The electro-mechanical enthalpy of fracture in ferroelectrics considering traction-free, electrically permeable and free-polarisation of the crack is

$$E(\boldsymbol{u},\boldsymbol{p},\phi,v) = \int_\Omega \left[(v^2+\eta)\left(U(\boldsymbol{p}+W(\boldsymbol{u},\boldsymbol{p})+f(\boldsymbol{u},\boldsymbol{p})\right)+\chi(\boldsymbol{p})-\frac{\epsilon_0}{2}\phi_{,i}\phi_{,i}-\phi_{,i}p_i\right]\,\mathrm{d}\Omega+$$
$$G_c\int_\Omega\left[\frac{(1-v)^2}{4\kappa}+\kappa v_{,i}v_{,i}\right]\,\mathrm{d}\Omega-\int_{\Gamma_t}t_iu_i\,\mathrm{d}S+\int_{\Gamma_w}w\phi\,\mathrm{d}S-\int_{\Gamma_r}r_i\partial^n u_i\,\mathrm{d}S-\sum_{C_j}j_iu_i. \tag{5.22}$$

5.2.6 Governing equations of quasi-static phase-field model

We proposed a quasi-static approach for all systems presented in previous subsections. The evolution of the system is a gradient flow of the energy with respect to the polarisation, with the kinetics controlled by a mobility parameter $1/\mu$, and assuming that the displacement and the electric potential attain equilibrium instantly:

$$\mu\int_\Omega\frac{\partial p_i}{\partial t}\delta p_i\,\mathrm{d}\Omega=-\delta E(\boldsymbol{u},\boldsymbol{P},\phi,v;\delta\boldsymbol{P}), \tag{5.23a}$$
$$0=\delta E(\boldsymbol{u},\boldsymbol{P},\phi,v;\delta\boldsymbol{u}), \tag{5.23b}$$
$$0=\delta E(\boldsymbol{u},\boldsymbol{P},\phi,v;\delta\phi), \tag{5.23c}$$
$$0=\delta E(\boldsymbol{u},\boldsymbol{P},\phi,v;\delta v). \tag{5.23d}$$

The mobility parameter is difficult to quantify experimentally. Frazier and Kochmann (2017), Kannan *et al.* (2022) found that the mobility parameter can be estimated measuring the energy dissipated by the domain wall motion. Abdollahi and Arias (2011a) proposed a similar set of governing equations but having a gradient flow with respect to the damage also. We consider that the mobility of the damage field is so fast that the equilibrium is attained instantaneously as Muixí *et al.* (2021).

Note that not all of the systems described in this section present all the state variables in Eq. (5.23). For the numerical examples presented next, in each case we consider the relevant governing equations in Eq. (5.23).

5.3 Solution methods and validation tests

The quasi-static coupled system of governing partial differential equations stated in Eq. (5.23) is solved using a staggered iterative scheme. Both tools are validated using two different setups. The first one is a fracture splitting problem statement proposed by Ambati *et al.* (2015). The second one is the fracture in ferroelectrics proposed by Abdollahi and Arias (2011a). We use the body-fitted b-spline method explained in Section 3.1.2 for all simulatons in this chapter.

5.3.1 Staggered scheme for the quasi-static phase-field model

The solution of the discretised version of Eq. (5.23) is obtained by solving a non-linear problem. The monolithic schemes solve all variables simultaneously, and they are very fast but with high computation cost (non-linear system). We refer the reader to Liu *et al.* (2016b) to see a monolithic scheme for fracture. Instead of that, we propose the following four-step method:

For each time-step we repeat until convergence

- Compute polarisation in Eq. (5.23a), considering displacement, electric potential and damage field fixed. We use forward Euler for time integration.
- Compute displacement in Eq. (5.23b), considering polarisation, electric potential and damage field fixed.
- Compute electric potential in Eq. (5.23c), considering polarisation, displacement and damage field fixed.
- Compute damage field in Eq. (5.23d), considering polarisation, displacement and damage field fixed.

Convergence is achieved if $|\boldsymbol{p}_m - \boldsymbol{p}_{m-1}| < \delta_p$ and $|v_m - v_{m-1}| < \delta_v$ for a given δ_p and δ_v. We take $\delta_p = \delta_v = 0.001$ in our simulations. The staggered scheme solves four linear equations iteratively until equilibrium, which makes it a slower method compared to monolithic schemes.

5.3.2 Fracture splitting

For the first validation example, we use the problem statement by Ambati *et al.* (2015) for a purely elastic material. Thus, the electromechanical couplings, both ferroelectricity and flexoelectricity are set to zero. The body is a square of size 1×1 in dimensionless units. A precrack is assumed, as shown in Fig. 5.9. Horizontal displacements are prescribed on the top and bottom faces. 300 loading time steps t are used and the prescribed displacement is applied incrementally, following $u_D^t = 0.001t$. After 30% loading steps, the crack splits its horizontal trajectory as shown in Fig. 5.9, in qualitative agreement with Ambati *et al.* (2015). The material parameters are extracted from Ambati *et al.* (2015)

5.3.3 Fracture in ferroelectrics

To validate the implementation of the coupled fracture and microstructure evolution in ferroelectric single crystals, we compare our results with those by (Abdollahi and Arias, 2011a).

The problem setup is shown in Fig. 5.10 (left). A rectangular domain of 100×100 nm of a single-crystalline ferroelectric is considered, without flexoelectricity, i.e. $f \equiv 0$. The material parameters used are in Table 5.1. To mobilize model fracture, monotonically increasing opening vertical displacements are prescribed on the top and bottom sides, as well as on the left side to favour crack initiation from the left middle section of the boundary. The vertical right side is

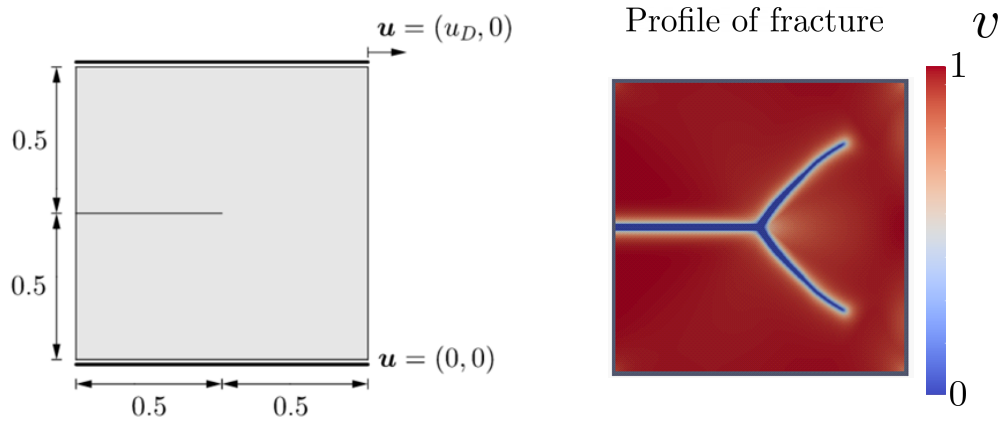

Figure 5.9: Problem statement and final crack distribution for split fracture. A split of the fracture is seen by applying a mechanical shear displacement to the body. The problem statement is taken from Ambati *et al.* (2015).

set to be free of tractions. The top and bottom sides are assumed to be free of surface charges and the left and right faces are grounded.

The initial polarisation of the sample is taken as right polarisation. The boundary conditions applied can be seen in Fig. 5.10. After some time steps, a crack is initiated in the middle of the sample. This crack propagates along the horizontal. The stress concentrations at the crack tip lead to localized domain switching which propagates throughout the domain, leading to the formation of the so-called domain twins, see Fig. 5.10 (right). The evolving ferroelectric domain size depend on the lengthscales of the problem, i.e. the sample size, the domain wall size a_0, creating up and down polarisations called twins. The final distribution of the polarization can be seen in Fig. 5.10, which is in qualitative agreement with the results in Fig. 5 in Abdollahi and Arias (2011a).

Finally, the evolution of the normalised surface energy has been stored and shown in Fig. 5.11. It shows the evolution of the surface energy for a single-phase crystal (no polarisation) and multi-phase crystal, considering a traction-free, permeable and free-polarisation crack. It is in agreement with the results in Fig. 6 in Abdollahi and Arias (2011a)

5.4 Eploration of flexoelectric effect in domain microstructure

We present next a set of numerical experiments to explore the effect of flexoelectricity on the ferroelectric domain microstructure formation and evolution. We consider a rectangular ferroelectric and flexoelectric sample of dimensions 80×80nm with random initial polarisation. The material parameters are given in Table 5.1, and different values for the flexoelectric coefficients are considered. Homogeneous Neumann boundary conditions have been considered for the

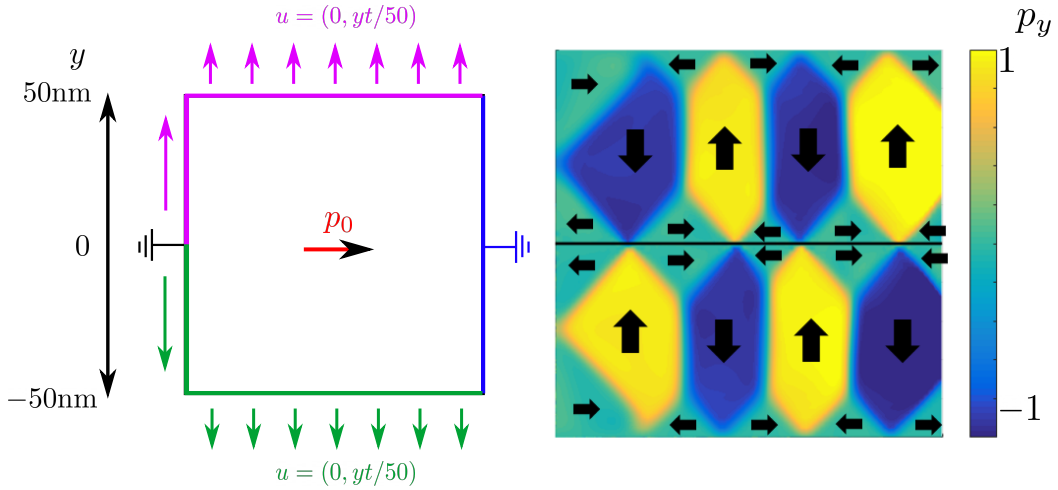

Figure 5.10: Example of a fracture in ferroelectrics. Left) A rectangular body of dimensions 100 × 100 nm, prescribed displacement is applied in the top, bottom and left faces, while the left and right sides are grounded. The sample is horizontally polarized initially. The variable t indicates the pseudo-time. Right) Final distribution of polarisation. The colourmap indicates the magnitude of the vertical polarisation. Regions with zero vertical polarisation correspond to horizontally polarised domains. The sign of this horizontal polarization is taken from plots of horizontal polarisation (not shown). Black arrows indicating the net domain polarization are added to the figure for illustration purpose..

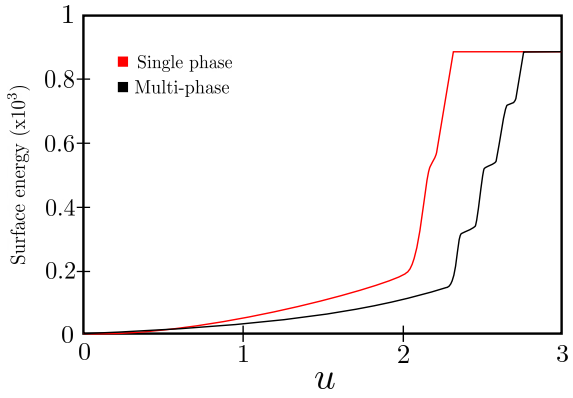

Figure 5.11: Evolution of the normalised surface energy for a single-phase crystal (no polarisation) and a multi-phase crystal.

surface charge, the double traction and the line force and the displacement of all boundaries have been set to zero. In Fig. 5.12, we report the final polarisation distribution on the sample after 50000 load increments, for four different combinations of longitudinal, transverse and shear flexocoupling coefficients, f_L, f_T and f_S. Fig. 5.12a corresponds to the case whithout

flexoelectricity. In this case, the final configuration is, in most cases (depending on the random initial configuration), a homogeneous polarisation in the whole body or at most, one domain wall close to the boundary, as seen in Fig. 5.12 a).

The other three configurations are very similar. For simplicity, as a first approach we have analysed the effect of each component of the cubic flexocoupling tensor independently, setting the others to zero. Different values in the 0-15V range have been considered for the non-vanishing flexocoupling coefficient. For all three flexocoupling coefficients, increasing the value of the flexocoupling, leads to more domains. Indeed, flexoelectricity seems to favour the creation of domain walls. This effect can be seen in Fig. 5.12b-d for longitudinal, transversal and shear coefficient values of 5V, 5V and 3V, respectively.

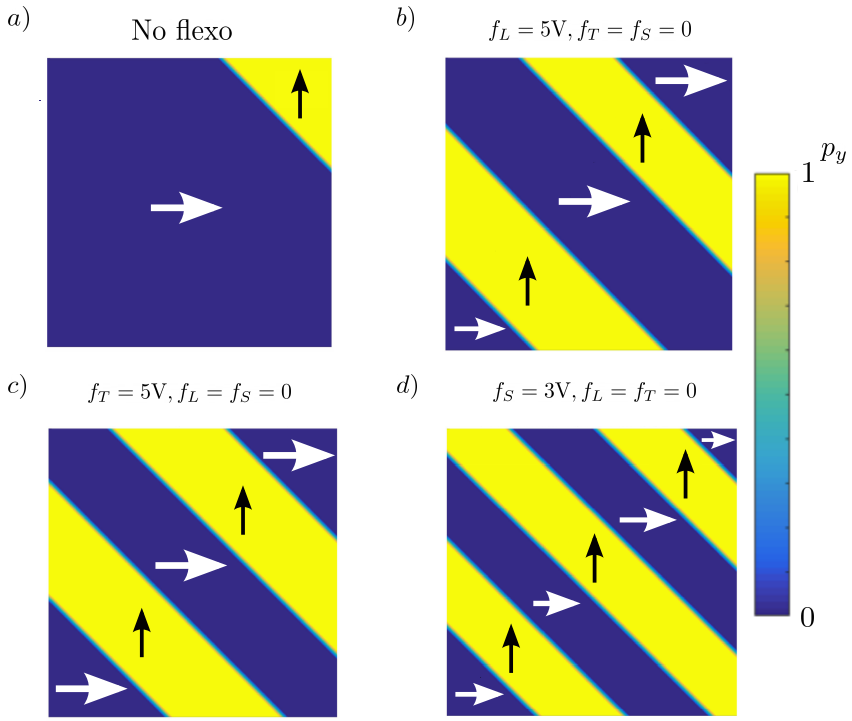

Figure 5.12: Magnitude of vertical polarisation after 50000-time steps for: a) no flexoelectricity, b) only longitudinal flexoelectricity with a value equal to 5V, c) only transversal flexoelectricity with a value equal to 5V and d) only shear flexoelectricity with a value equal to 3V. Regions with zero vertical polarisation correspond to horizontally polarised domains. The sign of this horizontal polarization is taken from plots of horizontal polarisation (not shown). Black Arrows indicating the net domain polarization are added to the figure for illustration purposes.

For large flexocoupling values, the number of domains increases dramatically, as shown in Fig. 5.13. Interestingly, a similar behaviour was observed by Ahluwalia *et al.* (2014) and was attributed to a modulation effect when considering equilibrium dynamics of the displacement.

In the present simulations the displacement is quasi-static, and thus the origin of the observed response is different. The following possible explanation is currently under investigation and needs yet to be confirmed.

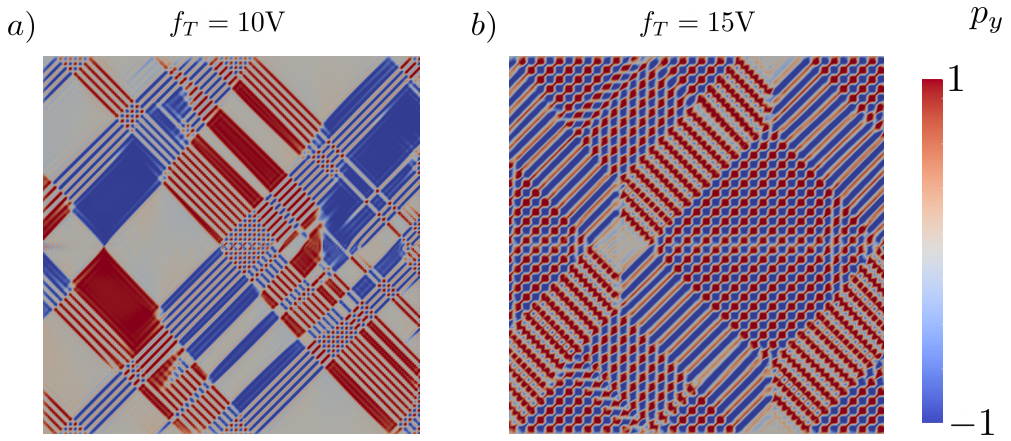

Figure 5.13: Polarisation in ferroelectrics after 50000-time steps with transversal flexoelectricity values of 10V and 15V, respectively.

The ferroelectric enthalpy density in Eq. (5.1) has a convex term concerning the gradient of polarisation, which means that the stress-free solution that minimises the energy also has a gradient of polarisation equal to zero. When adding the flexoelectric terms to the energy in Eq. (5.19), the energy can no longer be convex concerning the polarisation, giving an unstable solution to the system or an unbounded solution with respect to the gradient of polarisation. We derive next the necessary conditions on the flexoelectric parameters to correctly solve the minimisation problem.

Following the derivation in Section 5.2.1, we derived the stress as

$$\sigma_{11} = \frac{\partial \mathcal{H}}{\partial \varepsilon_{11}} = c_1\varepsilon_{11} + c_2\varepsilon_{22} - \frac{b_1}{2}p_1^2 - \frac{b_2}{2}p_2^2 + f_L p_{1,1} + f_T p_{2,2}, \tag{5.24a}$$

$$\sigma_{22} = \frac{\partial \mathcal{H}}{\partial \varepsilon_{22}} = c_1\varepsilon_{22} + c_2\varepsilon_{11} - \frac{b_1}{2}p_2^2 - \frac{b_2}{2}p_1^2 + f_L p_{2,2} + f_T p_{1,1}, \tag{5.24b}$$

$$\sigma_{12} = \frac{\partial \mathcal{H}}{\partial \varepsilon_{12}} = c_3\varepsilon_{12} - b_3 p_1 p_2 + f_S(p_{1,2} + p_{2,1}). \tag{5.24c}$$

Note that we have considered only the converse term of the flexoelectricity because we can use the divergence theorem in the direct part without loss of generality to convert it into the converse one (Codony, 2021).

Considering a stress-free state, the spontaneous strain is

$$\varepsilon^0_{11} = \frac{(c_1 b_1 - c_2 b_2)p_1^2 + (c_1 b_2 - c_2 b_1)p_2^2 + 2(f_T c_2 - f_L c_1)p_{1,1} + 2(f_L c_2 - f_T c_1)p_{2,2}}{2(c_1^2 - c_2^2)}, \tag{5.25a}$$

$$\varepsilon^0_{22} = \frac{(c_1 b_2 - c_2 b_1)p_1^2 + (c_1 b_1 - c_2 b_2)p_2^2 + 2(f_T c_1 - f_L c_2)p_{1,1} + 2(f_L c_1 - f_T c_2)p_{2,2}}{2(c_1^2 - c_2^2)}, \tag{5.25b}$$

$$\varepsilon^0_{12} = \frac{b_3 p_1 p_2 - f_S(p_{1,2} + p_{2,1})}{c_3}. \tag{5.25c}$$

Now, we consider the terms associated with the gradient of polarisation in the enthalpy with a stress-free state. Those terms should provide a convex enthalpy to have a stable solution. This condition should be imposed by looking at the eigenvalues of the associated matrix and verifying that those values are positive. A weaker condition is that all elements in the diagonal of that matrix should be positive. The diagonal terms of this matrix are

$$\frac{a_0}{2} + \frac{2f_L f_T c_2 - f_L^2 c_1 - f_T^2 c_1}{c_1^2 - c_2^2} > 0, \tag{5.26a}$$

$$\frac{a_0}{2} + \frac{2f_L f_T c_1 - f_L^2 c_2 - f_T^2 c_2}{c_1^2 - c_2^2} > 0, \tag{5.26b}$$

$$\frac{a_0}{2} - \frac{2f_S^2}{c_3} > 0. \tag{5.26c}$$

Considering a similar approach to the one done in the previous examples, where only one coefficient of the flexoelectric tensor was different from zero, the conditions for the flexoelectric coefficient would be

$$f_L < \min\left\{\sqrt{\frac{(c_1^2 - c_2^2)a_0}{2c_2}}, \sqrt{\frac{(c_1^2 - c_2^2)a_0}{2c_1}}\right\} = 14.8\text{V}, \tag{5.27a}$$

$$f_T < \min\left\{\sqrt{\frac{(c_1^2 - c_2^2)a_0}{2c_2}}, \sqrt{\frac{(c_1^2 - c_2^2)a_0}{2c_1}}\right\} = 14.8\text{V}, \tag{5.27b}$$

$$f_S < \frac{\sqrt{c_3 a_0}}{2} = 4.3\text{V}. \tag{5.27c}$$

This result agrees with the behaviour seen in Fig. 5.13 where the solution was unstable for transversal flexoelectricity equal to 15V. The solution for 10 V was also unstable, although the coefficient satisfies the inequality in Eq. (5.27). This is explained by the fact that the inequalities in Eq. (5.27) are necessary conditions, but not sufficient conditions for stability.

5.5 Eploration of flexoelectric effect in fracture in ferroelectrics

To explore the effect of flexoelectricity in fracture in ferroelectrics, two different sets of simulations have been done. The first explores the effect of flexoelectricity in fracture propagation considering a homogeneous static polarisation, i.e. there are no domain walls and polarisation switching is precluded. The interaction of fracture and a fixed domain wall is studied in a second example, where switching is also precluded.

Consider a rectangular sample of dimensions 100 × 100 nm and an initial polarisation that remains fixed throughout the simulation with the four orientations: up, down, left and right, see Fig. 5.14 (left). The boundary conditions and loading are the same as in the example in Fig. 5.10. Without considering flexoelectricity, taking $f_L = f_T = f_S = 0$ V, the velocity of propagation of the fracture in the four initial configurations are the same. Note that this does not contradict the well-known fracture anisotropy in ferroelectric materials, i.e. the fact that cracking in ferroelectrics along the poling direction has a shorter length and consequently a higher effective fracture toughness than that normal to the poling direction, in Vicker's indentation tests. Abdollahi and Arias (2011b) show that the fracture toughening mechanism leading to the above anisotropy is a result of domain switching in the vicinity of the crack. This mechanism is not available in the present simulations, since the polarization is kept fixed. In Fig. 5.14 (right), we plot the phase field v after the first 30% of all the loading steps. The position of the crack tip is at $x = 13.2$nm for the four orientations considered. We observe no fracture anisotropy with respect to the poling direction in the absence of flexoelectricity.

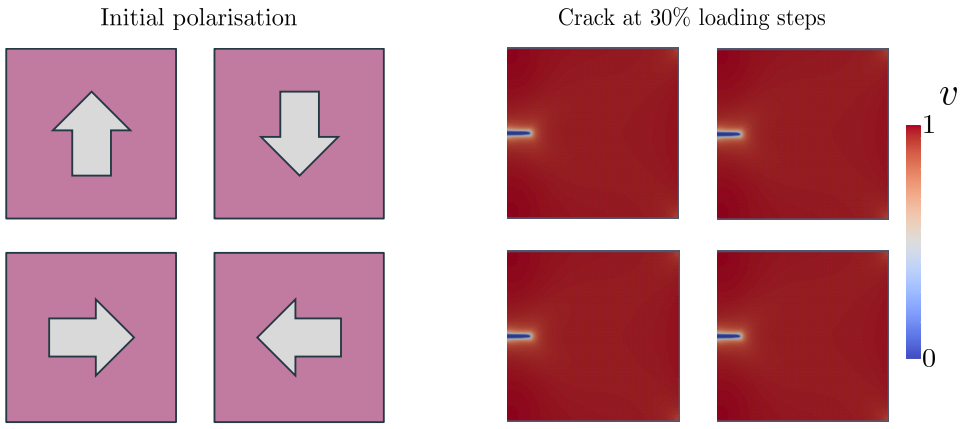

Figure 5.14: Crack propagation in a poled piezoelectric (without switching) for the four different poling directions. Left) Initial polarisation. Right) Phase v after 30% of the final loading.

This situation changes in the presence of flexoelectricity. We consider the same 4 poled piezoelectrics with an isotropic flexocoupling tensor given by $f_L = f_T = 5$ V and $f_S = 0$

V, as shown in Fig. 5.15 (left). According to Fig. 5.15 (right), in the presence of isotropic flexoelectricity, we observe faster crack propagation as compared with the case without flexoelectricity. This weakening effect is strongest for cracking orthogonal to poling. In these two cases, the sign of the orthogonal poling does not affect crack propagation. In the case of cracking along the poling direction, the weakening effect is smaller, and asymmetric with respect to the poling sign, being stronger for the antiparallel case. These results seem to contradict Abdollahi *et al.* (2015c), and thus need further investigation.

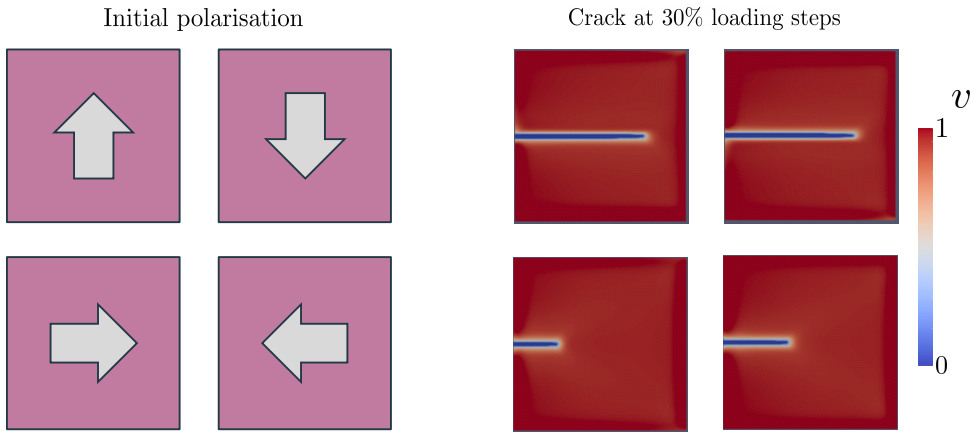

Figure 5.15: Crack propagation in a poled piezoelectric (without switching) for the four different poling directions considering flexoelectricity. Left) Initial polarisation. Right) Phase v after 30% of the final loading.

Now, consider the same rectangle as before, but with a fixed polarisation orientation containing a domain wall as shown in Fig. 5.16. We consider the same loading and boundary conditions as in the previous examples, and illustrated in Fig. 5.10. In these simulations the crack trajectory slows down as it approaches the domain wall and deviates from the horizontal trajectory briefly as it crosses the domain wall. After that, it continues propagating along a horizontal trajectory through the vertically polarized domain at a faster speed as expected, see Fig. 5.16.

5.6 Ongoing and future work

The ongoing and future work is presented here, and it is divided into the following tasks:

- The necessary conditions for stability of flexoelectric ferroelectrics were derived in Section 5.2.4. The sufficient conditions are still unknown and they are ongoingly investigated.
- The effect of flexoelectricity on the fracture of ferroelectrics is analysed in Section 5.5. We have shown a slight deviation from the natural propagation of the fracture in

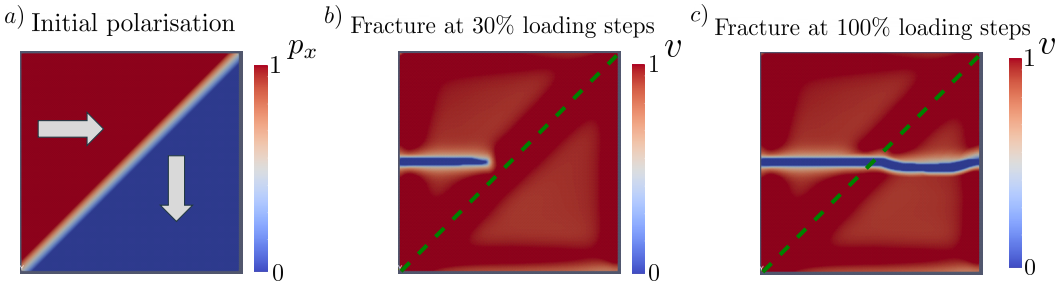

Figure 5.16: Crack propagation in the presence of a fixed 90° domain wall (ferroelastic). a) Fixed initial polarisation, red means right polarisation and blue means down polarisation. b) Fracture profile after 30% loading steps, blue means broken material and red means unbroken material. The discontinuous green line represent the domain wall c) Fracture profile after 100% loading steps.

the presence of a domain wall. We expected a significant effect due to the gradient of polarisation of the domain wall. The interplay between fracture and domain wall is a rich and complex phenomenon that remains unknown. This example should be studied extensively to see different interactions of the fracture depending on the direction of the domain wall.

- The fully coupled interaction of fracture and ferroelectric microstructure evolution accounting for flexoelectricity is yet to be investigated. Some preliminary results are shown in Fig. 5.17 and Fig. 5.18, for the same setup as the one presented in Section 5.3.3. The propagating crack interacts with the domain microstructure in a similar way as shown by Abdollahi and Arias (2011a). The effect of flexoelectricity on this interaction is yet to be fully investigated and understood.

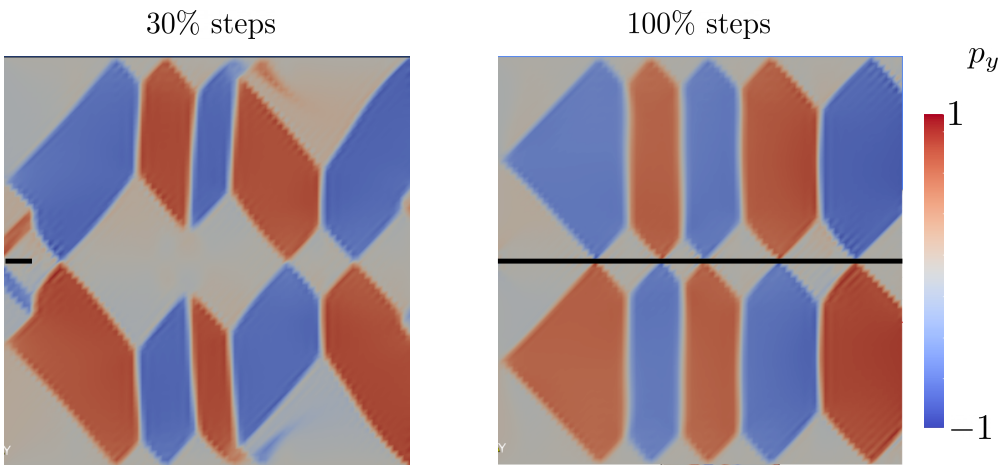

Figure 5.17: Vertical polarisation after 30% and 100% steps considering the boundary conditions explained in Fig. 5.10. Left) The little wings created on the top and bottom of the crack tip interact with the opposite polarisation domains, reducing the velocity of the crack. Right) The final polarisation is very similar to the final one without considering flexoelectricity, showing that the flexoelectric effect in the fracture is a very local phenomenon where the strain gradients are significant.

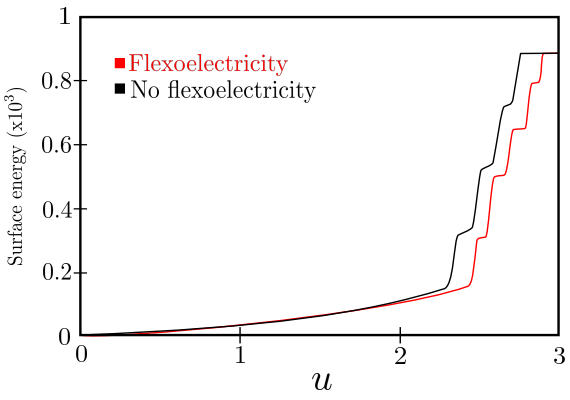

Figure 5.18: Evolution of the normalised surface energy for multi-phase crystal with and without flexoelectricity.

Chapter 6

Asymmetric tribology due to flexoelectricity

In this chapter we explore computationally the effect of flexoelectricity on friction, in close collaboration with experimentalists. This chapter is partially included in Cho *et al.* (2022). We present numerical simulations of indentation experiments of vertically polarised ferroelectric thin films accounting for flexoelectricity and confirm that flexoelectricity can induce a different friction response for up and down ferroelectric domains. Firstly, we describe the experimentally observed asymmetry in friction and wear in ferroelectrics, which is attributed to the interplay between piezoelectricity and flexoelectricity, similarly to previous evidences in fracture (Abdollahi *et al.*, 2015c, Cordero-Edwards *et al.*, 2019). Next, an axisymmetric formulation of the continuum and computational model of flexoelectricity in ferroelectrics is presented. The model for the contact of the indenter and the ferroelectric thin film is also described in detail, along with its validation. Finally, simulations of indentation depth and contact area upon indentation of polarised thin films are presented, showing apparent differences for up and down polarised ferroelectric domains. These results are then related to asymmetric friction coefficients via one-asperity friction models.

6.1 Observation of asymmetry

Understanding and controlling the interplay between piezoelectricity and flexoelectricity in ferroelectric materials can enrich critical opportunities in the area of condensed matter physics and functional materials engineering. For instance, this non-trivial interplay has been shown to be constructive or destructive depending on design (Abdollahi and Arias, 2015b). Furthermore, the interplay between piezoelectricity and flexoelectricity at scales where they have competing magnitudes, has been shown to be the origin of asymmetric fracture in ferroelectrics (Abdollahi *et al.*, 2015c). In a similar way, Cordero-Edwards *et al.* (2017) have shown that this interplay causes down domains to be stiffer than up domains.

Here, we show that the interplay between flexoelectricity and piezoelectricity leads to an asymmetric friction and wear response. This nanotribological asymmetry is used to develop a top-down, chemical-free lithography technique to edge complicated nanopatterns, following the underlying domain patterns.

In this project, uniaxial ferroelectric LiNbO3 single crystals and thin films are scanned with a diamond probe. The samples are vertically polarised, with domains with polarisation pointing upwards (up domains) and downwards (down domains), see Fig. 6.1a). After a few scans, down domains are less strongly etched than the up domains. This effect can be seen in Fig. 6.1a-b). Also, a polarisation-dependent friction contrast is observed with higher friction in the up domains concerning the down domains (see Fig. 6.1b)) after 50 milling scans. Apart from an increasing friction force, an apparent difference in the height of the sample is visible. Fig. 6.1d) shows the strong height and friction difference in up and down domains.

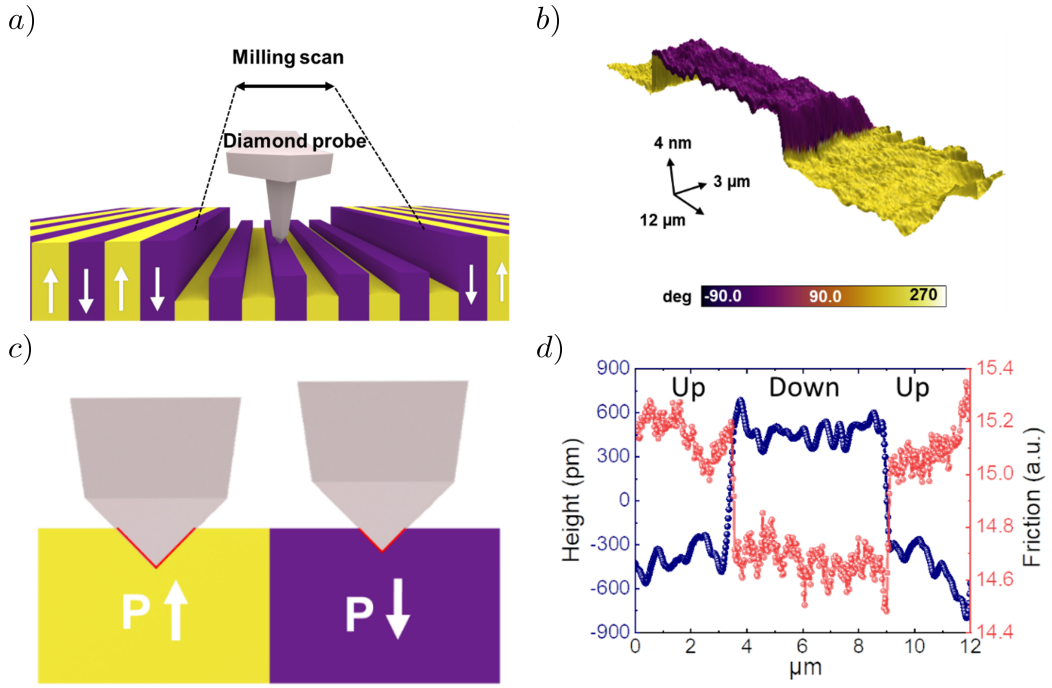

Figure 6.1: Observation of friction and indentation depth of ferroelectric LiNbO3. a) Sketch of the asymmetric milling for up and down domains. b) 3D plot of the surface after 50 scans. c) Sketch of the difference of contact area between up and down polarisation. d) Height and friction signal during a 50th milling scan. Figure adapted from Cho *et al.* (2022)

Friction and wear are complex tribological phenomena and can result from the contributions of several possible microscopic or nanoscopic mechanisms, which could lead to the observed asymmetry of these responses in ferroelectrics (Carpick and Salmeron, 1997, Chung *et al.*, 2005).

The flexoelectric field induced by the AFM tip due to the strain gradient originated is a possible mechanism of the asymmetry. This strain-gradient-induced polarisation has been shown to lead to asymmetric mechanical response in the stiffness in ferroelectrics (Cordero-Edwards *et al.*, 2017), down-domains being stiffer than up-domains. At the same loading force in up and down domains, we should therefore expect a larger contact area and indentation depths in up-domains during the etching scan, as schematically illustrated in Fig. 6.1c). Because friction strongly depends on the real contact area (Bowden and Tabor, 1939), as does the mechanical wear rate, we would consequently expect higher friction and wear in up domains, in agreement with the experimental observations, Fig. 6.1d).

Other possible explanations of the observed asymmetric tribology are an electrostatic effect or inhomogeneous defect distribution, but both have been studied in detail and ruled out by Cho *et al.* (2022). Here, we propose a model to compute the contact area and indentation depth of an indenter acting on a vertically polarised ferroelectric solid accounting for flexoelectricity. We then relate the contact area to the friction coefficients through a single-asperity model and quantitatively confirm the observed asymmetry in the friction coefficient.

6.2 Theoretical and computational model

In the experiments, milling scans are performed with a loading force range of $5 - 10\mu$N. These loading forces are large enough to observe significant etching and a consistent asymmetry, but low enough to preclude fracture and mechanically induced domain switching (Lu *et al.*, 2012). Thus, the continuum model presented in Section 5 is simplified here for a polarised linear piezoelectric, without polarisation reversal (Abdollahi and Arias, 2012), augmented with flexoelectricity. An axisymmetric formulation of the problem is derived next, reducing the indentation problem to two dimensions. The AFM tip is idealised as a rigid indenter in contact with an ideally flat sample surface. The sample shape is rectangular, and thus a body-fitted B-spline approximation as described in Section 3.1.2 is used. The interpolation properties of open B-splines at the boundary allow us to impose essential boundary conditions strongly. To model a frictionless contact, we follow the well-known Signorini-Hertz-Moreau model, which allows us to either control the tip indentation and measure force, or control force and measure the displacement of the indenter (Wriggers and Laursen, 2006, Yastrebov, 2013). The iterative algorithm to compute the contact area and indentation depth is described in detail.

6.2.1 Axisymmetric flexoelectricity

We follow the linear continuum model of piezoelectricity (Abdollahi and Arias, 2012) for spontaneous polarisation augmented with flexoelectricity (Barceló-Mercader *et al.*, 2022, Codony *et al.*, 2019). The total enthalpy considered is

$$\mathcal{H}(\varepsilon_{ij}, \varepsilon_{ij,k}, E_i) = \int_\Omega \frac{1}{2}\mathbb{C}_{ijkl}\varepsilon_{ij}\varepsilon_{kl} - e_{ikl}E_i\varepsilon_{kl} - \mu_{ijkl}E_i\varepsilon_{jk,l} - \frac{1}{2}\epsilon_{ij}E_iE_j + \frac{1}{2}h_{ijklmn}\varepsilon_{ij,k}\varepsilon_{lm,n}\,\mathrm{d}\Omega \quad (6.1)$$

where Ω is the solid domain, $\mathbb{C}$ is the fourth-rank elasticity tensor, e is the third-rank piezoelectricity tensor, μ is the fourth-rank flexoelectricity tensor, k is the second-rank dielectricity tensor and g is the six-rank strain gradient elasticity tensor. The strain gradient term is needed in order to guarantee thermodynamic stability of the model in the presence of flexoelectricity (Eliseev *et al.*, 2009b, Mao and Purohit, 2014, Maranganti *et al.*, 2006b).

The traction $t_i(\boldsymbol{u}, \phi)$, double traction $r_i(\boldsymbol{u}, \phi)$, electric charge density $w(\boldsymbol{u}, \phi)$ and edge forces $j_i(\boldsymbol{u}, \phi)$ are

$$t_i(\boldsymbol{u}, \phi) = \left(\hat{\sigma}_{ij}(\boldsymbol{u}, \phi) - \tilde{\sigma}_{ijk,k}(\boldsymbol{u}, \phi) - \tilde{\sigma}_{ikj,l}(\boldsymbol{u}, \phi)\left(\delta_{lk} - n_l n_k\right)\right) n_j + \tilde{\sigma}_{ijk}(\boldsymbol{u}, \phi)\tilde{N}_{jk} \quad (6.2a)$$

$$r_i(\boldsymbol{u}, \phi) = \tilde{\sigma}_{ijk}(\boldsymbol{u}, \phi)n_j n_k, \quad (6.2b)$$

$$w(\boldsymbol{u}, \phi) = -\hat{D}_l(\boldsymbol{u}, \phi)n_l, \quad (6.2c)$$

$$j_i(\boldsymbol{u}, \phi) = \tilde{\sigma}_{ijk}(\boldsymbol{u}, \phi)(m_j^L n_k^L + m_j^R n_k^R), \quad (6.2d)$$

where $\tilde{N}_{ij} = -n_{i,l}(\delta_{lj} - n_l n_j) + n_{f,g}(\delta_{fg} - n_f n_g)n_i n_j$. $\mathbf{n}$ is the unitary exterior normal vector. The superscripts L and R refer to the first and second surface sharing the edge, and $\mathbf{m}$ is the conormal vector on each surface, tangent to the surface, normal to the edge and pointing outward to the surface.

The stress $\hat{\sigma}_{ij}$, double stress $\tilde{\sigma}_{ijk}$ and electric displacement $\hat{D}_l$ in Eq. (6.2) are derived from the bulk enthalpy density, as work-conjugates to strain ε_{ij}, strain gradient $\varepsilon_{ij,k}$ and electric field E_l, respectively, as

$$\hat{\sigma}_{ij}(\boldsymbol{u}, \phi) = \left.\frac{\partial \mathcal{H}^\Omega[\boldsymbol{\varepsilon}, \nabla\boldsymbol{\varepsilon}, \boldsymbol{E}]}{\partial \varepsilon_{ij}}\right|_{\substack{\nabla\boldsymbol{\varepsilon} \\ \boldsymbol{E}}} = \mathbb{C}_{ijkl}\varepsilon_{kl}(\boldsymbol{u}) - e_{lij}E_l(\phi), \quad (6.3)$$

$$\tilde{\sigma}_{ijk}(\boldsymbol{u}, \phi) = \left.\frac{\partial \mathcal{H}^\Omega[\boldsymbol{\varepsilon}, \nabla\boldsymbol{\varepsilon}, \boldsymbol{E}]}{\partial \varepsilon_{ij,k}}\right|_{\substack{\boldsymbol{\varepsilon} \\ \boldsymbol{E}}} = h_{ijklmn}\varepsilon_{lm,n}(\boldsymbol{u}) - \mu_{lijk}E_l(\phi), \quad (6.4)$$

$$\hat{D}_l(\boldsymbol{u}, \phi) = -\left.\frac{\partial \mathcal{H}^\Omega[\boldsymbol{\varepsilon}, \nabla\boldsymbol{\varepsilon}, \boldsymbol{E}]}{\partial E_l}\right|_{\substack{\boldsymbol{\varepsilon} \\ \nabla\boldsymbol{\varepsilon}}} = \epsilon_{lm}E_m(\phi) + e_{lij}\varepsilon_{ij}(\boldsymbol{u}) + \mu_{lijk}\varepsilon_{ij,k}(\boldsymbol{u}). \quad (6.5)$$

The previous equations are subject to appropriate boundary conditions as

$$\begin{aligned} u_i &= u_i^{\mathrm{D}} \quad \text{on } \Gamma_u & t_i &= t_i^{\mathrm{N}} \quad \text{on } \Gamma_t, \\ \partial^n u_i &= v^{\mathrm{D}} \quad \text{on } \Gamma_v & r_i &= r_i^{\mathrm{N}} \quad \text{on } \Gamma_r, \\ \phi &= \phi^{\mathrm{D}} \quad \text{on } \Gamma_\phi & w &= w^{\mathrm{N}} \quad \text{on } \Gamma_w, \\ u_i &= u_i^{\mathrm{D}} \quad \text{on } C_u & j_i &= j_i^{\mathrm{N}} \quad \text{on } C_j, \end{aligned} \tag{6.6}$$

with the normal derivative operator $\partial^n(A) := \partial A/\partial \mathbf{n}$. u_i^{D} is the prescribed displacement on the first order Dirichlet boundary, Γ_u; t_i^{N} is the traction on the first order Neumann boundary, Γ_t with $\partial\Omega = \Gamma_t \cup \Gamma_u$; v_i^{D} is the normal derivative of the displacement $\partial^n \boldsymbol{u}$ on the second order Dirichlet boundary, Γ_v, and r_i^{N} is the double traction on the second order Neumann boundary, Γ_r with $\partial\Omega = \Gamma_r \cup \Gamma_v$. ϕ^{D} is the prescribed potential on the Dirichlet boundary Γ_ϕ, and w^{N} is the surface charge density on the Neumann boundary Γ_w, with $\partial\Omega = \Gamma_\phi \cup \Gamma_w$. The domain boundary is assumed to be composed of smooth surfaces (curves in 2D) that are joined on sharp boundary edges (corners in 2D). C_j denotes the union of the boundary edges that are shared by two surfaces with first-order Neumann conditions, i.e. the edges of Γ_t, where a line (punctual in 2D) force j_i^{N} is set. C_u denotes the union of all other edges, i.e. those shared by at least one Dirichlet surface, where the value of u_i is assumed to be that of the adjacent Dirichlet surface, i.e. $u_i = u_i^{\mathrm{D}}$ on $C_u \subset \overline{\Gamma}_u$.

Considering 2D axisymmetric problem with rotationally symmetric structures and axisymmetric material tensor under axisymmetric loading we obtain

$$\delta\Pi^{\mathrm{Axi}}[\boldsymbol{u}, \phi; \delta\boldsymbol{u}, \delta\phi] = 2\pi \int_\Omega \Big(\hat{\sigma}_{ij}(\boldsymbol{u}, \phi)\varepsilon_{ij}(\delta\boldsymbol{u}) + \tilde{\sigma}_{ijk}(\boldsymbol{u}, \phi)\varepsilon_{ij,k}(\delta\boldsymbol{u}) - \hat{D}_l(\boldsymbol{u}, \phi)E_l(\delta\phi) \Big) r \,\mathrm{d}r \,\mathrm{d}z, \tag{6.7}$$

where the strain ε, strain gradient $\nabla\varepsilon$ and electric field E are defined, component-wise, as

$$\begin{aligned} \varepsilon_{rr} &= \partial u_r/\partial r, & \varepsilon_{rz} &= \varepsilon_{zr} = \frac{1}{2}\Big(\partial u_r/\partial z + \partial u_z/\partial r \Big), \\ \varepsilon_{zz} &= \partial u_z/\partial z, & \varepsilon_{\varphi\varphi} &= u_r/r, \end{aligned} \tag{6.8}$$

$$\begin{aligned} \varepsilon_{rr,r} &= \partial u_r/\partial r^2, & \varepsilon_{rz,r} &= \varepsilon_{zr,r} = \frac{1}{2}\Big(\partial^2 u_r/\partial r\partial z + \partial^2 u_z/\partial r^2 \Big), \\ \varepsilon_{\varphi\varphi,r} &= \frac{1}{r}\partial u_r/\partial r - \frac{u_r}{2r^2}, & \varepsilon_{zz,r} &= \partial^2 u_z/\partial r\partial z, \\ \varepsilon_{r\varphi,\varphi} &= \varepsilon_{\varphi r,\varphi} = \frac{1}{r}\partial u_r/\partial r - \frac{3u_r}{4r^2}, & \varepsilon_{z\varphi,\varphi} &= \varepsilon_{\varphi z,\varphi} = \frac{1}{2r}\Big(\partial u_r/\partial z + \partial u_z/\partial r \Big), \\ \varepsilon_{rr,z} &= \partial^2 u_r/\partial r\partial z, & \varepsilon_{rz,z} &= \varepsilon_{zr,z} = \frac{1}{2}\Big(\partial^2 u_z/\partial r\partial z + \partial^2 u_z/\partial z^2 \Big), \\ \varepsilon_{\varphi\varphi,z} &= \frac{1}{r}\partial u_r/\partial z, & \varepsilon_{zz,z} &= \partial^2 u_z/\partial z^2, \end{aligned} \tag{6.9}$$

$$E_r = -\partial\phi/\partial r, \qquad E_z = -\partial\phi/\partial z, \tag{6.10}$$

The weak form of the associated flexoelectric problem considering 2D axisymmetry is

$$\text{Find } (\boldsymbol{u}, \phi) \in \mathcal{U}_{\mathrm{D}} \otimes \mathcal{P}_{\mathrm{D}}, \text{ such that } \delta\Pi^{\mathrm{Axi}} = 0 \; \forall (\delta\boldsymbol{u}, \delta\phi) \in \mathcal{U}_0 \otimes \mathcal{P}_0, \tag{6.11}$$

with

$$\mathcal{U}_{\mathrm{D}} = \left\{ \boldsymbol{u} \in [H^2(\Omega)]^2 | \boldsymbol{u} = \boldsymbol{u}^{\mathrm{D}} \text{ on } \partial\Omega_u \text{ and } C_u \text{ and } \partial^n(\boldsymbol{u}) = \boldsymbol{v}^{\mathrm{D}} \text{ on } \partial\Omega_v \right\}, \tag{6.12a}$$

$$\mathcal{P}_{\mathrm{D}} = \left\{ \phi \in H^2(\Omega) | \phi = \phi^{\mathrm{D}} \text{ on } \partial\Omega_\phi \right\} \tag{6.12b}$$

$$\mathcal{U}_0 = \left\{ \boldsymbol{u} \in [H^2(\Omega)]^2 | \boldsymbol{u} = 0 \text{ on } \partial\Omega_u \text{ and } C_u \text{ and } \partial^n(\boldsymbol{u}) = 0 \text{ on } \partial\Omega_v \right\}, \tag{6.12c}$$

$$\mathcal{P}_0 = \left\{ \phi \in H^2(\Omega) | \phi = 0 \text{ on } \partial\Omega_\phi \right\}, \tag{6.12d}$$

6.2.2 Contact model

For the contact problem, we follow the frictionless Signorini-Hertz-Moreau model defined in Wriggers and Laursen (2006) and Yastrebov (2013). This model considers two points of contact (x, x_0) where x is a point in the flat surface and x_0 the corresponding point of the rigid cone which is coming into contact (see Fig. 6.2), stating

$$g_n \sigma_n = 0 \quad \text{on} \quad \Gamma_c, \tag{6.13a}$$

$$g_n \leq 0, \tag{6.13b}$$

$$\sigma_n = \boldsymbol{n} \cdot \sigma \cdot \boldsymbol{n}, \tag{6.13c}$$

where Γ_c is the contact region, and g_n is the gap function that can be described as

$$g_n = \boldsymbol{u} \cdot \boldsymbol{n} + (x - x_0) \cdot \boldsymbol{n}. \tag{6.14}$$

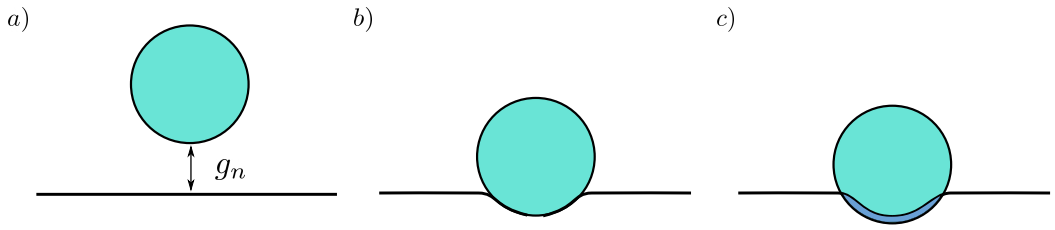

Figure 6.2: Signorini-Hertz-Moreau contact model. a) Definition of the gap function in Eq. (6.14). b) Signorini-Hertz-Moreau model applied to the sphere and the flat surface. c) The penalty term added in Eq. (6.15) penalises the penetration zone depicted in dark blue.

We enforce the non-penetration constraint by adding a new penalty term to the enthalpy

functional $\mathcal{H}$ as

$$\mathcal{H}_t = \mathcal{H} + \int_{\Gamma_c} \frac{1}{2}\beta_c \langle g_n \rangle^2 \mathrm{d}\Gamma, \tag{6.15}$$

where β_c is a penalty parameter and the Macaulay bracket is defined as

$$\langle A \rangle = \begin{cases} A & \text{if } A > 0, \\ 0 & \text{otherwise.} \end{cases} \tag{6.16}$$

The contact force F is defined, considering 2D axisymmetry, as

$$F = 2\pi \int_0^{R_c} \beta_c \langle g_n \rangle r \, \mathrm{d}r. \tag{6.17}$$

where R_c is the contact radius (see Fig. 6.3). An iterative algorithm is used to compute the indentation for a given force.

6.2.2.1 Validation in a purely elastic solid

We validate the previous model for the purely mechanical case (without piezoelectricity and flexoelectricity) by comparison against the analytical model by Popov *et al.* (2019). We set the penalty parameter to $\beta_c = 10$ for all simulations with accurate results. The problem statement is seen in Fig. 6.3, where a conical indenter is pushed against a flat surface, creating an indentation depth d and a contact radius R_c. We consider an angle of the cone θ to be $42,5°$.

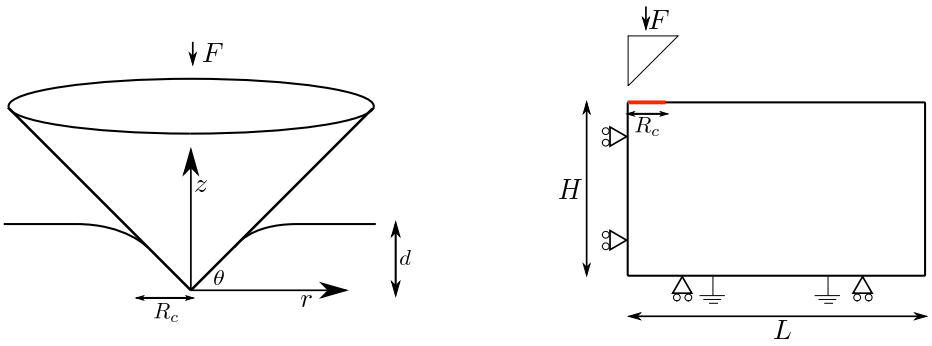

Figure 6.3: Problem statement for the conical indentation. Image adapted from Cho *et al.* (2022)

The analytical relation between the contact radius and the indentation depth is

$$d(R_c) = \frac{\pi}{2} R_c \tan\theta, \tag{6.18}$$

and the analytical relation between the contact radius and the force applied is

$$F = \frac{\pi R_c^2}{2} E^* \tan\theta, \tag{6.19}$$

where $E^* = E/(1-\nu^2)$. For the validation of the contact model, we have just considered a purely elastic material with $E = 164$ GPa and $\nu = 0.3$. The sample dimensions are $L = 100$nm and $H = 50$nm. The perfect agreement between the simulation and the analytical model is shown in Fig. 6.4.

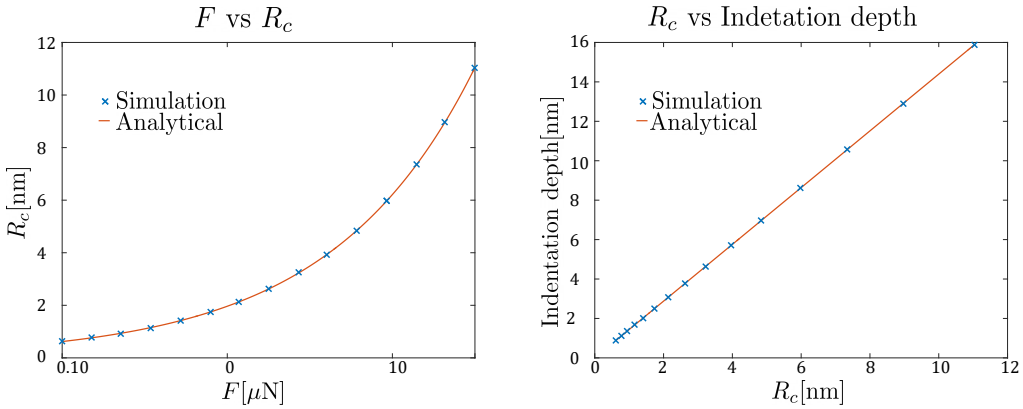

Figure 6.4: Validation of the numerical model versus the analytical one. Left) A plot of the applied force versus the contact radius. Right) A plot of the contact radius versus the indentation depth.

6.3 Simulations

For the following simulations, the displacement along the contact line (shown in red in Fig. 6.3) is prescribed, the left and bottom sides of the rectangle are mechanically clamped horizontally and vertically, respectively, see Fig. 6.3. The bottom boundary is electrically grounded, while all other boundaries are assumed to be free of surface charges and traction-free, also all boundaries and corners are assumed to be double traction-free and line force free. The material parameters for the elastic, piezoelectric and dielectric tensors are taken from Persson (2014). For the strain-gradient elasticity tensor, we considered the definition in Appendix A and a length-scale $\ell = 10$nm. The definition of the flexoelectric tensor is also given in Appendix A. Here, only isotropic flexoelectric tensors are considered, i.e. $\mu_S = (\mu_L - \mu_T)/2$, with $\mu_L = \mu_T = \varepsilon_0 \varepsilon_r f$, $\mu_S = 0$, and different values for the flexocoupling coefficient f are considered. A simulation of the 2D axisymmetric model is shown in Fig. 6.5 for illustration purposes.

Fig. 6.6 depicts the computed indentation depth (left) and contact radius (right) as a function of the applied force for different values of the flexoelectric parameters. In the absence of

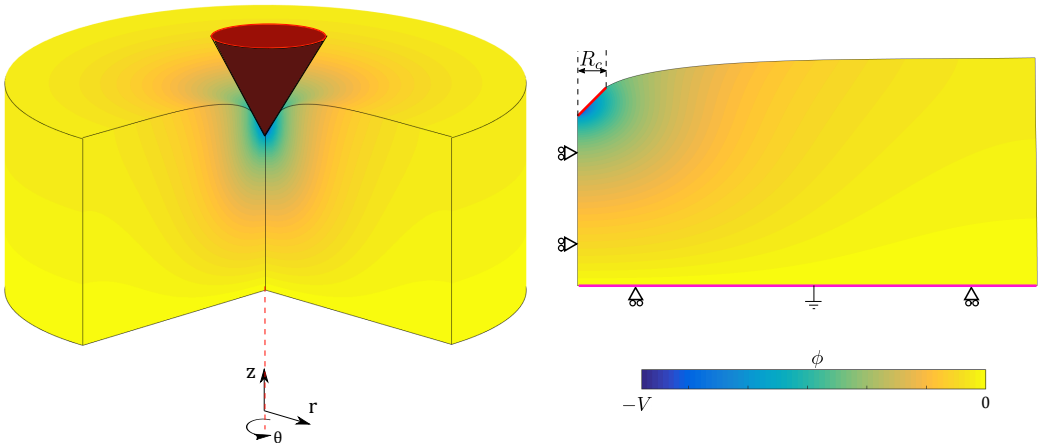

Figure 6.5: 3D model (left) and the 2D axisymmetric simulation (right). The flexoelectric tensor considered is $f_L = f_T = 10V$ and $f_S = 0$. The colourmap represents the resulting electric potential on the sample upon mechanical indentation. Image adapted from Cho *et al.* (2022)

flexoelectricity ($f = 0$), we obtain the same response for up-domains (solid lines) and down-domains (dashed lines). When flexoelectricity is accounted for, the response depends clearly on the polarisation direction and the asymmetry increases with the flexocoupling coefficient. Results for two values of the flexocoupling coefficient $f = 10, 40$V are shown in the figure. The asymmetry of the response is apparent and can be explained by the direction of the flexoelectric polarisation and piezoelectric polarisation shown in Fig. 6.7, where the flexoelectrically induced polarisation and piezoelectric polarisation are plotted separately, for the case of upward and downward polarised domains. While the flexoelectric polarisation is largely independent of the direction of ferroelectric polarisation, the piezoelectric polarisation has opposite signs for up and down domains. Hence, their combination is the origin of the observed asymmetric response. Within the range where flexoelectric and piezoelectric polarisations are comparable in magnitude, the observed difference in the response for up and down domains depends on the magnitude of flexoelectric parameters, being larger for stronger flexoelectricity.

We relate next the asymmetry in the contact radius with the friction coefficient by means of the following relation (Enachescu *et al.*, 1999), which holds at the nanoscale:

$$F_f = \tau A_c = \tau \pi R_c \sqrt{R_c^2 + d^2}, \tag{6.20}$$

where τ is the shear strength and A_c is the area of contact. Estimating friction forces for up and down domains is difficult in the experiment because of the lack of calibration, and the shear strength is also unknown in the current setting. Thus, we compute the ratio between the friction force in up and down domains F_f^{up}/F_f^{down}. In the experiment, we obtain values around $F_f^{up}/F_f^{down} = 1.0272$. We perform some simulations considering different values for the flexocoupling coefficient, which is also unknown for the samples used in the experiments. The

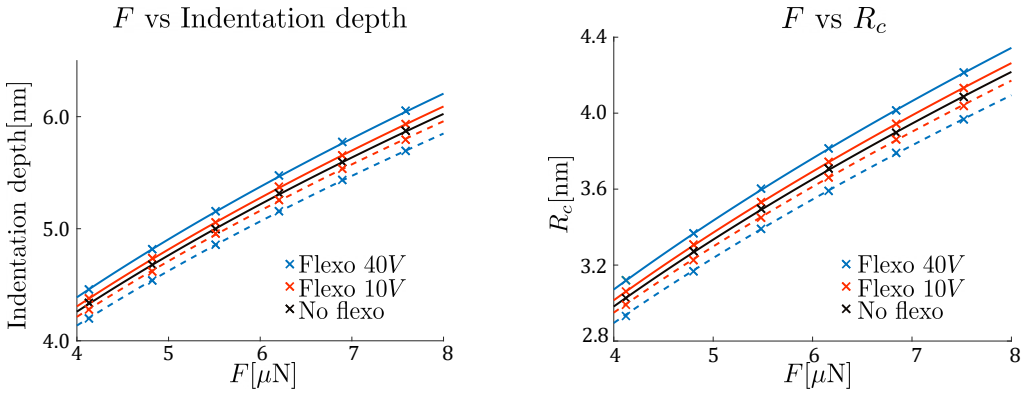

Figure 6.6: Force applied vs Indentation depth (left) and Force applied vs Contact radius (right). Solid and dashed lines mean up and down initial polarisation, respectively. Two values for the flexocoupling coefficients f = 10V and f = 40V are considered.

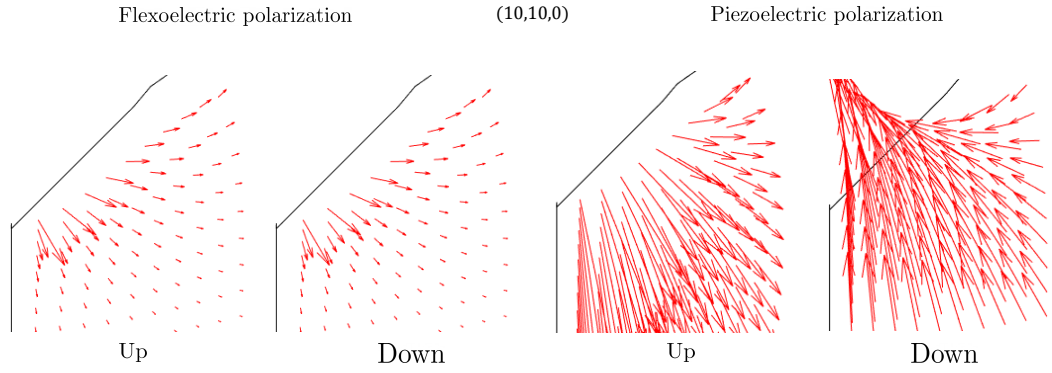

Figure 6.7: Flexoelectric polarisation and piezoelectric polarisation for up and down domains.

results of these simulations can be seen in Table 6.1, with the last column calculated using

$$\frac{F_f^{up}}{F_f^{down}} = \frac{R_c^{up}\sqrt{(R_c^{up})^2 + (d^{up})^2}}{R_c^{down}\sqrt{(R_c^{down})^2 + (d^{down})^2}}. \tag{6.21}$$

f_L	f_T	f_S	F_f^{up}/F_f^{down}
54	54	0	1.1881
40	40	0	1.1236
10	10	0	1.0361
1	1	0	1.0036

Table 6.1: Relation between up and down friction for different values of flexoelectricity.

6.3.1 Spherical indenter

During the milling scans, the originally conical indenter wears out and is better modelled by a spherical shape. Here, we provide results for a spherical indenter, as shown in Fig. 6.8. The same boundary conditions described in Section 6.3 are considered here. The 3D model reconstructed from axisymmetric simulations is shown in Fig. 6.9.

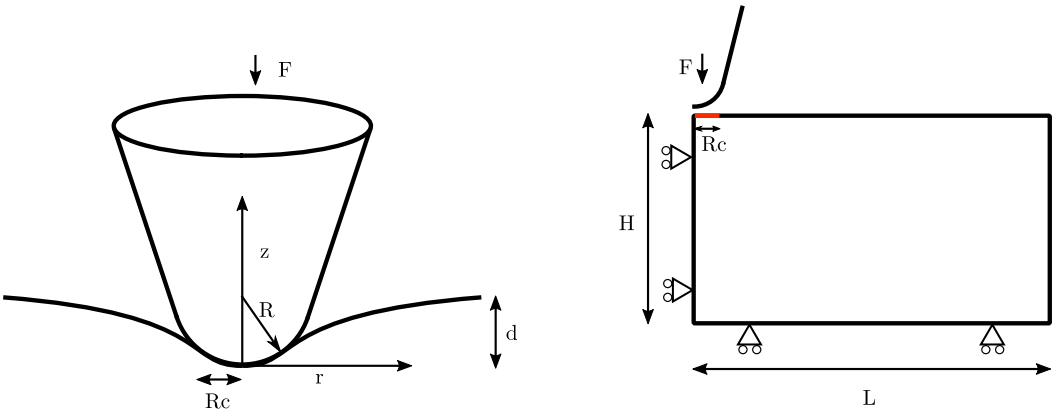

Figure 6.8: Problem statement for the spherical indentation.

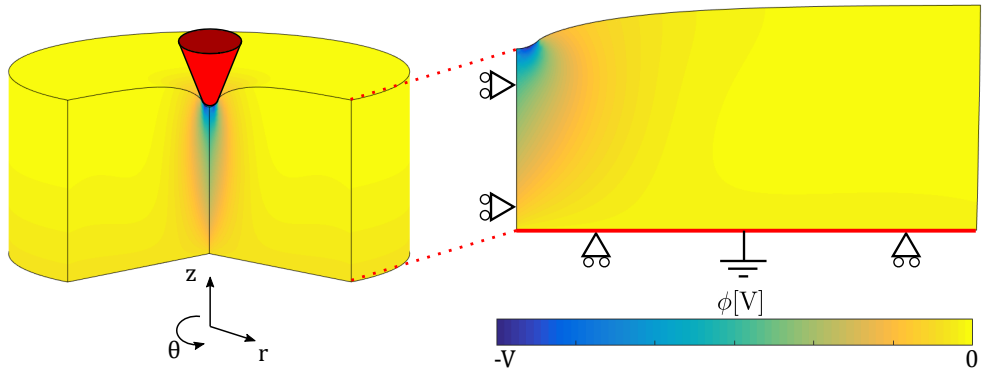

Figure 6.9: 3D model (left) and the 2D axisymmetric simulation (right) for the spherical indenter. The flexoelectric tensor considered is $f_L = f_T = 10V$ and $f_S = 0$. The colormap represents the resulting electric potential on the sample upon mechanical indentation.

In the spherical case, the resulting friction force is

$$F_f = \tau A_c = \tau 4\pi R^2 \left(1 - \cos\frac{R_c}{R}\right). \tag{6.22}$$

The computed friction forces are reported in Table 6.2, yielding similar results to those obtained for the conical indenter (Table 6.1).

f_L	f_T	f_S	F_f^{up}/F_f^{down}
54	54	0	1.1390
40	40	0	1.1095
10	10	0	1.0375
1	1	0	1.0037

Table 6.2: Relation between up and down friction for different values of flexoelectricity for the spherical indenter.

6.4 Discussion and conclusions

We have shown that flexoelectricity can explain the observed friction asymmetry in ferroelectrics between up and down domains. We performed several B-spline simulations to quantify the indentation depth and contact area depending on the poling direction in the presence or absence of flexoelectric coupling, using the well-known Signorini-Hertz-Moreau model for contact. The tip of the indenter was modelled by a cone or sphere in contact with a flat surface made by LiNbO3, as seen in Fig. 6.5.

The flexoelectric polarisation induced by the strain gradient of the indentation produces asymmetric interactions between up and down domains, as shown in Fig. 6.7. One consequence of this asymmetric interaction is the result in larger indentation depth and contact area for the up domain as compared to down domains, as seen in Fig. 6.6. The higher the flexoelectric coefficient, the bigger the effect until it reaches the maximum. If we keep increasing the flexoelectric coefficient, the flexoelectric polarisation becomes dominant, and no asymmetry is seen, as shown in Fig. 6.10, where the indentation depth with f = 300V is very similar to f = 10V.

The experimental and simulated data comparison has been made using a single asperity contact model that predicts a linear relationship between the contact area and the friction force. The ratio between the predicted friction force for up and down domains has been computed for several simulations. The comparison shows a good agreement between the experimental data and the simulated values for flexoelectric coefficients close to 10V.

All in all, the experimental observation and simulations results suggest that flexoelectricity is the dominant mechanism for asymmetric tribology. Furthermore, the electrically switched down domain shows a lower friction coefficient than the up domain.

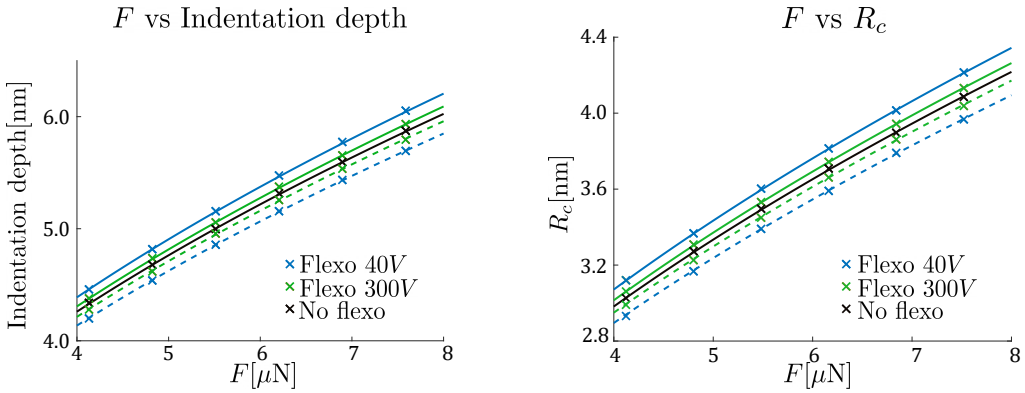

Figure 6.10: Force applied vs Indentation depth (left) and Force applied vs Contact radius (right) for the conical indenter. Solid and dashed lines mean up and down initial polarisation, respectively. Two values for the flexocoupling coefficients f = 40V and f = 300V are considered. The indentation depth for f = 300V is similar to f = 10V

6.5 Ongoing work

Although the continuum and numerical model presented in this chapter give accurate results, some improvements can be made, and they are:

- 2D axisymmetric simulations give a good approximation of the solution in 3D only in the cases where everything in the problem exhibits rotational symmetry. In order to study more general situations, we are currently developing the full 3D contact model.
- The proposed model in the present form does not account for the effect of shear forces.
- Furthermore, the proposed model is quasistatic. For higher scanning rates, dynamic effects should be taken into account.

Chapter 7

Conclusions

In this thesis, a theoretical and computational model for flexoelectricity in the presence of interfaces has been developed and implemented in the context of the hierarchical B-spline immersed boundary approach proposed by Codony *et al.* (2019). This framework has been used to study physical material interfaces, as well as fictitious interfaces such as generalised periodicity unit cell boundaries. The former has been used in multimaterial symmetry-breaking arrangements up-scaling flexoelectricity in electromechanical devices. For the latter case, an elegant and efficient implementation making use of the periodicity of the B-spline bases functions has been derived. The developments presented here have been instrumental in the design and analysis of flexoelectric architected periodic lattice metamaterials. Moving interfaces such as cracks and ferroelectric domain boundaries have also been studied by coupling phase-field models for fracture and ferroelectric microstructure accounting for flexoelectricity. Finally, flexoelectricity has been shown as a plausible cause for the asymmetric tribology observed in ferroelectrics in tight collaboration with experimentalists. The main contributions of the thesis are summarised next.

- High-order interface conditions for flexoelectricity have been formulated. These conditions are encoded through an enthalpy function which is suitable for unfitted discretisations. Interface conditions for other high-order PDEs have a similar form and thus, can be extended to other problems.
- Interface conditions are used to enforce generalised periodicity conditions weakly. These conditions were the first approach to generalised periodicity conditions which mimics the behaviour of a large periodic structure.
- Generalised periodicity conditions are derived using a second method. This method splits the response of a unit cell in two parts: a macroscopic and a microscopic part. All macroscopic functional are derived and the new weak form of flexoelectricity for unit cells is shown.

- The effect of flexoelectricity in graded structure has been analysed. Graded structure can replace piezoelectric sensors with non-piezoelectrics.
- From a numerical point of view, two different methods were implemented. The first is the body-fitted B-spline method which is suitable for rectangular domains. The second is the immersed B-spline method which allows to simulate any desired structure without geometric limitations. An upgrade of the immersed approach is done, such that generalised periodicity conditions can be imposed strongly. It is achieved through the creation of generalised periodicity space of approximation which is formed using a periodic and a generalised periodic approximation space.
- An axisymmetric formulation of flexoelectricity is derived and used in combination with a Hertzian contact model to simulate contact of conical and spherical indenters on poled ferroelectric thin films. Our simulations confirm flexoelectricity as a source of asymmetric friction with respect to the poling direction in ferroelectrics.
- The effect of flexoelectricity in ferroelectric domain microstructure has been explored showing that flexoelectricity increases the number of polarisation domains. Also, an upper limit for the flexoelectric coefficient values is derived based on stability arguments.
- The effect of flexoelectricity on crack propagation in ferroelectrics has also been studied. Preliminary results show fracture toughening mechanisms that should be further studied.

A big step in understanding the coupling of flexoelectricity with other physics has been done. But there are a lot of questions that remain open. The high-order generalised periodicity conditions stated are assumed to have a linear behaviour of the macroscopic displacement, which implies that the macroscopic strain-gradient tensor vanishes, i.e. it aims to simulate macroscopic uniform tension only. A generalisation of this formulation would be needed in order to simulate macroscopic bending.

Regarding the study of the influence on flexoelectricity on the interaction between crack propagation and ferreoelectric microstructure, only preliminaries results have been presented. These results allow us to understand some of the limitations of the current implementation and further developments involving probably higher order phase fields are currently under investigation. The hypothesis that polarisation and strain gradients at domain walls should play a role through the flexoelectric effect on the reduced toughness along these interfaces has not been fully validated and will require further investigation to provide convincing qualitative and quantitative evidence. Regarding the tribological behaviour of poled ferroelectrics, qualitative evidence has been provided to support flexoelectricity as one plausible cause of the experimentally observed asymmetric friction and wear. Our simulations have addressed the axisymmetric case, assuming isotropic material tensors, already providing convincing evidence that flexoelectricity can produce friction asymmetry in ferroelectrics depending on the poling direction. A fully 3D simulation is underway, which will allow us to explore the effect of shear tractions, as well as material anisotropy.

Appendices

A Material characterization

In the following Appendix, the material characterisation is presented. The appendix is divided into multiples section depending on the type of material considered.

A.1 Infinitesimal deformation for direct flexoelectricity

In this section, the material tensor for direct flexoelectricity in Section 2.1.1 is presented. They are described component-wise (non-zero components) and d is the number of dimensions of the physical space (Barceló-Mercader *et al.*, 2022).

Isotropic elasticity tensor is defined in terms of the Young modulus E and Poisson ratio ν as

$$\begin{aligned} \mathbb{C}_{iiii} &= C_L, && i = 1,\dots,d; \\ \mathbb{C}_{iijj} &= C_T, && i,j = 1,\dots,d \ : \ i \neq j; \\ \mathbb{C}_{ijij} = \mathbb{C}_{ijji} &= C_S, && i,j = 1,\dots,d \ : \ i \neq j, \end{aligned} \tag{A.1}$$

where the parameters C_L, C_S and C_T are

$$C_L := \frac{E(1-\nu)}{(1+\nu)(1-2\nu)}, \qquad C_T := \frac{E\nu}{(1+\nu)(1-2\nu)}, \qquad C_S := \frac{E}{2(1+\nu)}. \tag{A.2}$$

We consider an isotropic version of the general model in (Mindlin and Eshel, 1968) that is described in (Altan and Aifantis, 1997). The strain gradient tensor is defined in terms of the Young modulus E, the Poisson ratio ν and the mechanical length scale ℓ_{mech} as

$$\begin{aligned} h_{iikiik} &= \ell_{\text{mech}}^2 C_L, && i,k = 1,\dots,d; \\ h_{iikjjk} &= \ell_{\text{mech}}^2 C_T, && i,j,k = 1,\dots,d \ : \ i \neq j; \\ h_{ijkijk} = h_{ijkjik} &= \ell_{\text{mech}}^2 C_S, && i,j,k = 1,\dots,d \ : \ i \neq j \end{aligned} \tag{A.3}$$

where the parameters C_L, C_S and C_T are defined in Eq. (A.2).

Isotropic dielectricity is described as

$$\epsilon_{ii} = \epsilon, \qquad i = 1,\dots,d. \tag{A.4}$$

Piezoelectricity is represented by the third-order tensor $\boldsymbol{e}$, where tetragonal symmetry is considered, which has a principal direction. It involves longitudinal, transversal and shear couplings represented by the parameters e_L, e_T and e_S, respectively. For a material with

principal direction $\boldsymbol{x}_1$, the piezoelectric tensor $\boldsymbol{e}^{<\boldsymbol{x}_1>}$ is

$$\begin{aligned} e^{<\boldsymbol{x}_1>}{}_{111} &= e_L; \\ e^{<\boldsymbol{x}_1>}{}_{1jj} &= e_T, && j = 2, \dots, d; \\ e^{<\boldsymbol{x}_1>}{}_{j1j} = e^{<\boldsymbol{x}_1>}{}_{jj1} &= e_S, && j = 2, \dots, d. \end{aligned} \tag{A.5}$$

The piezoelectric tensor $\boldsymbol{e}$ oriented in an arbitrary direction $\boldsymbol{d}$ is obtained by rotating $\boldsymbol{e}^{<\boldsymbol{x}_1>}$ as

$$e_{lij} = R_{lL} R_{iI} R_{jJ} e_{LIJ}, \tag{A.6}$$

where R is the rotation matrix. Flexoelectricity is represented by the fourth-order tensor $\boldsymbol{\mu}$ where cubic symmetry is considered. It leads to a tensor involving longitudinal, transversal and shear couplings represented by the parameters μ_L, μ_T and μ_S, respectively. The components of the flexoelectric tensor $\boldsymbol{\mu}^{<\boldsymbol{x}>}$ of a material oriented in the Cartesian axes are the following:

$$\begin{aligned} \mu^{<\boldsymbol{x}>}{}_{iiii} &= \mu_L, && i = 1, \dots, d; \\ \mu^{<\boldsymbol{x}>}{}_{ijji} &= \mu_T, && i, j = 1, \dots, d \ : \ i \neq j; \\ \mu^{<\boldsymbol{x}>}{}_{iijj} = \mu^{<\boldsymbol{x}>}{}_{ijij} &= \mu_S, && i, j = 1, \dots, d \ : \ i \neq j. \end{aligned} \tag{A.7}$$

The flexoelectric tensor $\boldsymbol{\mu}$ oriented in an arbitrary orthonormal basis is obtained by rotating $\boldsymbol{\mu}^{<\boldsymbol{x}>}$ as

$$\mu_{lijk} = R_{lL} R_{iI} R_{jJ} R_{kK} \mu_{LIJK}. \tag{A.8}$$

The condition for an isotropic flexoelectric tensor is

$$\mu_S = (\mu_L - \mu_T)/2. \tag{A.9}$$

A.2 Infinitesimal deformation for Lifshitz-invariant flexoelectricity

In this section, the material tensor for Lifshitx-invariant flexoelectricity in Section 2.1.2 is presented. Apart from the material tensor described in Appendix A.1, we incorporate isotropic gradient dielectricity. It is represented by the fourth-order tensor M. We take a simple form depending on the electric permittivity ϵ and the dielectric length scale ℓ_{elec} as

$$M_{ijij} = \epsilon \ell_{\text{elec}}^2 \qquad i, j = 1, \dots, d. \tag{A.10}$$

B Variational formulation for generalised periodicity using interface conditions for four types of sensors and actuators.

In Section 2.3.1, we have presented the four cases we are interested in: 2 types of sensors and 2 types of actuators. But, we have shown only one variational formulation for simplicity. In this Appendix all four variational formulation for the enthalpy associated with generalised periodicity is presented for clarity and completeness. We will show the associated enthalpy $\Pi^{\mathrm{P,y}}$ and $\Pi^{\mathrm{P,x}}$.

B.1 Unconfined vertical displacement sensor

$$
\begin{aligned}
&\delta\Pi^{\mathrm{P,y}}[\boldsymbol{u},\phi,\check{\boldsymbol{u}},\check{\phi};\delta\boldsymbol{u},\delta\phi,\delta\check{\boldsymbol{u}},\delta\check{\phi}] = \\
&\int_{\mathcal{I}^y}\left[\beta^{uy}\left[\!\left[\delta u_i\right]\!\right]^y\left(\left[\!\left[u_i\right]\!\right]^y-\hat{u}_i^y\right)-\left[\!\left[\delta u_i\right]\!\right]^y\left[\!\left[t_i(\boldsymbol{u},\phi)\right]\!\right]_\gamma^y-\left(\left[\!\left[u_i\right]\!\right]^y-\hat{u}_i^y\right)\left[\!\left[t_i(\delta\boldsymbol{u},\delta\phi)\right]\!\right]_\gamma^y\right]\mathrm{d}\Gamma \\
&+\int_{\mathcal{I}^y}\left[\beta^{vy}\left[\!\left[\frac{\partial u_i}{\partial y}\right]\!\right]^y\left[\!\left[\frac{\partial\delta u_i}{\partial y}\right]\!\right]^y-\left[\!\left[\frac{\partial\delta u_i}{\partial y}\right]\!\right]^y\left\{r_i(\boldsymbol{u},\phi)\right\}_\gamma^y-\left[\!\left[\frac{\partial u_i}{\partial y}\right]\!\right]^y\left\{r_i(\delta\boldsymbol{u},\delta\phi)\right\}_\gamma^y\right]\mathrm{d}\Gamma+ \\
&+\int_{\mathcal{I}^y}\left[\left(\left[\!\left[\delta\phi\right]\!\right]^y-\delta\check{\phi}^y\right)\left[\!\left[w(\boldsymbol{u},\phi)\right]\!\right]_\gamma^y+\left(\left[\!\left[\phi\right]\!\right]^y-\check{\phi}^y\right)\left[\!\left[w(\delta\boldsymbol{u},\delta\phi)\right]\!\right]_\gamma^y\right]\mathrm{d}\Gamma \\
&+\sum_{x\in C^y}\left[\beta^{C_u y}\left[\!\left[\delta u_i\right]\!\right]^y\left(\left[\!\left[u_i\right]\!\right]^y-\hat{u}_i^y\right)-\left[\!\left[\delta u_i\right]\!\right]^y\left[\!\left[j_i(\boldsymbol{u},\phi)\right]\!\right]_\gamma^y-\left(\left[\!\left[u_i\right]\!\right]^y-\hat{u}_i^y\right)\left[\!\left[j_i(\delta\boldsymbol{u},\delta\phi)\right]\!\right]_\gamma^y\right].
\end{aligned}
\tag{B.1}
$$

$$
\begin{aligned}
&\delta\Pi^{\mathrm{P,x}}[\boldsymbol{u},\phi,\check{\boldsymbol{u}},\check{\phi};\delta\boldsymbol{u},\delta\phi,\delta\check{\boldsymbol{u}},\delta\check{\phi}] = \\
&\int_{\mathcal{I}^x}\left[-\left(\left[\!\left[\delta u_i\right]\!\right]^x-\delta\check{u}_i^x\right)\left[\!\left[t_i(\boldsymbol{u},\phi)\right]\!\right]_\gamma^x-\left(\left[\!\left[u_i\right]\!\right]^x-\check{u}_i^x\right)\left[\!\left[t_i(\delta\boldsymbol{u},\delta\phi)\right]\!\right]_\gamma^x\right]\mathrm{d}\Gamma \\
&+\int_{\mathcal{I}^x}\left[\beta^{vx}\left[\!\left[\frac{\partial u_i}{\partial x}\right]\!\right]^x\left[\!\left[\frac{\partial\delta u_i}{\partial x}\right]\!\right]^x-\left[\!\left[\frac{\partial\delta u_i}{\partial x}\right]\!\right]^x\left\{r_i(\boldsymbol{u},\phi)\right\}_\gamma^x-\left[\!\left[\frac{\partial u_i}{\partial x}\right]\!\right]^x\left\{r_i(\delta\boldsymbol{u},\delta\phi)\right\}_\gamma^x\right]\mathrm{d}\Gamma+ \\
&+\int_{\mathcal{I}^x}\left[\left(\left[\!\left[\delta\phi\right]\!\right]^x-\delta\check{\phi}^x\right)\left[\!\left[w(\boldsymbol{u},\phi)\right]\!\right]_\gamma^x+\left(\left[\!\left[\phi\right]\!\right]^x-\check{\phi}^x\right)\left[\!\left[w(\delta\boldsymbol{u},\delta\phi)\right]\!\right]_\gamma^x\right]\mathrm{d}\Gamma \\
&+\sum_{y\in C^x}\left[-\left(\left[\!\left[\delta u_i\right]\!\right]^x-\delta\check{u}_i^x\right)\left[\!\left[j_i(\boldsymbol{u},\phi)\right]\!\right]_\gamma^x-\left(\left[\!\left[u_i\right]\!\right]^x-\check{u}_i^x\right)\left[\!\left[j_i(\delta\boldsymbol{u},\delta\phi)\right]\!\right]_\gamma^x\right].
\end{aligned}
\tag{B.2}
$$

B.2 Confined vertical displacement sensor

$$
\begin{aligned}
&\delta\Pi^{\mathrm{P,y}}[\boldsymbol{u},\phi,\check{\boldsymbol{u}},\check{\phi};\delta\boldsymbol{u},\delta\phi,\delta\check{\boldsymbol{u}},\delta\check{\phi}] = \\
&\int_{\mathcal{I}^y}\left[\beta^{uy}\,[\![\delta u_i]\!]^y\left([\![u_i]\!]^y-\hat{u}_i^y\right)-[\![\delta u_i]\!]^y\,[\![t_i(\boldsymbol{u},\phi)]\!]_\gamma^y-\left([\![u_i]\!]^y-\hat{u}_i^y\right)[\![t_i(\delta\boldsymbol{u},\delta\phi)]\!]_\gamma^y\right]\mathrm{d}\Gamma \\
&+\int_{\mathcal{I}^y}\left[\beta^{vy}\left[\!\left[\frac{\partial u_i}{\partial y}\right]\!\right]^y\left[\!\left[\frac{\partial\delta u_i}{\partial y}\right]\!\right]^y-\left[\!\left[\frac{\partial\delta u_i}{\partial y}\right]\!\right]^y\left\{r_i(\boldsymbol{u},\phi)\right\}_\gamma^y-\left[\!\left[\frac{\partial u_i}{\partial y}\right]\!\right]^y\left\{r_i(\delta\boldsymbol{u},\delta\phi)\right\}_\gamma^y\right]\mathrm{d}\Gamma+ \\
&+\int_{\mathcal{I}^y}\left[\left([\![\delta\phi]\!]^y-\delta\check{\phi}^y\right)[\![w(\boldsymbol{u},\phi)]\!]_\gamma^y+\left([\![\phi]\!]^y-\check{\phi}^y\right)[\![w(\delta\boldsymbol{u},\delta\phi)]\!]_\gamma^y\right]\mathrm{d}\Gamma \\
&+\sum_{x\in C^y}\left[\beta^{C_uy}\,[\![\delta u_i]\!]^y\left([\![u_i]\!]^y-\hat{u}_i^y\right)-[\![\delta u_i]\!]^y\,[\![j_i(\boldsymbol{u},\phi)]\!]_\gamma^y-\left([\![u_i]\!]^y-\hat{u}_i^y\right)[\![j_i(\delta\boldsymbol{u},\delta\phi)]\!]_\gamma^y\right]. \qquad \text{(B.3)}
\end{aligned}
$$

$$
\begin{aligned}
&\delta\Pi^{\mathrm{P,x}}[\boldsymbol{u},\phi,\check{\boldsymbol{u}},\check{\phi};\delta\boldsymbol{u},\delta\phi,\delta\check{\boldsymbol{u}},\delta\check{\phi}] = \\
&\int_{\mathcal{I}^x}\left[\beta^{ux}\,[\![\delta u_i]\!]^y\left([\![u_i]\!]^y-\hat{u}_i^y\right)-[\![\delta u_i]\!]^x\,[\![t_i(\boldsymbol{u},\phi)]\!]_\gamma^x-\left([\![u_i]\!]^x-\check{u}_i^x\right)[\![t_i(\delta\boldsymbol{u},\delta\phi)]\!]_\gamma^x\right]\mathrm{d}\Gamma \\
&+\int_{\mathcal{I}^x}\left[\beta^{vx}\left[\!\left[\frac{\partial u_i}{\partial x}\right]\!\right]^x\left[\!\left[\frac{\partial\delta u_i}{\partial x}\right]\!\right]^x-\left[\!\left[\frac{\partial\delta u_i}{\partial x}\right]\!\right]^x\left\{r_i(\boldsymbol{u},\phi)\right\}_\gamma^x-\left[\!\left[\frac{\partial u_i}{\partial x}\right]\!\right]^x\left\{r_i(\delta\boldsymbol{u},\delta\phi)\right\}_\gamma^x\right]\mathrm{d}\Gamma+ \\
&+\int_{\mathcal{I}^x}\left[\left([\![\delta\phi]\!]^x-\delta\check{\phi}^x\right)[\![w(\boldsymbol{u},\phi)]\!]_\gamma^x+\left([\![\phi]\!]^x-\check{\phi}^x\right)[\![w(\delta\boldsymbol{u},\delta\phi)]\!]_\gamma^x\right]\mathrm{d}\Gamma \\
&+\sum_{y\in C^x}\left[\beta^{C_ux}\,[\![\delta u_i]\!]^x\left([\![u_i]\!]^x-\hat{u}_i^x\right)-[\![\delta u_i]\!]^x\,[\![j_i(\boldsymbol{u},\phi)]\!]_\gamma^x-\left([\![u_i]\!]^x-\check{u}_i^x\right)[\![j_i(\delta\boldsymbol{u},\delta\phi)]\!]_\gamma^x\right]. \qquad \text{(B.4)}
\end{aligned}
$$

B.3 Unconfined vertical displacement actuator

$$
\begin{aligned}
&\delta\Pi^{\mathrm{p,y}}[\boldsymbol{u},\phi,\check{\boldsymbol{u}},\check{\phi};\delta\boldsymbol{u},\delta\phi,\delta\check{\boldsymbol{u}},\delta\check{\phi}] = \\
&\int_{\mathcal{I}^y}\left[-\left(\llbracket\delta u_i\rrbracket^y-\delta\check{u}_i^y\right)\llbracket t_i(\boldsymbol{u},\phi)\rrbracket_\gamma^y-\left(\llbracket u_i\rrbracket^y-\hat{u}_i^y\right)\llbracket t_i(\delta\boldsymbol{u},\delta\phi)\rrbracket_\gamma^y\right]\mathrm{d}\Gamma \\
&+\int_{\mathcal{I}^y}\left[\beta^{vy}\left\llbracket\frac{\partial u_i}{\partial y}\right\rrbracket^y\left\llbracket\frac{\partial\delta u_i}{\partial y}\right\rrbracket^y-\left\llbracket\frac{\partial\delta u_i}{\partial y}\right\rrbracket^y\left\{r_i(\boldsymbol{u},\phi)\right\}_\gamma^y-\left\llbracket\frac{\partial u_i}{\partial y}\right\rrbracket^y\left\{r_i(\delta\boldsymbol{u},\delta\phi)\right\}_\gamma^y\right]\mathrm{d}\Gamma+ \\
&+\int_{\mathcal{I}^y}\left[\llbracket\delta\phi\rrbracket^y\llbracket w(\boldsymbol{u},\phi)\rrbracket_\gamma^y+\left(\llbracket\phi\rrbracket^y-\check{\phi}^y\right)\llbracket w(\delta\boldsymbol{u},\delta\phi)\rrbracket_\gamma^y-\beta^{\phi y}\llbracket\delta\phi\rrbracket^y\left(\llbracket\phi\rrbracket^y-\check{\phi}^y\right)\right]\mathrm{d}\Gamma \\
&+\sum_{x\in C^y}\left[-\left(\llbracket\delta u_i\rrbracket^y-\delta\check{u}_i^y\right)\llbracket j_i(\boldsymbol{u},\phi)\rrbracket_\gamma^y-\left(\llbracket u_i\rrbracket^y-\hat{u}_i^y\right)\llbracket j_i(\delta\boldsymbol{u},\delta\phi)\rrbracket_\gamma^y\right].
\end{aligned}
\tag{B.5}
$$

$$
\begin{aligned}
&\delta\Pi^{\mathrm{p,x}}[\boldsymbol{u},\phi,\check{\boldsymbol{u}},\check{\phi};\delta\boldsymbol{u},\delta\phi,\delta\check{\boldsymbol{u}},\delta\check{\phi}] = \\
&\int_{\mathcal{I}^x}\left[-\left(\llbracket\delta u_i\rrbracket^x-\delta\check{u}_i^x\right)\llbracket t_i(\boldsymbol{u},\phi)\rrbracket_\gamma^x-\left(\llbracket u_i\rrbracket^x-\hat{u}_i^x\right)\llbracket t_i(\delta\boldsymbol{u},\delta\phi)\rrbracket_\gamma^x\right]\mathrm{d}\Gamma \\
&+\int_{\mathcal{I}^x}\left[\beta^{vx}\left\llbracket\frac{\partial u_i}{\partial x}\right\rrbracket^x\left\llbracket\frac{\partial\delta u_i}{\partial x}\right\rrbracket^x-\left\llbracket\frac{\partial\delta u_i}{\partial x}\right\rrbracket^x\left\{r_i(\boldsymbol{u},\phi)\right\}_\gamma^x-\left\llbracket\frac{\partial u_i}{\partial x}\right\rrbracket^x\left\{r_i(\delta\boldsymbol{u},\delta\phi)\right\}_\gamma^x\right]\mathrm{d}\Gamma+ \\
&+\int_{\mathcal{I}^x}\left[\llbracket\delta\phi\rrbracket^x\llbracket w(\boldsymbol{u},\phi)\rrbracket_\gamma^x+\left(\llbracket\phi\rrbracket^x-\check{\phi}^x\right)\llbracket w(\delta\boldsymbol{u},\delta\phi)\rrbracket_\gamma^x-\beta^{\phi x}\llbracket\delta\phi\rrbracket^x\left(\llbracket\phi\rrbracket^x-\check{\phi}^x\right)\right]\mathrm{d}\Gamma \\
&+\sum_{y\in C^x}\left[-\left(\llbracket\delta u_i\rrbracket^x-\delta\check{u}_i^x\right)\llbracket j_i(\boldsymbol{u},\phi)\rrbracket_\gamma^x-\left(\llbracket u_i\rrbracket^x-\hat{u}_i^x\right)\llbracket j_i(\delta\boldsymbol{u},\delta\phi)\rrbracket_\gamma^x\right].
\end{aligned}
\tag{B.6}
$$

B.4 Confined vertical displacement actuator

$$
\begin{aligned}
&\delta\Pi^{\mathrm{P,y}}[\boldsymbol{u},\phi,\check{\boldsymbol{u}},\check{\phi};\delta\boldsymbol{u},\delta\phi,\delta\check{\boldsymbol{u}},\delta\check{\phi}] = \\
&\int_{\mathcal{I}^y}\left[-\left(\llbracket\delta u_i\rrbracket^y-\delta\check{u}_i^y\right)\llbracket t_i(\boldsymbol{u},\phi)\rrbracket_\gamma^y-\left(\llbracket u_i\rrbracket^y-\hat{u}_i^y\right)\llbracket t_i(\delta\boldsymbol{u},\delta\phi)\rrbracket_\gamma^y\right]\mathrm{d}\Gamma \\
&+\int_{\mathcal{I}^y}\left[\beta^{vy}\left\llbracket\frac{\partial u_i}{\partial y}\right\rrbracket^y\left\llbracket\frac{\partial\delta u_i}{\partial y}\right\rrbracket^y-\left\llbracket\frac{\partial\delta u_i}{\partial y}\right\rrbracket^y\left\{r_i(\boldsymbol{u},\phi)\right\}_\gamma^y-\left\llbracket\frac{\partial u_i}{\partial y}\right\rrbracket^y\left\{r_i(\delta\boldsymbol{u},\delta\phi)\right\}_\gamma^y\right]\mathrm{d}\Gamma+ \\
&+\int_{\mathcal{I}^y}\left[\llbracket\delta\phi\rrbracket^y\llbracket w(\boldsymbol{u},\phi)\rrbracket_\gamma^y+\left(\llbracket\phi\rrbracket^y-\check{\phi}^y\right)\llbracket w(\delta\boldsymbol{u},\delta\phi)\rrbracket_\gamma^y-\beta^{\phi y}\llbracket\delta\phi\rrbracket^y\left(\llbracket\phi\rrbracket^y-\check{\phi}^y\right)\right]\mathrm{d}\Gamma \\
&+\sum_{x\in C^y}\left[-\left(\llbracket\delta u_i\rrbracket^y-\delta\check{u}_i^y\right)\llbracket j_i(\boldsymbol{u},\phi)\rrbracket_\gamma^y-\left(\llbracket u_i\rrbracket^y-\hat{u}_i^y\right)\llbracket j_i(\delta\boldsymbol{u},\delta\phi)\rrbracket_\gamma^y\right].
\end{aligned}
\tag{B.7}
$$

$$
\begin{aligned}
&\delta\Pi^{\mathrm{P,x}}[\boldsymbol{u},\phi,\check{\boldsymbol{u}},\check{\phi};\delta\boldsymbol{u},\delta\phi,\delta\check{\boldsymbol{u}},\delta\check{\phi}] = \\
&\int_{\mathcal{I}^x}\left[\beta^{ux}\llbracket\delta u_i\rrbracket^y\left(\llbracket u_i\rrbracket^y-\hat{u}_i^y\right)-\llbracket\delta u_i\rrbracket^x\llbracket t_i(\boldsymbol{u},\phi)\rrbracket_\gamma^x-\left(\llbracket u_i\rrbracket^x-\check{u}_i^x\right)\llbracket t_i(\delta\boldsymbol{u},\delta\phi)\rrbracket_\gamma^x\right]\mathrm{d}\Gamma \\
&+\int_{\mathcal{I}^x}\left[\beta^{vx}\left\llbracket\frac{\partial u_i}{\partial x}\right\rrbracket^x\left\llbracket\frac{\partial\delta u_i}{\partial x}\right\rrbracket^x-\left\llbracket\frac{\partial\delta u_i}{\partial x}\right\rrbracket^x\left\{r_i(\boldsymbol{u},\phi)\right\}_\gamma^x-\left\llbracket\frac{\partial u_i}{\partial x}\right\rrbracket^x\left\{r_i(\delta\boldsymbol{u},\delta\phi)\right\}_\gamma^x\right]\mathrm{d}\Gamma+ \\
&+\int_{\mathcal{I}^x}\left[\llbracket\delta\phi\rrbracket^x\llbracket w(\boldsymbol{u},\phi)\rrbracket_\gamma^x+\left(\llbracket\phi\rrbracket^x-\check{\phi}^x\right)\llbracket w(\delta\boldsymbol{u},\delta\phi)\rrbracket_\gamma^x-\beta^{\phi x}\llbracket\delta\phi\rrbracket^x\left(\llbracket\phi\rrbracket^x-\check{\phi}^x\right)\right]\mathrm{d}\Gamma \\
&+\sum_{y\in C^x}\left[-\left(\llbracket\delta u_i\rrbracket^x-\delta\check{u}_i^x\right)\llbracket j_i(\boldsymbol{u},\phi)\rrbracket_\gamma^x-\left(\llbracket u_i\rrbracket^x-\hat{u}_i^x\right)\llbracket j_i(\delta\boldsymbol{u},\delta\phi)\rrbracket_\gamma^x\right].
\end{aligned}
\tag{B.8}
$$

Bibliography

A. Abdollahi and I. Arias. Constructive and destructive interplay between piezoelectricity and flexoelectricity in flexural sensors and actuators. *J. Appl. Mech.* **82**, 121003 (2015a).

A. Abdollahi, C. Peco, D. Millán, M. Arroyo, and I. Arias. Computational evaluation of the flexoelectric effect in dielectric solids. *J. Appl. Phys.* **116**, 093502 (2014).

A. Abdollahi, C. Peco, D. Millán, M. Arroyo, G. Catalan, and I. Arias. Fracture toughening and toughness asymmetry induced by flexoelectricity. *Phys. Rev. B* **92**, 094101 (2015a).

A. Abdollahi and I. Arias. Phase-field modeling of the coupled microstructure and fracture evolution in ferroelectric single crystals. *Acta Materialia* **59**, 4733 (2011a).

A. Abdollahi and I. Arias. Phase-field simulation of anisotropic crack propagation in ferroelectric single crystals: effect of microstructure on the fracture process. *Modelling and Simulation in Materials Science and Engineering* **19**, 074010 (2011b).

A. Abdollahi and I. Arias. Phase-field modeling of crack propagation in piezoelectric and ferroelectric materials with different electromechanical crack conditions. *Journal of the Mechanics and Physics of Solids* **60**, 2100 (2012).

A. Abdollahi and I. Arias. Constructive and destructive interplay between piezoelectricity and flexoelectricity in flexural sensors and actuators. *Journal of Applied Mechanics* **82**, 121003 (2015b).

A. Abdollahi, N. Domingo, I. Arias, and G. Catalan. Converse flexoelectricity yields large piezoresponse force microscopy signals in non-piezoelectric materials. *Nature communications* **10**, 1266 (2019).

A. Abdollahi, D. Millán, C. Peco, M. Arroyo, and I. Arias. Revisiting pyramid compression to quantify flexoelectricity: A three-dimensional simulation study. *Physical Review B* **91**, 104103 (2015b).

A. Abdollahi, C. Peco, D. Millán, M. Arroyo, G. Catalan, and I. Arias. Fracture toughening and toughness asymmetry induced by flexoelectricity. *Physical Review B* **92**, 094101 (2015c).

R. Ahluwalia, A. K. Tagantsev, P. Yudin, N. Setter, N. Ng, and D. J. Srolovitz. Influence of flexoelectric coupling on domain patterns in ferroelectrics. *Physical Review B* **89**, 174105 (2014).

F. Ahmadpoor, Q. Deng, L. Liu, and P. Sharma. Apparent flexoelectricity in lipid bilayer membranes due to external charge and dipolar distributions. *Physical Review E* **88**, 050701 (2013).

F. Ahmadpoor and P. Sharma. Flexoelectricity in two-dimensional crystalline and biological membranes. *Nanoscale* **7**, 16555 (2015).

B. Altan and E. Aifantis. On some aspects in the special theory of gradient elasticity. *Journal of the Mechanical Behavior of Materials* **8**, 231 (1997).

E. Amanatidou and N. Aravas. Mixed finite element formulations of strain-gradient elasticity problems. *Computer Methods in Applied Mechanics and Engineering* **191**, 1723 (2002).

M. Ambati, T. Gerasimov, and L. De Lorenzis. A review on phase-field models of brittle fracture and a new fast hybrid formulation. *Computational Mechanics* **55**, 383 (2015).

L. Ambrosio and V. M. Tortorelli. Approximation of functional depending on jumps by elliptic functional via t-convergence. *Communications on Pure and Applied Mathematics* **43**, 999 (1990).

C. Annavarapu, M. Hautefeuille, and J. E. Dolbow. A robust Nitsche's formulation for interface problems. *Computer Methods in Applied Mechanics and Engineering* **225**, 44 (2012a).

C. Annavarapu, M. Hautefeuille, and J. E. Dolbow. Stable imposition of stiff constraints in explicit dynamics for embedded finite element methods. *International Journal for Numerical Methods in Engineering* **92**, 206 (2012b).

I. Babuška, U. Banerjee, and J. E. Osborn. Meshless and generalized finite element methods: A survey of some major results. in *Meshfree methods for partial differential equations* (Springer, 2003) pp. 1–20.

J. Barceló-Mercader. *Numerical solution of PDEs in periodical domains.* Master's thesis. UPC, Facultat de Matemàtiques i Estadística, Departament d'Enginyeria Civil i Ambiental (2018).

J. Barceló-Mercader, D. Codony, S. Fernández-Méndez, and I. Arias. Weak enforcement of interface continuity and generalized periodicity in high-order electromechanical problems. *International journal for numerical methods in engineering* **123**, 901 (2022).

J. Barceló-Mercader, A. Mocci, D. Codony, and I. Arias. *High-order generalized periodicity conditions for architected materials with application to flexoelectricity* (Submitted, 2023).

S. Baskaran, X. He, Q. Chen, and J. Fu. Experimental studies on the direct flexoelectric effect in α-phase polyvinylidene fluoride films. *Appl. Phys. Lett.* **98**, 242901 (2011a).

S. Baskaran, X. He, Y. Wang, and J. Fu. Strain gradient induced electric polarization in α-phase polyvinylidene fluoride films under bending conditions. *J. Appl. Phys.* **111**, 014109 (2012).

S. Baskaran, N. Ramachandran, X. He, S. Thiruvannamalai, H. Lee, H. Heo, Q. Chen, and J. Fu. Giant flexoelectricity in polyvinylidene fluoride films. *Phys. Lett. A* **375**, 2082 (2011b).

T. Belytschko, Y. Y. Lu, and L. Gu. Element-free Galerkin methods. *International journal for numerical methods in engineering* **37**, 229 (1994).

M. Beneš, V. Chalupeckỳ, and K. Mikula. Geometrical image segmentation by the Allen–Cahn equation. *Applied Numerical Mathematics* **51**, 187 (2004).

M. J. Borden, C. V. Verhoosel, M. A. Scott, T. J. Hughes, and C. M. Landis. A phase-field description of dynamic brittle fracture. *Computer Methods in Applied Mechanics and Engineering* **217**, 77 (2012).

B. Bourdin, G. A. Francfort, and J.-J. Marigo. Numerical experiments in revisited brittle fracture. *Journal of the Mechanics and Physics of Solids* **48**, 797 (2000).

B. Bourdin, G. A. Francfort, and J.-J. Marigo. The variational approach to fracture. *Journal of elasticity* **91**, 5 (2008).

F. P. Bowden and D. Tabor. The area of contact between stationary and moving surfaces. *Proceedings of the Royal Society of London. Series A. Mathematical and Physical Sciences* **169**, 391 (1939).

L. Breger, T. Furukawa, and E. Fukada. Bending piezoelectricity in polyvinylidene fluoride. *Japanese Journal of Applied Physics* **15**, 2239 (1976).

F. Brezzi, M. Fortin, L. D. Marini, *et al.*. Efficient rectangular mixed finite elements in two and three space variables. *ESAIM: Mathematical Modelling and Numerical Analysis* **21**, 581 (1987).

E. Burman. Ghost penalty. *CR Math.* **348**, 1217 (2010).

J. Bursian and O. Zaikovskii. Changes in curvature of a ferroelectric film due to polarization. *Sov. Phys. Solid State* **10**, 1121 (1968).

G. T. Camacho and M. Ortiz. Computational modelling of impact damage in brittle materials. *International Journal of solids and structures* **33**, 2899 (1996).

R. W. Carpick and M. Salmeron. Scratching the surface: fundamental investigations of tribology with atomic force microscopy. *Chemical reviews* **97**, 1163 (1997).

G. Catalan, L. Sinnamon, and J. Gregg. The effect of flexoelectricity on the dielectric properties of inhomogeneously strained ferroelectric thin films. *J. Condens. Matter Phys.* **16**, 2253 (2004).

G. Catalan, A. Lubk, A. Vlooswijk, E. Snoeck, C. Magen, A. Janssens, G. Rispens, G. Rijnders, D. H. Blank, and B. Noheda. Flexoelectric rotation of polarization in ferroelectric thin films. *Nature materials* **10**, 963 (2011).

X. Chen, S. Xu, N. Yao, and Y. Shi. 1.6 V nanogenerator for mechanical energy harvesting using PZT nanofibers. *Nano letters* **10**, 2133 (2010).

S. Cho, I. Gaponenko, K. Cordero-Edwards, J. Barceló-Mercader, I. Arias, C. Lichtensteiger, J. Yeom, L. Musy, H. Kim, G. Catalan, *et al.*. Switchable tribology of ferroelectrics. *arXiv preprint arXiv:2208.11373* (2022).

B. Chu and D. Salem. Flexoelectricity in several thermoplastic and thermosetting polymers. *Applied Physics Letters* **101**, 103905 (2012).

B. Chu, W. Zhu, N. Li, and L. E. Cross. Flexure mode flexoelectric piezoelectric composites. *J. Appl. Phys.* **106**, 104109 (2009).

K.-H. Chung, Y.-H. Lee, D.-E. Kim, J. Yoo, and S. Hong. Tribological characteristics of probe tip and PZT media for AFM-based recording technology. *IEEE transactions on magnetics* **41**, 849 (2005).

G. Ciofani and A. Menciassi. *Piezoelectric nanomaterials for biomedical applications* (Springer, 2012).

D. Codony, A. Mocci, J. Barceló-Mercader, and I. Arias. Mathematical and computational modeling of flexoelectricity. *Journal of Applied Physics* **130**, 231102 (2021a).

D. Codony. *Mathematical and computational modeling of flexoelectricity at mesoscopic and atomistic scales* (Universitat Politècnica de Catalunya, 2021).

D. Codony, I. Arias, and P. Suryanarayana. Transversal flexoelectric coefficient for nanostructures at finite deformations from first principles. *Physical Review Materials* **5**, L030801 (2021b).

D. Codony, P. Gupta, O. Marco, and I. Arias. Modeling flexoelectricity in soft dielectrics at finite deformation. *Journal of the Mechanics and Physics of Solids* **146**, 104182 (2021c).

D. Codony, O. Marco, S. Fernández-Méndez, and I. Arias. An Immersed Boundary Hierarchical B-spline method for flexoelectricity. *Comput. Meth. Appl. Mech. Eng.* **354**, 750 (2019).

K. Cordero-Edwards, N. Domingo, A. Abdollahi, J. Sort, and G. Catalan. Ferroelectrics as smart mechanical materials. *Advanced materials* **29**, 1702210 (2017).

K. Cordero-Edwards, H. Kianirad, C. Canalias, J. Sort, and G. Catalan. Flexoelectric fracture-ratchet effect in ferroelectrics. *Physical review letters* **122**, 135502 (2019).

J. A. Cottrell, T. J. Hughes, and Y. Bazilevs. *Isogeometric analysis: toward integration of CAD and FEA* (John Wiley & Sons, 2009).

E. Cross. Lead-free at last. *Nature* **432**, 24 (2004).

L. Cross. Flexoelectric effects: Charge separation in insulating solids subjected to elastic strain gradients. *J. Mater. Sci.* **41**, 53 (2006).

J. L. Cuy, A. B. Mann, K. J. Livi, M. F. Teaford, and T. P. Weihs. Nanoindentation mapping of the mechanical properties of human molar tooth enamel. *Archives of oral biology* **47**, 281 (2002).

C. Dagdeviren, P. Joe, O. L. Tuzman, K.-I. Park, K. J. Lee, Y. Shi, Y. Huang, and J. A. Rogers. Recent progress in flexible and stretchable piezoelectric devices for mechanical energy harvesting, sensing and actuation. *Extreme Mech. Lett.* **9**, 269 (2016).

C. Dagdeviren, B. D. Yang, Y. Su, P. L. Tran, P. Joe, E. Anderson, J. Xia, V. Doraiswamy, B. Dehdashti, X. Feng, *et al.*. Conformal piezoelectric energy harvesting and storage from motions of the heart, lung, and diaphragm. *Proceedings of the National Academy of Sciences* **111**, 1927 (2014).

F. de Prenter, C. Verhoosel, G. van Zwieten, and E. van Brummelen. Condition number analysis and preconditioning of the finite cell method. *Comput. Meth. Appl. Mech. Eng.* (2016).

Q. Deng, M. Kammoun, A. Erturk, and P. Sharma. Nanoscale flexoelectric energy harvesting. *Int. J. Solid. Struct.* **51**, 3218 (2014a).

Q. Deng, L. Liu, and P. Sharma. Flexoelectricity in soft materials and biological membranes. *J. Mech. Phys. Solids* **62**, 209 (2014b).

A. Devonshire. CIX. Theory of barium titanate—Part II. *The London, Edinburgh, and Dublin Philosophical Magazine and Journal of Science* **42**, 1065 (1951).

A. F. Devonshire. XCVI. Theory of barium titanate: Part I. *The London, Edinburgh, and Dublin Philosophical Magazine and Journal of Science* **40**, 1040 (1949).

J. Dolbow and I. Harari. An efficient finite element method for embedded interface problems. *International journal for numerical methods in engineering* **78**, 229 (2009).

G. Dong, S. Li, T. Li, H. Wu, T. Nan, X. Wang, H. Liu, Y. Cheng, Y. Zhou, W. Qu, *et al.*. Periodic Wrinkle-Patterned Single-Crystalline Ferroelectric Oxide Membranes with Enhanced Piezoelectricity. *Adv. Mater.* , 2004477 (2020).

C. E. Dreyer, M. Stengel, and D. Vanderbilt. Current-density implementation for calculating flexoelectric coefficients. *Phys. Rev. B* **98**, 075153 (2018).

K.-A. N. Duerloo and E. J. Reed. Flexural electromechanical coupling: a nanoscale emergent property of boron nitride bilayers. *Nano letters* **13**, 1681 (2013).

T. Dumitrică, C. M. Landis, and B. I. Yakobson. Curvature-induced polarization in carbon nanoshells. *Chemical Physics Letters* **360**, 182 (2002).

A. Düster, J. Parvizian, Z. Yang, and E. Rank. The finite cell method for three-dimensional problems of solid mechanics. *Comput. Meth. Appl. Mech. Eng.* **197**, 3768 (2008).

E. Eliseev, A. Morozovska, M. Glinchuk, and R. Blinc. Spontaneous flexoelectric/flexomagnetic effect in nanoferroics. *Phys. Rev. B* **79**, 165433 (2009a).

E. A. Eliseev, A. N. Morozovska, M. D. Glinchuk, and R. Blinc. Spontaneous flexoelectric/flexomagnetic effect in nanoferroics. *Physical Review B* **79**, 165433 (2009b).

M. Enachescu, R. Van den Oetelaar, R. Carpick, D. Ogletree, C. Flipse, and M. Salmeron. Observation of proportionality between friction and contact area at the nanometer scale. *Tribology Letters* **7**, 73 (1999).

G. Engel, K. Garikipati, T. Hughes, M. Larson, L. Mazzei, and R. L. Taylor. Continuous/discontinuous finite element approximations of fourth-order elliptic problems in structural and continuum mechanics with applications to thin beams and plates, and strain gradient elasticity. *Computer Methods in Applied Mechanics and Engineering* **191**, 3669 (2002).

X. Feng and A. Prohl. Error analysis of a mixed finite element method for the Cahn-Hilliard equation. *Numerische Mathematik* **99**, 47 (2004).

X. Feng, B. D. Yang, Y. Liu, Y. Wang, C. Dagdeviren, Z. Liu, A. Carlson, J. Li, Y. Huang, and J. A. Rogers. Stretchable ferroelectric nanoribbons with wavy configurations on elastomeric substrates. *Acs Nano* **5**, 3326 (2011).

S. Fernández-Méndez and A. Huerta. Imposing essential boundary conditions in mesh-free methods. *Comput. Meth. Appl. Mech. Eng.* **193**, 1257 (2004).

J. Fish and T. Belytschko. *A first course in finite elements*. Vol. 1 (Wiley New York, 2007).

J. Fousek, L. Cross, and D. Litvin. Possible piezoelectric composites based on the flexoelectric effect. *Mat. Lett.* **39**, 287 (1999).

G. A. Francfort and J.-J. Marigo. Revisiting brittle fracture as an energy minimization problem. *Journal of the Mechanics and Physics of Solids* **46**, 1319 (1998).

M. J. Frazier and D. M. Kochmann. Atomimetic mechanical structures with nonlinear topological domain evolution kinetics. *Advanced Materials* **29**, 1605800 (2017).

J. Y. Fu, W. Zhu, N. Li, and L. E. Cross. Experimental studies of the converse flexoelectric effect induced by inhomogeneous electric field in a barium strontium titanate composition. *J. Appl. Phys.* **100**, 024112 (2006).

J. Y. Fu, W. Zhu, N. Li, N. B. Smith, and L. Eric Cross. Gradient scaling phenomenon in microsize flexoelectric piezoelectric composites. *Appl. Phys. Lett.* **91**, 182910 (2007).

G. Gautschi. *Piezoelectric Sensorics: Force Strain Pressure Acceleration and Acoustic Emission Sensors Materials and Amplifiers* (Springer Science & Business Media, 2006).

M. Grasinger, K. Mozaffari, and P. Sharma. Flexoelectricity in soft elastomers and the molecular mechanisms underpinning the design and emergence of giant flexoelectricity. *Proceedings of the National Academy of Sciences* **118**, e2102477118 (2021).

M. Griebel and M. A. Schweitzer. A particle-partition of unity method part V: boundary conditions. in *Geometric analysis and nonlinear partial differential equations* (Springer, 2003) pp. 519–542.

J. K. Han, D. H. Jeon, S. Y. Cho, S. W. Kang, S. A. Yang, S. D. Bu, S. Myung, J. Lim, M. Choi, M. Lee, *et al.*. Nanogenerators consisting of direct-grown piezoelectrics on multi-walled carbon nanotubes using flexoelectric effects. *Sci. Rep.* **6**, 1 (2016).

P. Hana. Study of flexoelectric phenomenon from direct and from inverse flexoelectric behavior of PMNT ceramic. *Ferroelectrics* **351**, 196 (2007).

P. Hana, M. Marvan, L. Burianova, S. Zhang, E. Furman, and T. R. Shrout. Study of the inverse flexoelectric phenomena in ceramic lead magnesium niobate-lead titanate. *Ferroelectrics* **336**, 137 (2006).

B. Hassani and E. Hinton. A review of homogenization and topology optimization I—homogenization theory for media with periodic structure. *Computers & Structures* **69**, 707 (1998).

R. Hill. Elastic properties of reinforced solids: some theoretical principles. *Journal of the Mechanics and Physics of Solids* **11**, 357 (1963).

R. Hill. The essential structure of constitutive laws for metal composites and polycrystals. *Journal of the Mechanics and Physics of Solids* **15**, 79 (1967).

K. Höllig, J. Hörner, and A. Hoffacker. Finite element analysis with B-splines: weighted and isogeometric methods. in *International Conference on Curves and Surfaces* (Springer, 2012) pp. 330–350.

K. Höllig, U. Reif, and J. Wipper. Weighted extended B-spline approximation of Dirichlet problems. *SIAM J. Numer. Anal.* **39**, 442 (2001).

C.-H. Hong, H.-P. Kim, B.-Y. Choi, H.-S. Han, J. S. Son, C. W. Ahn, and W. Jo. Lead-free piezoceramics–Where to move on? *J. Materiomics* **2**, 1 (2016).

J. Hong and D. Vanderbilt. First-principles theory and calculation of flexoelectricity. *Phys. Rev. B* **88**, 174107 (2013).

S. Huang, T. Kim, D. Hou, D. Cann, J. L. Jones, and X. Jiang. Flexoelectric characterization of BaTiO3-0.08 Bi (Zn1/2Ti1/2) O3. *Appl. Phys. Lett.* **110**, 222904 (2017).

W. Huang, K. Kim, S. Zhang, F.-G. Yuan, and X. Jiang. Scaling effect of flexoelectric (Ba, Sr) TiO3 microcantilevers. *Phys. Stat. Solid. RRL* **5**, 350 (2011).

W. Huang, X. Yan, S. R. Kwon, S. Zhang, F.-G. Yuan, and X. Jiang. Flexoelectric strain gradient detection using Ba0. 64Sr0. 36TiO3 for sensing. *Applied Physics Letters* **101**, 252903 (2012).

R. Indergand, A. Vidyasagar, N. Nadkarni, and D. M. Kochmann. A phase-field approach to studying the temperature-dependent ferroelectric response of bulk polycrystalline PZT. *Journal of the Mechanics and Physics of Solids* **144**, 104098 (2020).

D. Jacqmin. Calculation of two-phase Navier–Stokes flows using phase-field modeling. *Journal of computational physics* **155**, 96 (1999).

W. Jiang, C. Annavarapu, J. E. Dolbow, and I. Harari. A robust Nitsche's formulation for interface problems with spline-based finite elements. *International Journal for Numerical Methods in Engineering* **104**, 676 (2015).

S. V. Kalinin and V. Meunier. Electronic flexoelectricity in low-dimensional systems. *Phys. Rev. B* **77**, 033403 (2008).

V. Kannan, M. Trassin, and D. M. Kochmann. Kinetics of ferroelectric switching in poled barium titanate ceramics: Effects of electrical cycling rate. *Materialia* **25**, 101553 (2022).

B. Karlsson, D. Pourcelot, L. Pourcelot, and M. Berson. Miniature sensor for Doppler ultrasound Fetal Heart Rate monitoring. Increased patient comfort and ergonomy in use. in *Quality Measurement: The Indispensable Bridge between Theory and Reality (No Measurements? No Science! Joint Conference-1996: IEEE Instrumentation and Measurement Technology Conference and IMEKO Tec.* Vol. 2 (IEEE, 1996) pp. 1336–1338.

S. M. Kogan. Piezoelectric effect during inhomogeneous deformation and acoustic scattering of carriers in crystals. *Sov. Phys. Solid State* **5**, 2069 (1964).

A. Kolpakov. Calculation of the characteristics of thin elastic rods with a periodic structure. *Journal of Applied Mathematics and Mechanics* **55**, 358 (1991).

S. Krichen and P. Sharma. Flexoelectricity: A perspective on an unusual electromechanical coupling. *J. Appl. Mech.* **83**, 030801 (2016).

S. Kumar, D. Codony, I. Arias, and P. Suryanarayana. Flexoelectricity in atomic monolayers from first principles. *Nanoscale* **13**, 1600 (2021).

S. R. Kwon, W. Huang, L. Shu, F.-G. Yuan, J.-P. Maria, and X. Jiang. Flexoelectricity in barium strontium titanate thin film. *Appl. Phys. Lett.* **105**, 142904 (2014).

L. D. Landau. On the theory of phase transitions. I. *Zh. Eksp. Teor. Fiz.* **11**, 19 (1937).

L. D. Landau and E. M. Lifshitz. *Statistical Physics: Volume 5.* Vol. 5 (Elsevier, 2013).

T. A. Laursen, M. A. Puso, and J. Sanders. Mortar contact formulations for deformable–deformable contact: past contributions and new extensions for enriched and embedded interface formulations. *Computer methods in applied mechanics and engineering* **205**, 3 (2012).

H. Le Quang and Q.-C. He. The number and types of all possible rotational symmetries for flexoelectric tensors. *Proceedings of the Royal Society of London A: Mathematical, Physical and Engineering Sciences* **467**, 2369 (2011).

G. Legrain. A NURBS enhanced extended finite element approach for unfitted CAD analysis. *Comput. Mech.* **52**, 913 (2013).

Y. Li, L. Shu, W. Huang, X. Jiang, and H. Wang. Giant flexoelectricity in Ba0. 6Sr0. 4TiO3/Ni0. 8Zn0. 2Fe2O4 composite. *Appl. Phys. Lett.* **105**, 162906 (2014).

Y. Li, L. Shu, Y. Zhou, J. Guo, F. Xiang, L. He, and H. Wang. Enhanced flexoelectric effect in a non-ferroelectric composite. *Appl. Phys. Lett.* **103**, 142909 (2013).

Z. Li, G. Zhu, R. Yang, A. C. Wang, and Z. L. Wang. Muscle-driven in vivo nanogenerator. *Advanced materials* **22**, 2534 (2010).

C. Liu, H. Wu, and J. Wang. Giant piezoelectric response in piezoelectric/dielectric superlattices due to flexoelectric effect. *Appl. Phys. Lett.* **109**, 192901 (2016a).

G. Liu, Q. Li, M. A. Msekh, and Z. Zuo. Abaqus implementation of monolithic and staggered schemes for quasi-static and dynamic fracture phase-field model. *Computational Materials Science* **121**, 35 (2016b).

L. Liu. An energy formulation of continuum magneto-electro-elasticity with applications. *J. Mech. Phys. Solids* **63**, 451 (2014).

H. Lu, C.-W. Bark, D. E. De Los Ojos, J. Alcala, C.-B. Eom, G. Catalan, and A. Gruverman. Mechanical writing of ferroelectric polarization. *Science* **336**, 59 (2012).

W. Ma and L. Cross. Flexoelectric polarization of barium strontium titanate in the paraelectric state. *Appl. Phys. Lett.* **81**, 3440 (2002).

W. Ma and L. E. Cross. Large flexoelectric polarization in ceramic lead magnesium niobate. *Applied Physics Letters* **79**, 4420 (2001a).

W. Ma and L. E. Cross. Observation of the flexoelectric effect in relaxor Pb ($Mg_{1/3}$ $Nb_{2/3}$) O_3 ceramics. *Applied Physics Letters* **78**, 2920 (2001b).

W. Ma and L. E. Cross. Strain-gradient-induced electric polarization in lead zirconate titanate ceramics. *Applied Physics Letters* **82**, 3293 (2003).

S. Mao and P. K. Purohit. Insights into flexoelectric solids from strain-gradient elasticity. *Journal of Applied Mechanics* **81** (2014).

R. Maranganti, N. Sharma, and P. Sharma. Electromechanical coupling in nonpiezoelectric materials due to nanoscale nonlocal size effects: Green's function solutions and embedded inclusions. *Phys. Rev. B* **74**, 014110 (2006a).

R. Maranganti, N. Sharma, and P. Sharma. Electromechanical coupling in nonpiezoelectric materials due to nanoscale nonlocal size effects: Green's function solutions and embedded inclusions. *Physical Review B* **74**, 014110 (2006b).

O. Marco, R. Sevilla, Y. Zhang, J. J. Ródenas, and M. Tur. Exact 3D boundary representation in finite element analysis based on Cartesian grids independent of the geometry. *Int. J. Num. Meth. Eng.* **103**, 445 (2015).

M. Marvan and A. Havránek. Flexoelectric effect in elastomers. in *Relationships of Polymeric Structure and Properties* (Springer, 1998) pp. 33–36.

V. S. Mashkevich and K. B. Tolpygo. Electrical, optical and elastic properties of diamond type cristals. 1. *Sov. Phys. Solid State* **5**, 435 (1957).

V. I. Merupo, B. Guiffard, R. Seveno, M. Tabellout, and A. Kassiba. Flexoelectric response in soft polyurethane films and their use for large curvature sensing. *Journal of Applied Physics* **122**, 144101 (2017).

R. B. Meyer. Piezoelectric effects in liquid crystals. *Phys. Rev. Lett.* **22**, 918 (1969).

C. Miehe, F. Welschinger, and M. Hofacker. Thermodynamically consistent phase-field models of fracture: Variational principles and multi-field FE implementations. *International journal for numerical methods in engineering* **83**, 1273 (2010).

R. D. Mindlin and N. N. Eshel. On first strain-gradient theories in linear elasticity. *Int. J. Solids Struct.* **4**, 109 (1968).

R. Mindlin. Archives for Rational Mechanics and Analysis 16, 51-78. (1964).

A. Mocci. *Computational modeling and rational design of flexoelectric metamaterials and devices* (Universitat Politècnica de Catalunya, 2021).

A. Mocci, A. Abdollahi, and I. Arias. *Characterization of the elusive shear flexoelectric coefficient* (Submitted, 2023).

A. Mocci, J. Barceló-Mercader, D. Codony, and I. Arias. Geometrically polarized architected dielectrics with apparent piezoelectricity. *Journal of the Mechanics and Physics of Solids* **157**, 104643 (2021).

N. Moës, J. Dolbow, and T. Belytschko. A finite element method for crack growth without remeshing. *International journal for numerical methods in engineering* **46**, 131 (1999).

A. Muixí, O. Marco, A. Rodríguez-Ferran, and S. Fernández-Méndez. A combined XFEM phase-field computational model for crack growth without remeshing. *Computational Mechanics* **67**, 231 (2021).

J. Narvaez and G. Catalan. Origin of the enhanced flexoelectricity of relaxor ferroelectrics. *Appl. Phys. Lett.* **104**, 162903 (2014).

J. Narvaez, S. Saremi, J. Hong, M. Stengel, and G. Catalan. Large flexoelectric anisotropy in paraelectric barium titanate. *Phys. Rev. Lett.* **115**, 037601 (2015).

T. D. Nguyen, S. Mao, Y.-W. Yeh, P. K. Purohit, and M. C. McAlpine. Nanoscale flexoelectricity. *Advanced Materials* **25**, 946 (2013).

J. Nitsche. Über ein Variationsprinzip zur LBsung van Dirichlet–Problemen bei Verwendung van Teilrümen, die keinen Handbedingungen unterworfen sind. in *Abhandlungen aus dem mathematischen Seminar der Universität Hamburg*. Vol. 36 (1970) pp. 1970–1971.

J. S. Oghalai, H.-B. Zhao, J. W. Kutz, and W. E. Brownell. Voltage-and tension-dependent lipid mobility in the outer hair cell plasma membrane. *Science* **287**, 658 (2000).

J. Oliver, A. E. Huespe, M. Pulido, and E. Chaves. From continuum mechanics to fracture mechanics: the strong discontinuity approach. *Engineering fracture mechanics* **69**, 113 (2002).

K.-I. Park, S. Xu, Y. Liu, G.-T. Hwang, S.-J. L. Kang, Z. L. Wang, and K. J. Lee. Piezoelectric $BaTiO_3$ thin film nanogenerator on plastic substrates. *Nano letters* **10**, 4939 (2010).

S. M. Park, B. Wang, S. Das, S. C. Chae, J.-S. Chung, J.-G. Yoon, L.-Q. Chen, S. M. Yang, and T. W. Noh. Selective control of multiple ferroelectric switching pathways using a trailing flexoelectric field. *Nat. Nanotech.* **13**, 366 (2018).

A. W. Peng, F. T. Salles, B. Pan, and A. J. Ricci. Integrating the biophysical and molecular mechanisms of auditory hair cell mechanotransduction. *Nat. Commun.* **2**, 1 (2011).

K. Persson. Materials Data on LiNbO3 (SG:161) by Materials Project. (2014). an optional note.

A. G. Petrov. Flexoelectricity of model and living membranes. *Biochimica et Biophysica Acta (BBA)-Biomembranes* **1561**, 1 (2002).

L. Piegl and W. Tiller. *The NURBS Book*. Monographs in Visual Communication (Springer Berlin Heidelberg, 2012).

V. L. Popov, M. Heß, and E. Willert. *Handbook of contact mechanics: exact solutions of axisymmetric contact problems* (Springer Nature, 2019).

R. Resta. Towards a bulk theory of flexoelectricity. *Phys. Rev. Lett.* **105**, 127601 (2010).

T. Rüberg and F. Cirak. Subdivision-stabilised immersed b-spline finite elements for moving boundary flows. *Comput. Meth. Appl. Mech. Eng.* **209**, 266 (2012).

T. Rüberg, F. Cirak, and J. M. García Aznar. An unstructured immersed finite element method for nonlinear solid mechanics. *Advanced Modeling and Simulation in Engineering Sciences* **3**, 22 (2016).

M. Safaei, H. A. Sodano, and S. R. Anton. A review of energy harvesting using piezoelectric materials: state-of-the-art a decade later (2008–2018). *Smart Materials and Structures* **28**, 113001 (2019).

E. Sahin and S. Dost. A strain-gradients theory of elastic dielectrics with spatial dispersion. *Int. J. Eng. Sci.* **26**, 1231 (1988).

Y. Saito, H. Takao, T. Tani, T. Nonoyama, K. Takatori, T. Homma, T. Nagaya, and M. Nakamura. Lead-free piezoceramics. *Nature* **432**, 84 (2004).

D. Schillinger and M. Ruess. The Finite Cell Method: A Review in the Context of Higher-Order Structural Analysis of CAD and Image-Based Geometric Models. *Archives of Computational Methods in Engineering* **22**, 391 (2015).

R. Sevilla and S. Fernández-Méndez. Numerical integration over 2D NURBS-shaped domains with applications to NURBS-enhanced FEM. *Finite Elements in Analysis and Design* **47**, 1209 (2011).

R. Sevilla, S. Fernández-Méndez, and A. Huerta. NURBS-enhanced finite element method (NEFEM). *Int. J. Num. Meth. Eng.* **76**, 56 (2008).

R. Sevilla, S. Fernández-Méndez, and A. Huerta. 3D NURBS-enhanced finite element method (NEFEM). *Int. J. Num. Meth. Eng.* **88**, 103 (2011a).

R. Sevilla, S. Fernández-Méndez, and A. Huerta. NURBS-enhanced finite element method (NEFEM). *Archives of Computational Methods in Engineering* **18**, 441 (2011b).

N. Sharma, C. Landis, and P. Sharma. Piezoelectric thin-film superlattices without using piezoelectric materials. *Journal of Applied Physics* **108**, 024304 (2010).

N. Sharma, R. Maranganti, and P. Sharma. On the possibility of piezoelectric nanocomposites without using piezoelectric materials. *Journal of the Mechanics and Physics of Solids* **55**, 2328 (2007).

S. Shen and S. Hu. A theory of flexoelectricity with surface effect for elastic dielectrics. *J. Mech. Phys. Solids* **58**, 665 (2010).

W. Shi, Y. Guo, Z. Zhang, and W. Guo. Flexoelectricity in Monolayer Transition Metal Dichalcogenides. *The Journal of Physical Chemistry Letters* **9**, 6841 (2018).

L. Shu, S. Ke, L. Fei, W. Huang, Z. Wang, J. Gong, X. Jiang, L. Wang, F. Li, S. Lei, *et al.*. Photoflexoelectric effect in halide perovskites. *Nat. Mater.* , 1 (2020).

L. Shu, T. Li, Z. Wang, F. Li, L. Fei, Z. Rao, M. Ye, S. Ke, W. Huang, Y. Wang, *et al.*. Flexoelectric behavior in PIN-PMN-PT single crystals over a wide temperature range. *Appl. Phys. Lett.* **111**, 162901 (2017).

L. Shu, T. Wang, X. Jiang, and W. Huang. Verification of the flexoelectricity in barium strontium titanate through d_{33} meter. *AIP Adv.* **6**, 125003 (2016).

L. Shu, X. Wei, L. Jin, Y. Li, H. Wang, and X. Yao. Enhanced direct flexoelectricity in paraelectric phase of $Ba(Ti_{0.87}Sn_{0.13})O_3$ ceramics. *Appl. Phys. Lett.* **102**, 152904 (2013).

L. Shu, X. Wei, T. Pang, X. Yao, and C. Wang. Symmetry of flexoelectric coefficients in crystalline medium. *J. Appl. Phys.* **110**, 104106 (2011).

N. Sinha, G. E. Wabiszewski, R. Mahameed, V. V. Felmetsger, S. M. Tanner, R. W. Carpick, and G. Piazza. Piezoelectric aluminum nitride nanoelectromechanical actuators. *Applied Physics Letters* **95**, 053106 (2009).

M. Stengel. Flexoelectricity from density-functional perturbation theory. *Phys. Rev. B* **88**, 174106 (2013).

M. Stengel. Surface control of flexoelectricity. *Phys. Rev. B* **90**, 201112 (2014).

S. Su, H. Huang, Y. Liu, and Z. H. Zhu. Wrinkling of flexoelectric nano-film/substrate systems. *J. Phys. D* **51**, 075309 (2018).

A. K. Tagantsev. Piezoelectricity and flexoelectricity in crystalline dielectrics. *Phys. Rev. B* **34**, 5883 (1986).

A. K. Tagantsev. Electric polarization in crystals and its response to thermal and elastic perturbations. *Phase Transitions: A Multinational Journal* **35**, 119 (1991).

S. Terry, J. Eckerle, R. Kornbluh, T. Low, and C. Ablow. Silicon pressure transducer arrays for blood-pressure measurement. *Sensors and Actuators A: Physical* **23**, 1070 (1990).

A. Todorov, A. Petrov, M. O. Brandt, and J. H. Fendler. Electrical and real-time stroboscopic interferometric measurements of bilayer lipid membrane flexoelectricity. *Langmuir* **7**, 3127 (1991).

K. Tolpygo. Long wavelength oscillations of diamond-type crystals including long range forces. *Sov. Phys. Solid State* **4**, 1297 (1963).

F. Vásquez Sancho. *Flexoelectricity in biomaterials*. Ph.D. thesis. Universitat Autònoma de Barcelona (2018).

F. Vasquez-Sancho, A. Abdollahi, D. Damjanovic, and G. Catalan. Flexoelectricity in bones. *Adv. Mater.* **30**, 1705316 (2018).

J. Ventura, D. Codony, and S. Fernández-Méndez. A C0 interior penalty finite element method for flexoelectricity. *Journal of Scientific Computing* **88**, 1 (2021).

B. Wang, Y. Gu, S. Zhang, and L.-Q. Chen. Flexoelectricity in solids: Progress, challenges, and perspectives. *Prog. Mater Sci.* (2019).

Y. Wang, Y. Tang, Y. Zhu, Y. Feng, and X. Ma. Converse flexoelectricity around ferroelectric domain walls. *Acta Materialia* **191**, 158 (2020).

Z. Wang, J. Hu, and M.-F. Yu. Axial polarization switching in ferroelectric BaTiO3 nanowire. *Nanotechnology* **18**, 235203 (2007).

J. C. Weaver, G. W. Milliron, A. Miserez, K. Evans-Lutterodt, S. Herrera, I. Gallana, W. J. Mershon, B. Swanson, P. Zavattieri, E. DiMasi, *et al.*. The stomatopod dactyl club: a formidable damage-tolerant biological hammer. *Science* **336**, 1275 (2012).

U. G. Wegst, H. Bai, E. Saiz, A. P. Tomsia, and R. O. Ritchie. Bioinspired structural materials. *Nature materials* **14**, 23 (2015).

F. Witherden and P. Vincent. On the identification of symmetric quadrature rules for finite element methods. *Computers & Mathematics with Applications* **69**, 1232 (2015).

P. Wriggers and T. A. Laursen. *Computational contact mechanics*. Vol. 2 (Springer, 2006).

J. Wu. Perovskite lead-free piezoelectric ceramics. *Journal of Applied Physics* **127**, 190901 (2020).

W. Wu, S. Bai, M. Yuan, Y. Qin, Z. L. Wang, and T. Jing. Lead zirconate titanate nanowire textile nanogenerator for wearable energy-harvesting and self-powered devices. *ACS nano* **6**, 6231 (2012).

X.-P. Xu and A. Needleman. Numerical simulations of fast crack growth in brittle solids. *Journal of the Mechanics and Physics of Solids* **42**, 1397 (1994).

Z. Yan and L. Jiang. Flexoelectric effect on the electroelastic responses of bending piezoelectric nanobeams. *J. Appl. Phys.* **113**, 194102 (2013).

M.-M. Yang, D. J. Kim, and M. Alexe. Flexo-photovoltaic effect. *Science* **360**, 904 (2018).

N. A. Yaraghi, N. Guarín-Zapata, L. K. Grunenfelder, E. Hintsala, S. Bhowmick, J. M. Hiller, M. Betts, E. L. Principe, J.-Y. Jung, L. Sheppard, *et al.*. A sinusoidally architected helicoidal biocomposite. *Adv. Mater.* **28**, 6835 (2016).

V. A. Yastrebov. *Numerical methods in contact mechanics* (John Wiley & Sons, 2013).

P. Yudin and A. Tagantsev. Fundamentals of flexoelectricity in solids. *Nanotechnology* **24**, 1 (2013).

W. Zhang and K. Bhattacharya. A computational model of ferroelectric domains. Part I: model formulation and domain switching. *Acta materialia* **53**, 185 (2005).

Y. Zhou, J. Liu, X. Hu, B. Chu, S. Chen, and D. Salem. Flexoelectric effect in PVDF-based polymers. *IEEE Transactions on Dielectrics and Electrical Insulation* **24**, 727 (2017).

T. Zhu and S. Atluri. A modified collocation method and a penalty formulation for enforcing the essential boundary conditions in the element free Galerkin method. *Computational Mechanics* **21**, 211 (1998).

W. Zhu, J. Y. Fu, N. Li, and L. Cross. Piezoelectric composite based on the enhanced flexoelectric effects. *Applied physics letters* **89**, 192904 (2006).

X. Zhuang, B. H. Nguyen, S. S. Nanthakumar, T. Q. Tran, N. Alajlan, and T. Rabczuk. Computational Modeling of Flexoelectricity: A Review. *Energies* **13**, 1326 (2020).

P. Zubko, G. Catalan, A. Buckley, P. Welche, and J. Scott. Strain-gradient-induced polarization in $SrTiO_3$ single crystals. *Phys. Rev. Lett.* **99**, 167601 (2007).

P. Zubko, G. Catalan, and A. K. Tagantsev. Flexoelectric effect in solids. *Annu. Rev. Mat. Res.* **24**, 387 (2013).